

6

FINAL SCIENTIFIC REPORT

for the period

1 October 1979 - 30 September 1983

on

CONSTITUTIVE MODELS FOR STATIC AND DYNAMIC RESPONSE
OF GEOTECHNICAL MATERIALS

Grant No. AFOSR-80-0017

S. Nemat-Nasser, Principal Investigator
Northwestern University, Evanston, IL 60201

AD A139293

DTIC FILE COPY

November 1983

DTIC
ELECTE
MAR 23 1984
S D

Approved for public release;
distribution unlimited.

84 03 22 110

REPORT DOCUMENTATION PAGE

1a. REPORT SECURITY CLASSIFICATION Unclassified		1b. RESTRICTIVE MARKINGS	
2a. SECURITY CLASSIFICATION AUTHORITY		3. DISTRIBUTION/AVAILABILITY OF REPORT Approved for public release; distribution unlimited	
2b. DECLASSIFICATION/DOWNGRADING SCHEDULE			
4. PERFORMING ORGANIZATION REPORT NUMBER(S)		5. MONITORING ORGANIZATION REPORT NUMBER(S) AFOSR-TR- 84-0161	
6a. NAME OF PERFORMING ORGANIZATION Department of Civil Engrg. Northwestern University	6b. OFFICE SYMBOL (If applicable)	7a. NAME OF MONITORING ORGANIZATION AFOSR	
6c. ADDRESS (City, State and ZIP Code) Evanston, IL 60201		7b. ADDRESS (City, State and ZIP Code) Bolling Air Force Base, D.C. 20332	
8a. NAME OF FUNDING/SPONSORING AIR FORCE OFFICE OF SCIENTIFIC RESEARCH	8b. OFFICE SYMBOL (If applicable) AFOSR/NA	9. PROCUREMENT INSTRUMENT IDENTIFICATION NUMBER AFOSR 80-0017	
8c. ADDRESS (City, State and ZIP Code) Bldg. 410 Bolling AFB, DC 20332		10. SOURCE OF FUNDING NOS.	
		PROGRAM ELEMENT NO. 61102F	PROJECT NO. 2307
		TASK NO. 61	WORK UNIT NO.
11. TITLE (Include Security Classification) "Constitutive Models ...of Geotechnical Materials" (Unclassified)			
12. PERSONAL AUTHOR(S) Nemat-Nasser, S.			
13a. TYPE OF REPORT Final Report	13b. TIME COVERED FROM 10/1/79 TO 9/30/83	14. DATE OF REPORT (Yr., Mo., Day) November 1983	15. PAGE COUNT 284
16. SUPPLEMENTARY NOTATION			
17. COSATI CODES		18. SUBJECT TERMS (Continue on reverse if necessary and identify by block number)	
FIELD	GROUP	SUB. GR.	Nonlinear constitutive relations; soils; rocks; liquefaction.
19. ABSTRACT (Continue on reverse if necessary and identify by block number) The objective of this research program has been to develop realistic macroscopic constitutive relations which describe static and dynamic properties of geotechnical materials (soils and rocks). To this end a coordinated theoretical and experimental activity has been followed. The theoretical work includes a balanced combination of statistical microscopic (at the grain size level) modeling and a nonclassical elasto-plastic macroscopic formulation. The latter includes the effects of internal friction, plastic compressibility, and pressure sensitivity, as well as anisotropy which is commonly observed in geotechnical materials. The following specific goals have been sought: (a) to develop three-dimensional constitutive relations under ordinary or high pressures (such as those induced by blasting or tectonic forces which may cause a large amount of densification by relative motion and possible crushing of grains); and (b) to examine and characterize the behavior of saturated granular materials under dynamic loading. The latter item includes characterization of possible liquefaction and subsidence (cont'd on reverse)			
20. DISTRIBUTION/AVAILABILITY OF ABSTRACT UNCLASSIFIED/UNLIMITED <input checked="" type="checkbox"/> SAME AS RPT. <input checked="" type="checkbox"/> DTIC USERS <input type="checkbox"/>		21. ABSTRACT SECURITY CLASSIFICATION Unclassified	
22a. NAME OF RESPONSIBLE INDIVIDUAL LAWRENCE D HOKANSON, Lt Col, USAF		22b. TELEPHONE NUMBER (Include Area Code) (202) 767-4935	22c. OFFICE SYMBOL AFOSR/NA

19. ABSTRACT (cont'd)

which may be induced in granular materials under confining pressure by ground vibration or passage of waves.

The theoretical work has been carefully coordinated with key experiments in order to: (a) understand the basic physics of the process, both at macroscopic and microscopic levels; (b) to verify the corresponding theoretical predictions; and (c) to establish relevant material parameters.

Accession For	
NTIS GRA&I	<input checked="" type="checkbox"/>
DTIC TAB	<input type="checkbox"/>
Unannounced	<input type="checkbox"/>
Justification	
By	
Distribution/	
Availability Codes	
Dist	Avail and/or Special
ALL	

DTIC
COPY
INSTRUMENTS

S DTIC
ELECTE **D**
MAR 23 1984
D

FINAL SCIENTIFIC REPORT

for the period

1 October 1979 - 30 September 1983

on

CONSTITUTIVE MODELS FOR STATIC AND DYNAMIC RESPONSE
OF GEOTECHNICAL MATERIALS

Grant No. AFOSR 80-0017

S. Nemat-Nasser, Principal Investigator
Northwestern University, Evanston, IL 60201

Table of Contents

	Page
RESEARCH OBJECTIVES	iii
ORGANIZATION OF THIS REPORT	iv
CHAPTER I	1
Research Accomplishments	3
1. Mechanics of Granular Materials	3
2. Mechanics of Rocks	12
3. List of Publications Completed Under This Grant	15
4. Professional Personnel Associated with the Research Project; Degrees Awarded	18
5. Interactions (Coupling Activities)	20
CHAPTER II	25
"Liquefaction and Densification of Cohesionless Granular Masses in Cyclic Shearing" by S. Nemat-Nasser	25
CHAPTER III	77
"Does Preliquefaction or Prestraining Reduce Sands' Resistance to Reliquefaction or Densification?" by S. Nemat-Nasser and K. Takahashi	77
CHAPTER IV	129
"Compression-Induced Micro-Crack Growth in Brittle Solids: Axial Splitting and Shear Failure" by H. Horii and S. Nemat-Nasser	129
CHAPTER V	211
"Finite Strain Rock Plasticity: Stress Triaxiality, Pressure, and Temperature Effects" by B. Rowshandel and S. Nemat-Nasser	211

AIR FORCE OFFICE OF SCIENTIFIC RESEARCH (AFOSR)
NOTICE OF TECHNICAL INFORMATION

November 1983 This technical report has been reviewed and is approved for public release in accordance with AFOSR 190-12. Distribution is unlimited.

MATTHEW J. KERPER
Chief, Technical Information Division

RESEARCH OBJECTIVES

The objective of this research program has been to develop realistic macroscopic constitutive relations which describe static and dynamic properties of geotechnical materials (soils and rocks). To this end a coordinated theoretical and experimental activity has been followed.

The theoretical work includes a balanced combination of statistical microscopic (at the grain size level) modeling and a nonclassical elasto-plastic macroscopic formulation. The latter includes the effects of internal friction, plastic compressibility, and pressure sensitivity, as well as anisotropy which is commonly observed in geotechnical materials. The following specific goals have been sought: (a) to develop three-dimensional constitutive relations under ordinary or high pressures (such as those induced by blasting or tectonic forces which may cause a large amount of densification by relative motion and possible crushing of grains); and (b) to examine and characterize the behavior of saturated granular materials under dynamic loading. The latter item includes characterization of possible liquefaction and subsidence which may be induced in granular materials under confining pressure by ground vibration or passage of waves.

The theoretical work has been carefully coordinated with key experiments in order to: (a) understand the basic physics of the process, both at macroscopic and microscopic levels; (b) to verify the

corresponding theoretical predictions; and (c) to establish relevant material parameters.

ORGANIZATION OF THIS REPORT

This report is organized in the following manner.

In Chapter I we divide the basic research area into several logical units, discuss briefly each logical unit, and list papers that have been completed in each unit, together with a brief abstract of each paper. At the end of Chapter I a list of scientific articles completed under this project is given. In Chapter I, we also give the list of participants and related information. Chapters II-V each presents a complete research effort which although finished, has not yet been published.

CHAPTER I

Table of Contents

	Page
RESEARCH ACCOMPLISHMENTS	3
1. MECHANICS OF GRANULAR MATERIALS	3
1.1. Fabric and Micromechanics of Granular Materials	4
1.2. The Influence of Fabric on Densification and Liquefaction of Granular Masses	9
1.3. Phenomenological Plasticity Approach	10
2. MECHANICS OF ROCKS	12
3. LIST OF PUBLICATIONS COMPLETED UNDER THIS GRANT	15
4. PROFESSIONAL PERSONNEL ASSOCIATED WITH THE RESEARCH PROJECT; DEGREES AWARDED	18
5. INTERACTIONS (COUPLING ACTIVITIES)	20
A. Participation of Principal Investigator at Meetings; Papers Presented, Lectures at Seminars	20
B. Consultative and Advisory Functions to Other Agencies or Laboratories	23

CHAPTER I

RESEARCH ACCOMPLISHMENTS

The research carried out at Northwestern University under grant No. AFOSR 80-0017 has been a coordinated experimental and theoretical effort to understand and quantify the mechanical behavior of geomaterials (soil and rocks) under moderate, as well as high pressures. The research includes both micromechanical modeling and phenomenological plasticity. Broadly speaking, two categories of investigation can be identified: the mechanics of granular materials; and the mechanics of rocks. In the sequel, effort in each of these areas is examined in greater detail.

1. MECHANICS OF GRANULAR MATERIALS

Attention has been focused on the mechanical response of cohesionless granular masses which support the overall applied loads through contact friction. It is shown that the fabric of the granular mass plays a dominant role in characterizing its overall behavior. Fabric refers to the relative arrangement of the grains at the micro-level. It has the most fundamental influence on the densification and liquefaction potentials of granular bodies. Our research, therefore, focuses on the following basic aspects: 1) description of fabric and its relation to other fundamental quantities that characterize the behavior of granular masses; 2) the influence of fabric on densification and liquefaction potentials of granular masses; and 3) phenomenological plasticity approach to the

description of the flow of granular masses.

In the sequel we list papers pertaining to each of the above two areas, together with a brief abstract of each paper.

1.1. Fabric and Micromechanics of Granular Materials

The basic aim here is to obtain a macroscopic description of the mechanical behavior of granular masses from an examination of the microscopic, grain-to-grain interaction which brings into focus the importance of fabric and anisotropy. Significant progress in this fundamental direction has been made, as summarized below in connection with each publication that has been completed.

- (1) "A Micromechanical Description of Granular Material Behavior," by J. Christoffersen, M. M. Mehrabadi, and S. Nemat-Nasser, Journal of Applied Mechanics, 48 (1981) 339-344.

Considered is a sample of cohesionless granular material, in which the individual granules are regarded rigid, and which is subjected to overall macroscopic average stresses. On the basis of the principle of virtual work, and by an examination of the manner by which adjacent granules transmit forces through their contacts, a general representation is established for the macroscopic stresses in terms of the volume average of the (tensorial) product of the contact forces and the vectors which connect the centroids of adjacent contacting granules. Then the corresponding kinematics is examined and the overall macroscopic deformation rate and spin tensors are developed in terms of the volume average of relevant microscopic kinematical variables. As an illustration of the application of the general expressions developed, two explicit macroscopic results are deduced: (1) a dilatancy equation which both qualitatively and quantitatively seems to be in accord with experimental observation, and (2) a noncoaxiality equation which seems to support the vertex plasticity model. Since the development is based on a microstructural consideration, all material coefficients entering the results have well-defined physical interpretations.

- (2) "On statistical Description of Stress and Fabric in Granular Materials," by M. M. Mehrabadi, S. Nemat-Nasser, and M. Oda, International Journal for Numerical and Analytical Methods in Geomechanics, 6 (1982) 95-108.

The notion of overall macroscopic stress in granular masses is examined from a fundamental point of view by a statistical consideration of the contact forces that are transmitted by the contacting granules at the microscale. This examination leads in a natural way to relations between the macroscopic stress and the resulting granular fabric. The overall stresses are expressed in terms of the contact forces in two different but complementary ways: (1) by a statistical averaging over the sample volume of contact forces and "branches" which are vectors connecting the centroids of two contacting granules; and (2) by defining the overall tractions transmitted across an interior imagined plane as the sum of the contact forces which represent the mechanical effect of granules on one side of a unit area of this plane, upon those on the other side. Conditions under which the two representations of overall stresses are equivalent, are examined in detail. In addition, explicit results are given, which define stresses in terms of the fabric and other microstructural characteristics of the granular mass.

- (3) "A Statistical Study of Fabric in a Random Assembly of Spherical Granules," by M. Oda, S. Nemat-Nasser, and M. M. Mehrabadi, International Journal for Numerical and Analytical Methods in Geomechanics, 6 (1982) 77-94.

It is commonly accepted that the mechanical behavior of granular masses is strongly affected by their microstructure, namely the relative arrangement of voids and particles, i.e. the granular fabric. Therefore, parameters which characterize the granular fabric are of paramount importance in a fundamental description of the overall macroscopic stresses and deformation measures. In this paper several measures of granular fabric are introduced for a random assembly of spherical granules, using a statistical approach. In particular, a second-order symmetric tensor, F_{ij} , emerges from this consideration, which seems to be of fundamental importance for the description of fabric, and which is closely related to the distribution of the contact normals in the assembly. The relation between fabric measures presented here and those discussed by other investigators is also discussed.

- (4) "Some Experimentally Based Fundamental Results on the Mechanical Behavior of Granular Materials," by M. Oda, J. Konishi, and S. Nemat-Nasser, Géotechnique, 30 (1980) 479-495.

This work shows, on the basis of experimental results, the importance of fabric on the mechanical behavior of granular masses. It is summarized as follows:

Porosity (or void ratio) is one of the most important index measures of granular materials. It alone is not, however, enough for a reasonably complete description of the basic properties of materials of this kind. The fabric ellipsoid appears to be a good second index measure. It is closely related to the probability density function $E(\alpha, \beta)$ which defines the angular distribution of the contact normals. Based on experimental evidence the following is concluded. The fabric ellipsoid is closely related to the stress ellipsoid and characterizes a second-order tensor with a clear physical meaning; the principal axes of the fabric ellipsoid seem to tend toward those of the stress ellipsoid and this appears to hold whether the principal stress axes rotate gradually or discontinuously during a course of deformation; and there seems to exist a quantitative relation between the fabric ellipsoid and the overall applied stresses, especially in the post-failure states. It appears that the function $E(\alpha, \beta)$ continuously changes in a manner so as to increase the ability of the material to withstand the increased applied stresses. The changes of the fabric, characterized by the changes of $E(\alpha, \beta)$, result in the hardening (or softening) of the granular materials in a given deformation course.

- (5) "Anisotropic Strength of Cohesionless Sands," by M. Oda, Journal of the Geotechnical Engineering Division, ASCE, 107, No. GT9 (1981) 1219-1231.

Natural in situ soils are neither isotropic nor homogeneous. They often possess layered structures, e.g., alternating layers having quite different particle size distribution, where in each homogeneous layer nonspherical particles have a strong tendency to exist parallel or nearly parallel to the layered structures. The anisotropy and heterogeneity may have considerable influence on the strength and other properties of soils; e.g., on the shear strength of clays and sands, and on the bearing capacity of sand.

In this paper, the writer reports some results of plane strain tests on samples having layered structures as well as being anisotropic. The results may provide guidance for estimating the internal friction angle of soils with complicated properties.

- (6) "Fabric and Its Influence on Mechanical Behavior of Granular Materials," by S. Nemat-Nasser, Deformation and Failure of Granular Materials, Proc. IUTAM Symp., Delft, The Netherlands, Aug. 31-Sept. 3, 1982, P. A. Vermeer and H. J. Luger (eds.), A. A. Balkema/Rotterdam (1982) 37-42.

Some relevant measures of granular fabric are reviewed in relation to the overall stress and the dilatant behavior of granular masses, and the results are illustrated for simple shearing of two-dimensional granules. Recent experimental results are cited, which show the influence of fabric on the overall shear-induced rate of volume expansion and volume contraction.

- (7) "Inherent Anisotropy and Shear Strength of Assembly of Oval Cross-Sectional Rods," by J. Konishi, M. Oda, and S. Nemat-Nasser, Deformation and Failure of Granular Materials, Proc. IUTAM Symp., Delft, The Netherlands, Aug. 31-Sept. 3, 1982, P. A. Vermeer and H. J. Luger (eds.), A. A. Balkema/Rotterdam (1982) 403-412.

The authors have conducted an experimental study on biaxial deformation of two-dimensional assemblies of rod-shaped photoelastic particles with oval cross section to understand and quantify the behavior of granular materials and the evolution of their microstructure. In each test the overall deformation and corresponding forces are measured and at various stages of deformation photoelastic photographs are taken to measure various microscopic quantities to evaluate the microstructure and its relation to the overall macroscopic mechanical behavior. In this paper, the effect of inherent anisotropy associated with the initial orientation of the long (cross-sectional) axis of the particles with respect to the bedding plane, and the influence of inter-particle friction and particle shape are discussed relating to the macroscopic behavior.

- (8) "Experimental Micromechanical Evaluation of Strength of Granular Materials: Effects of Particle Rolling," by M. Oda, J. Konishi, and S. Nemat-Nasser, Mechanics of Materials 1 (1982) 269-283.

Biaxial compression tests have been performed on assemblies of oval cross-sectional rods, in an effort to evaluate the effects of interparticle friction, particle shape, and initial fabric on the overall strength of granular materials. The variation in the spatial arrangement of the particles (fabric) and particle rolling and sliding are monitored by taking photoelastic pictures at various stages during the course of deformation. Based on this, the following conclusions are obtained: (1) Particle rolling appears to be a major microscopic deformation mechanism, especially when interparticle friction is large. (2) There are relatively few contacts at which relative sliding is dominant, and this seems to be true even when the assembly reaches the overall failure state; this observation is in contradiction to the common assumption that particle sliding is the major microscopic deformation mode. (3) During the course of deformation and up to the peak stress, new contacts are continually formed in such a manner

that the contact unit normals tend to concentrate more in a direction parallel to the maximum principal compression. This concentration of unit normals seems to be closely related to the formation of new column-like load paths which carry the increasing axial stress under constant lateral force. After the peak stress, such a column-like microstructure disappears and considerable rearrangement of the load paths takes place, leading to a more diffused (homogeneous) microstructure in the critical state. (4) If a fabric tensor F_{ij} , $i, j = 1, 2, 3$, is defined to be proportional to the volume average of the quantity $m_i m_j$, when m_i 's are the rectangular Cartesian components of a unit vector along a vector that connects the centroids of two typical contacting granules, then it appears that the overall stress with components σ_{ij} tends to become coaxial with the fabric tensor F_{ij} , as the overall deformation continues. For two-dimensional granules the result $\sigma_{ij} = \alpha_0 F_{ij} + \beta_0 F_{ik} F_{kj}$ (k summed) obtained by Mehrabadi, Nemat-Nasser, and Oda (Int. J. Numer. Anal. Methods Geomech. 6, 1982, 95) by micromechanical modeling is confirmed experimentally; α_0 and β_0 are material parameters.

- (9) "Induced Anisotropy in Assemblies of Oval Cross-Sectional Rods in Biaxial Compression," by J. Konishi, M. Oda, and S. Nemat-Nasser, Mechanics of Granular Materials: New Models and Constitutive Relations, Proc. U.S.-Japan Seminar, Ithaca, NY, Aug. 23-27, 1982, J. T. Jenkins and M. Satake (eds.), Elsevier Science Publishers (1983) 31-39.

The microstructure (or the fabric) of granular materials changes during their plastic flow in response to applied loads, resulting in load-induced anisotropy. Based on previous experiments (by the present authors and by other researchers) we have concluded that the evolution of fabric is closely related to the variation in the distribution of the contact normals, and that this distribution seems to have a close relation to the overall applied stress: the distribution of contact normals changes in such a manner as to produce a greater concentration of contact normals along an orientation which parallels the direction of maximum principal compression. How does an initially strongly anisotropic fabric change in response to an applied load? In order to investigate this problem, we have performed a series of biaxial compression tests on two-dimensional assemblies of photoelastic rods with oval cross-sections, where each assembly is formed by stacking the rods within a tilted loading frame at desired angle, producing a strong initial anisotropy.

- (10) "Micromechanically Based Rate Constitutive Descriptions for Granular Materials," by S. Nemat-Nasser, and M. M. Mehrabadi, Mechanics of Engineering Materials, C. S. Desai and R. H. Gallagher (eds.), John Wiley & Sons, in press.

For a granular mass which supports the overall applied loads through contact friction, the overall stress is related to suitable measures of fabric (or microstructure). An active contact is viewed as the basic micro-element, and the associated local velocity gradient is decomposed into an inelastic contribution that does not affect the fabric, and an accommodating contribution due to fabric changes. Local objective stress rate measures are developed and related to the local deformation rate by means of simple suitable stress rate - fabric strain rate relations, and a simple frictional flow rule. In terms of the nominal stress rate and the velocity gradient, a generalized self-consistent method is used to obtain the overall instantaneous moduli from the corresponding local quantities.

1.2. The Influence of Fabric on Densification and Liquefaction of Granular Masses

Chapters II and III give comprehensive accounts of the liquefaction phenomenon, emphasizing some very recent discoveries on the influence of fabric on this phenomenon. Below we list published papers relating to liquefaction, together with their summaries.

- (1) "Liquefaction of Soil During Earthquakes," by S. Nemat-Nasser, Dynamic Response of Structures. Proc. ASCE-EMD Speciality Conf., Atlanta, Georgia, Jan. 15-16, 1981, G. Hart (ed.), Am. Soc. Civil Engineers (1980) 376-385.

Recent theoretical results on liquefaction of cohesionless saturated sand are summarized. Then some experimental observations of the effect of prior straining on the liquefaction resistance are mentioned.

- (2) "On Dynamic and Static Behavior of Granular Materials," by S. Nemat-Nasser, Soil Mechanics--Transient and Cyclic Loads, G. N. Pande and O. C. Zienkiewicz (eds.), John Wiley & Sons (1982), Ch. 16, 439-458.

The paper summarizes some recent work by the author and his associates on the dynamic and static behavior of granular materials (saturated undrained, or drained sands), consisting of three complementary aspects: (1) densification and liquefaction of sand in cyclic shearing (strain- or stress-controlled cases); (2) application of plasticity theory (with

plastic volumetric changes and including internal friction) for the description of the sand behavior in monotone loading regimes; and (3) development of the basic rate constitutive relations by a statistical averaging which is based on the behavior of individual grains at microscale.

- (3) "Influence of Fabric on Liquefaction and Densification Potential of Cohesionless Sand," by S. Nemat-Nasser and Y. Tobita, Mechanics of Materials, 1 (1982) 43-62.

For simple shearing under constant pressure, the effects of fabric on liquefaction and densification potentials of saturated cohesionless granular materials are examined theoretically and experimentally. The fabric is identified with the distribution of the dilatancy angles (the angle between the sliding and the macroscopic shearing directions), and the influence of prestraining on this distribution and hence on the macroscopic sample behavior is studied. It is shown that prestraining with zero residual stress can reduce resistance to liquefaction by one or even two orders of magnitude, although the sample density and other conditions are kept the same. The micromechanical features responsible for this and related behaviors, are examined in some detail. Finally, some tentative results on the effect of the inherent anisotropy that is produced during sample preparation are reported, showing that a method which yields samples more resistive in triaxial cyclic tests may provide samples less resistive in cyclic shearing.

1.3. Phenomenological Plasticity Approach

Two fundamental features distinguish soil response from that of metals: 1) soils are frictional materials and, therefore, highly pressure-sensitive, whereas, for metals, pressure sensitivity is secondary; 2) soils are highly dilatant and undergo permanent volumetric strains, whereas most metals are essentially incompressible plastically. Therefore, classical plasticity does not apply directly to soils. Under this research project, we have developed some nonclassical plasticity theories which, while quite simple, seem to provide good descriptions of soil response at high pressures and

even at high temperatures. Chapter V gives an account of this theory and provides a number of illustrations. Below we list related published papers together with their summaries.

- (1) "On Constitutive Behavior of Fault Materials," by S. Nemat-Nasser, in Solid Earth Geophysics and Geotechnology, Proc. ASME Symp., Chicago, IL, Nov. 16-21, 1980, S. Nemat-Nasser (ed.), AMD-Vol. 42, The Am. Soc. Mech. Engineers (1980) 31-37.

It is commonly believed that the assessment of precursory events which may lead to instability in shallow earthquakes hinges critically on the constitutive law of both the intact elastic earth and the nonlinear fault zone. A rate-independent plasticity theory of deformation and flow of geological materials is presented, and the effects of pressure, temperature, dilatancy, stress triaxiality, noncoaxiality of stress and plastic strain rate tensors, rate of loading, and pore water pressure are reviewed in the context of the theory.

- (2) "A Plasticity Model for Flow of Granular Materials under Triaxial Stress States," by J. F. Dorris and S. Nemat-Nasser; International Journal of Solids and Structures, 18 (1982) 497-531.

For finite deformations of granular materials, a plasticity theory is developed which accounts for the true stress triaxiality, pressure sensitivity, and dilatancy. The effect of stress triaxiality is introduced by including the third deviatoric stress invariant in the yield function and the flow potential. For illustration, the true triaxial test on the cubical sample is analyzed in detail, the results are compared with experimental observations of true triaxial test on loose and dense samples of sand, and good correlation is obtained.

- (3) "Instability of a Half-Space with Frictional Materials," by H. Horii and S. Nemat-Nasser, Journal of Applied Mathematics and Physics (ZAMP), 33 (1982) 1-16.

The instability of an initially half-space which consists of dilatant frictional materials is examined. It is assumed that the material response is governed by elastoplastic constitutive relations that include plastic compressibility (or dilatancy) and frictional effects, and hence involves a nonassociative flow rule. Stability limits are established, and it is shown that (unlike for elastic materials) for this class of materials folding by surface instability can be initiated at compressive forces that are considerably smaller than the initial shear modulus. The results are illustrated in terms of some published data on certain sandstones.

2. MECHANICS OF ROCKS

Another area in which significant fundamental results have been obtained during the course of this research is the mechanics of rocks, with particular attention to the influence of microcracks on the overall behavior of rocks, and on the basic failure mechanisms at various confining pressures. Chapter IV gives a comprehensive account of our latest findings in the description of the failure mechanism. Below is a list of the related published papers, together with their summaries.

- (1) "Compression Induced Nonplanar Crack Extension with Application to Splitting, Exfoliation, and Rockburst," by S. Nemat-Nasser and H. Horii, Journal of Geophysical Research, 87, No. B8, August 10 (1982) 6805-6821.

Uniaxial compression of plates of brittle materials containing pre-existing planar cracks oriented at certain angles with respect to the direction of overall compression has revealed that the relative frictional sliding of the faces of the pre-existing cracks may produce, at their tips, tension cracks which deviate at sharp angles from the sliding plane. These tension cracks then continue to grow in a stable manner with increasing axial compression, curving toward an orientation parallel to the direction of axial compression. Within the framework of linear fracture mechanics, the out-of-plane extension of a pre-existing straight crack, induced by overall far-field compression, is analyzed, and various parameters which characterize the growth process are quantified. It is shown analytically that, for a wide range of pre-existing crack orientations, the out-of-plane crack extension initiates at an angle close to 70° from the direction of pre-existing crack; the exact value of this angle, of course, depends on the friction factor and the orientation of the pre-existing crack. It is found that the growth process is stable initially, but the rate of increase of the length of the extended portion with respect to the increasing axial compression dramatically increases after a certain extension length is attained, and in fact, this length becomes unbounded if a small lateral tension also exists. Various limiting cases are examined and the corresponding analytical estimates are compared with the numerical results, arriving at good

correlations. A series of qualitative experiments is performed on thin plates of Columbian Resin CR 39, arriving at excellent agreement with the analytical results. In light of the analysis, the phenomena of axial splitting, exfoliation (or sheet fracture), and rockburst are examined, and it is suggested that they may all be the results of the out-of-plane (tensile) extension of pre-existing cracks, induced by large overall far-field compressions. This assertion is then supported by a series of experiments which show that the relative frictional sliding of the faces of one or even an array of pre-existing cracks does not result in coplanar (sliding mode) crack growth, but rather leads to the formation of tension cracks which grow in the direction of maximum compression. Moreover, a pre-existing crack close to a free boundary grows in a similar manner under compression parallel to the boundary, and shows no tendency to move toward the free surface. Possible lateral buckling which may result, and which may cause further unstable crack extension, is illustrated experimentally, and discussed in an effort to shed light on the phenomena of rockburst and surface spalling.

- (2) "Curved Crack Growth in Brittle Solids under Farfield Compression," by H. Horii and S. Nemat-Nasser, 1982 Advances in Aerospace Structures and Materials, Symp., ASME Winter Annual Meeting, Phoenix, AZ, Nov. 14-19, 1982, R. M. Laurenson and U. Yuceoglu, (eds.), ASME Publ. AD-03 (1982) 75-81.

In the presence of a closed crack which undergoes frictional sliding, first Muskhelishvili's complex stress potentials are obtained for a pair of dislocations which are symmetrically situated with respect to the origin; plane strain or plane stress conditions are assumed. Then these potentials are used to formulate the required integral equation for the dislocation density function defined on the path of the curved extension of the pre-existing straight closed crack, in such a manner that traction-free conditions are satisfied there. With the aid of this integral equation the curved extension path is estimated incrementally, using the criterion that the crack grows in the direction which renders the Mode II stress intensity factor zero, i.e., the criterion of local symmetry; this condition yields essentially the same results as the criterion of the maximum Mode I stress intensity factor. It is shown that the crack path curves in the direction of the maximum compression, and may grow in an unstable manner if some lateral tension also acts. On the basis of this, phenomena of axial splitting, sheet fracture, and rockburst are explained, and results are verified by experiments.

- (3) "Overall Moduli of Solids with microcracks: Load-Induced Anisotropy," by H. Horii and S. Nemat-Nasser, Journal of the Mechanics and Physics of Solids, 31 (1983) 155-171.

For a linearly elastic brittle solid containing microcracks that may be closed or may undergo frictional sliding, a general method is developed for estimating the overall instantaneous moduli which depend on the loading conditions. When the cracks are all open and when they are randomly distributed, then the overall response is isotropic. The moduli for this case have been obtained by Budiansky and O'Connell (Int. J. Solids Struct. 12, 1976, 81). On the other hand, when some cracks close, and when some closed cracks undergo frictional sliding, then the overall response becomes anisotropic and dependent on the loading conditions, as well as on the loading path. The self-consistent method is used to estimate the overall moduli. The effects of crack closure and load-induced anisotropy are included. Several illustrative examples are worked out, showing the important influence of the load path on the overall response when crack closure and frictional sliding are involved.

- (4) "Estimate of Stress Intensity Factors for Interacting Cracks," by H. Horii and S. Nemat-Nasser, 1983 Advances in Aerospace Structures, Materials and Dynamics, Symp. on Composites, ASME Winter Annual Meeting, Boston, MA, Nov. 13-18, 1983, U. Yuceoglu, R. L. Sierakowski, and D. A. Glasgow (eds.), ASME Publ. AD-06 (1983) 111-117.

An effective method, called the method of "pseudo-tractions", is proposed, which can be used to solve two-dimensional problems of an infinitely extended linearly elastic solid containing cracks. The method places no restriction on the number and geometry of cracks, and provides convergent series solutions, as well as simple approximate analytic estimates for problems of this kind. The application of the results to the problem of shear failure of rock samples and other brittle solids under axial compression and confining pressure, is also briefly discussed.

- (5) "Growth of Microcracks in Rocks, and Load-Induced Anisotropy," by H. Horii and S. Nemat-Nasser, Hydraulic Fracturing and Geothermal Energy, Proc. Japan-U.S. Seminar, Tokyo & Post-Seminar Symposium, Sendai, Nov. 2-9, 1982, S. Nemat-Nasser, H. Abé, and S. Hirakawa (eds.), Martinus Nijhoff (1983) 519-528.

The effect of microcracks on overall mechanical properties of rocks and other brittle solids is considered, emphasizing their influence on the overall moduli, on the load-induced anisotropy, and on the failure of the solid by the formation of tension cracks at tips of sliding microcracks under the overall farfield compression.

3. LIST OF PUBLICATIONS COMPLETED UNDER THIS GRANT

- M. Oda, J. Konishi, and S. Nemat-Nasser, "Some Experimentally Based Fundamental Results on the Mechanical Behavior of Granular Materials," Géotechnique, 30 (1980) 479-495.
- S. Nemat-Nasser, "On Constitutive Behavior of Fault Materials," Solid Earth Geophysics and Geotechnology, Proc. ASME Symp., Chicago, IL, Nov. 16-21, 1980, S. Nemat-Nasser (ed.), ASME Publ. AMD-Vol. 42, (1980) 31-37.
- J. Christoffersen, M. M. Mehrabadi, and S. Nemat-Nasser, "A Micromechanical Description of Granular Material Behavior," Journal of Applied Mechanics, 48 (1981) 339-344.
- M. Oda, "Anisotropic Strength of Cohesionless Sands," J. Geotechnical Engrg. Div., ASCE, 107, No. GT9 (1981) 1219-1231.
- S. Nemat-Nasser, "Liquefaction of Soil During Earthquakes," Dynamic Response of Structures, Proc. ASCE-EMD Specialty Conf., Atlanta, GA, Jan. 15-16, 1981, G. Hart (ed.), American Society of Civil Engineers (1981), 376-385.
- M. Oda, S. Nemat-Nasser, and M. M. Mehrabadi, "A Statistical Study of Fabric in a Random Assembly of Spherical Granules," Int'l J. for Numerical and Analytical Methods in Geomechanics, 6 (1982) 77-94.
- M. M. Mehrabadi, S. Nemat-Nasser, and M. Oda, "On Statistical Description of Stress and Fabric in Granular Materials," Int'l J. for Numerical and Analytical Methods in Geomechanics, 6 (1982) 95-108.
- S. Nemat-Nasser, "On Dynamic and Static Behavior of Granular Materials," Soil Mechanics--Transient and Cyclic Loads, G. N. Pande and O. C. Zienkiewicz (eds.), John Wiley & Sons (1982), Ch. 16, 439-458.
- J. F. Dorris and S. Nemat-Nasser, "A Plasticity Model for Flow of Granular Materials under Triaxial Stress States," Int'l J. Solids Structures, 18 (1982) 497-531.
- S. Nemat-Nasser and Y. Tobita, "Influence of Fabric on Liquefaction and Densification Potential of Cohesionless Sand," Mechanics of Materials, 1 (1982) 43-62.
- H. Horii and S. Nemat-Nasser, "Instability of a Half-Space with Frictional Materials," ZAMP, 33 (1982) 1-16.
- S. Nemat-Nasser and H. Horii, "Compression Induced Crack Kinking and Curving with Application to Splitting, Exfoliation, and

- Rockburst," Journal of Geophysical Research, 87, No.B8, Aug. 10 (1982) 6805-6821.
- S. Nemat-Nasser, "Fabric and Its Influence on Mechanical Behavior of Granular Materials," Deformation and Failure of Granular Materials, P. A. Vermeer and H. J. Luger (eds.), Proc. IUTAM-symp., Delft, The Netherlands, Aug. 31-Sept. 3, 1982; A. A. Balkema/Rotterdam (1982) 37-42.
- J. Konishi, M. Oda, and S. Nemat-Nasser, "Inherent Anisotropy and Shear Strength of Assemblies of Oval Cross-Sectional Rods," Deformation and Failure of Granular Materials, P. A. Vermeer and H. J. Luger (eds.), Proc. IUTAM-Symp., Delft, The Netherlands, Aug. 31-Sept. 3, 1982; A. A. Balkema/Rotterdam (1982) 403-412.
- H. Horii and S. Nemat-Nasser, "Curved Crack Growth in Brittle Solids under Farfield Compression," 1982 Advances in Aerospace Structures and Materials, Proc. ASME Symp., Phoenix, AZ, Nov. 14-19, 1982, R. M. Laurenson and U. Yuceoglu (eds.), ASME Publ. AD-03 (1982) 75-81.
- M. Oda, J. Konishi, and S. Nemat-Nasser, "Experimental Micromechanical Evaluation of Strength of Granular Materials: Effects of Particle Rolling," Mechanics of Materials, 1 (1982) 269-283.
- H. Horii and S. Nemat-Nasser, "Overall Moduli of Solids with Microcracks: Load-Induced Anisotropy," J. Mech. Phys. Solids, 31 (1983) 155-171.
- J. Konishi, M. Oda, and S. Nemat-Nasser, "Induced Anisotropy in Assemblies of Oval Cross-Sectional Rods in Biaxial Compression," Mechanics of Granular Materials: New Models and Constitutive Relations, Proc. U.S.-Japan Seminar, Ithaca, NY, Aug. 23-27, 1982, J. T. Jenkins and M. Satake (eds.), Elsevier Science Publishers (1983) 31-39.
- S. Nemat-Nasser and H. Horii, "Growth of Microcracks in Rocks, and Load-Induced Anisotropy," Hydraulic Fracturing and Geothermal Energy, Proc. Japan-U.S. Seminar, Tokyo & Post-Seminar Symposium, Sendai, Nov. 2-9, 1982, S. Nemat-Nasser, H. Abé, and S. Hirakawa (eds.), Martinus Nijhoff (1983) 519-528.
- H. Horii and S. Nemat-Nasser, "Estimate of Stress Intensity Factors for Interacting Cracks," 1983 Advances in Aerospace Structures, Materials and Dynamics, U. Yuceoglu, R. L. Sierakowski, and D. A. Glasgow (eds.), ASME Publ. AD-06 (1983) 111-117.
- S. Nemat-Nasser and M. M. Mehrabadi, "Micromechanically Based Rate Constitutive Descriptions of Granular Materials," Mechanics of Engineering Materials, C. S. Desai and R. H. Gallagher (eds.), John Wiley & Sons, in press.

- S. Nemat-Nasser, "Liquefaction and Densification of Cohesionless Granular Masses in Cyclic Shearing," Numerical Models in Geomechanical Engineering Practice, A. A. Balkema, in press.
- S. Nemat-Nasser and K. Takahashi, "Does Preliquefaction or Prestraining Reduce Sands' Resistance to Reliquefaction or Densification?" J. Geotech. Engrg. ASCE, submitted.
- H. Horii and S. Nemat-Nasser, "Compression-Induced Micro-Crack Growth in Brittle Solids: Axial Splitting and Shear Failure," J. Geophys. Research, submitted.
- B. Rowshandel and S. Nemat-Nasser, "Finite Strain Rock Plasticity: Stress Triaxiality, Pressure, and Temperature Effects", to be submitted for publication in J. Geophys. Research.

4. PROFESSIONAL PERSONNEL ASSOCIATED WITH THE RESEARCH PROJECT;
DEGREES AWARDED

Principal Investigator: S. Nemat-Nasser

Postdoctoral Research Associates and Visiting Scholars:

MASAHIRO AI (Associate Professor, Department of Civil Engineering, Hosei University, Tokyo, Japan)

HIDEYUKI HORII (Postdoctoral Research Associate, Department of Civil Engineering, Northwestern University, Evanston, IL)

YUJI KISHINO (Lecturer, Department of Civil Engineering, Tohoku University, Sendai, Japan)

JUNICHI KONISHI (Associate Professor of Civil Engineering, Shinshu University, Wakasato, Japan)

MORTEZA M. MEHRABADI (Presently: Assistant Professor, Department of Mechanical Engineering, Tulane University, New Orleans, LA)

MASANOBU ODA (Associate Professor, Department of Foundation Engineering, Saitama University, Saitama, Urawa, Japan)

BADIOLLAH ROWSHANDEL (Postdoctoral Research Associate, Department of Civil Engineering, Northwestern University, Evanston, IL)

KUNIO TAKAHASHI (Senior Research Engineer, Port & Harbor Research Institute, Yokusuka, Japan)

YOSHIO TOBITA (Research Engineer, Tohoku University, Sendai, Japan)

Graduate Students:

Degrees Awarded (AFOSR Support)

HIDEYUKI HORII

- M.S. degree, August 1981, Northwestern University

Thesis: Crack Kinking and the Axial Splitting of Compressed Brittle Solids.

- Ph.D. degree, August 1983, Northwestern University

Dissertation: Overall Response and Failure of Brittle Solids Containing Micro-Cracks.

BADIOLLAH ROWSHANDEL - Ph.D.degree, August 1983, Northwestern University
Dissertation: A Plasticity Model for Crustal Rocks with Application to Strike-Slip Fault Deformation.

Other Graduate Students (partially supported)

JAMES F. DORRIS

TETSUOKA IWAKUMA

YOSHIO TOBITA

Other Researchers Who Have Been Involved in the Project:

JES CHRISTOFFERSEN (Professor, Department of Solid Mechanics, The Technical University of Denmark, Lyngby, Denmark)

ARSALAN SHOKOOH (Assistant Professor, Department of Mathematics, University of Puerto Rico, Humacao, PR)

5. INTERACTIONS (COUPLING ACTIVITIES)

A. Participation of Principal Investigator at Meetings -- Papers Presented; Lectures at Seminars*

"On Dynamic and Static Behavior of Granular Materials," University of Riyadh, Riyadh, Saudi Arabia, January 2, 1980.

"On Dynamic and Static Behavior of Granular Materials" (General Lecture), International Symposium on Soils under Cyclic and Transient Loading, Swansea, U.K., January 7-11, 1980.

"On Mechanics of Granular Materials," University of Missouri-Rolla, Rolla, Missouri, March 1980.

"Plasticity and Flow of Geological Materials" Rensselaer Polytechnic Institute, Troy, New York, April 8, 1980.

"Plasticity and Flow of Geological Materials," Danish Center for Applied Mathematics and Mechanics, The Technical University of Denmark, Lyngby, Denmark, June 16, 1980.

"Constitutive Descriptions Pertinent to Localization Problems" Workshop on Nonuniform and Localized Plasticity, Salva Regina College, Newport, RI, August 5-9, 1980.

"A Micromechanical Description of Granular Material Behavior," XVth International Congress of Theoretical and Applied Mechanics, Toronto, Canada, August 17-23, 1980.

"On Constitutive Behavior of Fault Materials," ASME Symposium on Solid Earth Geophysics and Geotechnology, ASME Winter Annual Meeting, Chicago, IL, November 16-21, 1980.

"Liquefaction of Soil During Earthquakes," ASCE-EMD Specialty Conference on Dynamic Response of Structures, Atlanta, GA, January 15-16, 1981.

"A Micromechanical Description of Granular Material Behavior in Simple Shear: Theory and Experiments," Colloquium on Modern Topics in Mechanics, Northwestern University, Evanston, IL, February 27, 1981.

"The Effects of Soil Fabric in Densification and Liquefaction in Simple Shear: Theory and Experiments," Graduate Seminar, Illinois Institute of Technology, Chicago, IL, March 12, 1981.

*Presented by S. Nemat-Nasser unless indicated otherwise.

"Mechanics of Granular Materials," Colloquia Series, Department of Aerospace Engineering and Mechanics, University of Minnesota, Minneapolis, MN, November 6-8, 1981.

"Earthquake Induced Ground Failure; Liquefaction: Experiment and Theory," Department of Applied Mechanics and Engineering Science, University of California, San Diego, La Jolla, CA, January 25-26, 1982.

"Crack Propagation in Rocks with Application to Exfoliation and Rock Bursts," Department of Geological Sciences, Northwestern University, Evanston, IL, May 14, 1982.

U.S.-Japan Seminar on New Models and Constitutive Relations in the Mechanics of Granular Materials, Ithaca, NY, August 22-27, 1982:

Three papers were presented:

- 1) "Stress, Dilatancy, and Fabric in Granular Materials";
- 2) "Experimental Micromechanical Evaluation of Strength of Granular Materials: Effects of Particle Rolling" (presented by M. Oda);
- 3) "Induced Anisotropy in Assemblies of Oval Cross-Sectional Rods in Biaxial Compression" (presented by J. Konishi).

IUTAM Symposium on Deformation and Failure of Granular Materials, Delft, The Netherlands, August 31-September 3, 1982:

Two papers were presented:

- 1) "Fabric and Its Influence on Mechanical Behavior of Granular Materials";
- 2) "Inherent Anisotropy and Shear Strength of Assemblies of Oval Cross-Sectional Rods" (presented by J. Konishi).

International Workshop on Constitutive Behavior of Soils, Grenoble, France, September 6-8, 1982: Chairman of Session on Complex Elastic-Plastic Laws.

"Some Micromechanical Aspects of Geotechnical Materials," Keynote Lecture, International Symposium on Numerical Models in Geomechanics, Zurich, Switzerland, September 13-17, 1982.

AFOSR Workshop on the Research Aspects of Blast-Induced Liquefaction of Soils, September 28, 1982: Participated in discussion on present and future research.

"Compression Induced Crack Kinking and Curving with Application to Splitting, Exfoliation, and Rockburst," 19th Annual Meeting of the Society of Engineering Science, Rolla, MO, October 27-29, 1982.

"Growth of Microcracks in Rocks, and Load-Induced Anisotropy," Symposium on Fracture Mechanics Approach to Hydraulic Fracturing and Geothermal Energy, Sendai, Japan, November 8-9, 1982.

"Curved Crack Growth in Brittle Solids Under Far-Field Compression," ASME Winter Annual Meeting, Aerospace Division Symposium on Advances in Aerospace Structures and Materials, Phoenix, AZ, November 14-19, 1982 (presented by H. Horii).

"A Micromechanically Based Rate Constitutive Description of Granular Materials," International Conference on Constitutive Laws for Engineering Materials: Theory and Application, Tucson, AZ, January 10-14, 1983.

"On Micromechanical Aspects of Rock Failure and Mechanical Response," Mechanics Seminar Series, The University of Utah, Salt Lake City, UT, January 14, 1983.

"Macroscopic Response and Failure of Solids with Microcracks: Theory and Experiment," Workshop on Media with Microstructure and Wave Propagation Houghton, MI, January 24-25, 1983.

"Induced Anisotropy and Texture in Elastoplastic Composites and Jointed Rocks at Finite Strains," CNRS International Colloquium on Failure Criteria of Structured Media, Grenoble, France, June 20-24, 1983. (Invited Lecture).

ASME-AMD Symposium on the Mechanics of Ice, Rocks, and Soils, held at the ASME Applied Mechanics, Biomechanics, and Fluids Engineering Conference, Houston, TX, June 20-22, 1983:

- 1) Organizer of the four-session symposium for the Committee on Geomechanics (SNN Chairman) of the Applied Mechanics Division, ASME;
- 2) Presented a paper: "Microcracking and Failure in Axial Compression";
- 3) Chaired one session at the symposium;
- 4) Coordinator of symposium proceedings: Geomechanics, AMD-Vol. 57, ASME (1983).

20th Annual Meeting of the Society of Engineering Science, Newark, DE, August 22-24, 1983:

- 1) Coordinator of three sessions on Geomechanics of the Committee on Geophysics of SES;
- 2) Organizer of one of the Geomechanics sessions;
- 3) Presented a paper: "Microcrack Interaction and Rock Failure".

1983 ASCE Annual Convention, Houston, TX, October 17-21, 1983:

- 1) Organizer of a session on Developments in Analytical and Theoretical Aspects of Constitutive Modelling for the Engineering Mechanics Division, Committee on Mathematical Methods, ASCE;
- 2) Presented a paper: "Micromechanics of Rock and Concrete Failure".

"Micromechanics of Brittle Failure in Compression," ASME Winter Annual Meeting, Boston, MA, November 13-18, 1983 (presented by H. Horii).

B. Consultative and Advisory Functions to Other Agencies or Laboratories

Consulting for the Department of Defense, Defense Advanced Research Projects Agency:

- 1) Organizer of a Workshop -- sponsored by DARPA and NSF -- on the Theoretical Foundation for Large-Scale Computations of Nonlinear Material Behavior, Northwestern University, Evanston, IL, October 24-26, 1983;
- 2) Local chairman and coordinator for the workshop;
- 3) Presented a general lecture: "Theoretical Foundations of Plasticity";
- 4) Editor of the workshop proceedings (to be published by Martinus Nijhoff, The Hague, The Netherlands).

CHAPTER II

LIQUEFACTION AND DENSIFICATION OF COHESIONLESS GRANULAR MASSES IN CYCLIC SHEARING*

by

S. Nemat-Nasser

Table of Contents

	Page
ABSTRACT	27
1. INTRODUCTION	28
2. A SIMPLE LIQUEFACTION AND DENSIFICATION THEORY	32
3. EFFECT OF FABRIC ON LIQUEFACTION AND DENSIFICATION POTENTIAL OF GRANULAR MASSES	40
ACKNOWLEDGMENT	52
REFERENCES	53
TABLE	57
FIGURE CAPTIONS	58
FIGURES 1 - 14	62-75

*Submitted to: Numerical Models in Geomechanical Engineering Practice
(Keynote Lectures, presented at the International Symposium on Numerical Models in Geomechanics, September 13-17, 1982, Zurich, Switzerland), A. A. Balkema, in press.

LIQUEFACTION AND DENSIFICATION OF COHESIONLESS GRANULAR MASSES
IN CYCLIC SHEARING

S. Nemat-Nasser
Department of Civil Engineering
Northwestern University
Evanston, IL 60201

ABSTRACT

For cyclic shearing of saturated cohesionless granular masses, first the unified liquefaction (undrained sample) and densification (drained sample) theory of Nemat-Nasser and Shokooh (1978, 1979) is summarized, the basic equations are reported, and the theoretical predictions are compared with the corresponding experimental results. Then, the effect of pre-straining (drained) or pre-liquefaction (undrained) of the sample on its subsequent response is examined in the light of Nemat-Nasser's (1980) micro-mechanical consideration of simple shearing. In particular, it is shown that the liquefaction potential of the sample under cyclic shearing does not necessarily decrease because of pre-liquefaction or pre-straining, but, rather, that this resistance increases if the pre-liquefaction (or pre-straining) test is terminated at zero residual strain, and it decreases if the pre-liquefaction is terminated at zero residual stress; a similar tendency is observed for the sample resistance to densification.

1. INTRODUCTION

Cyclic shearing of a sample of cohesionless granules (sand) under fixed confining pressure produces overall densification. The granules move relative to each other in response to the applied shearing, and the sample tends to compact after each cycle in the presence of confinement. If the sample is saturated and is undrained, the densification tendency produces an increase in pore water pressure which in turn reduces the interparticular friction forces. These frictional forces diminish considerably when the pore water pressure attains values close to the confining pressure. The shearing resistance of the sample at such a state is very small, and the sample momentarily behaves like a liquid (hence, the term liquefaction). If on the other hand, the saturated sample is drained, its cyclic shearing at suitably small frequencies increases its density and hence, its shearing resistance.

Large-scale liquefaction has been observed as a result of earthquake ground motion, as well as of explosions. Well-known examples are earthquake-induced liquefaction in Niigata, Japan (1964), and massive soil failure in Anchorage, Alaska (1964). A brief historical account is given by Seed and Idriss (1982), in a recent monograph addressed to practical aspects of this phenomenon. Since the Niigata and Alaska earthquakes, considerable effort has been devoted to examining the mechanism of liquefaction; Seed and Lee (1966), Seed and Idriss (1967), Peacock and Seed (1968), Finn, Emery, and Gupta (1970), De Alba, Chan, and Seed (1975), Ishihara, Tatsuoka, and Yasuda

(1975), Martin, Finn, and Seed (1975), and Nemat-Nasser and Shokooh (1977, 1978, 1979). Although a major part of this activity has been experimental, some attempt has been made to quantify the estimate of the liquefaction potential of cohesionless sand by relating the number of cycles required for liquefaction to the normalized shear stress amplitude; see, e.g., Martin, Finn, and Seed (1975). A systematic approach based on an energy consideration, for both liquefaction and densification estimates, has been presented by Nemat-Nasser and Shokooh (1978, 1979); see also Nemat-Nasser (1982), where, in addition to the energy approach, liquefaction is analyzed with the aid of dimensional analysis.

Theories of this kind assume isotropic materials and are essentially of a one-parameter description; this parameter usually is the initial void ratio, or equivalently, the relative density. Therefore, they do not take into account any anisotropy that may exist prior to shearing.

It has been shown experimentally by Finn, Bransby, and Pickering (1970), and later confirmed by Ishihara, Tatsuoka, and Yasuda (1975), Seed, Mori, and Chan (1977), Ishihara and Okada (1978), and Nemat-Nasser and Tobita (1982), that pre-shear-straining of a drained sample at a relatively large shear-strain amplitude reduces considerably the sample's resistance to liquefaction. Nemat-Nasser and Tobita (1982) have employed a micro-mechanical model of dilatancy, proposed by Nemat-Nasser (1980b), in order to explain this phenomenon.

The micro-mechanical consideration suggests, and laboratory experiments confirm, that the resistance to liquefaction of a pre-shear-strained (drained), or pre-liquefied (undrained) sample diminishes considerably if the pre-straining or the pre-liquefaction in simple shearing under fixed confinement is terminated at zero shear stress, whereas this resistance certainly does not decrease, and perhaps increases, if the pre-straining or the pre-liquefaction is terminated at zero shear strain; see Nemat-Nasser and Tobita (1982), and Nemat-Nasser and Takahashi (1983).

This remarkable result seems to have important practical implications, because it is of considerable concern whether or not a site liquefied during an earthquake possesses any resistance to further liquefaction in aftershocks.

In this review paper, first the unified liquefaction and densification theory of Nemat-Nasser and Shokooh (1978, 1979) is summarized, and it is indicated how the theory has been used to estimate liquefaction potential for random loading; see, Pires, Wen, and Ang (1983). The basic equations are reported and the experimental verifications used by Nemat-Nasser and Shokooh are reproduced. Then, the micro-mechanical theory of Nemat-Nasser (1980b) is summarized and its application to the analysis of liquefaction phenomena is reviewed. Finally, some recent experimental results by Nemat-Nasser and Tobita (1982) and Nemat-Nasser and Takahashi (1983), are reported. The experiments have been designed in the light of the micro-mechanical consideration of Nemat-Nasser (1980b), with the specific purpose of

bringing into the open the influence of induced, as well as inherent, anisotropy (fabric) on the mechanical response of cohesionless granules subjected to cyclic shearing.

2. A SIMPLE LIQUEFACTION AND DENSIFICATION THEORY

First we consider cyclic shearing at constant shear stress amplitude, $\bar{\tau}$, and a fixed wave-form under constant pressure, σ_c . Then we examine cyclic shearing with variable amplitude and wave-form.

2.1 Cyclic Shearing

For cyclic shearing, we set

$$\tau(t) = \tau_0 \phi(t), \quad -1 \leq \phi(t) \leq 1, \quad \tau_0 = \bar{\tau} / \sigma_c, \quad (2.1)$$

where $\phi(t)$ defines the wave-form, and τ_0 is the normalized shear stress amplitude. We also normalize the pore water pressure, p_w , as

$$p = p_w / \sigma_c, \quad (2.2)$$

and note that liquefaction initiation corresponds to the state at which $p \rightarrow 1$.

2.2 An Energy Approach (Nemat-Nasser and Shokooh, 1979)

To change the void ratio of a saturated drained granular sample from e to $e + de$ by cyclic shearing, an increment of energy, dW , is required for rearranging the particles. This required energy increases as the void ratio, e , decreases, and becomes rather large when e attains its absolute minimum e_m . If the sample is undrained, then the tendency toward densification results in an increase in the pore water pressure. This in turn decreases the effective forces between contacting granules, and therefore reduces the energy, dW ,

required for particle rearrangement. Hence one may write

$$dW = -\tilde{v} \frac{de}{f(1+p) g(e-e_m)}, \quad (2.3)$$

where \tilde{v} is a constant with the physical dimensions of dW , and f and g are two non-decreasing material functions with the following properties:

$$f(1) = 1, \quad f' \geq 0, \quad g(0) = 0, \quad g' \geq 0. \quad (2.4)$$

For the undrained sample, we have

$$de = -\frac{e\sigma_c}{\kappa_w} dp \quad (2.5)$$

which reduces (2.3) to

$$dW = v \frac{edp}{f(1+p) g(e-e_m)}, \quad v = \tilde{v}\sigma_c/\kappa_w. \quad (2.6)$$

The liquefaction initiation is identified with the state where the value of the pore water pressure approaches that of the confining pressure, i.e. when $p (= p_w/\sigma_c) \rightarrow 1$. For problems relating to earthquake-induced liquefaction, the confining pressure σ_c is rather small, say, of the order of 10 to 100 psi; most experimental data are for $\sigma_c < 10$ psi. Since the bulk modulus of water is about 300,000 psi, the volumetric strain and the corresponding work per unit volume per unit confining pressure (dimensionless work) are of the order of 10^{-5} to 10^{-4} , and hence can be ignored without introducing any measurable error. Therefore, the void ratio e in (2.6) can be replaced by its initial value e_0 . With this substitution and upon integration, we obtain, from (2.6),

$$\Delta W = \frac{ve_0}{g(e_0 - e_m)} \int_0^p \frac{dp'}{f(1+p')} \quad (2.7)$$

It should be noted that the representation (2.3) is somewhat special in the sense that no coupling between p and $(e - e_m)$ is included. A more general form would be to use, instead of $f(1+p)g(e - e_m)$, the function $F(p, e - e_m)$. However, since for the drained case, $p = 0$, and for the undrained case, $e \sim e_0$, it appears that the form (2.3) is adequate for our purposes.

Nemat-Nasser and Shokooh (1977, 1978, 1979) consider the following simple approximations for f and g :

$$g(e - e_m) = (e - e_m)^n, \quad n > 1, \quad (2.8)$$

$$f(1+p) = (1+p)^r, \quad r > 1, \quad (2.9)$$

and obtain good correlation with some published experimental results for both densification of dry sand and liquefaction of saturated undrained sand. Pires, Wen, and Ang (1983), by relating the theory of Nemat-Nasser and Shokooh to experimentally-based observations of Seed, Martin, and Lysmer (1976), note an alternative form for the function f :

$$f(1+p) = \left[\theta \pi \sin^{2\theta-1} \left(\frac{\theta \pi p}{2} \right) \cos \left(\frac{\pi p}{2} \right) \right]^{-1}, \quad (2.10)$$

where $\theta = 0.7$, according to these authors. Being based on experimental observations, (2.10) may indeed produce better results than the simple form (2.9). In the present review, however, we side with simplicity and thus use (2.9) in the sequel.

Substitution from (2.9) into (2.7) yields

$$\Delta W = \frac{\bar{v}e_0}{g(e_0 - e_m)} [1 - (1+p)^{1-\tau}], \quad \tau > 1, \quad (2.11)$$

where $\bar{v} = v/(r-1)$.

For the densification of the drained sample, on the other hand, $p = 0$, and one obtains, from (2.3) and (2.8), by integration,

$$e = e_m + [(e_0 - e_m)^{1-n} + \bar{v}\Delta W]^{1/(1-n)}, \quad n > 1, \quad (2.12)$$

where $\bar{v} = (n-1)/\tilde{v}$.

In Eqs. (2.11) and (2.12) \bar{v} and \tilde{v} are as yet free parameters, and ΔW is the total energy used to attain the corresponding pore water pressure in (2.11), and densification in (2.12). To complete the formulation, we seek to estimate the energy increment ΔW in (2.11) and (2.12).

Since ΔW is the energy consumed in rearranging the granules, Nemat-Nasser and Shokooh (1979) suggest that it may be estimated in terms of the corresponding hysteretic loop. A typical loop of this kind is sketched in Fig. 1. Let A_i be the area enclosed by this loop. It is easy to show (Nemat-Nasser and Shokooh, 1979) that, in view of symmetry, one may set $A_i = h_i \tau_0^{1+\alpha}$ with α a positive even integer, and that h_i is an increasing function of the number of preceding cycles, N . If the incremental work for each cycle is taken to be proportional to A_i , one may write

$$\Delta W = \sum_{i=1}^N \lambda_i h_i \tau_0^{1+\alpha} = \bar{h}(N) \tau_0^{1+\alpha}. \quad (2.13)$$

Furthermore, for large stress amplitudes, one may assume \bar{h} proportional to N (see Nemat-Nasser and Shokooh for a discussion of this), i.e. $\bar{h} \sim hN$, and obtain

$$\tau_0^{1+\alpha} N = \bar{v} \frac{e_0}{g(e_0 - e_m)} [1 - (1+p)^{1-\tau}], \quad \bar{v} = \bar{v} / h. \quad (2.14)$$

Since α is even, it can be fixed immediately by inspection of experimental data. For Monterey No. 0 sand, data from De Alba, Chan, and Seed (1975) suggest $\alpha = 4$. This has been verified by experiments at Northwestern University by the author and his former student Mr. Y. Tobita. Indeed, setting $N = N_1$ for $p = 1$ (at liquefaction), (2.14) yields

$$\tau_0^{1+\alpha} = \frac{\eta e_0}{N_1 g(e_0 - e_m)}, \quad (2.15)$$

where η is a material constant. Figure 2 shows typical experimental results on circular cylindrical samples of Monterey No. 0 sand, tested in a dynamic simple shear apparatus; see Nemat-Nasser and Tobita (1982) for a description of the test procedure.

Nemat-Nasser and Shokooh use (2.8) and show that the quantity

$$\eta = N_1 \tau_0^{1+\alpha} (e_0 - e_m)^n / e_0, \quad (2.16)$$

with $\alpha = 4$ and $n = 3.5$, is indeed a constant for a number of experiments reported by De Alba, Chan, and Seed (1975) for relatively loose to dense (but not very dense, i.e. for D_r less than, say, 70%) samples; see Table 1. Nemat-Nasser and Shokooh suggest that, for dense

samples, h in the expression $\bar{h} = hN$, tends to become larger, and, since η is inversely proportional to h , Eq. (2.14)₂, it decreases with increasing D_r ; see Table 1.

With η fixed and g given by (2.8), Eq. (2.14) yields the pore water pressure in terms of the number of cycles, for various densities and stress amplitudes; Figs. 3 and 4. If the number of cycles is normalized with respect to N_1 , then we obtain the standard result given by Fig. 5. The fit here is as good as the simple assumption (2.9) permits. To improve this fit, a more elaborate expression, e.g. (2.10), must be used. Figure 6 compares the calculated results of (2.16) with the experimental data; additional comparison with experiments is given by Nemat-Nasser and Shokooh (1979).

To illustrate how the densification estimate (2.12) relates to experimental data on sand, we observe that most experimental results reported for the densification of drained sand in cyclic shearing are for strain-controlled tests. Hence, we must express ΔW in terms of the strain amplitude γ_0 and the number of cycles. A simple approach is to approximate the curve QOP in Fig. 1 by $\gamma_0 \sim A\tau_0^\beta$, where β must be an odd integer, and from (2.13) obtain

$$\Delta W = \bar{k}(N) \gamma_0^{(1+a)/\beta}. \quad (2.17)$$

Again, for large strain amplitudes, say, $\gamma_0 > 0.1\%$, we may assume $\bar{k}(N) \sim k_1 N$, whereas for small strain amplitudes the experimental results of Silver and Seed (1971a,b) and Youd (1970,1972) seem to suggest $\bar{k}(N) \sim k_2 N^{1/2}$. In this manner, (2.12) becomes

$$e = e_m + [(e_0 - e_m)^{1-n} + k_2 N^{1/2} \gamma_0^{(1-\alpha)/\beta}]^{1/(1-n)}, \quad (2.18)$$

for small strain amplitudes, and

$$e = e_m + [(e_0 - e_m)^{1-n} + k_1 N \gamma_0^{(1-\alpha)/\beta}]^{1/(1-n)} \quad (2.19)$$

for large strain amplitudes. To compare these results with experimental data, we follow Nemat-Nasser and Shokoh (1979), and use data reported by Youd (1972,1977). In this case, standard gradation Ottawa sands were densified in a Norwegian Geotechnical Institute type simple shear apparatus. Strains from 0.043% to 8.5% were used, with the number of cycles from 1 to 150,000. Figures 7 and 8 compare these with the estimates obtained from (2.18) and (2.19) with $\alpha = 4$, $\beta = 5$, $n = 3.5$, and $k_2 = 7000$ for (2.18) and $k_1 = 1000$ for (2.19).

It is clear that Eqs. (2.18) and (2.19) do encompass the essential features of the densification phenomenon of sand in cyclic shearing. These equations, however, assume no inherent anisotropy for the granular mass, and are intended to apply to cases where very large numbers of cycles are involved.

2.3 Irregular Shearing

Since the theory presented in the preceding subsection is based on an energy concept, it lends itself to extension for application to irregular and even random loading, as discussed by Pires, Wen, and Ang (1983).

The area of the hysteretic loop, in general, depends on the history of deformation, on the wave-form, and on the stress amplitude. To simplify, however, one may assume that, for the i^{th} cycle, the area A_i depends on the current stress amplitude. Let the wave-form be fixed. Then ΔW after N cycles may be expressed as

$$\Delta W = \sum_{i=1}^N h_i(e_i, \tau_i), \quad (2.20)$$

where e_i and τ_i are the void ratio and the shear stress amplitude in the i^{th} cycle, respectively. Some simplifying assumptions can be made in order to render (2.20) useful. A detailed account of a possible approach is given by Pires, Wen, and Ang (1983).

3. EFFECT OF FABRIC ON LIQUEFACTION AND DENSIFICATION POTENTIAL OF GRANULAR MASSES

It is well known that granular fabric (or anisotropy) greatly affects the overall response of the granular mass; see, e.g., Lafeber (1966), Arthur and Menzies (1972), Oda (1972), Mahmood and Mitchell (1974), Oda and Konishi (1974), Ladd (1977), Mulilis et al. (1977), and Oda, Konishi, and Nemat-Nasser (1980, 1982). In particular, it has been shown by Finn, Bransby, and Pickering (1970), and further confirmed by Ishihara, Tatsuoka, and Yasuda (1975), Seed, Mori, and Chan (1977), Ishihara and Okada (1978), Nemat-Nasser and Tobita (1982), and Nemat-Nasser and Takahashi (1983), that if the fabric of a saturated sand sample is changed by pre-liquefaction or pre-straining in a stress-controlled test, then the potential to subsequent liquefaction or densification under cyclic loading greatly increases. A remarkable fact, first noted by Nemat-Nasser and Tobita (1982) and recently thoroughly tested by Nemat-Nasser and Takahashi (1983), is that in cyclic shearing under constant confining pressure, the sample resistance to further liquefaction actually increases if the initial (pre)liquefaction cyclic test is terminated at zero residual strain, while this resistance is greatly reduced if the initial (pre)liquefaction cyclic test is terminated at zero residual shear stress. Thus it is not the pre-liquefaction per se that affects the subsequent sample strength, but rather, it is the fabric of the granular mass. Indeed, Nemat-Nasser and Tobita (1982) explain this rather dramatic change in the response of a pre-liquefied sample in

terms of the granular fabric characterized by the distribution of the microscopic dilatancy angles, i.e. the distribution of the orientation of the contact normals (at active contacts) measured relative to the normal of the overall macroscopic shear plane. They show that this distribution has a profound effect on the sample's potential to densification under drained conditions and, therefore, on its liquefaction potential when saturated and undrained. This result also suggests that the distribution of the dilatancy angles and, therefore, the fabric of a granular material in simple cyclic shearing, is more directly related to the total shear strain rather than to the shear stress.

In this section, we shall first review the micro-mechanical model of Nemat-Nasser (1980b), and then relate this model to the observed fabric-induced changes of the liquefaction and densification potential of sand in cyclic shearing.

3.1 A Micro-Mechanical Model in Simple Shearing (Nemat-Nasser, 1980b, and Nemat-Nasser and Tobita, 1982)

Consider uniform shearing of a sample of a granular mass under constant (uniform) normal stress σ , and variable (uniform) shear stress τ ; Figs. 9a,b. For the sake of modeling, it will be assumed that the sample area, A , is constrained to remain constant, so that volume changes are accompanied by appropriate changes of sample height, h . The macroscopic volume $V = Ah$ is regarded to be statistically representative.

The macroscopic shearing is in the x-direction, but on the micro-scale, grains must override each other and thus, their motion occurs over planes which pass through active contact points, as illustrated in Fig. 9c.

Denote by ν the angle which the "sliding" direction at a typical active contact (C in Fig. 9c) forms with the x-axis. ν is called the dilatancy angle. It is positive if the direction of motion is upward, and negative when it is downward, the first contributing to volume expansion, and the second to contraction; here positive dilatancy refers to volume expansion.

At each instant the macroscopic volume V contains a large number of active contacts, each associated with its own dilatancy angle. Let V contain n families with dilatancy angles ν_i , $i = 1, 2, \dots, n$. For the sake of modeling, we assign elementary volume V_i , area A_i , and height h_i to the i^{th} family, in such a manner that

$$V_i = A_i h_i, \quad V = \sum_{i=1}^n V_i, \quad (3.1)$$

and denote by

$$p_i = \frac{V_i}{V} \quad (3.2)$$

the volume fraction of the i^{th} family.

Consider the forces acting on the i^{th} family which are symbolically shown in Fig. 9d by a granule of dilatancy angle ν_i . The local stresses τ_i and σ_i , in general, are different from the overall

macroscopic stresses τ and σ . In Fig. 9d,

$$T_i = A_i \tau_i, \quad N_i = A_i \sigma_i. \quad (3.3)$$

The actual motion occurs in the x^* -direction. Therefore, in the x^* , y^* -coordinate system the tangential and normal forces, denoted by T_i^* and N_i^* , must relate in accordance with the friction law

$$T_i^* = N_i^* \tan \phi_\mu, \quad (3.4)$$

where ϕ_μ is regarded as the actual angle of friction. If we define

$$\tan \phi_i = \frac{\tau_i}{\sigma_i}, \quad (3.5)$$

then from the balance of forces we obtain

$$\tan \phi_\mu = \tan(\phi_i - \nu_i) \quad \text{or} \quad \phi_i - \nu_i = \phi_\mu, \quad (3.6)$$

showing that granules with negative dilatancy angles become active first.

Consider now the motion of the i^{th} granule in the x^* -direction, and calculate the rate of work per unit volume by

$$\dot{w}_i = \frac{\dot{W}_i}{V_i} = \frac{1}{V_i} T_i^* \frac{\dot{h}_i}{\sin \nu_i} = \frac{\tau_i \sin \phi_\mu}{\sin(\phi_\mu + \nu_i) \sin \nu_i} \frac{\dot{V}_i}{V_i}, \quad (3.7)$$

where $\dot{h}_i / \sin \nu_i$ is the velocity in the x^* -direction, and $\dot{V}_i = A_i \dot{h}_i$.

We assume that at the micro-level, the Mohr-Coulomb failure criterion applies. Then the local pressure \bar{p}_i equals $\tau_i / \sin \phi_i \cos \phi_i$, Fig. 9f, and hence

$$\dot{w}_i = \tau_i \dot{\gamma}_i - \bar{p}_i \frac{\dot{v}_i}{V_i} = \tau_i \dot{\gamma}_i - \frac{\tau_i}{\sin \phi_i \cos \phi_i} \frac{\dot{v}_i}{V_i} \quad (3.8)$$

From (3.7) and (3.8), we get

$$\frac{1}{V} \frac{\dot{V}}{\dot{\gamma}} = \sum_{i=1}^n \frac{\dot{\gamma}_i}{\dot{\gamma}} p_i \frac{\cos(\phi_\mu + v_i) \sin v_i}{\cos \phi_\mu} \quad (3.9)$$

where p_i is defined by (3.2).

For the considered macroscopic model problem, solution (3.9) is exact, subject to the basic assumptions that the Mohr-Coulomb failure criterion applies at the micro-level, and that ϕ_μ is constant. Let us now assume that $\dot{\gamma}_i$ of the micro-motion does not differ substantially from the macro-quantity* $\dot{\gamma}$, so that $\dot{\gamma}_i/\dot{\gamma} \sim 1$. Then (3.9) becomes (Nemat-Nasser, 1980b)

$$\frac{1}{V} \frac{\dot{V}}{\dot{\gamma}} = \sum_{i=1}^n p_i \frac{\cos(\phi_\mu + v_i) \sin v_i}{\cos \phi_\mu} \quad (3.10)$$

When the sample contains a very large number of active granules, one may consider a continuous distribution of the dilatancy angles, and write

$$\frac{1}{V} \frac{\dot{V}}{\dot{\gamma}} = \int_{v^-}^{v^+} p(v) \frac{\cos(\phi_\mu + v) \sin v}{\cos \phi_\mu} dv; \quad (3.11)$$

here, $p(v)dv$ is the volume fraction of active granules whose dilatancy angles are between v and $v + dv$, $p(v)$ is the corresponding density function, and v^+ and v^- are the upper and lower limits of the (active) dilatancy angles.

*Assumptions of this kind are extensively used in calculating the polycrystal response in terms of that of the single crystals, and date back to the work of G.I. Taylor (1938).

As has been pointed out by Nemat-Nasser (1980b), granules with negative dilatancy angles are initially activated and, therefore, $p(\nu)$ is initially biased toward negative dilatancy angles. Physically this is because the normal force N_i hinders the motion of an active granule with a positive dilatancy angle, whereas it assists if the granule has a negative dilatancy angle; compare Fig. 9d with Fig. 9e. This explains the observed initial densification. Note, however, that even with a distribution function $p(\nu)$ which is symmetrical with respect to $\nu = 0$ and hence $|\nu^-| = \nu^+$, the right-hand side of Eq. (3.11) would be negative; that is, Eq.(3.11) incorporates in a natural manner the nonsymmetrical influence of the normal stress σ on "upgoing" and "downgoing" granules.

As the shearing proceeds, the distribution function $p(\nu)$ becomes more biased toward the positive dilatancy angles. Hence, more weight is given to positive ν 's in Eq. (3.11), as shearing progresses. Eventually, when a suitable bias toward positive dilatancy angles is attained, the integral in (3.11) vanishes, marking the attainment of a minimum void ratio (or maximum density). After this state, continual shearing in the same direction results in a volume expansion, until the peak stress is reached, which, according to the theoretical considerations of Nemat-Nasser and Shokooh (1980), must correspond to a maximum rate of dilatancy. After that the rate of dilatancy begins to decrease in the post-failure regime, presumably becoming zero asymptotically at the critical state.

The three loading regimes -- initial densification (I) leading to dilatancy up to the peak stress (II) and then continuing in the post-failure behavior to the critical state (III) -- are shown schematically in Fig. 10. Subdivisions of this kind play an important role in the understanding of the effect of history on subsequent behavior of granular materials in cyclic loading. Before this is examined in connection with drained and undrained experiments, an important point relating to load reversal should be emphasized in the context of Eq. (3.11).

Suppose the sample in Fig. 9a is sheared clockwise under constant σ , beginning with $\tau = 0$ and continuing until a state in loading regime II is attained, where further shearing in the same direction results in volume expansion. At this state the distribution function $p(v)$ is strongly biased toward positive v 's. Suppose now the magnitude of the shear stress is gradually reduced to zero, keeping the normal stress σ constant. It is clear that some active contacts with previously (i.e. during the clockwise loading) large positive dilatancy angles, such as the one shown in Fig. 9d, may begin to move down as their corresponding shear stress is reduced; for example in Fig. 9d, if v_i is large enough and T_i is reduced, while N_i remains essentially the same, the particle may move down along the x^* -axis under the action of N_i , if there are no other constraints. Because of this, it is expected that the distribution of contact normals as well as the dilatancy angles will change somewhat as the shear stress is reduced to zero. However, it is reasonable to expect that even with

these changes, when τ in Fig. 9a is reduced to zero, a strong bias toward positive dilatancy angles for clockwise shearing still will remain. Now, upon load reversal, namely as τ is gradually increased counter-clockwise from zero in Fig. 9a, the direction of τ_i in Fig. 9d will change, and a previously positive dilatancy behaves now as a negative one; the direction of the x^* -axis is now reversed. Thus, a strong tendency toward large densification is expected upon shear load reversal. This means that, for example, a pre-straining into the loading regime II under undrained conditions can lead to immediate liquefaction, if load reversal is implemented under undrained (saturated) conditions. This is indeed observed by Finn, Bransby, and Pickering (1970) and Ishihara and Okada (1978) and is re-established by Nemat-Nasser and Tobita (1982) and Nemat-Nasser and Takahashi (1983). In the sequel we shall describe a number of experiments under both drained and undrained conditions, which were specifically designed to test the implications of Eq. (3.11) and, therefore, the effect of fabric.

Figure 11, taken from Nemat-Nasser and Tobita (1982), represents the results of a series of experiments on the effects of pre-straining and pre-liquefaction on subsequent behavior under undrained conditions. The saturated drained sample of initial void ratio 0.649 is first stressed over the path OC. At point C the drainage of the saturated sample is discontinued, so that branch CDE represents unloading (from C to D) and load reversal (from D to E) under undrained conditions. Since during the drained loading from O to B to

C the stress state moves into loading regime II with $p(v)$ developing a strong bias toward positive dilatancy angles, a tendency toward liquefaction occurs immediately upon load reversal. The test is terminated at point F with a residual strain of approximately 8.2%, the sample is drained and reconsolidated to the void ratio of 0.635, and a new test under undrained conditions is performed. The result is shown by the curve numbered 1 at the upper and lower peaks in Fig. 11. The other curves in this figure are obtained by reconsolidation of the sample after liquefaction. The numbers at the upper and lower peaks denote the number of times the sample has been pre-liquefied; the upper number within parentheses associated with each curve gives the corresponding void ratio, and the lower number the corresponding residual shear strain. As expected, the residual shear strain decreases with the number of pre-liquefactions, which may be attributed to the resulting smaller void ratio. The sample, once liquefied, shows a large displacement around an average shear stress of about 15 kN/m^2 , regardless of the number of preceding liquefactions. Thus, densification due to reconsolidation after liquefaction does not have much effect on the subsequent undrained behavior up to liquefaction initiation, although it does reduce the observed strain amplitude to a certain extent.

To further emphasize the directional dependency, namely, the fabric formation due to pre-straining, a virgin sample is subjected to loading, unloading, reverse loading, and then unloading to zero stress, with an overall stress amplitude of 67.4 kN/m^2 , under drained

conditions. The void ratio and the residual shear strain at the completion of this cycle are 0.649 and 5.1%, respectively. An undrained test is then performed at the overall stress amplitude of 21 kN/m^2 . The corresponding stress path is shown in Fig. 12. The loading path AB represents reloading in the same direction as the final half-cycle during the drained test. Hence, essentially no pore pressure build-up occurs. Some pressure is generated over the unloading branch BC, and a dramatic pore pressure is developed upon load reversal over the loading branch CD. This last loading branch is in the direction opposite to the direction of loading and unloading that has been implemented under the drained conditions, and which has resulted in 5.1% residual shear strain. Such strong directional dependency supports the concept of the formation of bias in the distribution of dilatancy angles during pre-straining. Branch DE corresponds to dilatancy and, therefore, pore pressure decreases. Thus, upon unloading from E to F and reverse loading from F to G, extensive pore pressure is generated.

In all the above tests the pre-straining is terminated at zero shear stress. From the micro-mechanical consideration of Nemat-Nasser (1980b), one concludes that, if the fabric as it is described by the distribution of the dilatancy angles, $p(v)$, is the key ingredient in introducing dramatic changes in sample behavior because of pre-straining, then a pre-straining over a cycle of relatively large strain amplitude which terminates with zero residual shear strain, should result in a considerably different subsequent

response from the one which terminates with zero residual shear stress. This is because, as the shear strain approaches zero, the particles tend to move into a more isotropic distribution of the dilatancy angles than when the shear stress is brought to zero. In fact, as discussed before, unless a very large strain amplitude is involved, unloading to zero shear stress does not completely destroy the fabric, whereas unloading to zero shear strain does to a large extent.

To provide experimental support for the above assertions, two tests are performed on a sample of essentially the same void ratio.

In the first test, shown in Fig. 13, the sample first is subjected to the stress half-cycle, ABC, under drained conditions, terminating at point C with zero shear stress. Then under undrained conditions cyclic stress of amplitude 21 kN/m^2 is applied, where the sample liquefies between the second and third cycles; note no pore pressure build-up from A to D; note also ratcheting toward the left in Fig. 13.

In the second test the pre-straining under drained conditions is terminated at zero shear strain, as shown in Fig. 14 by branches ABC. The sample is then subjected to cyclic loading of stress amplitude 21 kN/m^2 , and it is observed that liquefaction occurs during the seventh cycle, which essentially is the same as for the virgin sample. Further examination reveals that the pre-strained sample with zero residual shear strain does not show a strong directional depen-

dency, as does the pre-strained sample with finite residual shear strain (but zero residual shear stress).

In an effort to further verify these facts and, in addition, to examine the influence of the sample preparation on the mechanical response of cohesionless sands in cyclic shearing, Nemat-Nasser and Takahashi (1983) have made a series of strain-controlled tests on Monterey No. 0 sand samples. The same apparatus as the one used by Nemat-Nasser and Tobita (1982) is employed, except that the horizontal shearing device is modified in such a manner as to control the horizontal stroke and to measure the corresponding resulting horizontal force. Two sample preparation techniques are used: moist tamping and pluviating dry sand through air. The following basic results are obtained:

- (1) In cyclic simple shearing, the resistance to re-liquefaction (undrained) or densification (drained) of a pre-liquefied sample actually increases, because of the concomitant densification, if the pre-liquefaction is terminated at zero shear strain, but this resistance becomes very small, if the pre-liquefaction is terminated at zero residual shear stress.
- (2) The inherent anisotropy associated with sample preparation techniques affects both the densification and liquefaction potential of the sample.
- (3) Within each cycle of simple shearing, the induced anisotropy is essentially wiped out in the neighborhood of the zero shear

strain, and the anisotropy that exists at this state is basically due to the sample preparation techniques (i.e. it is the inherent anisotropy), provided that the sample is not very loose and the strain amplitude is not very large.

- (4) For simple cyclic shearing, the distribution of the dilatancy angles characterizing the fabric may be related to the shear strain and, in this manner, the densification pattern may be estimated.

ACKNOWLEDGMENT

This work has been supported by the U.S. Air Force Office of Scientific Research under grant no. AFOSR-80-0017 to Northwestern University.

REFERENCES

- Arthur, J.R.F. & B.K. Menzies 1972. Inherent anisotropy in a sand. Geotechnique 22(1): 115-128.
- De Alba, P.S., C.K. Chan & H.B. Seed 1975. Determination of soil liquefaction characteristics by large scale laboratory tests. Report no. EERC 75-14, College of Engineering, Univ. of California, Berkeley, CA.
- Finn, W.D.L., P.L. Bransby & D.J. Pickering 1970. Effect of strain history on liquefaction of sand. J. Soil Mech. Fdns. Div., ASCE, 96(SM6): 1917-1934.
- Finn, W.D.L., J.J. Emery & Y.P. Gupta 1970. A shaking table study of the liquefaction of saturated sands during earthquakes. In Proc. third European symposium on earthquake engineering, Sofia, Bulgaria. 253-262.
- Hardin, B.O. and V.P. Drnevich 1972. Shear modulus and damping in soils: measurement and parameter effects. J. Soil Mech. Fdns. Div., ASCE, 98(SM6): 603-624.
- Ishihara, K. & S. Okada 1978. Effects of stress history on cyclic behavior of sand. Soils and Foundations 18(4): 31-45.
- Ishihara, K., F. Tatsuoka & S. Yasuda 1975. Undrained deformation and liquefaction of sand under cyclic stresses. Soils and Foundations 15(1): 29-44.
- Ladd, R.S. 1977. Specimen preparation and cyclic stability of sands. J. Geotech. Engrg. Div., ASCE, 103(GT6): 535-547.
- Lafeber, D. 1966. Soil structural concepts. Engrg. Geology 1: 261-290.
- Mahmood, A. & J.K. Mitchell 1974. Fabric-property relationships in fine granular materials. Clays and Clay Minerals 22(5/6): 397-408.
- Martin, G.R., W.D.L. Finn & H.B. Seed 1975. Fundamentals of liquefaction under cyclic loading. J. Geotech. Engrg. Div., ASCE, 101(GT5): 423-438.
- Mulilis, J.P., H.B. Seed, C.K. Chan, J.K. Mitchell & K. Arulanandan 1977. Effects of sample preparation on sand liquefaction. J. Geotech. Engrg. Div., ASCE, 103(GT2): 91-108.
- Nemat-Nasser, S. 1980a. Liquefaction of soil during earthquakes. In G. Hart (ed.), Proc. of the second speciality conf. on dynamic response of structures: experimentation, observation, prediction and control, Atlanta, GA, 1981. ASCE, New

York. 376-385.

Nemat-Nasser, S. 1980b. On behavior of granular materials in simple shear. Soils and Foundations 20(3): 59-73.

Nemat-Nasser, S. 1982. On dynamic and static behaviour of granular materials. In G.N. Pande & O.C. Zienkiewicz (eds.), Soil mechanics--transient and cyclic loads, Int. symp. soils under cyclic loading, Swansea. Wiley, New York. 439-458.

Nemat-Nasser, S. & A. Shokooh 1977. A unified approach to densification and liquefaction of cohesionless sand. Earthquake Research and Engineering Laboratory technical report no. 77-10-3, Dept. of Civil Engineering, Northwestern University, Evanston, IL.

Nemat-Nasser S. & A. Shokooh 1978. A new approach for the analysis of liquefaction of sand in cyclic shearing. In Proc. of the second international conference on microzonation for safer construction--research & application, San Francisco, CA. 2: 957-969.

Nemat-Nasser, S. & A. Shokooh 1979. A unified approach to densification and liquefaction of cohesionless sand in cyclic shearing. Canadian Geotech. J. 16(4): 659-678.

Nemat-Nasser, S. & A. Shokooh 1980. On finite plastic flows of compressible materials with internal friction. Int. J. Solids Struct. 16(6): 495-514.

Nemat-Nasser S. & K. Takahashi 1983. Does preliquefaction or pretraining reduce sands' resistance to reliquefaction or densification? Earthquake Research and Engineering Laboratory technical report no. 83-7-54, Dept. of Civil Engineering, Northwestern University, Evanston, IL.

Nemat-Nasser, S. & Y. Tobita 1982. Influence of fabric on liquefaction and densification potential of cohesionless sand. Mechanics of Materials 1(1): 43-62.

Oda, M. 1972. The mechanism of fabric changes during compressional deformation of sand. Soils and Foundations 12(2): 1-18.

Oda, M. & J. Konishi 1974. Microscopic deformation mechanism of granular material in simple shear. Soils and Foundations 14(4): 25-38.

Oda, M., J. Konishi & S. Nemat-Nasser 1980. Some experimentally based fundamental results on the mechanical behavior of granular materials. Geotechnique 30(4): 479-495.

- Oda, M., J. Konishi & S. Nemat-Nasser 1982. Experimental micromechanical evaluation of strength of granular materials: effects of particle rolling. Mechanics of Materials 1(4): 269-283.
- Peacock, W.H. & H.B. Seed 1968. Sand liquefaction under cyclic loading simple shear conditions. J. Soil Mech. Fdns. Div., ASCE, 94(SM3): 689-708.
- Pires, J.E.A., Y.K. Wen & A.H-S. Ang 1983. Stochastic analysis of liquefaction under earthquake loading. Civil Engineering Studies, Structural Research series no. 504, technical report no. UILU-ENG-83-2005, ISSN: 0069-4274, Dept. of Civil Engineering, Univ. of Illinois at Urbana-Champaign, Urbana, IL.
- Seed, H.B. & I.M. Idriss 1967. Analysis of soil liquefaction: Niigata earthquake. J. Soil Mech. Fdns. Div., ASCE, 93(SM3): 83-108.
- Seed, H.B. & I.M. Idriss 1982. Ground motions and soil liquefaction during earthquakes. Earthquake Engineering Research Institute, Berkeley, CA.
- Seed, H.B. & K.L. Lee 1966. Liquefaction of saturated sands during cyclic loading. J. Soil Mech. Fdns. Div., ASCE, 92(SM6): 105-134.
- Seed, H.B., P.P. Martin & J. Lysmer 1976. Pore-water pressure changes during soil liquefaction. J. Geotech. Engrg. Div., ASCE, 102(GT4): 323-346.
- Seed, H.B., K. Mori & C.K. Chan 1977. Influence of seismic history on liquefaction of sands. J. Geotech. Engrg. Div., ASCE, 103(GT4): 257-270.
- Silver, M.L. & H.B. Seed 1971a. Deformation characteristics of sands under cyclic loading. J. Soil Mech. Fdns. Div., ASCE, 97(SM8): 1081-1098.
- Silver, M.L. & H.B. Seed 1971b. Volume changes in sands during cyclic loading. J. Soil Mech. Fdns. Div., ASCE, 97(SM9): 1171-1182.
- Taylor, G.I. 1938. Plastic strain in metals. J. Inst. Metals 62(1): 307-324.
- Youd, T.L. 1970. Densification and shear of sand during vibration. J. Soil Mech. Fdns. Div., ASCE, 96(SM3): 863-880.
- Youd, T.L. 1972. Compaction of sands by repeated shear straining.

J. Soil Mech. Edns. Div., ASCE, 98(SM7): 709-725.

Youd, T.L. 1977. Personal communication.

Table 1. Results obtained from (2.16) on the basis of data of De Alba, Chan, and Seed (1975).

$e_0 - e_m$	σ_c (kPa (psi))	N_1	τ_0	$\eta \times 10^6$
0.132 ($D_r = 54\%$)	55.6 (8.07)	8	0.155	0.859
	55.4 (8.03)	3.25	0.185	0.846
	31.2 (4.53)	12.5	0.144	0.929
	55.3 (8.02)	16	0.135	0.861
0.092 ($D_r = 68\%$)	56.1 (8.14)	63	0.104	0.920
	55.8 (8.09)	15	0.171	0.790
	55.1 (7.99)	4	0.230	0.927
	55.7 (8.08)	53	0.134	0.824
0.052 ($D_r = 82\%$)	55.6 (8.06)	6	0.211	0.903
	55.2 (8.00)	10	0.239	0.406
	55.4 (8.03)	28.5	0.188	0.348
	55.7 (8.08)	15.5	0.211	0.406

FIGURE CAPTIONS

- Figure 1: A typical maximum shear stress-maximum shear strain curve in cyclic shearing (from Hardin and Drnevich, 1972).
- Figure 2: Normalized shear stress amplitude versus number of cycles to liquefaction (from Nemat-Nasser, 1980a).
- Figure 3: Normalized excess pore water pressure p versus number of cycles in cyclic shearing of undrained saturated sand (data from De Alba, Chan, and Seed, 1975).
- Figure 4: Normalized excess pore water pressure p versus number of cycles in cyclic shearing of undrained saturated sand (data from De Alba, Chan, and Seed, 1975).
- Figure 5: Normalized excess pore water pressure p versus normalized number of cycles in cyclic shearing of undrained saturated sand (data from De Alba, Chan, and Seed, 1975).
- Figure 6: Normalized shear stress amplitude τ_0 versus number of cycles to liquefaction (data from De Alba, Chan, and Seed, 1975).
- Figure 7: Void ratio e versus number of cycles in cyclic shearing of dry sand (data from Youd, 1972).
- Figure 8: Void ratio e versus number of cycles in cyclic shearing of dry sand (data from Youd, 1977).
- Figure 9: (a) Simple shearing (plane strain) under constant normal stress σ ; τ is the shear stress and γ is the corresponding shear strain.
(b) A statistically representative sample of volume $V =$

Ah ; $N = \sigma A$ is the total normal force and $T = \tau A$ is the total tangential force acting on the sample.

- (c) At the active contact C, the sliding direction makes the angle ν with the macroscopic shearing x-direction; ν is the dilatancy angle.
- (d) Forces acting on a granule with positive dilatancy angle ν_i ; note that normal force N_i hinders sliding for $\nu_i > 0$.
- (e) An active contact with negative dilatancy angle; note that normal force N_i assists sliding.
- (f) The Mohr-Coulomb failure criterion is assumed to apply at the local microlevel; σ_i and τ_i are the local normal shear stresses, and \bar{p}_i is the local pressure.

Figure 10: Three loading regimes in monotone shearing: Regime I corresponds to densification, regime II begins with dilatancy and ends at the peak stress, and regime III pertains to post-failure response.

Figure 11: Under 100 kN/m^2 confining pressure, a drained sample is quasi-statically sheared over the loading branch OBC. At C the drainage is discontinued, and over (quasi-static) unloading (C to D) and load reversal (D to E) the sample liquefies. At F, residual strain is 8.2%. The sample is drained and reconsolidated to 100 kN/m^2 showing 0.635 void ratio. Then the new liquefaction test is performed (curve marked 1). Other curves are obtained in the same

manner. Numbers at upper and lower peaks denote the number of pre-liquefactions. The upper number in parentheses denotes the void ratio, and the lower one, the corresponding residual shear strain (%). Shear stress and shear strain are the horizontal force and displacement divided respectively by the sample area and the sample height (from Nemat-Nasser and Tobita, 1982).

Figure 12: A drained sample is subjected quasi-statically to a stress cycle (solid line in the insert figure) of amplitude 67.4 kN/m^2 under 100 kN/m^2 confining pressure. ABCDEF is the load path of the subsequent quasi-static undrained test. AB is the reloading in the direction of the final half-cycle of the drained test; it shows no pore pressure build-up. CD is in the opposite direction; it shows dramatic pore pressure build-up (from Nemat-Nasser and Tobita, 1982).

Figure 13: Under 100 kN/m^2 confining pressure, a drained sample is subjected quasi-statically to a half-cycle of stressing (ABC) with zero residual shear stress at C. The sample liquefies in the third cycle of 21 kN/m^2 average shear stress amplitude applied quasi-statically under undrained conditions (from Nemat-Nasser and Tobita, 1982).

Figure 14: Under 100 kN/m^2 confining pressure, a drained sample is subjected quasi-statically to a half-cycle of straining (ABC) with zero residual shear strain at C. The sample liquefies in the seventh cycle of 21 kN/m^2 average shear

stress amplitude applied quasi-statically under undrained conditions (from Nemat-Nasser and Tobita, 1982).

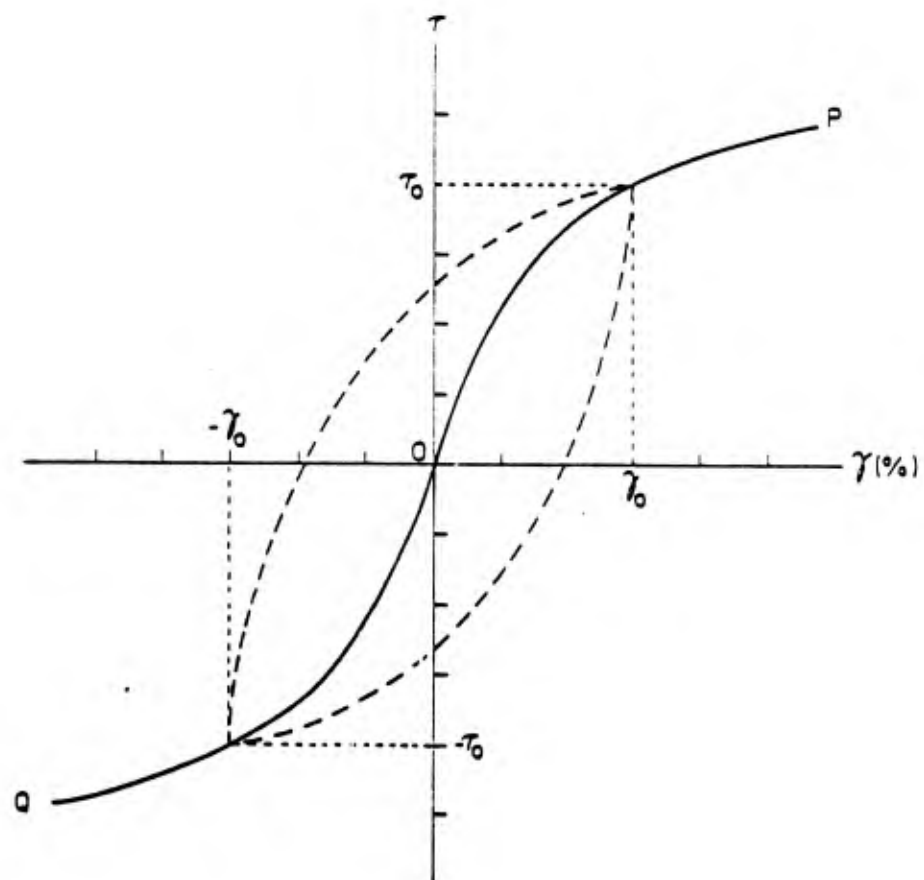


Figure 1

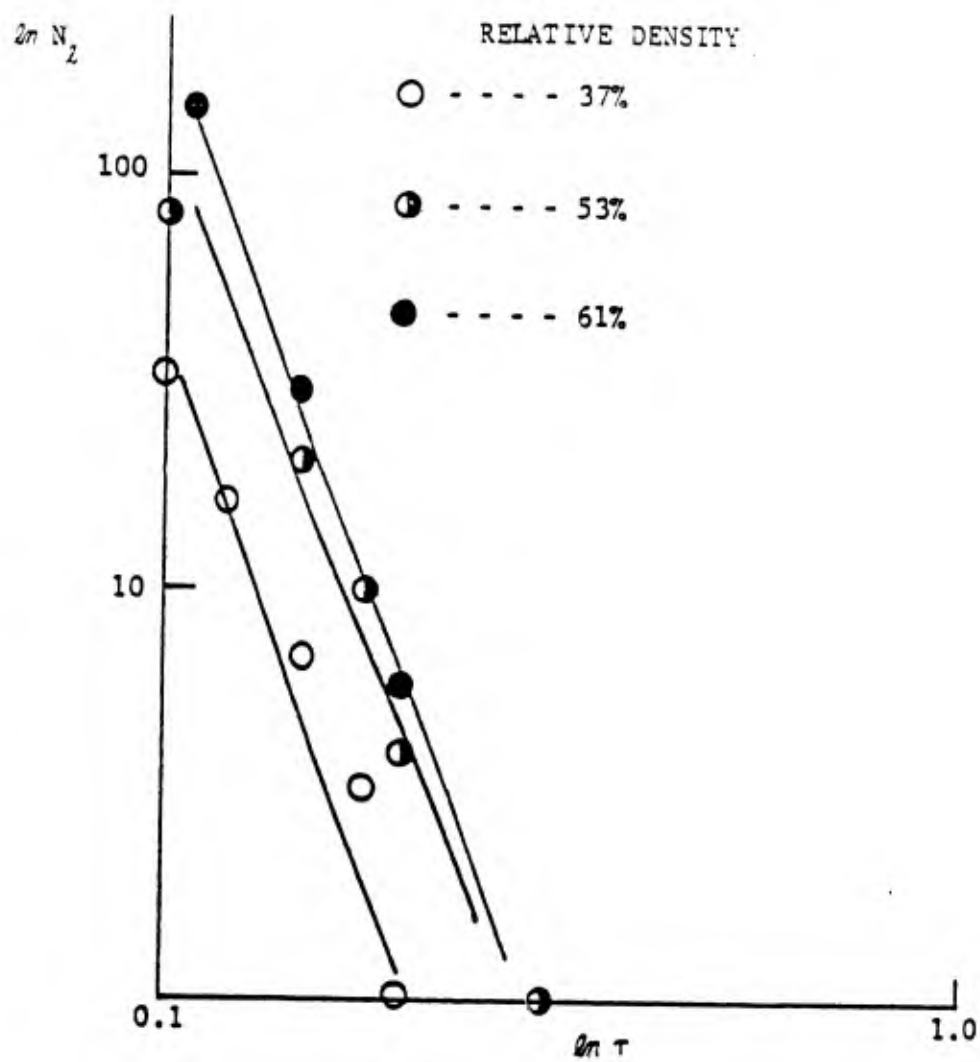


Figure 2

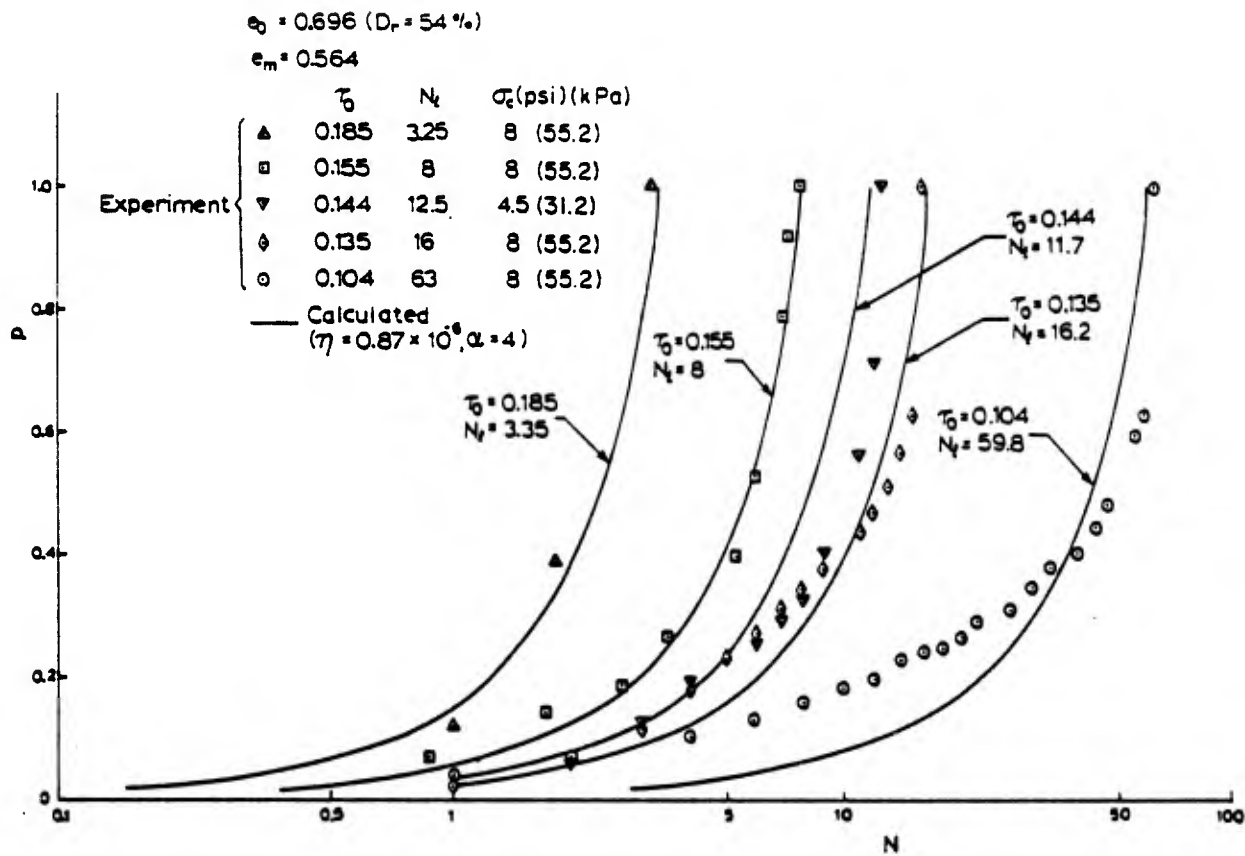


Figure 3

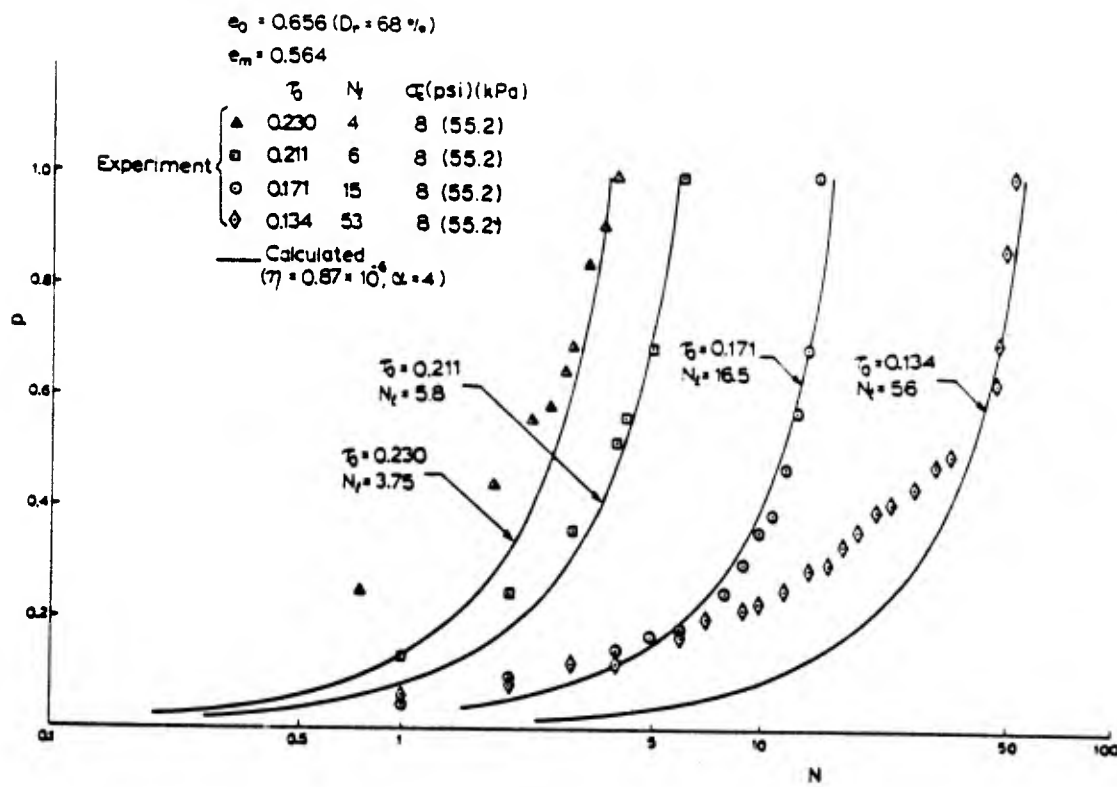


Figure 4

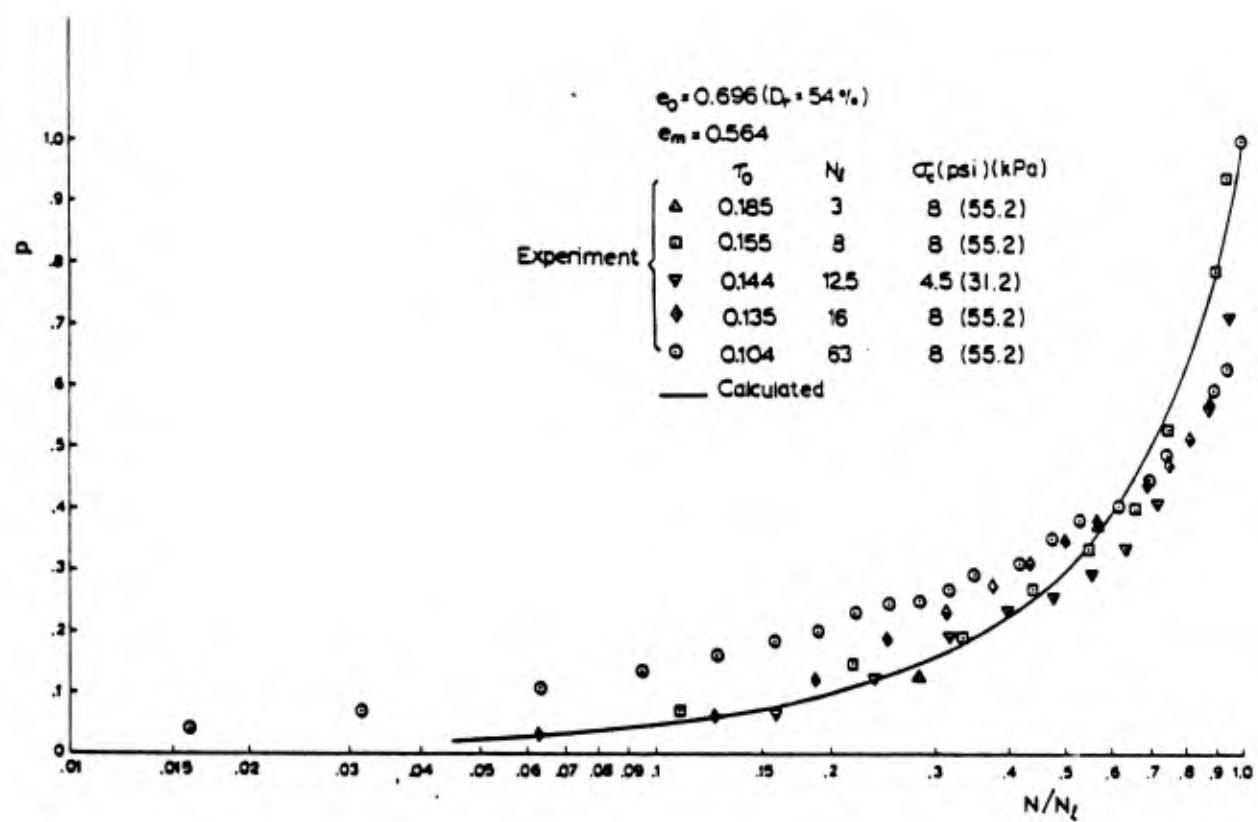


Figure 5

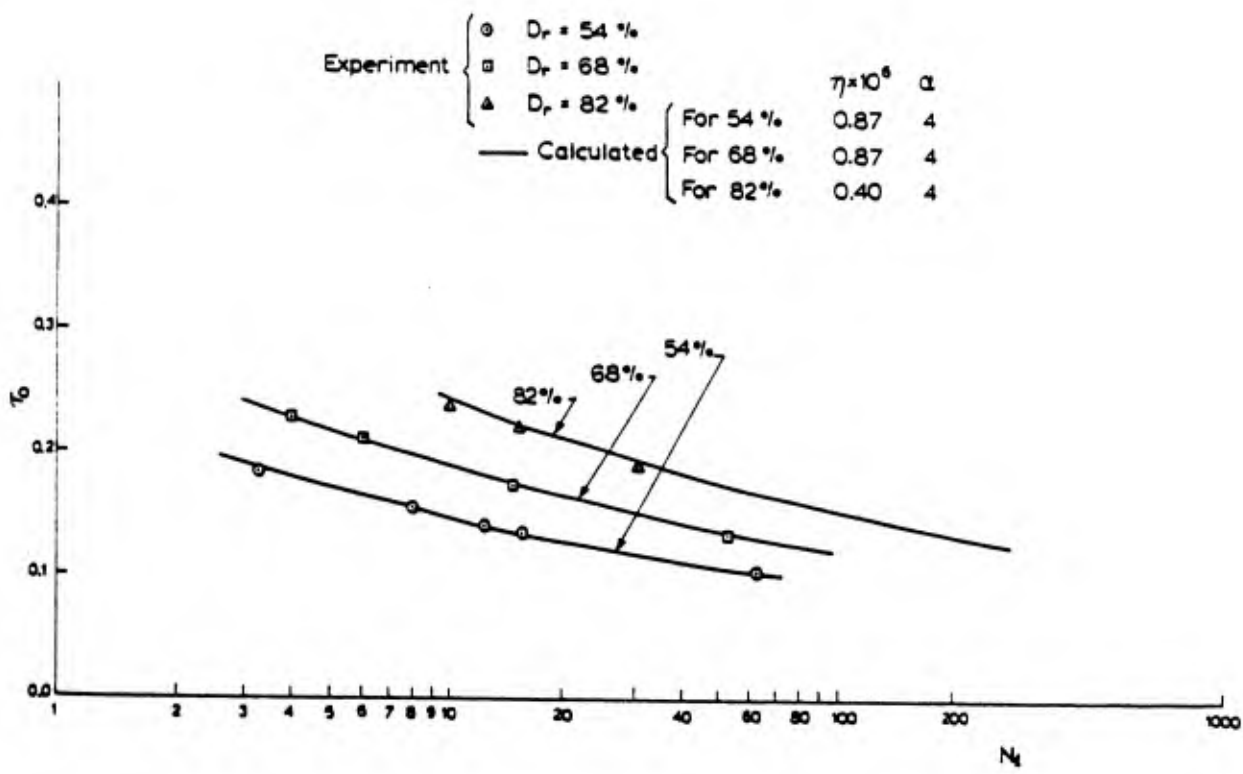


Figure 6

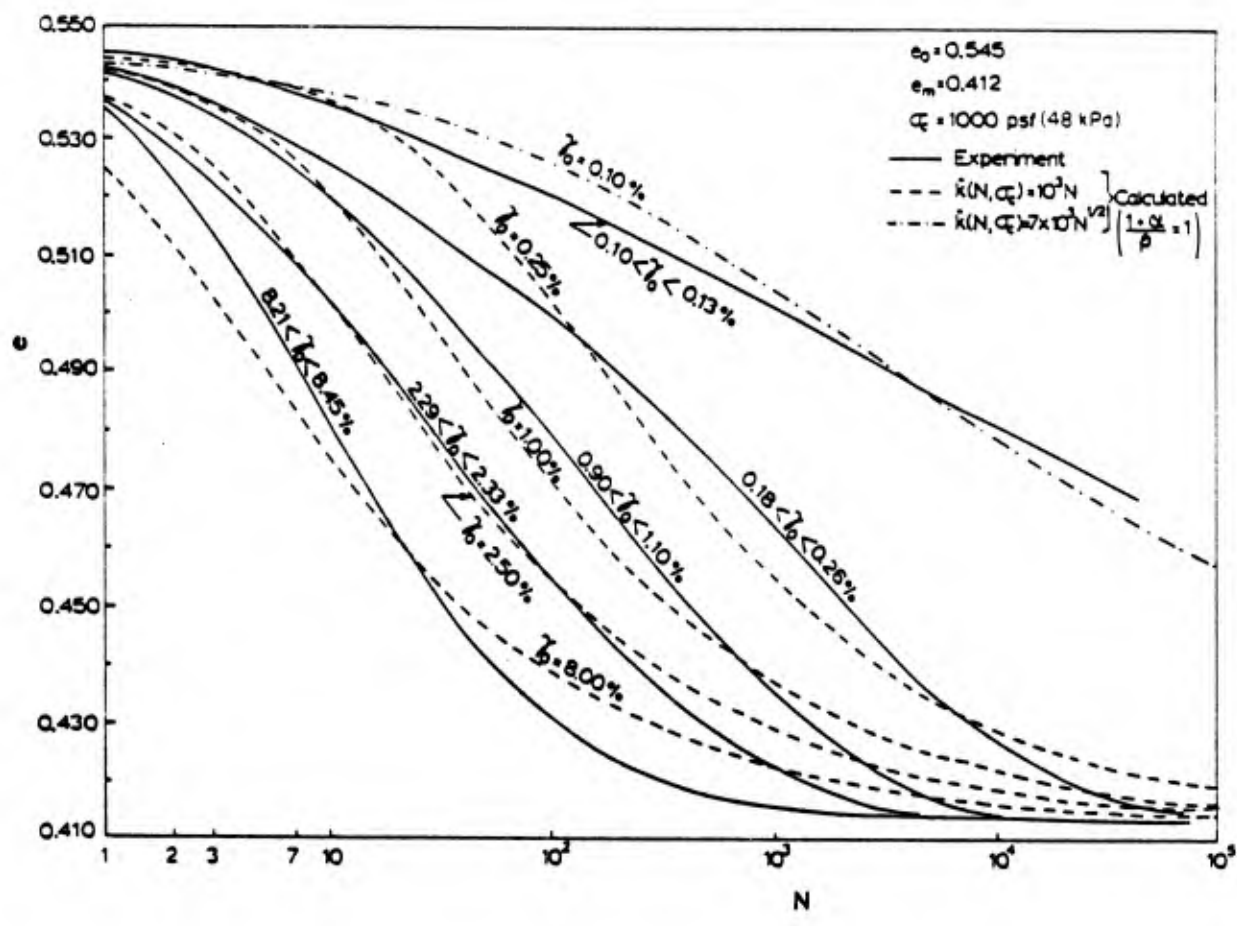


Figure 7

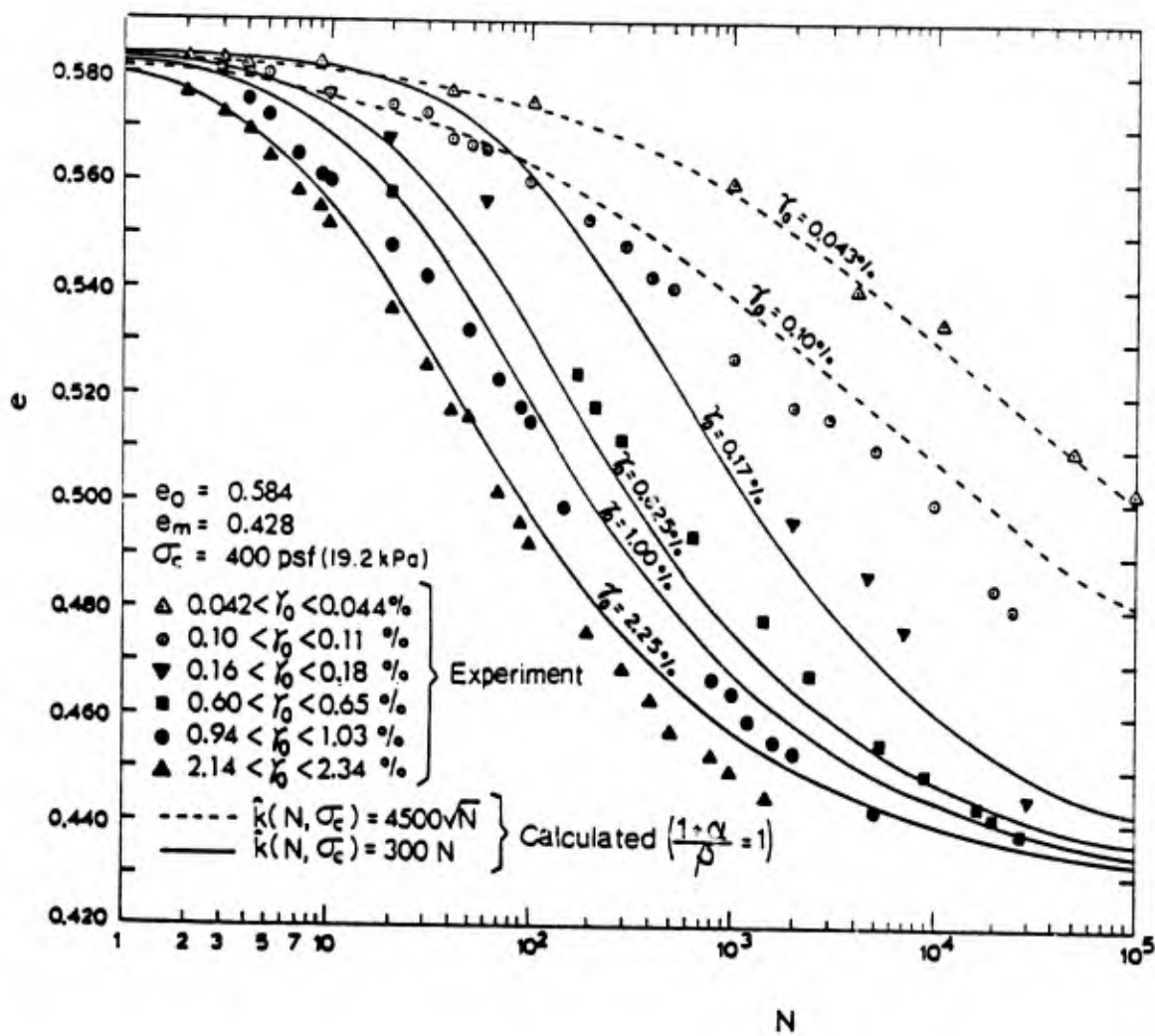


Figure 8

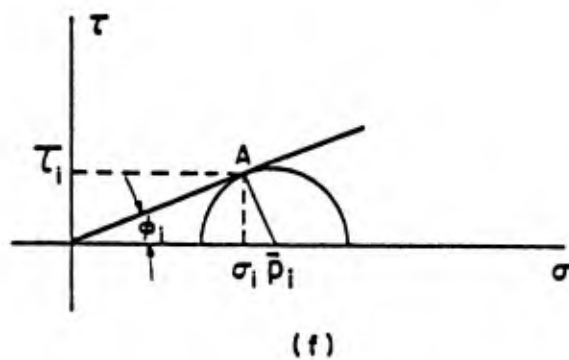
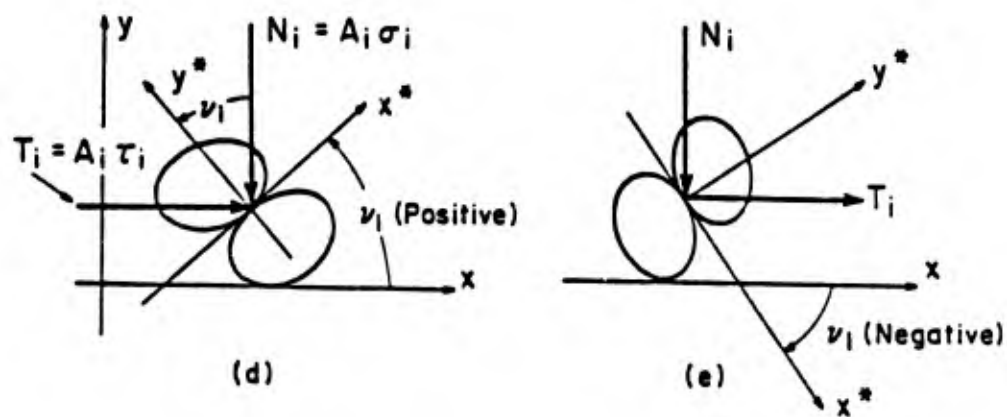
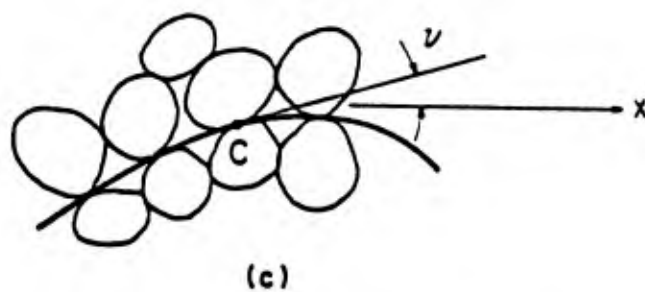
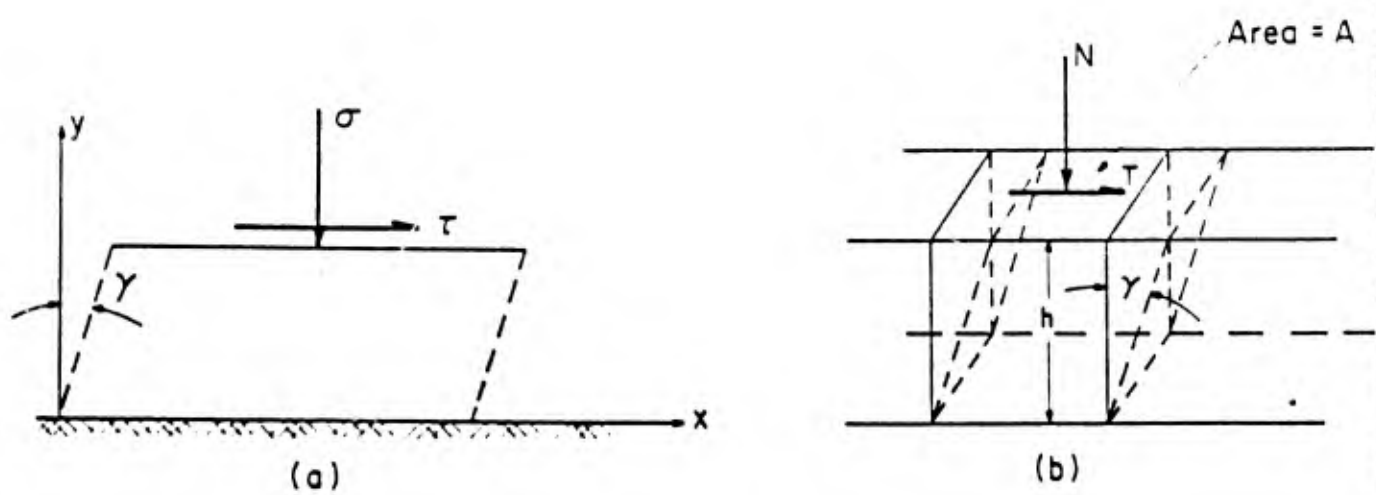


Figure 9

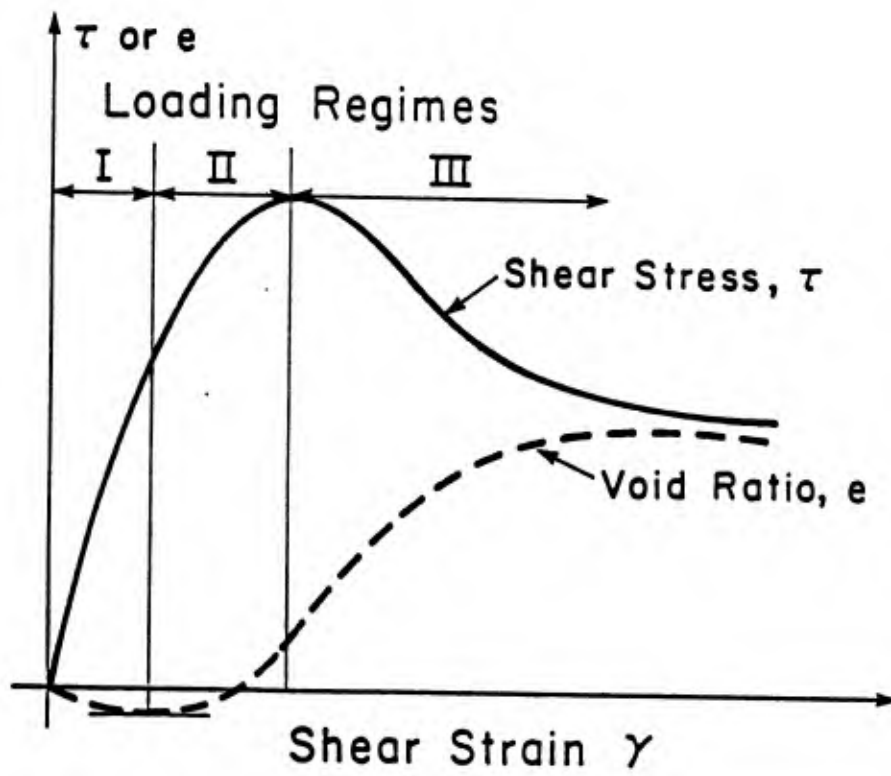
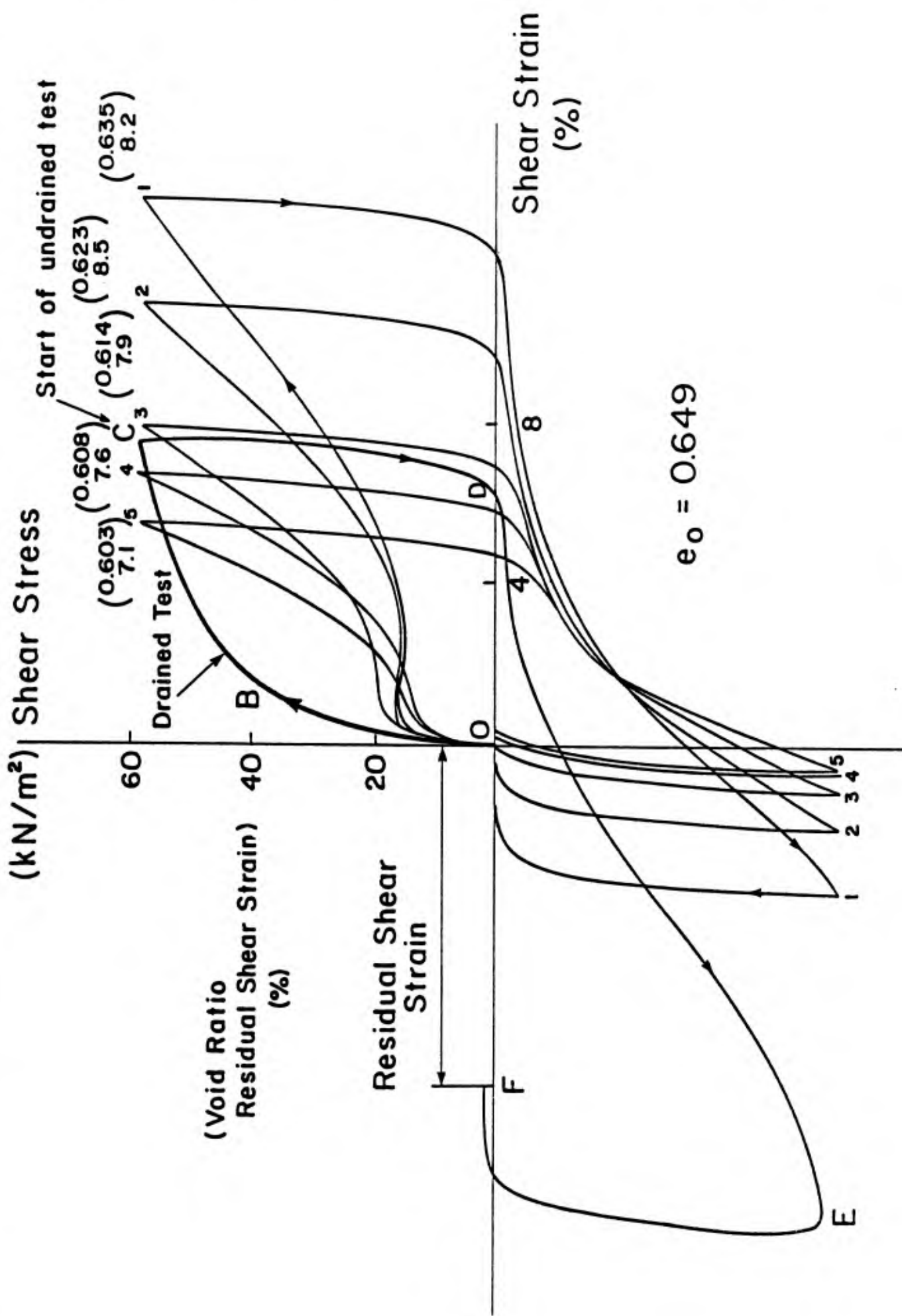


Figure 10



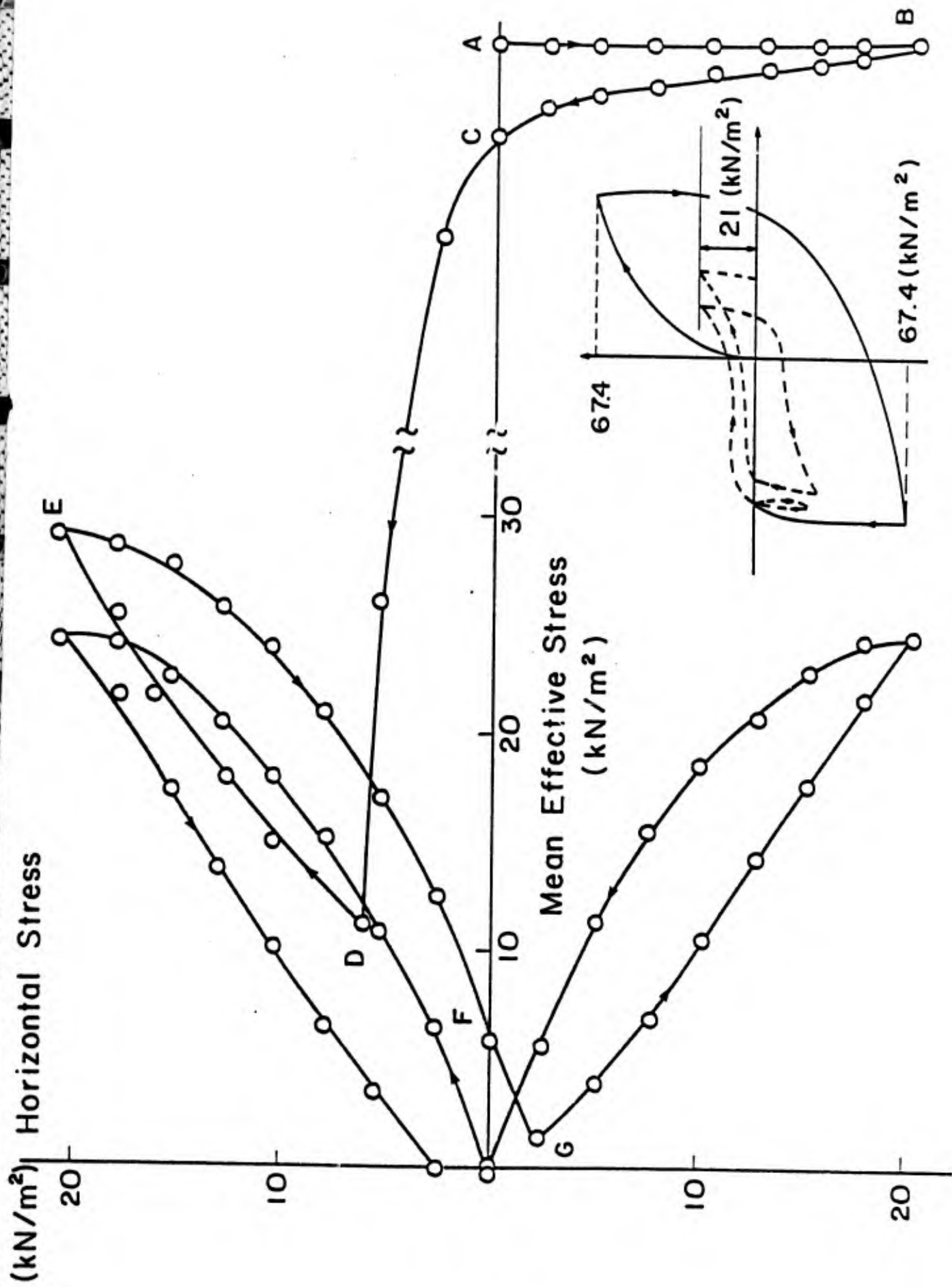


Figure 12

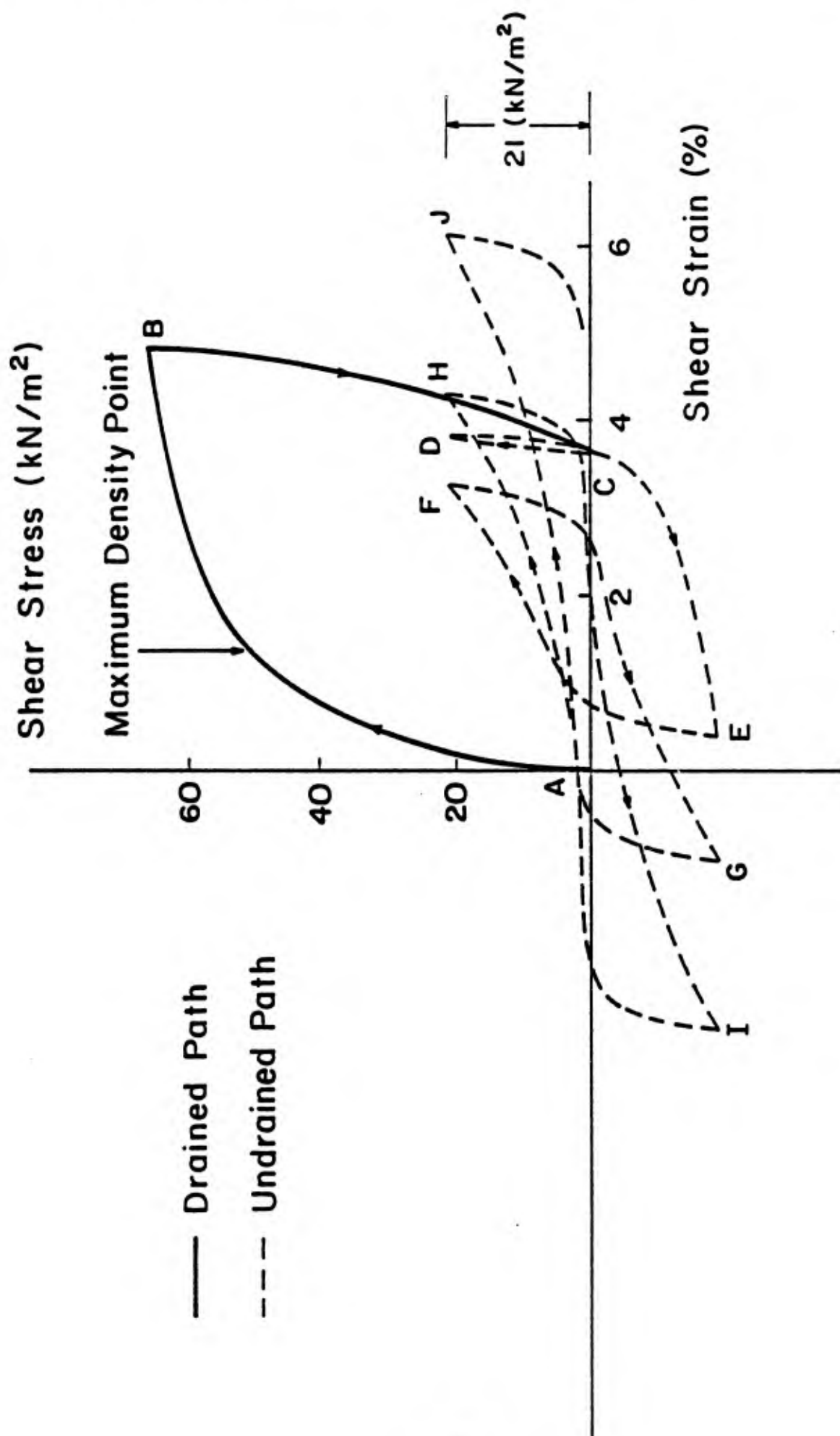


Figure 13

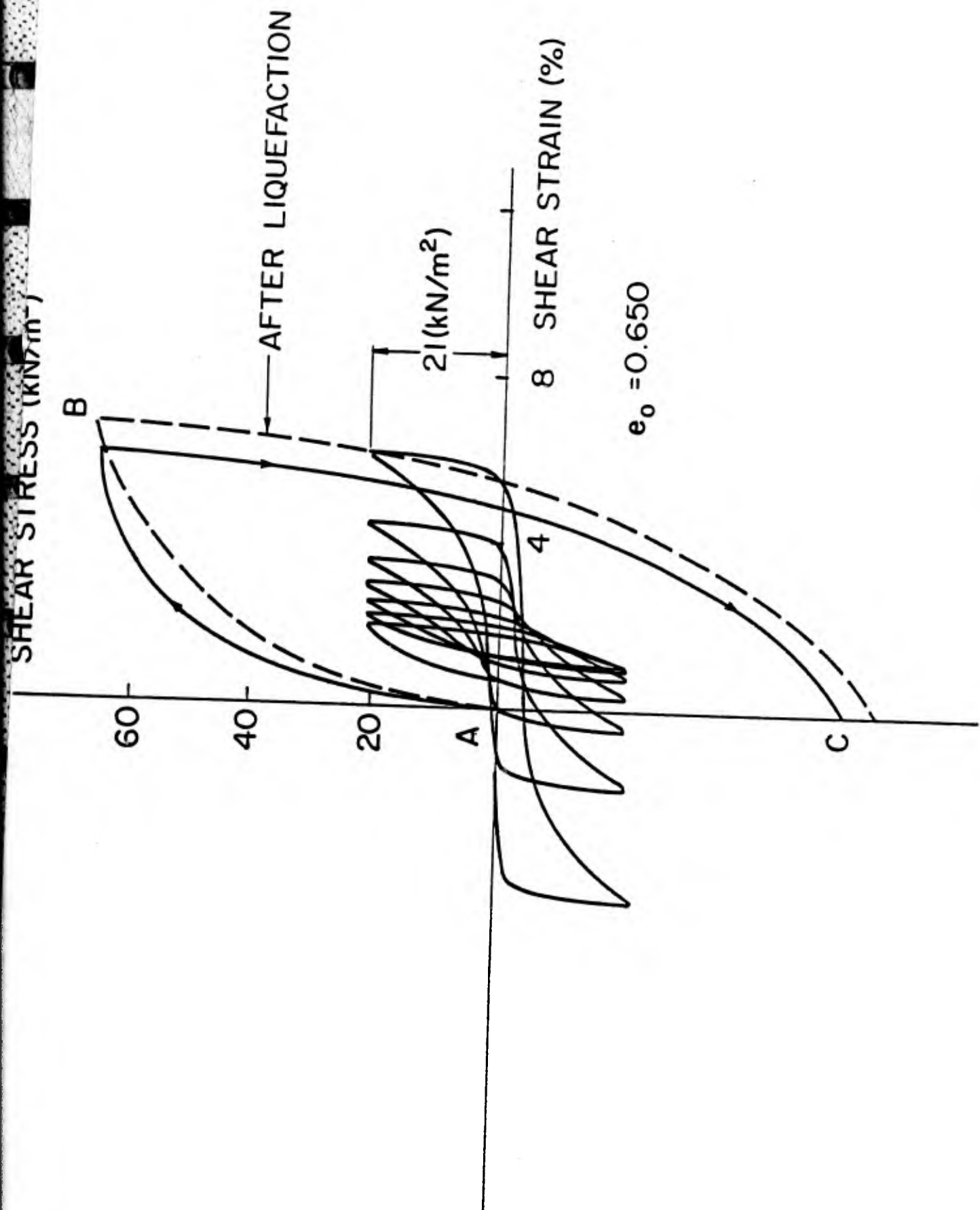


Figure 14

CHAPTER III

DOES PRELIQUEFACTION OR PRESTRAINING REDUCE SANDS' RESISTANCE TO
RELIQUEFACTION OR DENSIFICATION?*

by

S. Nemat-Nasser and K. Takahashi

Table of Contents

	Page
ABSTRACT	79
1. INTRODUCTION	80
2. SIMPLE SHEAR TEST	84
3. DEFORMATION DURING CONSOLIDATION	87
4. INFLUENCE OF PRETRAINING AND PRELIQUEFACTION	89
5. DEFORMATION DURING CYCLIC SHEARING	92
6. STRESS-DILATANCY CHARACTERISTICS	97
ACKNOWLEDGMENT	103
REFERENCES	104
TABLE 1	107
LIST OF FIGURES	108
FIGURES 1 - 12	111 - 127

*Submitted to: Journal of Geotechnical Engineering Division, ASCE

DOES PRELIQUEFACTION OR PRETRAINING REDUCE
SANDS' RESISTANCE TO RELIQUEFACTION OR DENSIFICATION?

by

S. Nemat-Nasser and K. Takahashi

Department of Civil Engineering
Northwestern University
Evanston, IL 60201

ABSTRACT

It is shown for simple shearing that the liquefaction and densification potentials of a cohesionless sample of sand do not necessarily decrease because of preliquefaction or because of large amplitude (drained) prestraining. In fact, in simple shearing, the resistance to liquefaction (undrained) or densification (drained) of a preliquefied sample actually increases, as a result of the concomitant densification, if the preliquefaction is terminated at zero residual shear strain, whereas this resistance is reduced considerably, if the preliquefaction is terminated at zero residual shear stress. The inherent anisotropy associated with dry pluviating and moist tamping sample preparation techniques is shown to affect the sample response to consolidation and to simple cyclic shearing. It is found that, within each cycle of simple shearing, the induced anisotropy is essentially wiped out in the neighborhood of the zero shear strain (but not at zero shear stress), and the anisotropy that remains at this state basically stems from the sample preparation technique. With the aid of the dilatancy fabric-relation proposed by Nemat-Nasser (1980) for simple shearing, the volumetric strain of the sample is estimated using a simple distribution function for illustration purposes, and the results are compared with the experimental data.

1. INTRODUCTION

Roughly speaking, two types of anisotropy (or fabric) are often distinguished when describing the mechanical response of granular materials: (1) inherent anisotropy which arises in laboratory samples from the sample preparation technique, and in natural settings from the deposition process; and (2) induced anisotropy which emerges in the course of deformation in response to applied loads. For example, when a sample is formed from slightly elongated granules by pluviating (dry) through air, the granules tend to lie with their longer axes in the horizontal plane, whereas when the granules are moist and the sample is formed by layering and tamping, the distribution of the orientations of the longer axes tends to be more or less random. On the other hand, a sample formed under uniform confining pressure from identical spherical granules does not have any inherent anisotropies, but it may be rendered anisotropic by subjecting it to a history of, say, shearing. In this case, the particles rearrange themselves because of the loading, and this results in the redistribution of the contact normals, which, to a large extent, characterizes the fabric.

It is commonly accepted and experimentally demonstrated that both types of anisotropy may have a profound effect on the mechanical response and on the strength of granular masses; see, e.g., Lafeber (1966), Arthur and Menzies (1972), Oda (1972), Mahmood and Mitchell (1974), Oda and Konishi (1974), Ladd (1977), Mulilis et al. (1977), and Oda, Konishi and Nemat-Nasser (1980). In particular, the liquefaction potential of saturated undrained granular bodies, as

well as their tendency toward densification under drained conditions, may be altered dramatically by suitable prestraining which results in a change in the granular fabric; see Finn, Bransby and Pickering (1970), Tatsuoka and Ishihara (1974), Ishihara, Tatsuoka and Yasuda (1975), Ishihara and Okada (1978), and Nemat-Nasser and Tobita (1982).

An interesting observation first made by Finn, Bransby and Pickering (1970), and later confirmed by, e.g., Ishihara, Tatsuoka and Yasuda (1975), Seed, Mori and Chan (1977), Ishihara and Okada (1978), and Nemat-Nasser and Tobita (1982), is that, once a sample is liquefied, its resistance (after reconsolidation) to further liquefaction is considerably diminished, even though the density of the reconsolidated sample may have increased. From a practical point of view, this has far-reaching implications, as it suggests that a site that has been liquefied in an earthquake may not possess much resistance to liquefaction during possible aftershocks. In a recent work, Nemat-Nasser and Tobita (1982) illustrate experimentally that, while this may be true for certain cyclic loading, it may not have general validity. Indeed, these authors report results of experiments where a saturated sample of Monterey No. 0 sand is liquefied in cyclic shearing under constant confining pressure, and where the sample resistance to further liquefaction is considerably reduced if the initial liquefaction is terminated at zero residual shear stress, while the resistance to further liquefaction is essentially unaltered if the initial liquefaction is terminated at zero residual shear

strain. Nemat-Nasser and Tobita explain this rather dramatic change in the response of a preliquefied sample in terms of the granular fabric characterized by the distribution of the microscopic dilatancy angles, i.e. the distribution of the orientation of the contact normals (at active contacts) measured relative to the normal of the overall macroscopic shear plane. They show that this distribution has a profound effect on the sample's potential to densification under drained conditions and, therefore, on its liquefaction potential when saturated and undrained. This result also suggests that the distribution of the dilatancy angles and, therefore, the fabric of a granular material in simple cyclic shearing, is more directly related to the total shear strain rather than to the shear stress. The bias in the fabric created either by drained prestraining of large shear strain amplitude,* or by liquefaction, is essentially wiped out if the test is terminated at zero shear strain, whereas the bias remains if the test is completed at zero shear stress.

In an effort to further verify these facts and, in addition, to examine the influence of the sample preparation on the mechanical response of cohesionless sands in cyclic shearing, we have made a series of strain-controlled tests on Monterey No. 0 sand samples. The same apparatus as the one used by Nemat-Nasser and Tobita (1982) is employed, except that the horizontal shearing device is modified in such a manner as to control the horizontal stroke, and to measure

*The strain amplitude is, however, kept below that corresponding to the peak stress.

the corresponding resulting horizontal force. Two sample preparation techniques are used: moist tamping and pluviating dry sand through air. The following basic results are obtained:

1) In cyclic simple shearing, the resistance to reliquefaction (undrained) or densification (drained) of a preliquefied sample actually increases, because of the concomitant densification, if the preliquefaction is terminated at zero residual shear strain, but this resistance becomes very small, if the preliquefaction is terminated at zero residual shear stress.

2) The inherent anisotropy associated with sample preparation techniques affects both the densification and liquefaction potential of the sample.

3) Within each cycle of simple shearing, the induced anisotropy is essentially wiped out in the neighborhood of the zero shear strain, and the anisotropy that exists at this state is basically due to the sample preparation techniques (i.e. it is the inherent anisotropy), provided that the sample is not very loose and the strain amplitude is not very large.

4) For simple cyclic shearing, the distribution of the dilatancy angles characterizing the fabric may be related to the shear strain and, in this manner, the densification pattern may be estimated.

2. SIMPLE SHEAR TEST

Samples are prepared from Monterey No. 0 sand with a specific gravity of 2.65, and maximum and minimum void ratios of 0.83 and 0.53, respectively.

On the average, the diameter and height of the samples are 7.1 cm and 3.1 cm, respectively.

Two sample preparation methods are used: moist tamping and dry pluviating. In the moist tamping method, sand which has been mixed with 8% water by weight is poured into the mold by spoon and then tamped with a rod, in order to obtain the desired height. The sample is poured in three layers, each about 1 cm thick. In the dry pluviating method, air-dried sand is pluviated through air from a certain height by means of a funnel and a vinyl pipe of 6 mm inner diameter. Although the drop-height is changed in order to change sample density, the method yields relatively dense samples, in general. The surface of the dry sand is trimmed in the manner suggested by Mulilis, Chan and Seed (1975).

Waterproof sandpaper is attached to the surfaces of the top and base platens to prevent slip between the platens and the specimen.

Carbon dioxide (CO_2) is percolated for half an hour through the specimen to obtain a satisfactory degree of saturation, and then de-aired water is circulated through the specimen for one hour. A back pressure of 100 kN/m^2 is applied to achieve saturation with a B-value

exceeding 0.95.

The test apparatus used is a simple shear apparatus with a deformation control system. Horizontal force is applied by a mechanical system with an electric motor through a load cell which controls the stroke and monitors the intensity of the load transmitted to the specimen. Vertical force is applied by a pneumatic device, and the load is monitored by a load cell on the top platen. Linear variable differential transformers (LVDT) are used to monitor the horizontal and vertical displacements. Drainage lines are provided through both the top and base platens. The pressure transducer is installed in the drainage line, and pore pressure is measured by preventing drainage through the specimen. In the case of drained tests, drainage lines are led to a standpipe and the change of volume of the specimen is measured from the water level in the standpipe.

Output from all transducers is recorded automatically in a micro-computer through an A/D converter (except for the volume change), and the load deformation relation is also recorded by an X,Y-plotter.

It should be pointed out that in experiments of this kind, neither the states of strain and stress within the sample, nor tractions applied over the boundaries of the sample are uniform. The limitations of the so-called simple shear test of this kind have been examined by Wood and Budhu (1980). Indeed, the stress distribution in circular cylindrical samples sheared in the sample shear apparatus,

is non-uniform and actually three-dimensional. Nevertheless, since all tests are made under similar basic conditions, the conclusions reflect the comparative changes that have been created in the sample by different histories and, therefore, they do capture the essential fundamental character of the material response.

Since flexible membranes are used, the sample area changes in the course of deformation. The average area is calculated from the measured volume and the vertical displacement. No effort is made to correct the measured volumetric strains for the effect of the "membrane penetration" which is known to be rather important in tests of this kind (see, e.g., Newland and Allely (1959) and El-Schby and Andrawes (1972)) because it is more the qualitative, rather than the quantitative, nature of the tests that is at focus in this paper. Moreover, since all tests are performed under essentially similar conditions, the comparative conclusions should remain valid even if there is a systematic error in the measured volumetric strains, especially when the confining pressure remains the same.

All tests are performed with the horizontal displacement controlled.

3. DEFORMATION DURING CONSOLIDATION

Consolidation (drained) produces different deformations in the sample, depending on the preparation technique. For samples prepared by pluviating dry sand through air, grains are packed with their longer axes in the horizontal plane, whereas in moist tamping the orientation of the grains is essentially random, in view of the capillary forces holding the grains together. Therefore, in the latter case, the sample tends to have a more random (isotropic) fabric, as suggested by Ladd (1977).

Table 1 lists the tests performed in this study. Figures 1 and 2 present the relations between the sample height change (Δh) and the sample volume change (ΔV), and between the sample height change and the sample diameter change (ΔD) for different indicated K-values ($K = \sigma_h / \sigma_v$, where σ_h is the effective lateral pressure, and σ_v is the effective vertical pressure).

The effect of the K-value on the test results is as expected, since an increase in the lateral pressure results in a greater lateral contraction, and, therefore, for larger K-values, smaller vertical contraction results. However, samples prepared by the dry pluviating method show smaller vertical contraction and even vertical expansion (for $K = 2$) than those prepared by moist tamping. The results of Figs. 1 and 2 clearly show a greater tendency toward diametral contraction for the dry pluviating samples than for the moist tamping ones, while the corresponding volume changes may be

nearly the same. It is therefore concluded that the biased particle orientation created by the preparation technique produces an inherent anisotropy in samples made by dry pluviating.

4. INFLUENCE OF PRETRAINING AND PRELIQUEFACTION

Figures 3a and b show the results of pretraining and preliquefaction on samples prepared by dry pluviating. In Fig. 3a the solid curve marked "0" represents drained cyclic shearing with strain amplitude of 4%, which produces initial densification followed by dilation, then densification upon strain reversal, changing to dilation at about zero strain, and continuing with dilation until strain reversal. The cycle is completed at zero residual shear strain. The sample is then reconsolidated and, under undrained conditions, it is subjected to cyclic shearing of 0.8% strain amplitude. The sample liquefies in 20 cycles, essentially the same as for a virgin sample; had the preliquefaction been terminated at zero residual shear stress, the sample would have then re-liquefied in only one cycle; see Nemat-Nasser and Tobita (1982, Figs. 13, 14, and 15, pp. 56-58).

The sample is then drained and consolidated and, under drained conditions, it is subjected to another cycle of straining of 4% maximum amplitude. The result is shown by the dash-dot curve marked "1" in Fig. 3a. As is seen, the response is essentially the same as that of the virgin sample.

It has been demonstrated by Nemat-Nasser and Tobita (1982, Figs. 7 and 8, p. 52) that a preliquefied sample shows a strong directional bias when the initial liquefaction test is terminated at zero residual shear stress. Specifically, if in the subsequent drained test the load path retraces the final half of the stress cycle which had

produced liquefaction, then the sample shows very small densification or even dilation, whereas when the load path in the drained test continues and completes the half terminal cycle that had caused liquefaction, then large densification is observed.

In contrast, no such directional bias in densification is observed when the preliquefaction test is terminated at zero residual shear strain.

After the second cycle of prestraining marked by "1" in Fig. 3a, the sample is subjected to another undrained cyclic shearing of 0.8% strain amplitude. It liquefies after 20.5 cycles. The dash-dot-dot curve marked "2" in Fig. 3a is the result of a subsequent cycle of the drained test. Since the sample has densified, and since, because of zero residual shear strain after each liquefaction, the fabric is essentially unbiased, considerably greater dilation is observed. As is seen from the result in Fig. 3b, the corresponding shear stress amplitudes have increased, so that the sample has become stronger, with greater resistance to densification and less potential toward liquefaction.

In Figs. 4a and b we report typical results of the effect of small amplitude prestraining and preliquefaction on a sample prepared by moist tamping. The solid curve in Fig. 4a marked "0" corresponds to the virgin sample. Continuous densification occurs, since the shear strain amplitude is small. Upon completion of the drained test (solid curve in Fig. 4a), the sample is consolidated and, under

undrained conditions, it is subjected to cyclic straining of 1% strain amplitude. It liquefies after 10 cycles, essentially the same as for the virgin sample. The dash-dot curve marked "1" in Fig. 4a is the result of a subsequent drained test on this preliquefied sample. The sample does not show any directional bias. Upon completion of this drained test, the sample is again liquefied by cyclic shearing of 1% strain amplitude. It shows no reduction in its resistance to liquefaction. Indeed, as is seen from Fig. 4b, the sample has strengthened in view of its greater density, after each liquefaction. The dash-dot-dot curve marked "2" in Fig. 4a represents the results of the final drained shear test on the same sample.

From the results presented in this section, which are typical for strain-controlled cyclic shearing, it is evident that prestraining with large shear strain amplitude, or preliquefaction, does not necessarily reduce the sample's resistance to liquefaction or densification. It all seems to depend on how preliquefaction or prestraining is terminated: if the termination is at zero residual shear stress, then resistance to subsequent liquefaction or densification is reduced considerably; on the other hand, if the termination is at zero residual shear strain, this resistance is not changed or even may be increased. These observations may be useful in developing techniques by which the liquefaction potential of sites which recently have liquefied during an earthquake may be estimated by field inspections.

5. DEFORMATION DURING CYCLIC SHEARING

In this section sample deformation during strain-controlled drained cyclic shearing is examined, focusing attention on the effects of inherent anisotropy induced by sample preparation techniques (i.e. dry pluviating versus moist tamping), on the effects of confinement (i.e. the K-value), and on the effects of sample density.

A set of typical results is shown in Figs. 5a to d, for a sample prepared by the dry pluviating method and strained for 20 cycles at 4% maximum shear strain amplitude. Thirty to sixty data points are obtained for the first three, the fifth, the tenth, and the twentieth cycles, and only six data points for the remaining cycles. These six data points are taken when the shear stress and shear strain are zero (4 points), and when the shear strain is maximum (2 points). The corresponding stress-strain loops are shown in Fig. 5a, where τ is the shear stress obtained by dividing the total horizontal force by the initial sample area, and σ_m is the mean stress. Figures 5b and c represent the history of the volumetric strain in terms of shear strain and normalized shear stress (i.e. τ/σ_m), respectively. Examination of Fig. 5b reveals that in each cycle, sample dilation changes to densification at points of shear strain reversal. Furthermore, starting at the point of strain reversal in each cycle, the sample begins to densify until a point close to zero shear strain, where densification ceases and dilation begins. This corresponds to the state termed by Ishihara, Tatsuoka and Yasuda (1975) "phase transition". It represents a state where significant changes in granular

fabric begin to take place;* see Nemat-Nasser and Tobita (1982). Indeed, it is precisely for this fact that, if a drained prestraining is terminated at this state (i.e. zero shear strain), the sample exhibits negligibly small bias in its fabric; see Section 3. Note from Fig. 5b that the state in question corresponds to the maximum volumetric strain over each half-cycle. To identify this state in the sequel, we shall refer to it as "point of zero dilatancy", and we shall assume (subject to negligibly small errors) that the point of zero dilatancy coincides with the point of zero shear strain for each half-cycle.**

Figure 5d gives the vertical strain (strain measured along the axis of the cylindrical sample) as a function of volumetric strain. In this figure the locus of points of zero dilatancy is identified by a solid curve. Numbers on this solid curve denote the corresponding cycle. We shall refer to the locus of points of zero dilatancy as the "zero dilatancy curve".

Figure 6 shows the zero dilatancy curves for all the tests listed in Table 1. The numbers written next to the circular or triangular marks designate the relative density of the sample. Open circles or triangles are data for dry pluviated samples, whereas the

*For triaxial tests, Luong (1980) attributes a similar significance to the zero dilatancy state which he calls the "characteristic state".

**It should be noted that these comments are intended to apply to simple cyclic shearing only. Their generalization to other cases requires further study.

corresponding solid geometric marks are for samples prepared by moist tamping.

There are four groups of data points, each associated with a different K-value, as indicated; see Table 1 for the list of strain amplitudes used.

The distribution of the data points in Fig. 6 closely correlates with that of Fig. 1. Indeed, the ratio of the abscissa over the ordinate of each data point in Fig. 6 is essentially the same as the corresponding ratio in Fig. 1. This fact appears to be rather important, because the distribution of data points in Fig. 1 closely relates to the influence of the inherent anisotropy. Therefore, it may be concluded that the distribution of the points of zero dilatancy in Fig. 6 also reflects the effects of inherent anisotropy. In other words, samples with the same K-value, with the same relative density, subjected to cyclic shearing of the same strain amplitude, will have distinct zero dilatancy curves, if and only if they have different inherent anisotropies.

In Fig. 6 there are eleven curves associated with isotropic confinement ($K = 1$). Six open circles represent the result of 20 cycles of straining of samples prepared by the dry pluviating method. Four open circles marked 75, 80, 82, and 80 (% relative density) from left to right, respectively, correspond to 0.5, 1, 2, and 4% maximum strain amplitudes. Therefore, the total volumetric strain at points of zero dilatancy increases with increasing maximum strain amplitude

for the same number of cycles. Continuing to examine data points in Fig. 6 for isotropic confinement, it is clearly seen that the volumetric strain for the sample obtained by dry pluviating far exceeds the corresponding volumetric strain of the sample obtained by moist tamping. In particular, since for $K = 1$ the vertical strain for all samples is rather small, the difference in volumetric strain essentially reflects the difference in the diametral strain: i.e. the dry pluviated sample has a greater tendency toward lateral contraction than the moist tamped sample.

The data associated with $K = 0.7$ reveals that the sample obtained by dry pluviating shows about 1% volumetric strain, while the moist tamped sample shows zero volumetric strain. A similar tendency is observed for $K = 0.5$: the sample obtained by moist tamping shows greater volumetric expansion than that obtained by dry pluviating. Data points associated with $K = 2$ correspond to tests where the lateral confinement pressure is twice the vertical one. For the three left-most curves marked with relative densities 81, 83, and 85 (%), rather dense samples, the volumetric strains are very small (about 0.1%). However, the sample obtained by dry pluviating exhibits 2%, whereas the sample prepared by moist tamping shows only 1% axial extension. This means that the decrease in the cross-sectional area of the dry pluviated sample is twice that of the moist tamped sample: under large lateral confinement pressure, the dry pluviated sample contracts more readily than the moist tamped one.

There are four curves for $K = 2$ associated with relative densities 72, 65, 51, and 43 (%). The above comments apply to the data points with relative densities 72 and 65%. However, curves associated with 51 and 43% relative densities undergo considerable densification, and, therefore, the differences caused by the sample preparation method seem to become secondary, especially since the sample with 43% initial relative density is subjected to shear straining of 8% maximum amplitude, and that with 51% relative density is subjected to shear straining of 5% maximum amplitude.

Summarizing the main points, it appears that in drained simple cyclic shearing of a granular material, the point of zero dilatancy occurs very close to the point of zero shear strain over each half-cycle. At this point the anisotropy or the fabric induced by shearing over the half-cycle seems to be negligibly small, so that only the inherent anisotropy manifests its effects. It is therefore reasonable to assume that the induced fabric over each half-cycle in this kind of test depends more directly on the magnitude of the shear strain, rather than the shear stress, provided that the shear strain amplitude is not too large (i.e. does not exceed that corresponding to the peak stress), and that the sample is not too loose.

6. STRESS-DILATANCY CHARACTERISTICS

Detailed stress-strain relations are obtained in drained cyclic shearing from closely spaced measured data points. From these, the "dilatancy parameter," $-\frac{1}{V_0} \frac{dV}{d\gamma}$, is calculated by numerical differentiation (using five neighboring points), for each stress ratio τ/σ_m . (The shear stress, τ , and the shear strain, γ , are regarded positive when clockwise; the volumetric strain, $\Delta V/V_0$, is taken positive in compaction; $\frac{1}{V_0} \frac{dV}{d\gamma} \approx \frac{\Delta V}{V_0} \frac{1}{\Delta\gamma}$ is the volumetric strain per unit shearing; and V_0 is the initial sample volume.)

Figure 7 shows for the same mean stress, σ_m , and the same maximum shear strain amplitude, γ_0 , results of a large number of cyclic tests corresponding to different K-values (14 loops for $K = 2$, 10 loops for $K = 1$, 4 loops for $K = 0.7$, 4 loops for $K = 0.5$, and 2 loops for $K = 0.4$) and different relative densities, and corresponding to both dry pluviating and moist tamping sample preparation techniques.

Two cycles for each test are included in Fig. 7. The loops consist of two parallel loading segments of positive slopes, and two unloading segments with vertical or negative inclinations. The unloading segments are not as clearly identifiable as the loading ones; see also Figs. 8 to 10.

For triaxial tests, Tatsuoka (1978) obtains stress, dilatancy relations which appear to be independent of the sample density, the initial fabric, and the mean pressure. Results of Fig. 7 suggest

that the stress-dilatancy behavior in simple shear may also be independent of the sample density* (at least when only a few cycles are involved) and the initial fabric, but, as we shall show in the sequel, it is not independent of the mean stress. Loops in Fig. 7 expand outward with decreasing K-values, showing that the dilatancy is affected by the K-value.

The effect of the mean pressure, σ_m , is displayed by the data of Figs. 8 and 9, and the effect of the maximum shear strain amplitude, γ_0 , by the results in Fig. 10. The loops expand with decreasing σ_m and with increasing γ_0 .

From Fig. 10, it is seen that the unloading segments of the loops associated with small values of γ_0 are almost vertical, whereas those for larger values of γ_0 show distinct negative slopes, the magnitude increases with increasing γ_0 . This suggests that, for large shear strain amplitudes,** the sample actually begins to densify even during the unloading, while for small strain amplitudes densification starts only close to the state of the stress reversal. Nemat-Nasser (1980) has presented a micromechanical model which seems to account

*This comment applies only to the relation between the dilatancy parameter, $-1/V_0 dV/d\gamma$, and the normalized shear stress, τ/σ_m , when a few cycles are involved. The total volumetric compaction and other dilatational factors are clearly dependent on the initial sample density; see Nemat-Nasser and Shokooh (1979).

**This and related comments may not apply when the shear strain amplitude is so large as to exceed that corresponding to the peak stress. Essentially all tests reported in the present work are at pre-peak strain amplitudes.

for this phenomenon. A brief review of this model will now be presented together with an illustrative estimate of the volumetric compaction.

The model considers two-dimensional shearing of a layer of a granular mass under uniform applied normal compressive stress, σ , and uniform shear stress, τ , which is viewed positive when clockwise. The macroscopic shear flow is the result of microscopic motion (rolling and sliding) of grains relative to each other at active contact points. Figure 11 illustrates this. The angle ν is called the (micro) dilatancy angle. It varies from active contact to active contact, and when there are a very large number of such contacts, one may assume a continuous change and introduce a distribution-density function $p(\nu)$ in such a manner that $p(\nu_0)d\nu$ represents the volume fraction of active granules whose dilatancy angles are between ν_0 and $\nu_0 + d\nu$. ν is positive when it produces volume expansion; Fig. 11. By considering the balance of forces transmitted across each active contact, and by equating the rate of frictional dissipation at active contacts within a unit volume to the rate of the overall stress-work, Nemat-Nasser (1980) obtains the following dilatancy equation:

$$\frac{1}{V} \frac{dV}{d\gamma} = \frac{1}{\cos \phi_\mu} \int_{\nu_0}^{\nu_0 + \nu} p(\nu) \cos(\phi_\mu + \nu) \sin \nu \, d\nu, \quad (1)$$

where ϕ_μ is the "grain-to-grain" friction angle, and where the Mohr-Coulomb failure criterion is used to characterize the local (at the micro-level) flow process.

Nemat-Nasser (1980) points out that upon shearing and under normal pressure, granules with negative dilatancy angles are activated first, leading to a distribution-density function $p(\nu)$ which initially is biased toward negative dilatancy angles. Intuitively, this follows from the physical observation that the local normal force N hinders the motion of an active granule with positive dilatancy angle ν , whereas it assists when ν is negative; Figs. 11b and c. Hence, upon shearing under confinement, an initial densification is expected and is invariably observed.

As shearing proceeds, the distribution-density function, $p(\nu)$, tends to become biased toward positive dilatancy angles, and this leads to subsequent dilation. During this stage, a greater number of active contacts have positive dilatancy angles, and this number increases with increasing shear strain amplitude, up to the strain corresponding to the peak stress. Now, if, after a microstate of this kind is attained, unloading begins, then some of the granules with suitably large dilatancy angles may actually start a downward motion under the action of the normal force N , which leads to densification. It is this micromechanical reason which seems to underlie the observed negative slopes during unloading in Figs. 8 to 10 for large (but still pre-peak) strain amplitudes and not for the small ones.

Other aspects of Eq. (1) are discussed and illustrated by Nemat-Nasser (1980) and Nemat-Nasser and Tobita (1982). Here we shall seek to apply (1) in order to estimate volumetric changes observed in a cycle of simple shearing.

To this end, and for illustration only, we shall use the simplest form for the distribution function $p(v)$, i.e.

$$p(v) = \frac{1}{2v_0} \quad \text{for } -v_0 + \varepsilon \leq v \leq v_0 + \varepsilon, \quad (2)$$

$$p(v) = 0 \quad \text{otherwise,}$$

and assume that the location of the centroid, ε , of this uniform distribution is a linear function of the strain over each half-cycle,

$$\varepsilon = a\gamma + b. \quad (3)$$

This is a crude approximation,* but it serves to illustrate the basic point.

From (1) and (2), we have

$$\frac{1}{V} \frac{dV}{d\gamma} = -\frac{1}{2} \tan \phi_\mu + \frac{\sin 2v_0}{4v_0 \cos \phi_\mu} \sin(2\varepsilon + \phi_\mu), \quad (4)$$

and integration from γ_1 to γ_2 , corresponding to V_1 to V_2 , now yields

$$\ln \frac{V_2}{V_1} = -\frac{1}{2}(\gamma_2 - \gamma_1) \tan \phi_\mu + \frac{\sin 2v_0}{4v_0 \cos \phi_\mu} \frac{1}{2a} [\cos(2a\gamma_1 + 2b + \phi_\mu) - \cos(2a\gamma_2 + 2b + \phi_\mu)], \quad (5)$$

where (3) is also used. Since small volumetric changes are involved, we set $V_2 = V_1 + \Delta V$, and obtain $\ln(V_2/V_1) = \ln(1 + \frac{\Delta V}{V_1}) \approx \frac{\Delta V}{V_1}$. Thus, for γ changing from $\gamma = 0$, at which $V = V_0$, to some $\gamma \leq \gamma_0$, we have

*Note that we do not suggest (2) and (3) as "good" functional forms for defining the distribution function $p(v)$, but that even with such simple and crude functions, reasonable estimates emerge from the general dilatancy, fabric-relation (1).

$$\frac{\Delta v}{v_0} = -\frac{\gamma}{2} \tan \phi_\mu + \frac{1}{2a} \frac{\sin 2v_0}{2v_0} \sin(a\gamma) [\sin(a\gamma + 2b) + \cos(a\gamma + 2b) \tan \phi_\mu]. \quad (6)$$

Note that in applying (4) to a full cycle, ϵ must be appropriately interpreted; Nemat-Nasser (1980), pp. 70-71. Equation (6) applies to a 1/4-cycle only, i.e. for $\gamma = 0$ to $\gamma = \gamma_0$. On the other hand, (5) applies over a full 1/2-cycle, e.g., for $\gamma = \gamma_0$ to $\gamma = 0$ to $\gamma = -\gamma_0$. Figure 12 illustrates these results for $\phi_\mu = 45^\circ$ (rather unrealistic, but illustrative), $v_0 = 25^\circ$, $a = 16$, and $b = 0.08$. In this figure, the experimental data are also shown. It is important to bear in mind that the net densification over each complete cycle decreases with an increasing number of cycles; see, e.g., Youd (1970, 1972) and Silver and Seed (1971). This is not directly reflected in Eq. (5). One may do this by combining Eq. (5) with the densification equation given by Nemat-Nasser and Shokoh (1979), which estimates the void ratio as a function of the shear strain amplitude and the number of cycles, i.e.

$$e = e_m + [(e_0 - e_m)^{1-n} + kN^{1/2} \gamma_0]^{1/(1-n)}, \quad (7)$$

where e_m is the minimum void ratio, N is the number of cycles, and k and n are free parameters which must be fixed from experimental results; the range of variation of n is about 3 to 4 and k may take values between 500 to 1500, for Monterey No. 0 sand. Since the total volumetric strain, measured per unit initial volume, relates to the void ratio by

$$\frac{\Delta v}{v_0} = \frac{e_0 - e}{1 + e_0}, \quad (8)$$

Eq. (7) may be used to "normalize" the dilatancy equation (5) in such a manner as to yield a net densification which reflects the number of preceding cycles N . Note, however, that Eq. (7) applies when a very large number of cycles are involved. For only a few cycles of shearing, the above-mentioned normalization may not be required.

ACKNOWLEDGMENT

This work has been supported in part by the United States Air Force Office of Scientific Research under Grant No. AFOSR-80-0017, and in part by the National Science Foundation under Grant No. CEE-8007764 to Northwestern University. The authors are pleased to acknowledge valuable comments and helpful suggestions that they received during the course of completing this work, from Professors J. Konishi, M. Oda, and F. Tatsuoka, as well as from Mr. Y. Tobita.

REFERENCES

- Arthur, J. R. F. and B. K. Menzies (1972). Inherent anisotropy in a sand. Géotechnique, 22, 115-128.
- El-Sohby, M. and K. Z. Andrawes (1972). Deformation characteristics of granular materials under hydrostatic compression. Canadian Geotech. J., 9, 338-350.
- Finn, W. D. L., P. L. Bransby and D. J. Pickering (1970). Effect of strain history on liquefaction of sand. J. Soil Mech. Fdns Div., Am. Soc. Civ. Engrs 96, SM6, 1917-1934.
- Ishihara, K. and S. Okada (1978). Effects of stress history on cyclic behavior of sand. Soils Fdns, 18, 31-45.
- Ishihara, K., F. Tatsuoka and S. Yasuda (1975). Undrained deformation and liquefaction of sand under cyclic stress. Soils Fdns, 15, 29-44.
- Ladd, R. S. (1977). Specimen preparation and cyclic stability of sands. J. Geotech. Engrg Div., Am. Soc. Civ. Engrs, 103, GT6, 535-547.
- Lafeber, D. (1966). Soil structural concepts. Engrg Geology, 1, 261-290.
- Luong, M. P. (1980). Stress-strain aspects of cohesionless soils under cyclic and transient loading. Proc. int. symp. on soils under cyclic and transient loading, Swansea (eds. G. N. Pande and O. C. Zienkiewicz), pp. 315-324. Rotterdam: A. A. Balkema.
- Mahmood, A. and J. K. Mitchell (1974). Fabric-property relationships in fine granular materials. Clays and Clay Minerals, 22, 397-408.
- Mulilis, J. P., C. K. Chan and H. B. Seed (1975). The effects of method of sample preparation on the cyclic stress-strain behavior of sands. Report EERC 75-18. Berkeley, CA: Earthquake Engineering Research Center, U. of California.

- Mulilis, J. P., H. B. Seed, C. K. Chan, J. K. Mitchell and K. Arulanandan (1977). Effects of sample preparation on sand liquefaction. J. Geotech. Engng Div., Am. Soc. Civ. Engrs. 103, GT2, 91-108.
- Nemat-Nasser, S. (1980). On behavior of granular materials in simple shear. Soils Edns. 20, 59-73.
- Nemat-Nasser, S. and A. Shokooh (1979). A unified approach to densification and liquefaction of cohesionless sand in cyclic shearing. Canadian Geotech. J., 16, 659-678.
- Nemat-Nasser, S. and Y. Tobita (1982). Influence of fabric on liquefaction and densification potential of cohesionless sand. Mechanics of Materials, 1, 43-62.
- Newland, P. L. and B. H. Allely (1959). Volume changes during undrained triaxial tests on saturated dilatant granular materials. Géotechnique, 9, 174-182.
- Oda, M. (1972). The mechanism of fabric changes during compressional deformation of sand. Soils Edns. 12, 1-18.
- Oda, M. and J. Konishi (1974). Microscopic deformation mechanism of granular material in simple shear. Soils Edns. 14, 25-38.
- Oda, M., J. Konishi and S. Nemat-Nasser (1980). Some experimentally based fundamental results on the mechanical behavior of granular materials. Géotechnique, 30, 479-495.
- Seed, H. B., K. Mori and C. K. Chan (1977). Influence of seismic history on liquefaction of sands. J. Geotech. Engng Div., Am. Soc. Civ. Engrs. 103, GT4, 257-270.
- Silver, M. L. and H. B. Seed (1971). Deformation characteristics of sands under cyclic loading. J. Soil Mech. Edns Div., Am. Soc. Civ. Engrs. 97, SM8, 1081-1098.
- Tatsuoka, F. (1978). On theoretical studies on deformation behavior of granular materials I (Studies by plasticity).

J. JSSMFE, Tsuchi-to-Kiso, 26, 82-89.

Tatsuoka, F. and K. Ishihara (1974). Drained deformation of sand under cyclic stresses reversing direction. Soils Edns, 14, 51-65.

Wood, D. M. and M. Budhu (1980). The behaviour of Leighton Buzzard sand in cyclic simple shear tests. Proc. int. symp. on soils under cyclic and transient loading, Swansea (eds. G. N. Pande and O. C. Zienkiewicz), pp. 9-21. Rotterdam: A. A. Balkema.

Youd, T. L. (1970). Densification and shear of sand during vibration. J. Soil Mech. Edns Div., Am. Soc. Civ. Engrs, 96, SM3, 863-880.

Youd, T. L. (1972). Compaction of sands by repeated shear straining. J. Soil Mech. Edns Div., Am. Soc. Civ. Engrs, 98, SM7, 709-725.

Table 1

Specimen Preparation Method	$K (= \frac{\sigma'_h}{\sigma'_0})$	σ'_v, σ'_h (kN/m ²)	No. of Specimens Tested	γ_0 (%)	Number of Cycles
Dry Pluviating	0.4	100, 40	1	8	2
	0.5	100, 50	1	8	2
	0.7	100, 70	1	8	2
	1	40, 40	2	2, 4	10,20
		80, 80	4	0.5,1,2,4	20
		100,100	3	8,10	2
		160,160	2	2, 4	10,20
	2	50,100	4	5,6,8	2
Moist Tamping	0.5	100, 50	1	8	2
	0.7	100, 70	1	8	2
	1	100,100	5	0.5,3,4,8,10	1,2
	2	50,100	3	5,6,8	2

LIST OF FIGURES

Figure 1: Relation between sample height change (Δh) and the sample volume changes (ΔV) for indicated K-values and the mean stress σ_m ; solid marks are for moist tamping (MT) and the others are for dry pluviating sample preparation techniques.

Figure 2: Relation between sample height change (Δh) and the sample diameter change (ΔD) for indicated K-values and the mean stress σ_m ; solid marks are for moist tamping (MT) and the others are for dry pluviating sample preparation techniques.

Figure 3(a): Volumetric strain, shear strain-relations for a dry pluviated sample: the solid curve marked "0" is for a virgin sample; the other curves are after liquefaction by cyclic shearing of 0.8% strain amplitude. All tests are terminated at zero residual strain, after which the sample shows no directional bias in densification.

Figure 3(b): Volumetric strain, stress ratio-relations associated with Fig. 3(a); note the sample resistance has increased by preliquefaction (terminated at zero residual strain).

Figure 4(a): Volumetric strain, shear strain-relations for a moist

tamped sample: the solid curve marked "0" is for a virgin sample; the other curves are after liquefaction by cyclic shearing of 1% strain amplitude. All tests are terminated at zero residual strain, after which the sample shows no directional bias in densification.

Figure 4(b): Volumetric strain, stress ratio-relations associated with Fig. 4(a).

Figure 5(a): Stress ratio, shear strain-relations for a dry pluviated sample: 20 cycles at 4% strain amplitude.

Figure 5(b): Volumetric strain, shear strain-relations associated with Fig. 5(a); note zero dilatancy occurring at about zero strain on each half-cycle.

Figure 5(c): Volumetric strain, stress ratio-relations associated with Fig. 5(a).

Figure 5(d): Vertical (axial) strain, volumetric strain-relations associated with Fig. 5(a): the solid curve is the locus of "points of zero dilatancy", and the numbers denote the corresponding cycle.

Figure 6: The zero dilatancy curves for all tests listed in Table 1: solid marks are for moist tamped, and others are for dry pluviated samples; numbers indicate the corresponding relative densities (%); the associated K-values are as indicated.

Figure 7: Stress ratio, dilatancy-relations at constant mean stress and strain amplitude.

Figure 8: Stress ratio, dilatancy-relations at 2% strain amplitude: --- $\sigma_m = 40 \text{ kN/m}^2$, — $\sigma_m = 80 \text{ kN/m}^2$, and -.- $\sigma_m = 160 \text{ kN/m}^2$.

Figure 9: Stress ratio, dilatancy-relations, at 4% strain amplitude: --- $\sigma_m = 40 \text{ kN/m}^2$, — $\sigma_m = 80 \text{ kN/m}^2$, and -.- $\sigma_m = 160 \text{ kN/m}^2$.

Figure 10: Stress ratio, dilatancy-relations at 100 kN/m^2 mean stress: — (outer) $\gamma_0 = 8\%$, --- (outer) $\gamma_0 = 4\%$, — (middle) $\gamma_0 = 2\%$, - - (inner) $\gamma_0 = 1\%$, and — (inner) $\gamma_0 = 0.5\%$.

Figure 11: (a) Simple shearing (plane strain) under constant overall shear stress τ and normal stress σ . (b) Forces acting on an active granule with positive dilatancy angle ν ; note that normal force N hinders the motion for $\nu > 0$. (c) Forces acting on an active granule with negative dilatancy angle ν ; note that normal force N assists the motion for $\nu < 0$.

Figure 12: Volumetric strain, shear-strain relations in cyclic shear at 2% strain amplitude: open circles are calculated results from Eq. (5) with $\phi_\mu = 45^\circ$, $\nu_0 = 25^\circ$, $a = 16$, and $b = 0.08$.

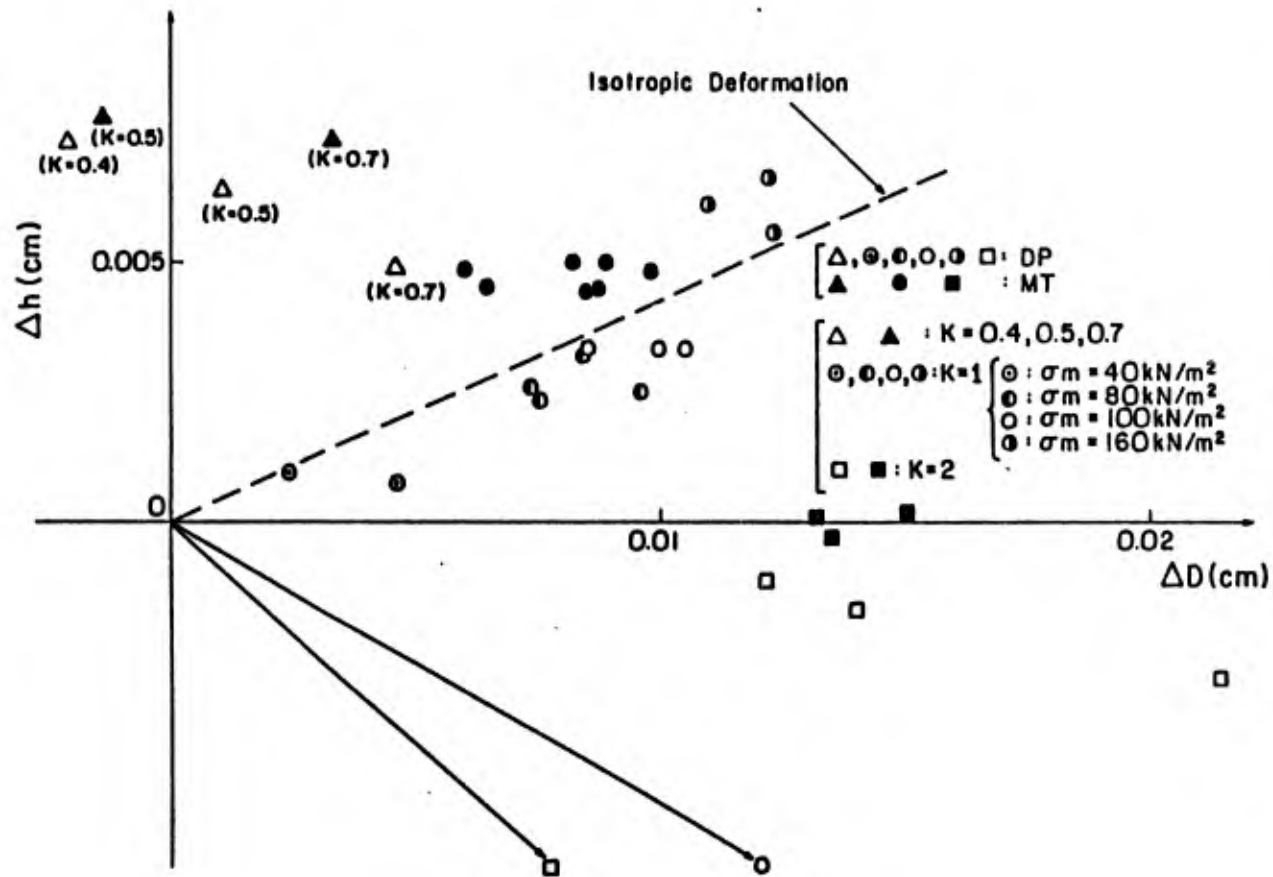


Figure 2

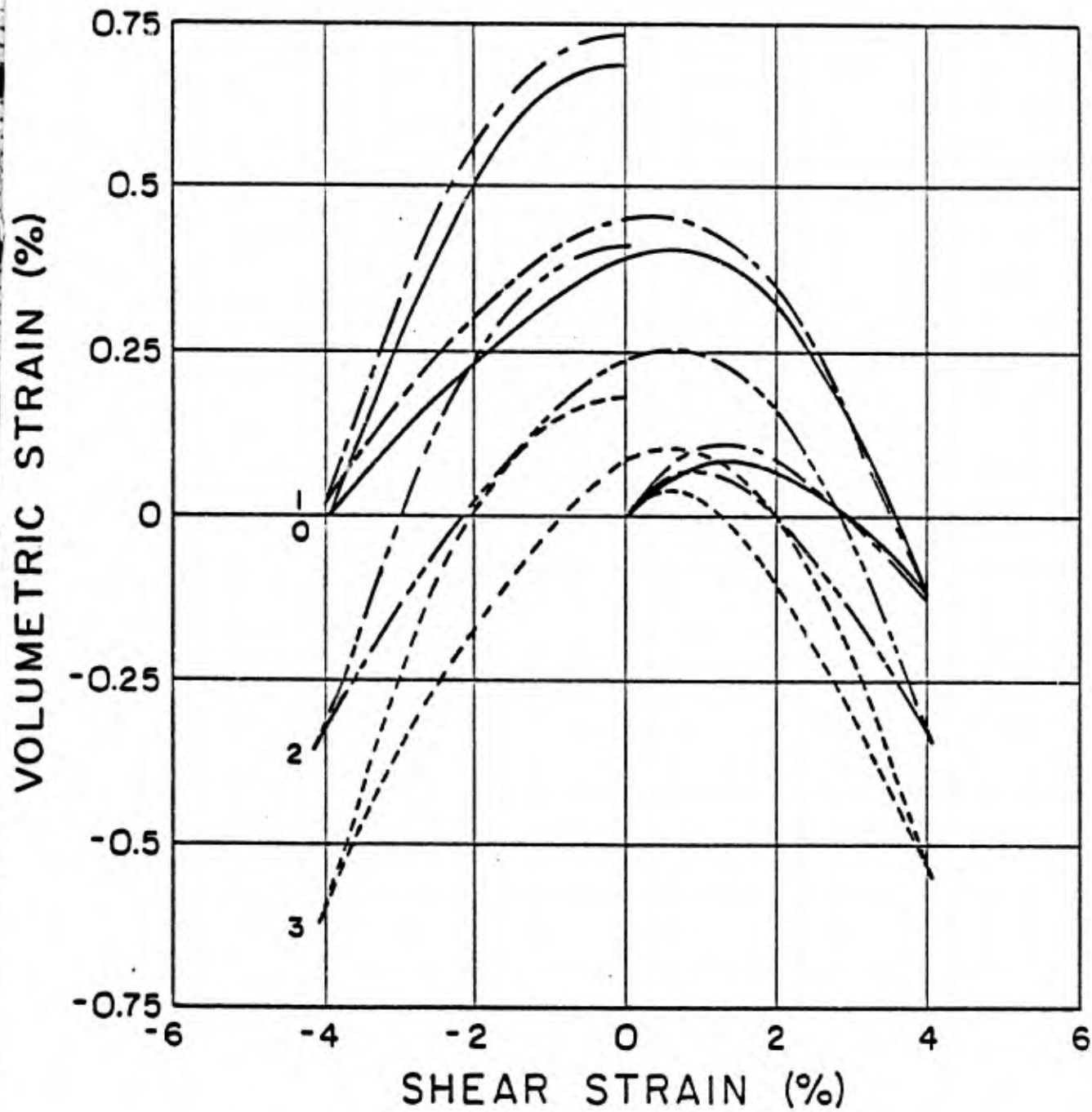


Figure 3(a)

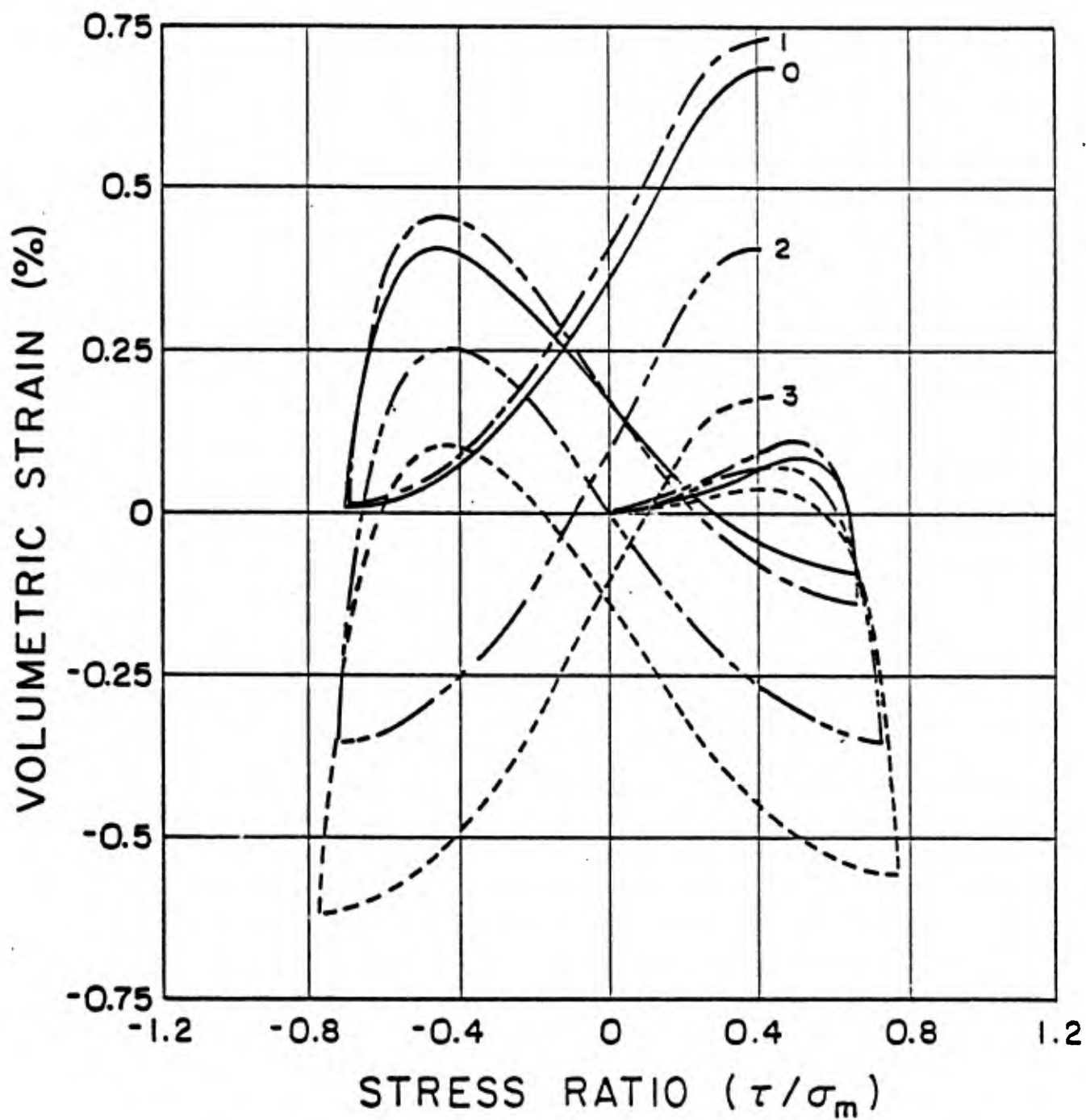


Figure 3(b)

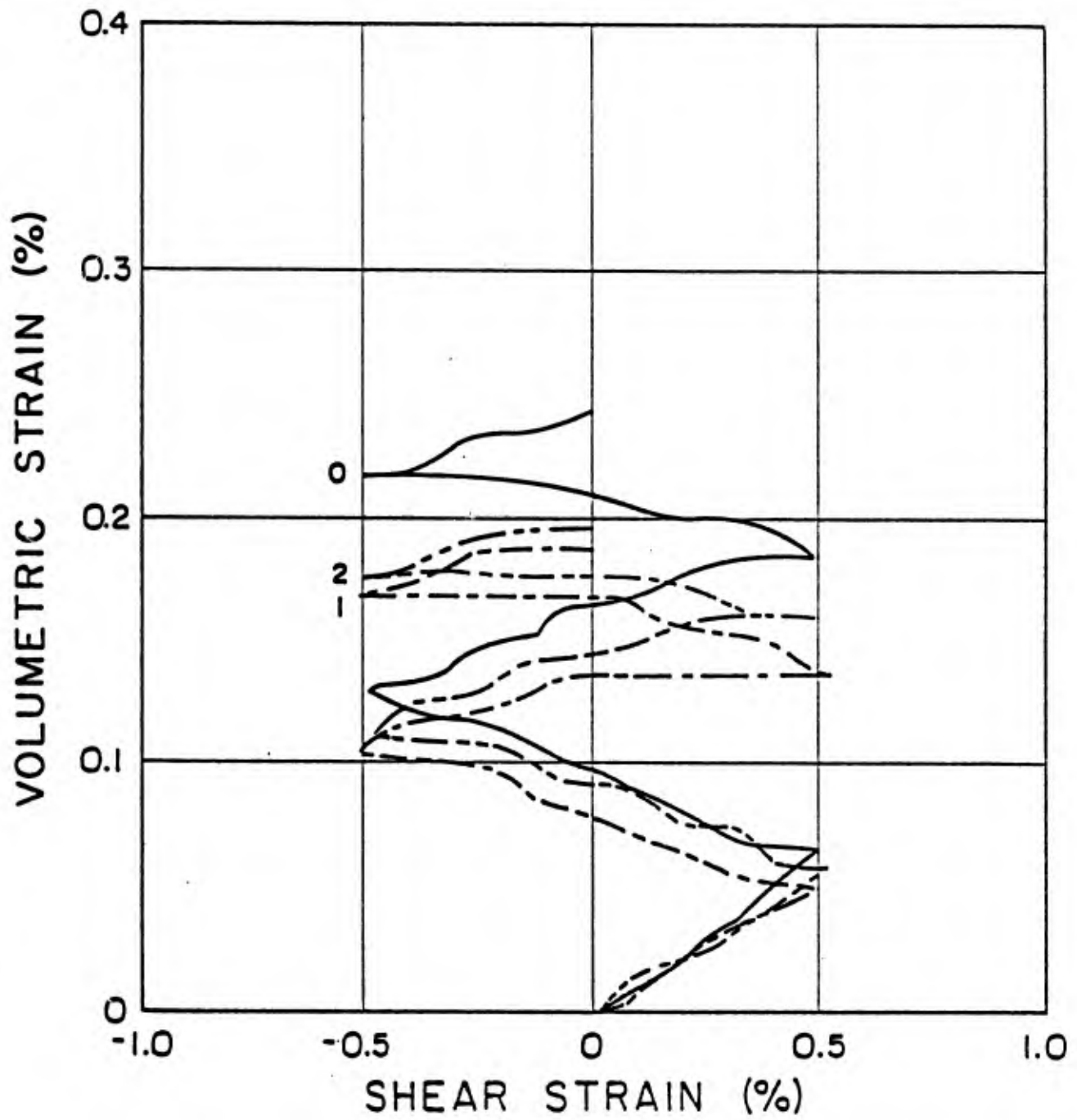


Figure 4(a)

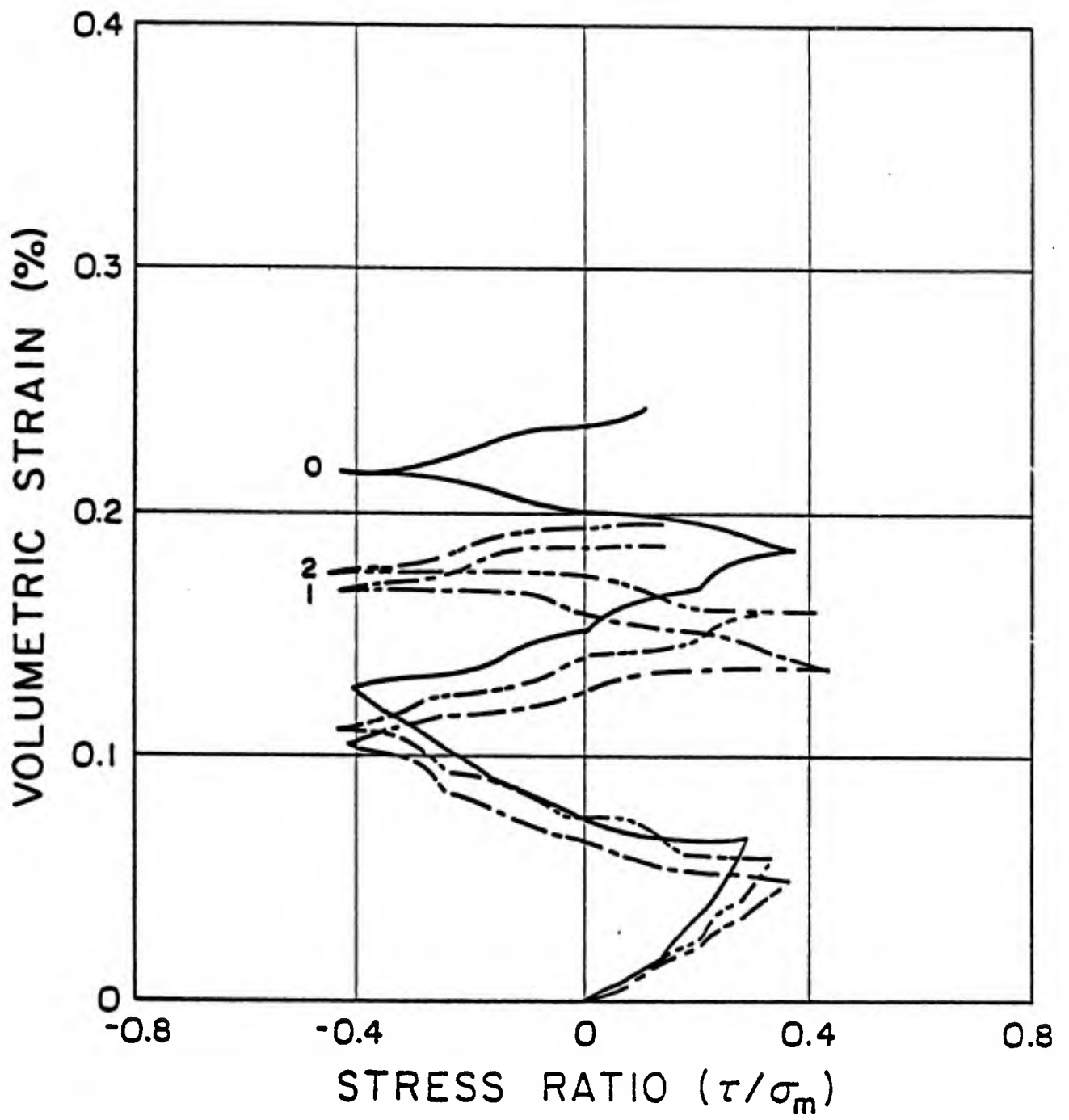


Figure 4(b)

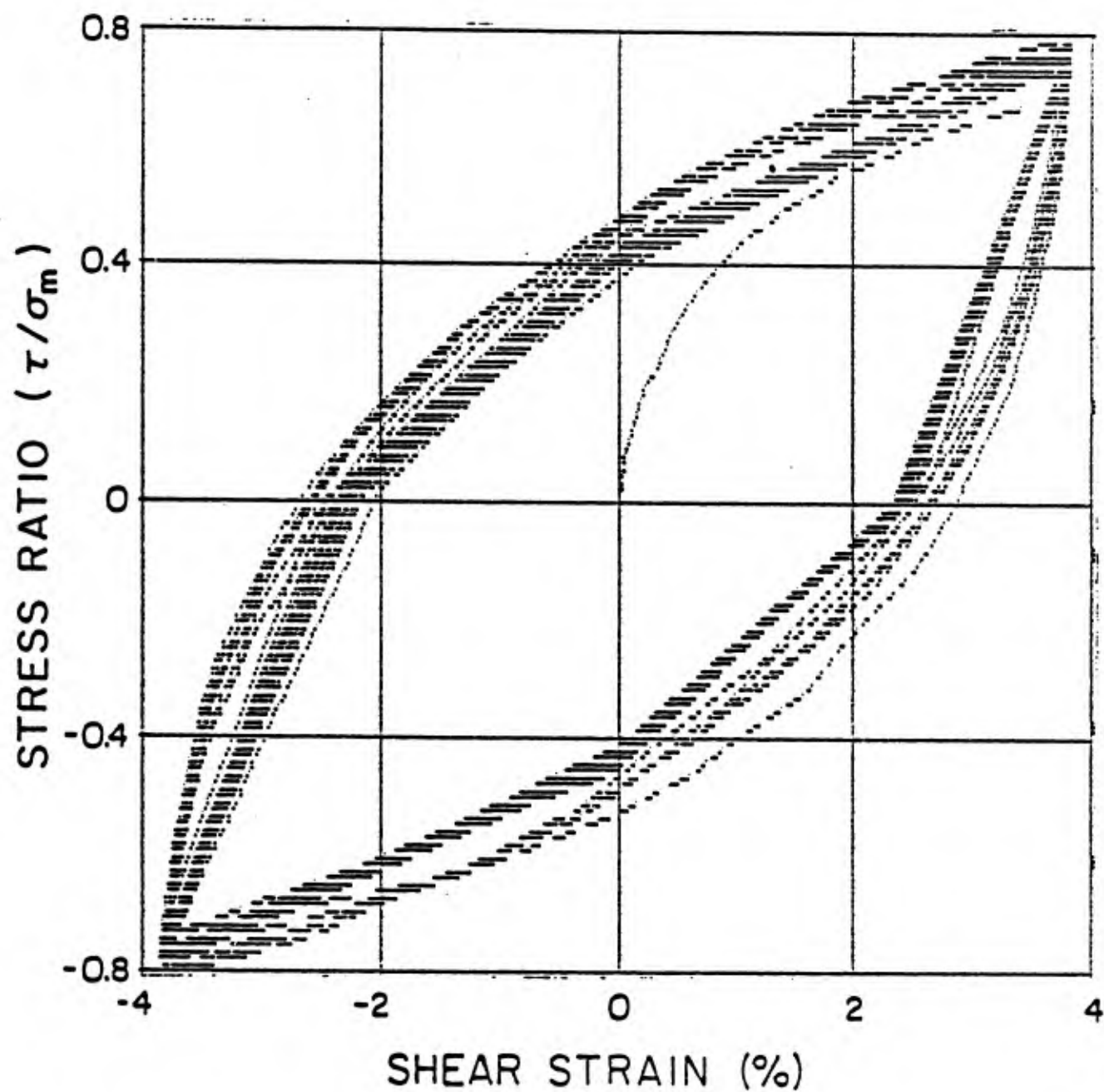


Figure 5(a)

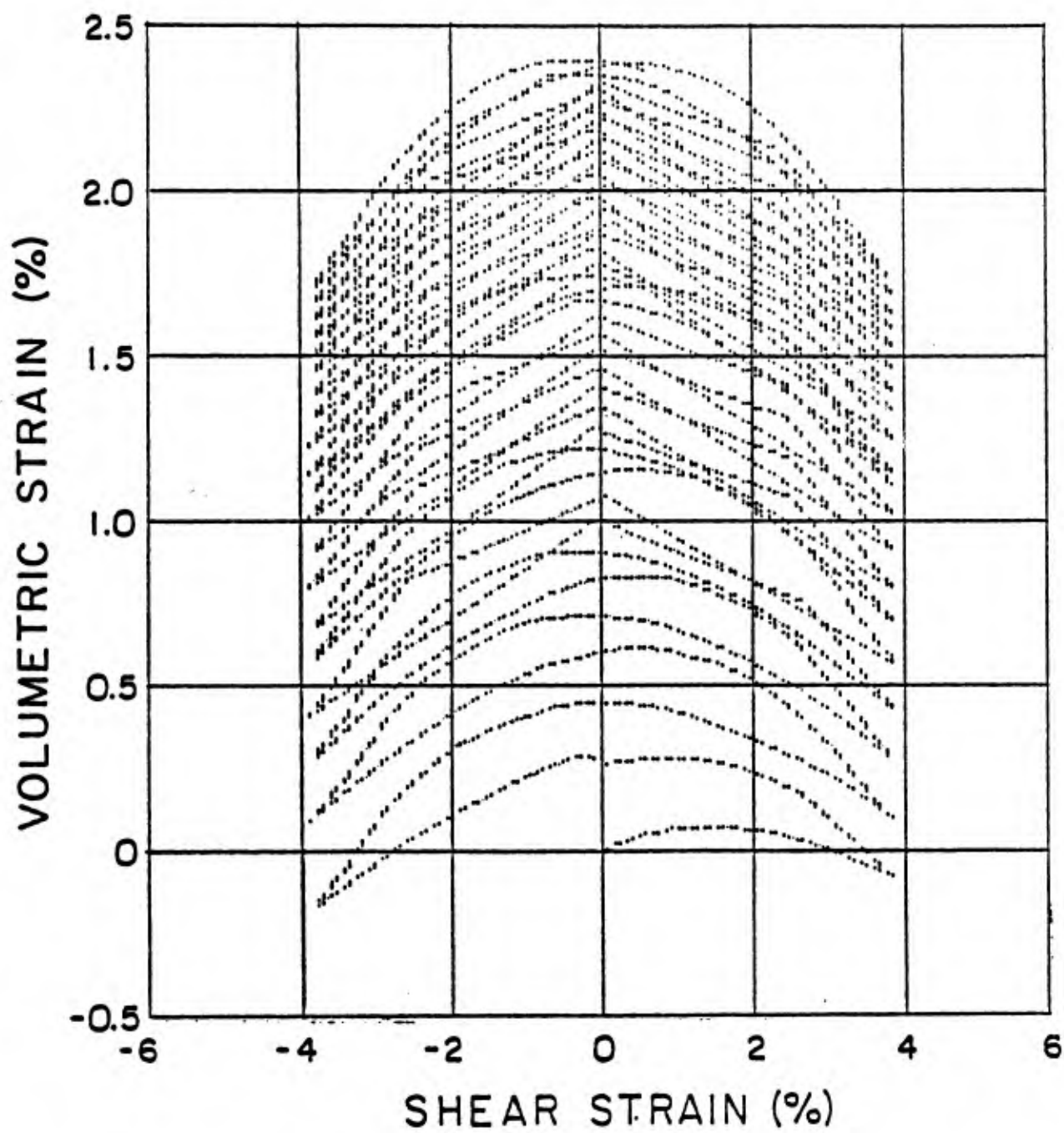


Figure 5(b)

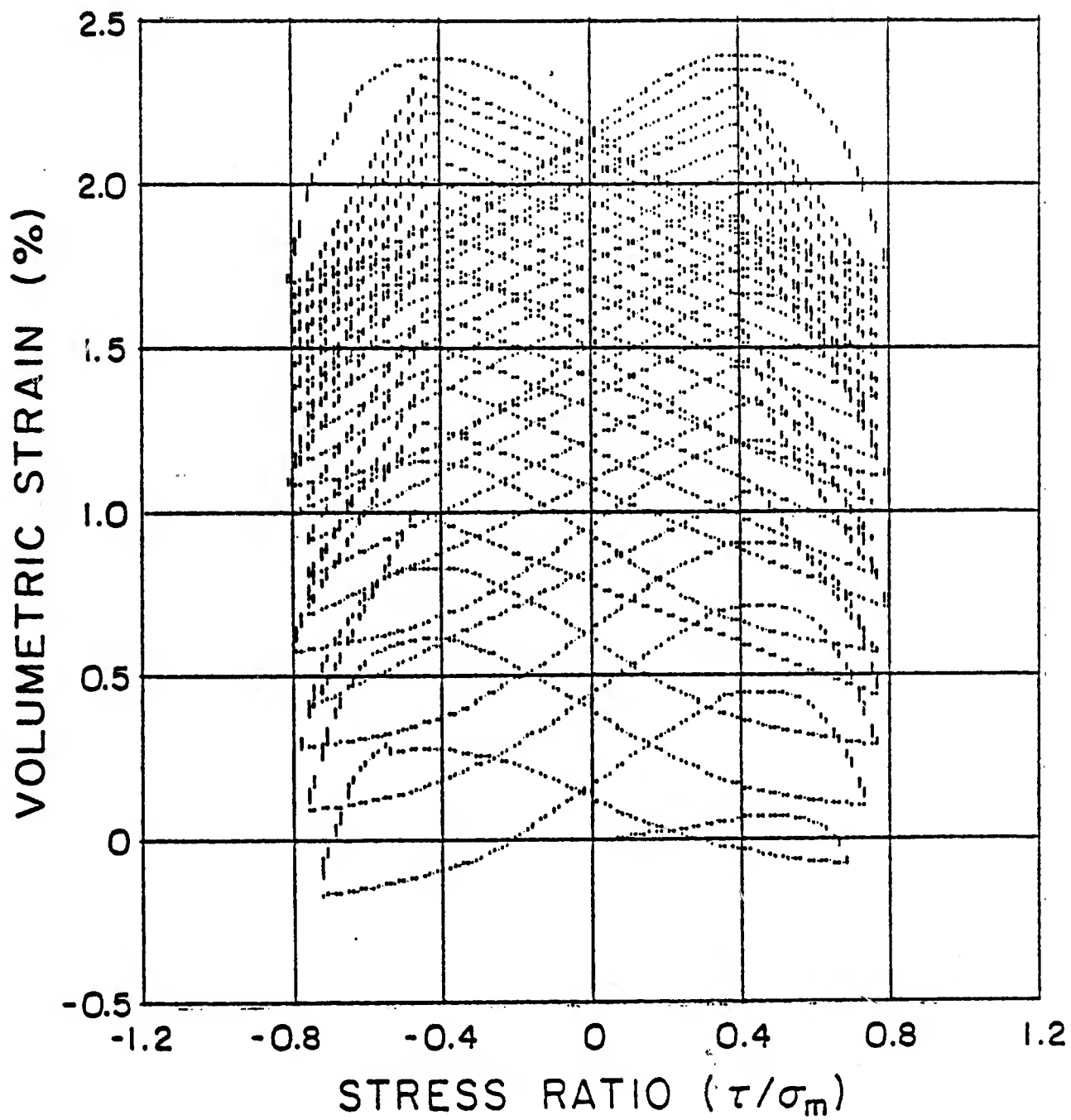


Figure 5(c)

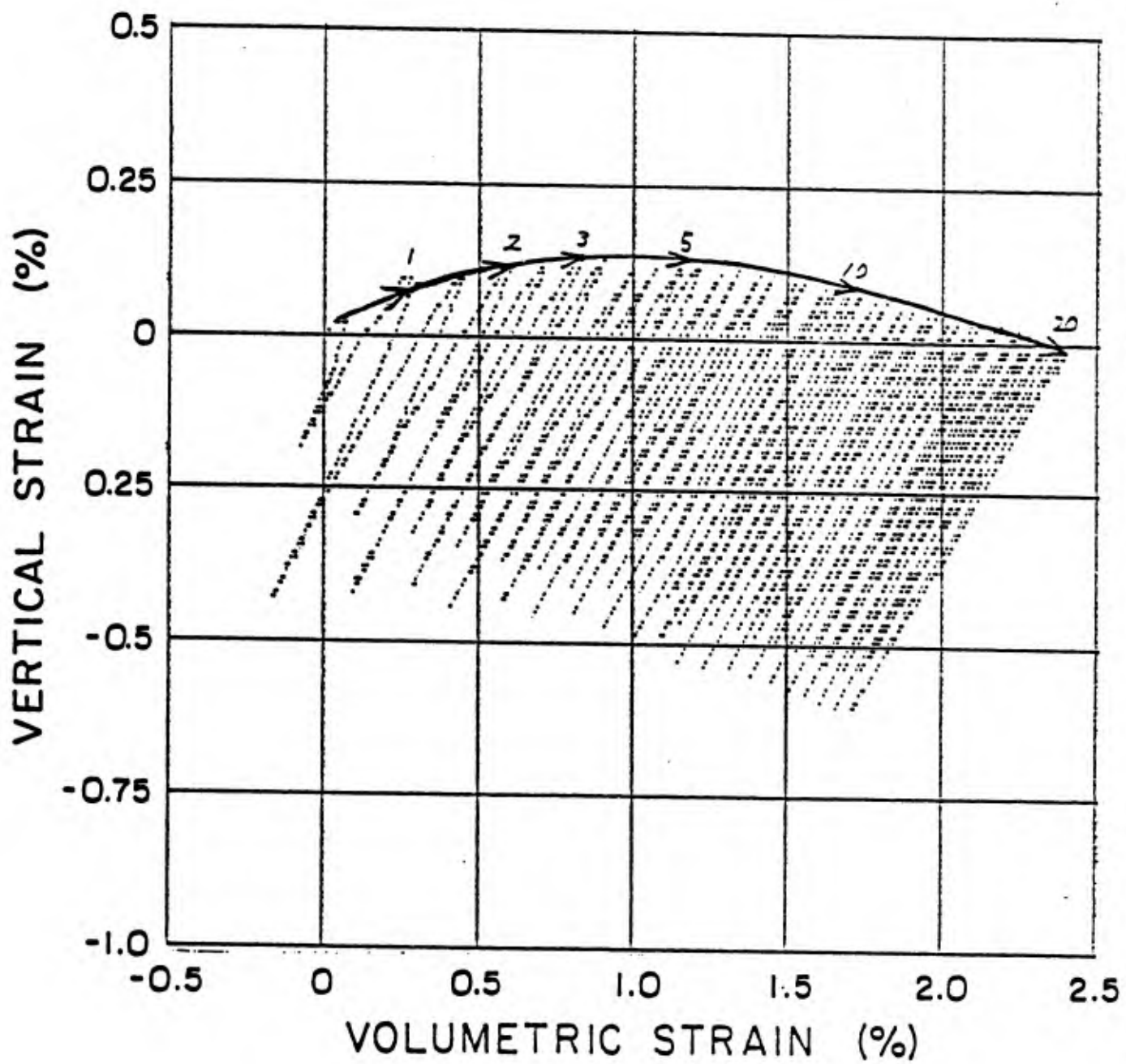


Figure 5(d)

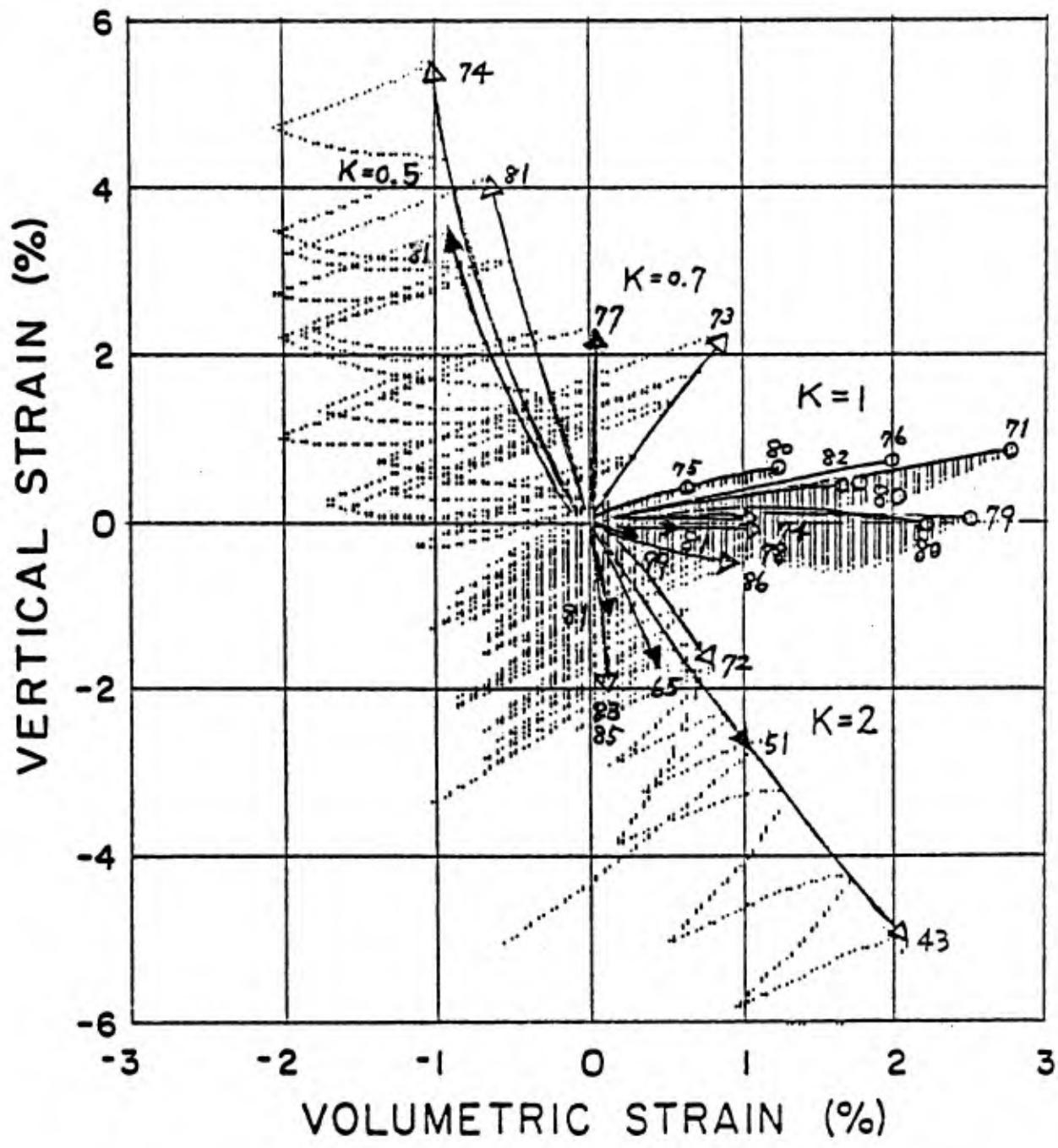
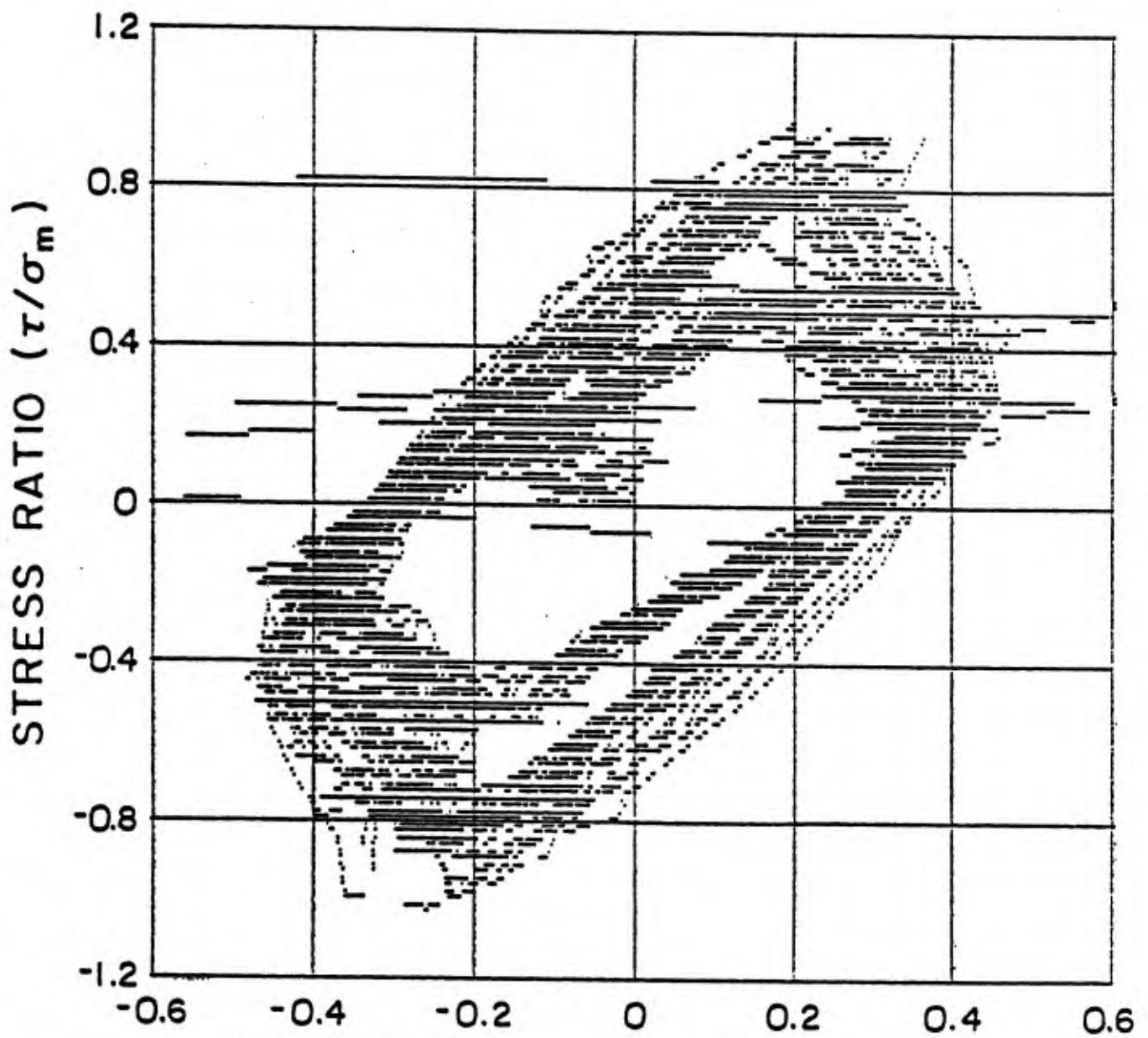


Figure 6



$$-\frac{1}{V_0} \frac{dV}{d\gamma}$$

Figure 7

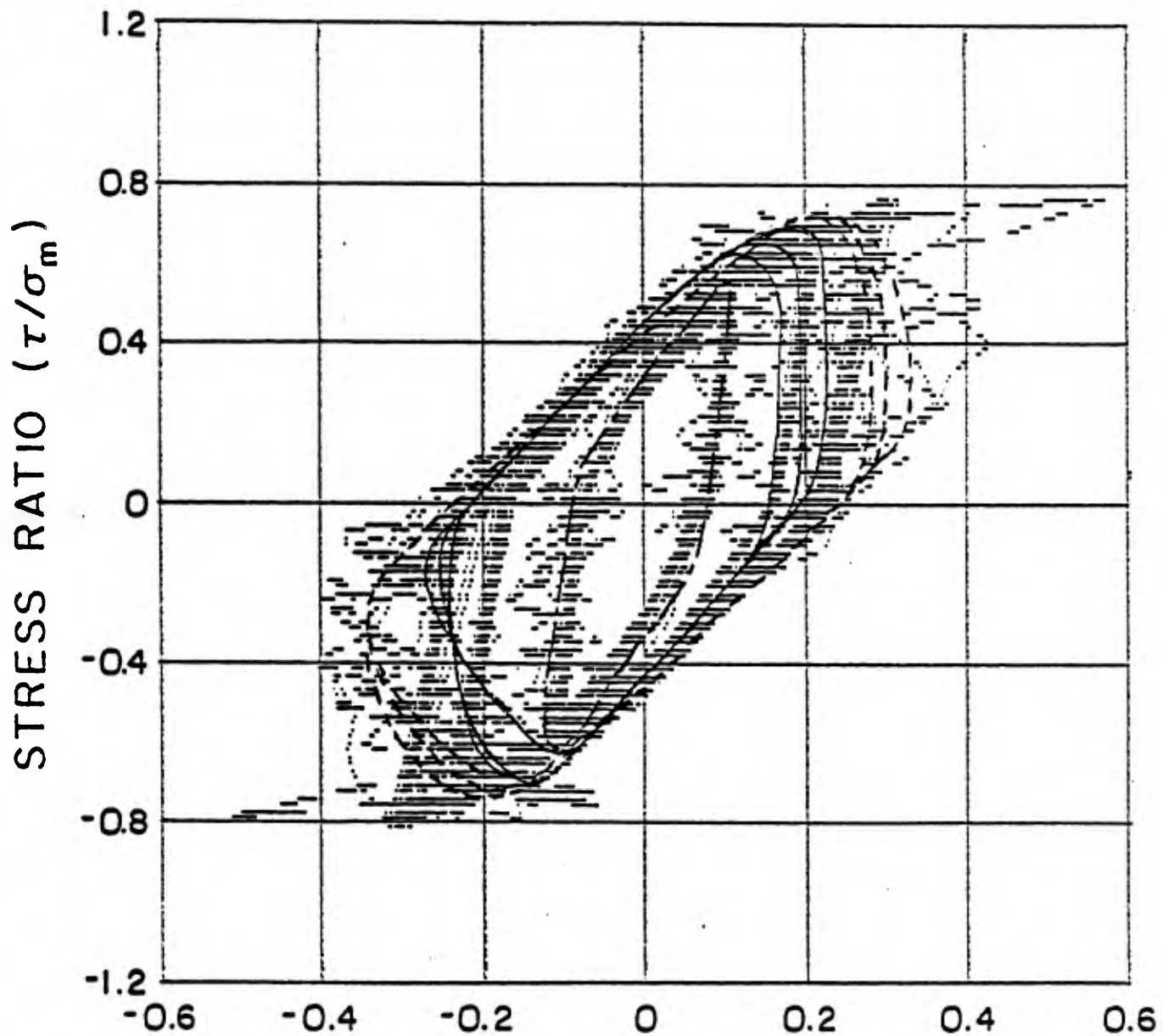


Figure 8

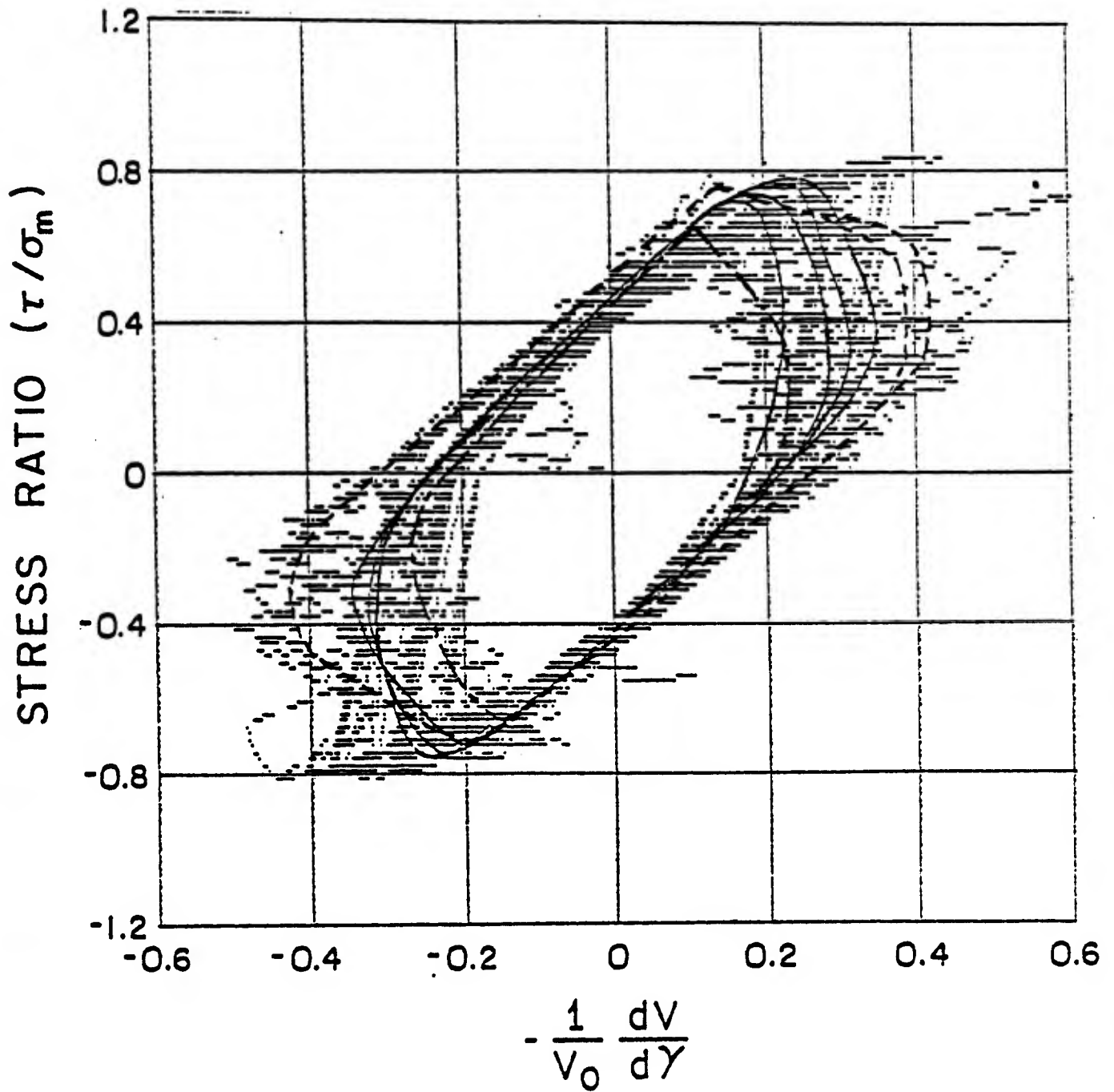


Figure 9

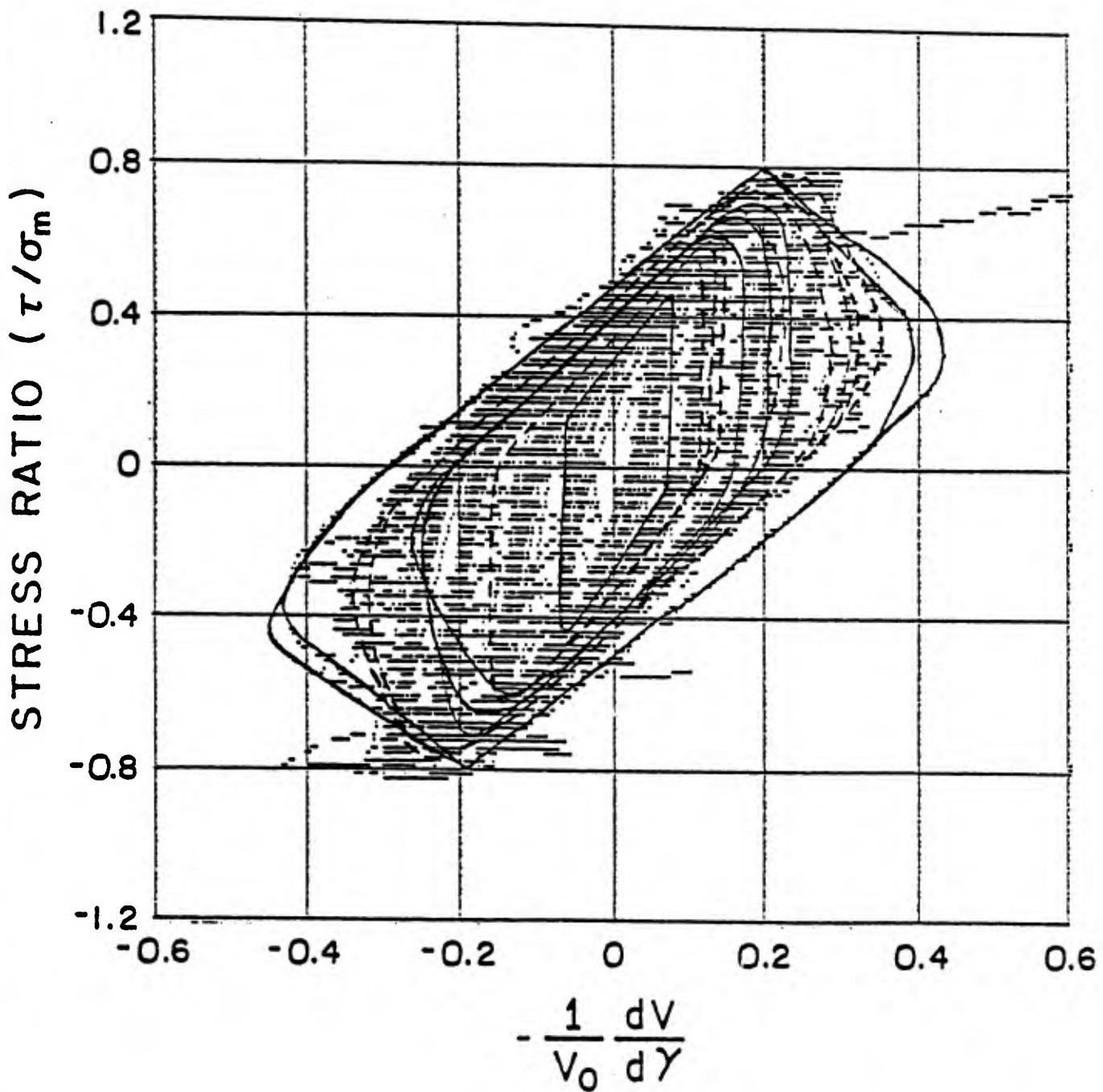


Figure 10

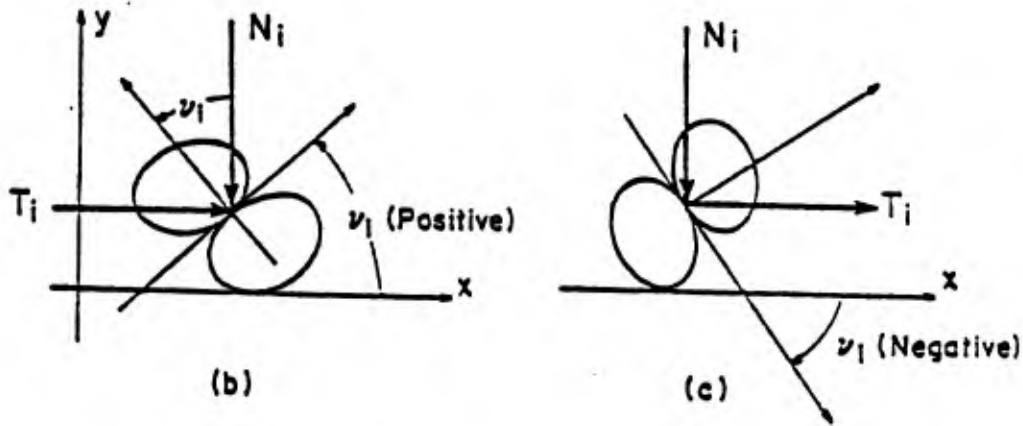
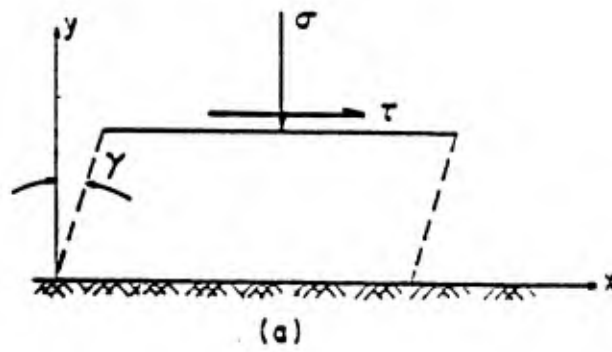


Figure 11

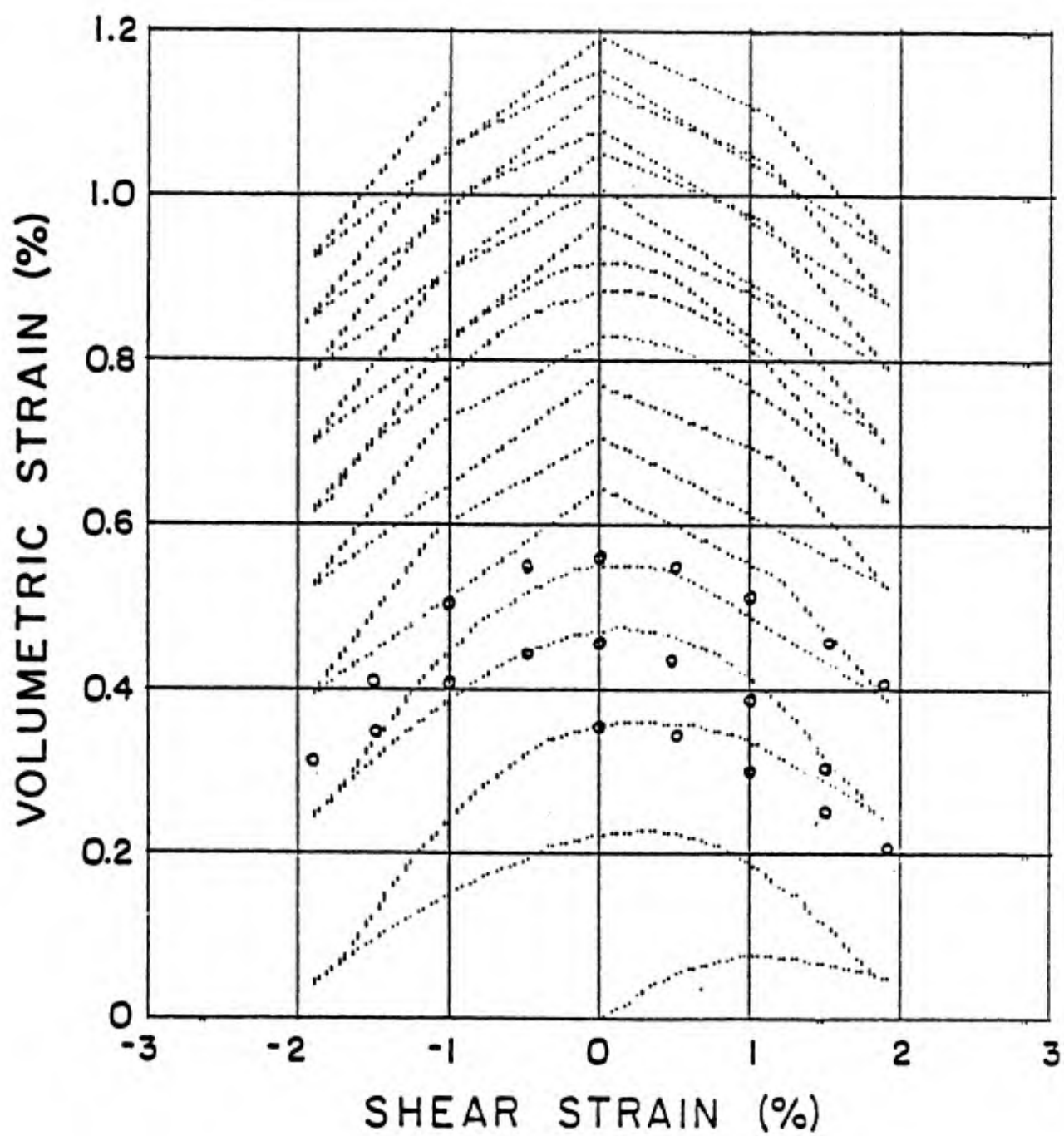


Figure 12

CHAPTER IV

COMPRESSION-INDUCED MICRO-CRACK GROWTH IN BRITTLE SOLIDS:
AXIAL SPLITTING AND SHEAR FAILURE*

by

H. Horii and S. Nemat-Nasser

Table of Contents

	Page
ABSTRACT	131
1. INTRODUCTION	133
2. AXIAL SPLITTING	138
3. SHEAR FAILURE	143
APPENDIX A	152
APPENDIX B	159
ACKNOWLEDGMENT	163
REFERENCES	164
LIST OF FIGURES	166
FIGURES 1a - 23e	169 - 202
FIGURES A1 - B2	203 - 209

*Submitted to: Journal of Geophysical Research

COMPRESSION-INDUCED MICRO-CRACK GROWTH
IN BRITTLE SOLIDS:
AXIAL SPLITTING AND SHEAR FAILURE

by

H. Horii and S. Nemat-Nasser

Department of Civil Engineering
Northwestern University
Evanston, IL 60201

ABSTRACT

Axial splitting is explained in terms of the out-of-plane growth of a pre-existing crack under far-field compression. It is shown analytically, and verified by model experiments, that, because of the frictional sliding of the faces of the pre-existing crack (induced by the resolved shear stress), tension cracks develop at the tips of the pre-existing crack. These tension cracks then grow with increasing compression and become parallel to the direction of the maximum far-field compression. When a lateral compression also exists, the crack growth is stable and stops at some finite length. With a small lateral tension, on the other hand, the crack growth becomes unstable after a certain extension length is attained. This is considered to be the fundamental mechanism of axial splitting observed in uniaxially compressed rock specimens.

To reveal the mechanism of shear failure, a row of suitably oriented cracks is considered, and their simultaneous out-of-plane unstable growth

which may lead to possible macroscopic faulting, is examined. On the basis of this model, the variations of the "ultimate strength" and the orientation of the overall fault plane with confining pressure are estimated, and the results are compared with some published experimental data. It turns out that the micro-cracking failure theory developed in this manner is in good agreement with published experimental data. The results of model experiments performed on plates of Columbia Resin CR39 which contain pre-existing cracks of suitable distributions and sizes, are shown to support qualitatively the analytical results.

1. INTRODUCTION

Solids such as rocks and concrete by their nature contain numerous micro-cracks and inhomogeneities. Materials of this kind fail under axial compression by axial splitting, when the confining pressure is zero or very small, and by faulting or shear failure, when the confining pressure is moderate, but still below the brittle-ductile transition value; see, for example, Peng and Johnson (1972). The inclination of the macroscopic fracture surfaces relative to the compression axis increases with increasing confining pressure, almost attaining the constant value of 30° in the shear failure stage. In the brittle-ductile transition stage, plastic flow takes place along the failure plane, and the fracture angle increases. Above the brittle-ductile transition pressure, a more uniform plastic flow of the specimen occurs; Griggs and Handin (1960).

In addition to their macroscopic failure features, the "strength" of rocks, and other similar brittle solids, is greatly affected by the confining pressure. Generally speaking, the strength versus confining pressure curve consists of a non-linear initial part, followed by a linear shear failure part, and then by a non-linear portion corresponding to pressures close to the brittle-ductile transition value; Mogi (1966).

In this paper we consider brittle failure at pressures below the brittle-ductile transition value. In this regime the growth and interaction of micro-cracks are considered to be the dominant controlling micro-mechanisms of macroscopic failure.

Peng and Johnson (1972) have studied the process of fracture propagation and faulting in specimens of Chelmsford granite with various end-boundary conditions. They have observed that axial splitting occurs when no confining pressure is applied, whereas failure by faulting takes place under triaxial stressing, the former being affected by the end conditions, the latter being essentially independent of the end-boundary conditions. One of the most remarkable microscopic observations is that of Hallbauer, Wagner and Cook (1973). Their photographic studies show how the development of fracture and micro-cracks is related to the overall stress-strain relations. Micro-cracking is observed to be mainly intra-granular and parallel to the direction of the maximum compression. The most interesting observation relevant to the main objective of the present article is that regions of high crack-density emerge along a plane which eventually becomes a macroscopic shear fracture, and that the shear fracture plane does not materialize until the applied axial compression is very close to the ultimate strength of the specimen.

Experiments on glass and photo-elastic plates by Brace and Bombolakis (1963) have shown that pre-existing cracks may be the source of compression-induced micro-cracking. McClintock and Walsh (1963) have proposed a modified Griffith theory which includes frictional effects. Nemat-Nasser and Horii (1982) have presented an analytical solution of compression-induced, out-of-plane crack extension which may become unstable, leading to axial splitting. These models are based on the idea that frictional sliding along pre-existing cracks results in the formation of tension cracks at the tips of the pre-existing cracks. Tension cracks may develop in brittle solids from other sources (or stress concentrators)

than the pre-existing cracks. Microscopic observations by Tapponnier and Brace (1976), Mosher et al. (1975), and Hallbauer et al. (1973) seem to support this. From the "modeling" point of view, on the other hand, it may be adequate to assume that these other micro-cracking sources have effects similar to those of the pre-existing cracks, and in fact may be represented by some equivalent pre-existing cracks.

Based on these observations, we seek in the present work to examine analytically and with model experimentation the consequences of the following micro-mechanical "model" of brittle failure.

In a sample containing micro-cracks of various sizes, larger pre-existing cracks are expected to be fewer in number and farther apart than smaller ones. Under axial compression, suitably oriented larger cracks begin to extend first. Relative frictional sliding of their faces produces at their tips tension cracks which deviate at sharp angles from the sliding plane. These tension cracks continue to grow with increasing axial compression, curving toward an orientation parallel to the direction of axial compression. In the absence of confining pressure, this growth regime may become unstable leading to axial splitting if some lateral tension exists because of the end-conditions. On the other hand, if a suitably large confining pressure exists, the out-of-plane growth of (pre-existing) large cracks is soon arrested. Then, as the axial load is further increased, smaller cracks become activated as they interact with each other. At a certain stage of loading, sets of suitably arranged small cracks of favorable inclination suddenly grow out of their own planes in an unstable fashion, which leads to the formation of the macroscopic fracture

plane. The orientation of this fracture plane and the critical axial load depend on the confining pressure.

This paper is organized in the following manner. In Section 2 we consider axial splitting. This follows our previous work, Nemat-Nasser and Horii (1982), where out-of-plane growth by frictional sliding of pre-existing cracks is shown to result in axial splitting under axial compression, if some small lateral tension also exists. Detailed calculations are given in Appendix A for a complete two-dimensional solution of out-of-plane curved growth of a pre-existing crack under far-field overall compression. Numerical results are presented which considerably improve and correct our previous approximate results, leading to a better correlation with model experiments.

Shear failure is examined in Section 3. As a "model" for simulating microscopic events which may be instrumental for the macroscopic shear failure, we consider a row of suitably oriented cracks, and examine their simultaneous out-of-plane unstable growth which may lead to possible macroscopic faulting. The physical implications of this model are discussed. The variations of the ultimate strength and the orientation of the overall fault plane with confining pressure are estimated, and the results are compared with some published experimental data. Here again, for the sake of clarity, only the results are discussed and the detailed mathematical calculations are presented in Appendix B. Sections 2 and 3 also include the results of a number of model studies on thin plates of Columbia resin CR39, containing suitably arranged pre-existing cracks of various sizes and distributions. In order to clearly demonstrate the influence of

confining pressure on the failure mechanism, two sets of specimens with essentially identical crack arrangements are tested, one with, the other without confinement. The results are discussed in Sections 2 and 3.

It turns out that the micro-cracking failure theory developed in this paper is not only in good qualitative accord with the results of laboratory experiments on rocks, but that it also allows specific quantitative estimates in agreement with some published data.

2. AXIAL SPLITTING

Under axial compression a suitably oriented pre-existing crack may grow out of its plane by the formation of tension cracks at its tips due to the relative sliding of its faces. The tension cracks grow at sharp angles relative to the orientation of the pre-existing crack and curve toward a direction parallel to the axial compression. This has been illustrated in plates of photo-elastic materials and glass containing pre-existing cracks, by Brace and Bombolakis(1963), Hoek and Bieniawski(1965), and Nemat-Nasser and Horii(1982). Typical examples are shown in Figs.1 and 2.

A remarkable result obtained analytically by Nemat-Nasser and Horii(1982), and illustrated experimentally in Figs.1 and 2, is that the presence of slight far-field lateral tension renders the out-of-plane curved crack growth unstable, in the sense that, after a suitable critical length is attained, the crack grows spontaneously and without an increase in axial compression, leading to the splitting of the specimen. On the other hand, if far-field lateral compression is present, then no such unstable growth is observed. Indeed, calculation shows and experiment verifies that, if the far-field lateral compression is a small percentage of the far-field axial compression, then the out-of-plane curved (tension) crack attains a finite length, and does not grow any further.

Figure 1 shows crack growth under axial compression of a barrel-shaped specimen. In this case, a slight lateral tension exists, because of the geometry of the specimen, and thus, out-of-plane crack extension is unstable. Figure 2 shows a dogbone-shaped specimen, where lateral compression accompanies the axial one. In this case, the crack growth is stable.

A complete analytic (two-dimensional) solution for the out-of-plane curved crack growth of the kind illustrated in Figs.1 and 2, is presented in Appendix A. This solution improves on and corrects our previous approximate estimates, Nemat-Nasser and Horii(1982). Consequently, the calculated crack profiles compare much better with the experimentally observed ones. Figure 3 illustrates this.

The most significant result that emerged from the analytical calculations is the relation between the axial compression and the length of the extended curved crack. This is affected by lateral tension and compression. Figure 4 defines the notation used, and Figs.5a,b show typical axial load versus extended crack length relations, for indicated lateral tensions in Fig.5a, and lateral compressions in Fig.5b. As is seen, the presence of lateral tension leads to instability after a peak axial stress is attained, whereas lateral compression arrests crack growth.

Since the ordinate in Fig.5a is $|\sigma_1| \sqrt{\pi c} / K_c$, where σ_1 is the axial compression, c is half the length of the pre-existing crack, and K_c is the critical value of the Mode I stress intensity factor, it is seen that, for a given curved extension length, l/c , the corresponding axial compression, σ_1 , is inversely proportional to $c^{1/2}$. Therefore, in a specimen which includes isolated pre-existing cracks, the larger cracks are activated first. Indeed, if some lateral tension exists or is produced as a consequence of sample geometry (Fig.1) or the presence of other inhomogeneities, or, in fact, as a consequence of the crack growth itself, then the large isolated cracks would extend in an unstable manner, joining each other and leading to axial splitting. Figure 6 is an illustration of such a split-

ting process. However, the most dramatic example is given in Fig.7. Here, the specimen contains (Fig.7a) a number of large cracks and a row of suitably arranged smaller cracks. Upon axial compression, the larger cracks are activated and begin to grow (Figs.7b,c), and finally lead to axial splitting (Fig.7c) and actual shattering of the specimen (Fig.7d), while the majority of the small cracks are not activated at all.

The significance of this result may be better appreciated if we compare Fig.7 with Fig.8 which shows the growth regime of the cracks in a sample with essentially the same pre-existing cracks, but with some lateral compression (produced by the Poisson effect in the presence of flexible lateral confinement) acting on the specimen. Here again, first large cracks are activated (Fig.8b). However, these are soon arrested and, at a certain stage, some of the smaller cracks (Fig.8c) are suddenly activated. Immediately after this, and without an increase in the load, the entire row of smaller cracks is suddenly and spontaneously activated (Fig.8d), leading to "macroscopic" shear failure upon further loading (Fig.8e).

The calculation for the optimal orientation and other aspects of this latter failure process is discussed in the following section, where the results of additional model experiments are also given.

As is pointed out in Appendix A, Eq.(8) of Nemat-Nasser and Horii(1982) involves an algebraic error which, although it does not affect the qualitative results discussed by the authors, does change the numerical results to a certain extent for large value of l/c . Figure 5b, for example, is the corrected version of Fig.5 of Nemat-Nasser and Horii(1982). Since these authors use the numerical results of their Fig.5 to explain

axial failure observed by Peng and Johnson(1972) for samples of Chelmsford granite with different inserts, it is appropriate to make some comments here.

Peng and Johnson report the following data for Chelmsford granite: The average initial crack length $2c \approx 0.025$ in, the fracture toughness $K_c = 500 \text{ psi in}^{1/2}$, tensile strength $T = 1,200$ psi, and compressive strength $C = 24,000$ psi for steel disk insert, 18,500 psi for teflon insert, and 15,000 psi for neoprene insert.

From the relation $K_c = T\sqrt{\pi c}$, the effective crack length for tensile fracture is $2c = 0.11$ in. Using this value, Nemat-Nasser and Horii(1982) report the normalized compressive strength $C\sqrt{\pi c}/K_c$, to be 20 for the steel disk insert, 15.4 for the teflon insert, and 12.5 for the neoprene insert. They plot these values in their Fig.5.

On the other hand, if we recognize that the fracture occurs under overall compressive force and, therefore, is different from that under tensile forces, and therefore use the reported observed initial crack length $2c = 0.025$ in, the normalized compressive strength, $C\sqrt{\pi c}/K_c$, becomes 9.5 for the steel insert, 7.3 for the teflon insert, and 5.9 for the neoprene insert. These values seem to agree well with the corrected numerical results of the present Fig.5b. Indeed, Peng(1971) reports radial tensile stress of 6-8% of applied compression for neoprene insert, and 4-6% for the teflon insert.

Nemat-Nasser and Horii(1982) also use the numerical results of their Fig.5 to estimate the order of magnitude of tectonic stresses required to

cause exfoliation. The corrected results of the present Fig.5b do not, however, affect such order-of-magnitude estimates, although they tend to suggest smaller necessary tectonic forces.

3. SHEAR FAILURE

Based on the observations by Hallbauer *et al.* (1973) and our own model studies, it appears that shear failure may be modeled to be the result of unstable growth of suitably oriented sets of small closely-spaced interacting pre-existing cracks. Indeed, Hallbauer *et al.* report a nearly uniform distribution of crack density in rock specimens, compressed axially under confining pressure, up to axial loads very close to their maximum values. These authors observe that, for axial compressions very close to the ultimate strength, a region of high crack density begins to emerge rapidly. Moreover, in this high-density crack zone the orientation of cracks is almost parallel to the axial compression, implying that these are tension cracks. The high-density crack zone eventually produces the macroscopic shear failure plane.

It therefore appears that one essential feature of shear failure is the interaction of smaller cracks which leads to their unstable growth. To capture this feature, we first consider a row of equally spaced cracks of equal initial size and of common orientation, and calculate for a given confining pressure the optimal common orientation in such a manner as to minimize the critical value of the axial compression (the ultimate strength) required to initiate their out-of-plane unstable growth. This calculation also yields a range for possible values of the overall orientation of the failure plane. Then by assuming a reasonable and simple relation between the spacing and the size of such optimally oriented cracks, we estimate the ultimate strength and a range of possible values of the overall fault plane orientation as functions of the confining pressure.

This leads to results which are in good qualitative and quantitative agreement with experimental data.

Figure 9 shows a typical array of cracks of the common initial length $2c$ and of overall orientation ϕ relative to the maximum axial compression, σ_1 . The cracks are spaced along the ϕ -orientation at the common distance d . The (common) orientation of each crack relative to the σ_1 -axis is denoted by γ . The pre-existing cracks are assumed to be closed, undergoing frictional sliding, with the coefficient of friction taken to be 0.4.

We fix the confining stress σ_2 , the crack spacing d/c , and the crack orientation γ , and calculate[†] the out-of-plane extension length l/c as a function of the axial compression σ_1 for different values of overall orientation ϕ . Typical results are shown in Fig.10.

In general, for a suitably large value of the overall orientation angle ϕ , the axial compression is a monotonically increasing function of l/c . For the example shown in Fig.10, where $d/c = 4$, $|\sigma_2|/\sqrt{\pi c}/K_c = 0.1$, and $\gamma = 0.24\pi$, this happens when ϕ exceeds 0.2π . However, for smaller values of ϕ , the axial compression first increases with increasing l/c , attains a peak value, drops monotonically to a minimum value, and then begins to rise again. This suggests that, at a critical value of the axial stress, a set of optimally oriented cracks of this kind can suddenly become unstable, and the cracks grow out of their planes.

[†]The method of solution and analytical details are given in Appendix B.

To calculate the optimal value for the orientation angle γ , we fix d/c , and plot the peak values of σ_1 for each σ_2 and each γ , as functions of ϕ . This is illustrated in Fig.11. We then choose that value of γ which leads to the smallest axial compression for a suitable overall orientation ϕ . This smallest axial compression is defined to be the ultimate strength. In the example of Fig.11, $\gamma = 0.24\pi$ is the optimal crack orientation.

Figure 12 shows the axial stress versus crack extension length curves at indicated constant values of the overall orientation ϕ . Several features of these curves require further consideration. First, the peak values of the axial stress for the value of ϕ from 0.16π to 0.2π fall in a very narrow range, i.e. $|\Delta\sigma_1|/\sqrt{\pi c}/K_c \sim 0.3$. This suggests that the presence of inhomogeneities and other imperfections invariably should introduce some uncertainty into the actual orientation of the final fracture plane. Indeed, the orientation of fracture planes observed in experiments has a wide variation even for similar samples. A second interesting feature of the curves in Fig.12 is that the difference between the peak values of the curves increases as the overall orientation angle ϕ decreases. This suggests that, for a given confining pressure, the range of the overall fracture angle is, in fact, limited. For example, for the data in Fig.12 it would be difficult to argue that secondary effects due to imperfections and inhomogeneities could be such that the "stress barrier" corresponding to $\phi < 0.16\pi$ could be overcome. Therefore, for the data of this figure, the final fracture orientation may be judged to fall somewhere between 0.16π and 0.195π , which relate to a maximum "stress barrier" of $|\Delta\sigma_2|/\sqrt{\pi c}/K_c = 0.3$; see Fig.11. A final noteworthy feature of the curves in Fig.12 is the emergence of second local minima for curves associated with smaller overall

orientations ϕ . As ϕ decreases, the out-of-plane extended portions of adjacent pre-existing cracks are more closely spaced and therefore, have stronger interaction. The first minimum is essentially due to the interaction between the extended parts of the adjacent cracks, and the second one is due to the interaction between the extended parts and the adjacent pre-existing cracks. This is illustrated in Fig.13, where, for three values of ϕ , the out-of-plane extension parts are given for three different indicated values of d/c .

So far, we have shown how to obtain the ultimate strength and a range for the possible values of the overall failure orientation for fixed values of d/c and σ_2 . Now we examine the influence of the confining pressure on the ultimate strength and the overall failure orientation, for constant $d/c = 4$. Figure 14a shows the ultimate strength as a function of the confining pressure, and Fig.14b gives the variation of the overall failure angle ϕ with the confining pressure, for indicated values of the "stress barrier" which must be overcome. It is interesting to note that for zero stress barrier, the orientation of the failure plane actually decreases with increasing confining pressure, although the introduction of a small stress barrier diminishes this decrease. This is quite an important fact which, when superficially viewed, may suggest a trend opposite to experimental observation. However, we have to note that in an actual specimen which contains many cracks of different sizes with different spacings, the optimal value of d/c may not remain constant as the confining pressure increases, and that the overall fault angle observed in experiments is not necessarily a smooth monotonically increasing function of the confining pressure. Hence a careful examination of the influence of d/c seems to be

in order.

Figures 15 and 16 represent results similar to those of Fig.14, but for different crack spacings, i.e. $d/c = 6$ for Fig.15, and $d/c = 8$ for Fig.16. It is seen that an increasing d/c increases the magnitude of the ultimate strength, as well as its rate of change with lateral compression, but it decreases the optimal overall fault orientation. This is further illustrated in Fig.17 which gives the variations of the ultimate strength, its rate of change with respect to the confining pressure, and the overall failure angle as functions of d/c , for zero confining pressure. Note that, in all these results the stresses are normalized, using the crack size c . Therefore, the influence of the crack size c , and the crack spacing d , may not be transparent.

We now consider a reasonable relation between the crack size and its spacing, and seek to determine the optimal crack spacing d/c as a function of confining pressure. For an actual sample, we assume that there are many optimally oriented sets of cracks with various d/c , each being "optimal" for a certain confining pressure.

The distribution of d/c depends on the crack size. Let the minimum crack size be denoted by c_m , and the corresponding crack spacing by d_m . Since smaller cracks are greater in number and closer in spacing, it is reasonable to expect that d/c_m is a monotonically increasing function of c/c_m . The simplest relation of this kind is

$$\frac{d}{c_m} = b \left(\frac{c}{c_m} \right)^{1+a}, \quad b = \frac{d_m}{c_m}, \quad a > 0, \quad (1)$$

or equivalently,

$$\frac{d}{c} = b \left(\frac{c}{c_m} \right)^a \quad (2)$$

In addition we introduce the largest crack size c_M since the size of cracks found in an actual sample is bounded. With this or a similar relation, we calculate the ultimate strength, $|\sigma_1|/\sqrt{\pi c}/K_c$, now normalized using c_m , as a function of d/c or c/c_m for each confining pressure. Typical results are shown in Fig.18 for $b = d_M/c_m = 3.5$, $a = 0.25$ and $c_M/c_m = 20$. Hence, for each confining pressure, we can identify the crack spacing and crack size which yield the smallest axial stress; this then is the ultimate strength for the considered confining pressure. In this manner, we obtain the ultimate strength, the range for the possible values of the fault orientation, and the optimal value of d/c or c/c_m as functions of the confining pressure. Typical results corresponding to Fig.18, are shown in Figs.19a,b, and c.

The strength, pressure-curve is separated into an initial nonlinear part and a relatively linear part. Comparing Figs.19a and c, it is seen that in the initial nonlinear part the size of active cracks decreases from the maximum c_M , to the minimum c_m , and in the linear part cracks of minimum size are active. As is seen in Fig.19b, the expected fault plane angle, ϕ , is rather small for small confining pressures, but increases sharply and stays around 30° at high pressures. In the first part, cracks of maximum size are active. In the second (transition) part, the size of active cracks decreases with increasing lateral pressure. And for the last part which corresponds to the linear segment of the strength, pressure-curve, cracks of minimum size are active. These qualitative results of our

"model" agree well with experimental observations; Griggs and Handin(1960), and Mogi(1966).

As shown above, once parameters which characterize crack distribution are given, one can estimate the ultimate strength and the range for the possible values of the fault orientation, as functions of the confining pressure. These parameters may be obtained from the strength, pressure-curve observed in experiments, as follows.

Since the linear part of the strength, pressure-curve corresponds to the minimum crack size, the spacing d_m/c_m may be specified from the slope of this linear part of the strength, pressure-curve. Figure 20a shows typical slopes of the strength curve, $\partial\sigma_1/\partial\sigma_2$, as functions of d/c , for indicated σ_2/σ_1 . Next we determine the parameter a , from the coordinates of the point which separates the initial nonlinear and linear parts of the observed strength, pressure-curve. Figure 20b shows the stress ratio σ_2/σ_1 at the separation point, as a function of the parameter a , for indicated values of d_m/c_m . Once d_m/c_m is established, the parameter a can be read off Fig.20b for a given stress ratio, σ_2/σ_1 . Note that a suitable value for c_m/c_m must also be chosen, but the final results are not sensitive to this parameter.

Since the stress ratio, σ_2/σ_1 , is independent of the normalization factor $K_c/\sqrt{\pi c_m}$, this factor is not needed in the above procedure. Its value may, however, be fixed in such a manner as to fit the observed data. The parameters used to obtain Figs.18 and 19 have been chosen from data on Westerly granite reported by Wawersik and Brace(1971). These data are plotted in Fig.19a, using the normalization factor $K_c/\sqrt{\pi c_m} = 27 \times 10^3$ psi.

The calculated strength, pressure-curve is in good agreement with the experimental data. This, of course, is expected, since the free parameters have been chosen in order to fit the experimental points. The orientation of the overall failure, however, seems to have the right trend, although the experimental data points are scattered over a wide range.

Figures 21a,b show a comparison with experimental data on Darley Dale sandstone reported by Murrell(1965). In this case, we have set $d_m/c_m = 3.0$, $a = 0.18$, $c_M/c_m = 10$, and $K_c/\sqrt{\pi c_m} = 8 \times 10^3$ psi. Both the calculated strength, pressure-curve and the orientation of the overall fault plane are in good accord with the observed data.

An interesting feature of our theory of shear failure is that the orientation of the final failure plane is, in general, different from the orientation of the individual cracks which participate in producing the failure plane. To test this and to further accentuate the fundamentally different mechanisms which may be involved in failure by axial splitting and shear failure, we have performed model experiments on two specimens with essentially identical pre-existing crack patterns, one with, and the other without confinement. These are shown in Figs.22 and 23.

As is seen from Figs.22a and 23a, both specimens contain a number of very small equal-sized cracks, each oriented at 45° relative to the axial compression. The test associated with Fig.22 is done under lateral compression, produced by the Poisson effect because of partial lateral constraint. As discussed in Section 2, the larger cracks are activated first, Figs.22b and 23b. These are soon arrested for the specimen with confinement (Fig.22c), whereas without confinement they continue to grow

(Fig.23c). Indeed, in the latter case, these cracks extend and join each other, leading to axial splitting (Fig.23d), while many of the smaller cracks remain inactive. The specimen eventually shatters, as shown in Fig.23e. On the other hand, in the presence of confinement, smaller cracks soon become activated (Fig.22d), as larger cracks are arrested. Then, a suitably oriented set of smaller cracks grows in an unstable manner, leading to a final fracture plane (Fig.22e) which is clearly distinct from the orientation of the participating individual cracks.

APPENDIX A

Consider a two-dimensional (plane strain or plane stress) problem of out-of-plane crack extension under compression, as shown in Fig. 4. The pre-existing crack PP' of length $2c$ has undergone frictional sliding under far-field compression, which has resulted in the formation of centrally symmetric tension crack extensions PQ and P'Q' of equal length l . With respect to the Oxy-coordinate system, let the crack extension profile be defined by $x = c+g(r)$ and $y = f(r)$ where r measures length along the curved crack. Here σ_1 and σ_2 are the principal stresses at infinity and γ is the angle between a principal direction and the x-axis. Let σ_x^∞ , σ_y^∞ and τ_{xy}^∞ denote the components of stresses at infinity in the Oxy-coordinate system. We consider the case where $\sigma_1 < 0$, $|\sigma_1| > |\sigma_2|$ and $0 < \gamma < \pi/2$. Then τ_{xy}^∞ is always negative.

It is assumed that the pre-existing crack PP' is closed and transmits frictional shear tractions. Hence the boundary conditions on PP' are

$$u_y^+ = u_y^-, \quad \tau_{xy}^+ = \tau_{xy}^- = -\tau_c + \mu\sigma_y^-, \quad (A1)$$

where superscripts "+" and "-" denote the values of the indicated quantity on the upper and lower faces of the pre-existing crack, respectively; τ_c and μ are the cohesive force and the coefficient of friction (both positive). Since PQ and P'Q' are tensile crack extensions, we assume stress free conditions along PQ and P'Q';

$$\sigma_\theta = \tau_{r\theta} = 0. \quad (A2)$$

Following Nemat-Nasser and Horii(1982), we consider Muskhelishvili's(1953) stress functions $\phi_D = \phi_O + \phi_R$ and $\psi_D = \psi_O + \psi_R$ for a pair of antisymmetric dislocations at z_0 and $-z_0$ in the complex z -plane, which satisfy the following conditions along PP' :

$$\tau_O + \tau_R = \mu\sigma_O, \quad \sigma_R = 0, \quad (A3)$$

and stress functions $\phi_\infty = \phi_{\infty O} + \phi_{\infty R}$ and $\psi_\infty = \psi_{\infty O} + \psi_{\infty R}$ for the external forces at infinity, which satisfy the following conditions along PP' :

$$\tau_{xy}^{\infty} + \tau_{\infty R} = -\tau_c + \mu\sigma_y^{\infty}, \quad \sigma_{\infty R} = 0, \quad (A4)$$

where σ_O and τ_O , σ_R and τ_R , σ_y^{∞} and τ_{xy}^{∞} , and $\sigma_{\infty R}$ and $\tau_{\infty R}$ are the normal and shear stresses due to ϕ_O and ψ_O , ϕ_R and ψ_R , $\phi_{\infty O}$ and $\psi_{\infty O}$, and $\phi_{\infty R}$ and $\psi_{\infty R}$, respectively, and

$$\begin{aligned} \phi_O &= a \ln \frac{z-z_0}{z+z_0}, \quad \psi_O = \bar{a} \ln \frac{z-z_0}{z+z_0} - a\bar{z}_0 \frac{2z}{z^2-z_0^2}, \\ \phi_R &= (\bar{a}\beta - a\beta)[F(z, z_0) + F(z, \bar{z}_0)] + (\bar{z}_0 - z_0)[\alpha\bar{\beta}G(z, z_0) + \alpha\beta G(z, \bar{z}_0)], \\ \psi_R &= \bar{\psi}_R' + \psi_R' - z\phi_R'', \\ \phi_{\infty O}' &= (\sigma_y^{\infty} + \sigma_x^{\infty})/4, \quad \psi_{\infty O}' = (\sigma_y^{\infty} - \sigma_x^{\infty})/2 + i\tau_{xy}^{\infty}, \\ \phi_{\infty R}' &= \frac{1}{2}(\tau_{xy}^{\infty} - \mu\sigma_y^{\infty} + \tau_c)i[1 - z/(z^2 - c^2)^{1/2}], \\ \psi_{\infty R}' &= \frac{1}{2}(\tau_{xy}^{\infty} - \mu\sigma_y^{\infty} + \tau_c)i[-zc^2/(z^2 - c^2)^{3/2} + 2z/(z^2 - c^2)^{1/2} - 2], \end{aligned} \quad (A5)$$

with

$$F(z, z_0) = \left[1 - \frac{z(z_0^2 - c^2)^{1/2}}{z_0(z^2 - c^2)^{1/2}} \right] \frac{z_0}{z^2 - z_0^2},$$

$$G(z, z_0) = \frac{\partial}{\partial z_0} F(z, z_0) = \left[1 - \frac{z(z_0^2 - c^2)^{1/2}}{z_0(z^2 - c^2)^{1/2}} \right] \frac{2zz_0}{(z^2 - z_0^2)^2} + \left[1 - \frac{zz_0}{(z_0^2 - c^2)^{1/2}(z^2 - c^2)^{1/2}} \right] / (z^2 - z_0^2). \quad (A6)$$

From (A3) and (A4), it is seen that the stress functions $\phi = \phi_D + \phi_\infty$ and $\psi = \psi_D + \psi_\infty$ automatically satisfy the second condition of \dagger (A1).

Suitably distributed dislocations are now introduced to represent the curved crack extensions with dislocation density $\alpha(r)$.

Since

$$\sigma_\theta + i\tau_{r\theta} = \phi' + \bar{\phi}' + e^{2i\theta}(\bar{z}\phi'' + \psi'), \quad (A7)$$

it follows from (A2) that

$$\int_0^l [\phi_D' + \bar{\phi}_D' + e^{2i\theta}(\bar{z}\phi_D'' + \psi_D')] dr + \phi_\infty' + \bar{\phi}_\infty' + e^{2i\theta}(\bar{z}\phi_\infty'' + \psi_\infty') = 0, \quad (A8)$$

with

$$z_0 = c + g(r) + if(r), \quad z = c + g(s) + if(s), \quad \alpha = \alpha(r), \quad \theta = \tan^{-1}[f'(s)/g'(s)]. \quad (A9)$$

The first condition of (A1) requires

$$\int_0^l [\alpha(r) + \bar{\alpha}(r)] dr = 0. \quad (A10)$$

Equation (A8) can be rewritten as

$$\int_0^l \frac{\alpha M_1 + \bar{\alpha} M_2}{s - r} dr + \int_0^l [\alpha L_1 + \bar{\alpha} L_2] dr + (\tau_{xy}^0 - \mu \sigma_y^0 + \tau_c) S + \sigma_\theta^0 + i\tau_{r\theta}^0 = 0, \quad (A11)$$

\dagger Note that in Eq.(8) of Nemat-Nasser and Horii(1982), and in Eq.(2.9) of Horii and Nemat-Nasser(1982), the term z/z_0 inside the brackets in the expression for $F(z, z_0)$ is missing. The expression for $G(z, z_0)$ must also be corrected accordingly; for detailed calculations, see Nemat-Nasser(1983).

where

$$M_1(r,s) = 1/h e^{-2i\theta} \bar{h}/h^2, \quad M_2(r,s) = 1/\bar{h} e^{2i\theta}/h;$$

$$h(r,s) = [g(s) - g(r) + i(f(s) - f(r))]/(s-r), \quad (A12)$$

$$L_1(r,z,\theta) = \beta U\{F(z,z_0) + F(z,\bar{z}_0)\} + \bar{\beta} U\{(z_0 - \bar{z}_0)G(z,z_0)\} - \frac{1}{z+z_0} + e^{2i\theta} \frac{z+z_0}{(z+z_0)^2},$$

$$L_2(r,z,\theta) = -\bar{\beta} U\{F(z,z_0) + F(z,\bar{z}_0)\} - \beta U\{(\bar{z}_0 - z_0)G(z,\bar{z}_0)\} - \frac{1}{\bar{z}+\bar{z}_0} + e^{2i\theta} \frac{1}{z+z_0},$$

$$U\{F(z,z_0)\} = U\{\theta; F(z,z_0)\} = -F(z,z_0) + F(\bar{z},z_0) + e^{2i\theta} [2F(z,z_0) + (z-\bar{z})F'(z,z_0)],$$

$$S(z,\theta) = \frac{1}{2}i \left\{ \frac{\bar{z}}{(\bar{z}^2 - c^2)^{1/2}} - \frac{z}{(z^2 - c^2)^{1/2}} + e^{2i\theta} \left[\frac{(\bar{z}-z)c^2}{(z^2 - z_0^2)^{3/2}} + \frac{2z}{(z^2 - c^2)^{1/2}} - 2 \right] \right\},$$

with $z = z(s)$, $z_0 = z_0(r)$ and $\theta = \theta(s)$ given by (A9). Equations (A11) with (A10) form a singular integral equation for dislocation density α . Solving this integral equation, we obtain the stress intensity factors at the tips of the out-of-plane extensions, i.e. at points Q and Q', from

$$K_{I} + iK_{II} = \lim_{r \rightarrow l} \frac{1}{2} (2\pi)^{3/2} (l-r)^{1/2} [\alpha(r)M_1(l,l) + \bar{\alpha}(r)M_2(l,l)]. \quad (A13)$$

For straight crack extensions we have

$$M_1 = 0, \quad M_2 = 2e^{2i\theta}, \quad \theta(s) = \theta = \text{const.}, \quad z = c + se^{i\theta}, \quad \text{and} \quad z_0 = c + re^{i\theta}. \quad (A14)$$

For the straight crack extension, the above formulation becomes identical with that of Nemat-Nasser and Horii (1982), except for $F(z,z_0)$ and $G(z,z_0)$ which are corrected according to (A6). This correction alters the numerical results of Nemat-Nasser and Horii (1982) somewhat for large values of l/c , and the new results are given in Figs. 3 and A1-5.

For curved crack extensions, with given crack profile, $f(r)$ and $g(r)$, the singular integral equation (A11) with (A10) is solved numerically using a method suggested by Gerasoulis(1982), and the stress intensity factors are obtained through (A16). The crack profile, defined by $f(r)$ and $g(r)$, is obtained by an incremental procedure where we consider a sequence of incremental straight extensions, each with an orientation which maximizes the opening mode stress intensity factor, K_I , at the extended crack tip. Typical results of curved extension are shown in Figs. 3 and 5 and are discussed in Section 2.

Nemat-Nasser and Horii(1982) suggest an approximate scheme for calculating the crack extension profile, on the basis of the results of straight crack extension calculations; see their Eqs.(21) and the corresponding discussion. Figure 3 compares the calculated crack extension profile for the approximate solution and the complete curved crack extension solution; for additional comparative results, see Horii and Nemat-Nasser(1983). It is seen that the straight crack extension model is in good qualitative accord with the more complete curved crack extension solution. Therefore, for the sake of simplicity in calculation, the straight crack extension model will be used in the sequel and in Appendix B.

As will be seen in Appendix B, the method of pseudo-tractions requires an explicit solution of the singular integral equation (A8). This integral equation can, of course, be solved as accurately as desired, in the manner discussed by Nemat-Nasser and Horii(1982). However, for application to the unstable growth of a row of pre-existing cracks, the stress intensity factors and other parameters must be calculated repeatedly for a range of

values of confining pressure, individual crack orientation, and other relevant parameters. To simplify this procedure, we introduce an approximate method for the solution of the singular integral equation (A8), which seems to yield results adequately accurate for our numerical estimates.

To this end we assume the following form for the distribution of dislocation density:

$$\alpha(r) = \frac{1}{[r(l-r)]^{1/2}} [\eta^R (2r/l-1) + i\eta^I r/l], \quad (A15)$$

which satisfies (A10), where η^R and η^I are two real unknown parameters to be determined. Furthermore, we approximate the integrand of the second term in (A11) as

$$\begin{aligned} \alpha(r)L_1(r,z,\theta) + \bar{\alpha}(r)L_2(r,z,\theta) = & \frac{1}{[r(l-r)]^{1/2}} \{ [(\eta^R + i\eta^I)L_1(l,z,\theta) \\ & + (\eta^R - i\eta^I)L_2(l,z,\theta)]r/l - \eta^I [L_1(0,z,\theta) + L_2(0,z,\theta)](1-r/l) \}. \end{aligned} \quad (A16)$$

Making use of (A15) and (A16), (A11) becomes

$$\begin{bmatrix} A_1 & A_2 \\ A_3 & A_4 \end{bmatrix} \begin{bmatrix} \eta^R \\ \eta^I \end{bmatrix} = \begin{bmatrix} (\tau_{xy}^{\infty} - \mu\sigma_y^{\infty})\text{Re}[S] + \sigma_{\theta}^{\infty} \\ (\tau_{xy}^{\infty} - \mu\sigma_y^{\infty})\text{Im}[S] + \tau_{r\theta}^{\infty} \end{bmatrix}, \quad (A17)$$

where

$$\begin{aligned} A_1 + iA_3 &= \frac{\pi r_0}{2l} e^{i\theta} [-L_1(l,z,\theta) - L_2(l,z,\theta) + L_1(0,z,\theta) + L_2(0,z,\theta)], \\ -A_4 + iA_2 &= \frac{\pi r_0}{2l} e^{i\theta} [L_1(l,z,\theta) + L_2(l,z,\theta)]. \end{aligned} \quad (A18)$$

Since s may be suitably chosen, we consider, for convenience, the following expressions:

$$s/l = \begin{cases} -0.075(l/c) + 0.475, & \text{for } l/c < 1 \\ -0.0074(l/c)^3 + 0.0156(l/c)^2 - 0.104(l/c) + 0.489, & \text{for } 1 < l/c < 4. \\ -0.015(l/c) + 0.335, & \text{for } 4 < l/c \end{cases} \quad (\text{A19})$$

From (A13), (A17) and (A18), we have

$$K_I + iK_{II} = (2\pi)^{3/2} e^{i\theta} (\eta^R - i\eta^I)^{1/2}. \quad (\text{A20})$$

Equations (A19) can be solved easily for η^R and η^I and the stress intensity factors at the tips of straight crack extensions are obtained from (A20). Adopting the fracture criterion that the most favorable orientation of the crack extension results in the maximum value of K_I , we can specify the kink angle, θ .

The results of the approximate solution are compared with the numerical solutions in Fig. A5. It is seen that the drastic approximation shown above provides a relatively good accuracy.

APPENDIX B

Consider an unbounded solid with a row of periodically extended pre-existing cracks which have grown out of their own planes, as a result of suitably applied far-field compressive forces. The pre-existing cracks are of equal size, $2c$, are equally spaced along the ϕ -orientation at a distance d , and have a common orientation, γ , with respect to the σ_1 -direction. The out-of-plane extensions are assumed to be straight with equal length, l , and equal "kink" angle, θ , measured with respect to the common orientation of the pre-existing cracks.

The boundary conditions (A1), with $\tau_c = 0$, are assumed to hold on all pre-existing cracks, and along their extensions the stress-free condition (A2) is applied.

The problem is solved by making use of the method of pseudo-tractions, Horii and Nemat-Nasser(1983), which is the method for the problem of an infinite solid containing micro-inhomogeneities such as cracks or holes. The solution to the original problem is obtained by the superposition of the solutions of a number of sub-problems, and of the solution of the problem of an infinitely extended homogeneous solid under applied far-field stresses; Fig. B1. Each sub-problem involves an infinite homogeneous solid containing only one of the cracks of the original solid. For each sub-problem, the boundary conditions along pre-existing crack PP' are

$$u_y^+ = u_y^-, \quad \tau_{xy} + \tau_{xy}^P + \tau_{xy}^{\bar{P}} = \mu(\sigma_y + \sigma_y^P + \sigma_y^{\bar{P}}), \quad (B1)$$

and along its extensions PQ and $P'Q'$,

$$\sigma_{\theta} + \sigma_{\theta}^P + \sigma_{\theta}^{\infty} = 0, \quad \tau_{r\theta} + \tau_{r\theta}^P + \tau_{r\theta}^{\infty} = 0. \quad (B2)$$

The quantities σ_y^P , τ_{xy}^P , σ_{θ}^P , and $\tau_{r\theta}^P$ will be called the "pseudo-tractions". They are the unknown functions which must be determined in such a manner as to satisfy all boundary conditions of the original problem. The requirement that the sum of the sub-problems must be equivalent to the original problem leads to a system of integral equations for these pseudo-tractions. These are the "consistency conditions". By discretizing the unknown pseudo-tractions, the system of integral equations is reduced to a system of algebraic equations. Because of symmetry, the pseudo-tractions are the same for all cracks. For simplicity, we approximate the pseudo-tractions by piece-wise constant functions, i.e., we assume that σ_y^P and τ_{xy}^P are constants along PP', and σ_{θ}^P and $\tau_{r\theta}^P$ are constants along PQ and P'Q'.

Following the approximate method proposed in Appendix A, the solution of a typical sub-problem is given by

$$\begin{bmatrix} A_1 & A_2 \\ A_3 & A_4 \end{bmatrix} \begin{bmatrix} \eta^R \\ \eta^I \end{bmatrix} = \begin{bmatrix} [\tau_{xy}^{\infty} + \tau_{xy}^P - \mu(\sigma_y^{\infty} + \sigma_y^P)] \text{Re}[S] + \sigma_{\theta}^{\infty} + \sigma_{\theta}^P \\ [\tau_{xy}^{\infty} + \tau_{xy}^P - \mu(\sigma_y^{\infty} + \sigma_y^P)] \text{Im}[S] + \tau_{r\theta}^{\infty} + \tau_{r\theta}^P \end{bmatrix}, \quad (B3)$$

where S is given in (A12), and A's are given in (A18).

The normal and shear tractions, σ_{ψ} and $\tau_{\rho\psi}$, acting at a point z on a plane inclined from the x-direction by the angle ψ , are given by

$$\sigma_{\psi} + i\tau_{\rho\psi} = B_1(z, \psi)\eta^R + B_2(z, \psi)\eta^I + [\tau_{xy}^{\infty} + \tau_{xy}^P - \mu(\sigma_y^{\infty} + \sigma_y^P)]S(z, \psi), \quad (B4)$$

where

$$B_1(z, \psi) = 2\text{Re}[2I_1 - I_2] + e^{2i\psi}(2I_1 - I_2 + 2II_1 - II_2)$$

$$+\frac{\pi}{2}[L_1(\ell, z, \psi)+L_2(\ell, z, \psi)-L_1(0, z, \psi)-L_2(0, z, \psi)], \quad (B5)$$

$$B_2(z, \psi) = -2\text{Im}[I_1] + ie^{2i\psi}(-I_1 + II_1) + i\frac{\pi}{2}[L_1(\ell, z, \psi) - L_2(\ell, z, \psi)].$$

with

$$I_1 = \frac{1}{\ell} \int \frac{r dr}{o[r(\ell-r)]^{1/2} (z-c-re^{i\theta})} = \frac{e^{-i\theta}}{\ell} \pi \left\{ \frac{z-c}{[(z-c)(z-z_c)]^{1/2}} - 1 \right\},$$

$$I_2 = \frac{1}{\ell} \int \frac{dr}{o[r(\ell-r)]^{1/2} z-c-re^{i\theta}} = \frac{\pi}{[(z-c)(z-z_c)]^{1/2}},$$

$$II_1 = \frac{1}{\ell} \int \frac{r(\bar{z}-c-re^{-i\theta}) dr}{o[r(\ell-r)]^{1/2} (z-c-re^{i\theta})^2},$$

$$= -\frac{e^{-3i\theta}}{\ell} \pi \left\{ \frac{(z-c)[(z-c)(3z-3z_c-z+c) + (\bar{z}-c)(z_c-c)e^{2i\theta}]}{2[(z-c)(z-z_c)]^{3/2}} - 1 \right\}, \quad (B6)$$

$$II_2 = -\frac{1}{\ell} \int \frac{(\bar{z}-c-re^{-i\theta}) dr}{o[r(\ell-r)]^{1/2} (z-c-re^{i\theta})^2}$$

$$= \frac{e^{-2i\theta}}{\ell} \frac{(z-c)(z_c-c) - (\bar{z}-c)(z-c+z-z_c)e^{2i\theta}}{2[(z-c)(z-z_c)]^{3/2}}.$$

Then the "consistency conditions" lead to

$$\sigma_y^P + i\tau_{xy}^P = C_1^c R + C_2^c I + [\tau_{xy}^e + \tau_{xy}^P - \mu(\sigma_y^e + \sigma_y^P)] F^c,$$

$$\sigma_\theta^P + i\tau_{r\theta}^P = C_1^e R + C_2^e I + [\tau_{xy}^e + \tau_{xy}^P - \mu(\sigma_y^e + \sigma_y^P)] F^e, \quad (B7)$$

where

$$C_j^c = \frac{2}{N} \sum_{n=1}^N B_j(z_{1n}^c, 0) + 2 \sum_{m=2}^{\infty} B_j(z_m, 0),$$

$$C_j^e = \frac{1}{N} \sum_{n=1}^N [B_j(z_{1n}^r, \theta) + B_j(z_{1n}^l, \theta)] + 2 \sum_{m=2}^{\infty} B_j(z_m, 0),$$

$$F^c = \frac{2}{N} \sum_{n=1}^N S(z_{1n}^c, 0) + 2 \sum_{m=2}^{\infty} S(z_m, 0), \quad (B8)$$

$$F^e = \frac{1}{N} \sum_{n=1}^N [S(z_{1n}^r, \theta) + S(z_{1n}^l, \theta)] + 2 \sum_{m=2}^{\infty} S(z_m, \theta).$$

with

$$\begin{aligned} z_{1n}^c &= d e^{i(\phi-\gamma)} - c + 2c(n-1)/(N-1), & z_m &= m d e^{i(\phi-\gamma)}, \\ z_{1n}^r &= d e^{i(\phi-\gamma)} + c + l e^{i\theta}(n-1)/(N-1), & & \\ z_{1n}^l &= d e^{i(\phi-\gamma)} - c - l e^{i\theta}(n-1)/(N-1). & & \end{aligned} \quad (B9)$$

In Eqs.(B7), the first term in the right-hand side of each equation corresponds to the tractions on one particular crack, produced because of the presence of the adjacent cracks, and the second term corresponds to those produced by all other cracks. The second term in (B7) can be expanded in even powers of c/md and, in this manner, each series can be summed, neglecting high order terms. In the calculations, N is taken to be 10, and terms of order higher than $(c/d)^{10}$ are neglected.

For given values of d/c , γ , ϕ , σ_2/σ_1 , l/c , and θ , the system of algebraic equations (B2) and (B6) is solved for η^R , η^I , σ_y^P , τ_{xy}^P , σ_θ^P , and $\tau_{r\theta}^P$. Then the stress intensity factors at the tips of the extended cracks are obtained from (A20). The "kink" angle θ is determined such that the opening mode stress intensity factor, K_I , is maximized, i.e. from (A21). Setting the value of K_I equal to the fracture toughness, K_c , we obtain the required axial compression, σ_1 , for a given crack extension length l/c .

For fixed values of d/c , γ , and ϕ , we calculate the axial compression σ_1 for each crack extension length l/c , and for different values of σ_2/σ_1 . It turns out that the plot of σ_1 as a function of σ_2 for each l/c , is a straight line. Typical results are shown in Fig. B2 for $d/c = 4$, $\gamma =$

0.24π , and $\phi = 0.16\pi$. From results of this kind, we can now calculate various required parameters for a constant confining pressure σ_2 , rather than for a constant stress-ratio, σ_2/σ_1 .

Acknowledgment

This work has been supported by the U.S. Air Force Office of Scientific Research grant AFOSR-80-0017 to Northwestern University.

REFERENCES

- Brace, W.F., and E.G. Bombolakis, A note on brittle crack growth in compression, J. Geophys. Res., 68(12), 3709-3713, 1963.
- Gerasoulis, A., The use of piecewise quadratic polynomials for the solution of singular integral equations of Cauchy type, Comp. & Maths. with Appls., 8(1), 15-22, 1982.
- Griggs, D., and J. Handin, Observations on fracture and a hypothesis of earthquakes, Rock deformation (edited by D. Griggs and J. Handin) Mem. geol. Soc. Am., 79, 347-364, 1960.
- Hallbauer, D.K., H. Wagner, and G.W. Cook, Some observations concerning the microscopic and mechanical behaviour of quartzite specimens in stiff, triaxial compression tests, Int. J. Rock Mech. Min. Sci. & Geomech. Abstr., 10, 713-726, 1973.
- Hoek, E., and Z.T. Bieniawski, Brittle fracture propagation in rock under compression, Int. J. Fract. Mech., 1, 137-155, 1965.
- Horii, H., and S. Nemat-Nasser, Curved crack growth in brittle solids under farfield compression, Advances in Aerospace Structures and Materials, AD-03, ASME, 75-81, 1982.
- Horii, H., and S. Nemat-Nasser, Estimate of stress intensity factors for interacting cracks; to appear in Advances in Aerospace Structures and Materials, AD-04, ASME, 1983.
- McClintock, F.A., and J.B. Walsh, Friction on Griffith cracks in rocks under pressure, Proc. 4th U.S. Nat. Congr. Appl. Mech. 1962, ASME, New York, 2, 1015-1021, 1963.
- Mogi, K., Pressure dependence of rock strength and transition from brittle fracture to ductile flow, Bull. Earthquake Res. Inst., 44, 215-232, 1966.
- Mosher, S., R.L. Berger, and D.E. Anderson, Fracturing characteristics of two granites, Rock Mechanics, 7, 167-232, 1975.
- Murrell, S.A.F., The effect of triaxial stress systems on the strength of rocks at atmospheric temperatures, Geophys. J. Roy. Astr. Soc., 10, 231-281, 1965.
- Muskhelishvili, N.I., Some Basic Problems in the Mathematical Theory of Elasticity, Noordhoff, Groningen, (1953).
- Nemat-Nasser, S., Non-coplanar crack growth, Proc. ICE Int. Symp. on Fract. Mech., Beijing, China, Nov. 22-26, 1983 (in press).

- Nemat-Nasser, S., and H. Horii, Compression-induced nonplanar crack extension with application to splitting, exfoliation, and rockburst, *J. Geophys. Res.*, **87**(B8), 6805-6821, 1982.
- Peng, S.D., Stresses within elastic circular cylinders loaded uniaxially and triaxially, *Int. J. Rock Mech. Min. Sci.*, **8**, 399-432, 1971.
- Peng, S.D., and A.M. Johnson, Crack growth and faulting in cylindrical specimens of Chelmsford granite, *Int. J. Rock Mech. Min. Sci.*, **9**, 37-86, 1972.
- Tapponnier, P., and W.F. Brace, Development of stress-induced microcracks in Westerly granite, *Int. J. Rock Mech. Min. Sci. & Geomech. Abstr.*, **13**, 103-112, 1976.
- Wawersik, W.R., and W.F. Brace, Post-failure behavior of a granite and diabase, *Rock Mech.*, **3**, 61-85, 1971.

LIST OF FIGURES

- Figure 1: (a) A barrel-shaped specimen containing a pre-existing crack; and (b) unstable out-of-plane crack extension under axial compression.
- Figure 2: (a) A dogbone-shaped specimen containing a pre-existing crack; and (b) stable out-of-plane crack extension under axial compression.
- Figure 3: Calculated and observed crack profiles.
- Figure 4: Pre-existing crack P'P and its curved extensions PQ and P'Q'.
- Figure 5: Compressive force required to attain the associated crack extension length.
- Figure 6: (a) Specimen containing a number of randomly distributed cracks; and (b) its failure pattern under overall axial compression (from Nemat-Nasser and Horii, 1982).
- Figure 7: (a) Specimen containing a row of small cracks and several larger cracks; (b) under axial compression without confinement, larger cracks beginning to grow first; (c) axial splitting by the growth of large cracks; and (d) shattering of the specimen while some smaller cracks are still inactive.
- Figure 8: (a) Specimen containing a row of small cracks and several larger cracks (same as in Fig. 7a); (b) under axial compression with confinement, larger cracks beginning to grow first; (c) growth of larger cracks arrested because of confinement, and several smaller cracks just activated; (d) without an increase in axial load, the entire row of smaller cracks being suddenly activated; and (e) fault formation due to interactive growth of smaller cracks.
- Figure 9: An unbounded solid with a row of periodically extended pre-existing cracks PP' and their out-of-plane extensions PQ and P'Q'.
- Figure 10: Variation of axial compression with the crack extension length and the overall orientation angle; $d/c = 4$, $|\sigma_2| \sqrt{\pi c} / K_c = 0.1$, $\gamma = 0.24\pi$, and $\mu = 0.4$.

- Figure 11: The peak value of axial compression as a function of overall orientation angle ϕ ; $d/c = 4$, and $\mu = 0.4$.
- Figure 12: Axial stress vs. crack extension length for indicated overall orientation; $d/c = 4$, $|\sigma_2| \sqrt{\pi c} / K_c = 0.1$, $\gamma = 0.24\pi$, and $\mu = 0.4$.
- Figure 13: The out-of-plane crack extension for indicated extension length and overall orientation; $\gamma = 0.24\pi$, and $\mu = 0.4$.
- Figure 14: Ultimate strength and the overall failure angle as functions of the confining pressure for indicated constant crack spacing; $\gamma = 0.24\pi$, and $\mu = 0.4$.
- Figure 15: Ultimate strength and the overall failure angle as functions of the confining pressure for indicated constant crack spacing; $\gamma = 0.24\pi$, and $\mu = 0.4$.
- Figure 16: Ultimate strength and the overall failure angle as functions of the confining pressure for indicated constant crack spacing; $\gamma = 0.24\pi$, and $\mu = 0.4$.
- Figure 17: Variations of the ultimate strength, its rate of change with respect to the confining pressure, and the overall failure angle as functions of relative crack spacing; $\gamma = 0.24\pi$, and $\mu = 0.4$.
- Figure 18: Ultimate strength, normalized using the minimum crack size, as a function of crack size or relative crack spacing; $\gamma = 0.24\pi$, and $\mu = 0.4$.
- Figure 19: Variation of (a) the ultimate strength, (b) overall failure orientation, and (c) active crack size or its relative spacing with confining pressure, compared with the experimental data on Westerly granite by Wawersik and Brace (1971).
- Figure 20: (a) The slope of the strength curve as a function of relative crack spacing; and (b) the stress ratio at the separation point between the initial nonlinear part and the following linear part of the strength curve as a function of the parameter a .
- Figure 21: Variation of (a) the ultimate strength and (b) overall failure orientation with confining pressure, compared with the experimental data on Darley Dale sandstone by Murrell (1965).

- Figure 22: (a) Specimen containing a band of small cracks and several larger cracks; (b) under axial compression with confinement, larger cracks being activated first; (c) larger cracks arrested because of confinement, and smaller cracks continuing to interact and extend; and (d,e) fault formation due to interactive growth of smaller cracks.
- Figure 23: (a) Specimen containing a band of small cracks and several larger cracks (same as in Fig. 22a); (b) under axial compression without confinement, larger cracks beginning to grow first; (c) larger cracks continuing to grow; (d) axial splitting by the growth of larger cracks; and (e) shattering of specimen while some smaller cracks are still inactive.
- Figure A1: Stress intensity factors at the tip, Q , of the straight crack extension, as functions of the kink angle for indicated extension length; $\tau_c = 0$, $\mu = 0.3$, $\sigma_2/\sigma_1 = 0$, and $\gamma = 0.2\pi$.
- Figure A2: (a) Maximum opening mode stress intensity factors and (b) optimal kink angle as functions of initial crack orientation; $\tau_c = 0$, and $\sigma_2/\sigma_1 = 0$.
- Figure A3: (a) Maximum opening mode stress intensity factors and (b) optimal kink angle as functions of initial crack orientation; $\tau_c = 0$, and $\sigma_2/\sigma_1 = 0$.
- Figure A4: (a) Maximum opening mode stress intensity factors and (b) optimal kink angle as functions of initial crack orientation; $\tau_c = 0$, and $\sigma_2/\sigma_1 = 0$.
- Figure A5: Variation of maximum stress intensity factor of opening mode with the crack extension length for indicated σ_2/σ_1 ; $\tau_c = 0$, and $\mu = 0.3$.
- Figure B1: Decomposition of an original problem into a homogeneous problem and sub-problems.
- Figure B2: Axial compressive force as a function of confining pressure for indicated crack extension length.

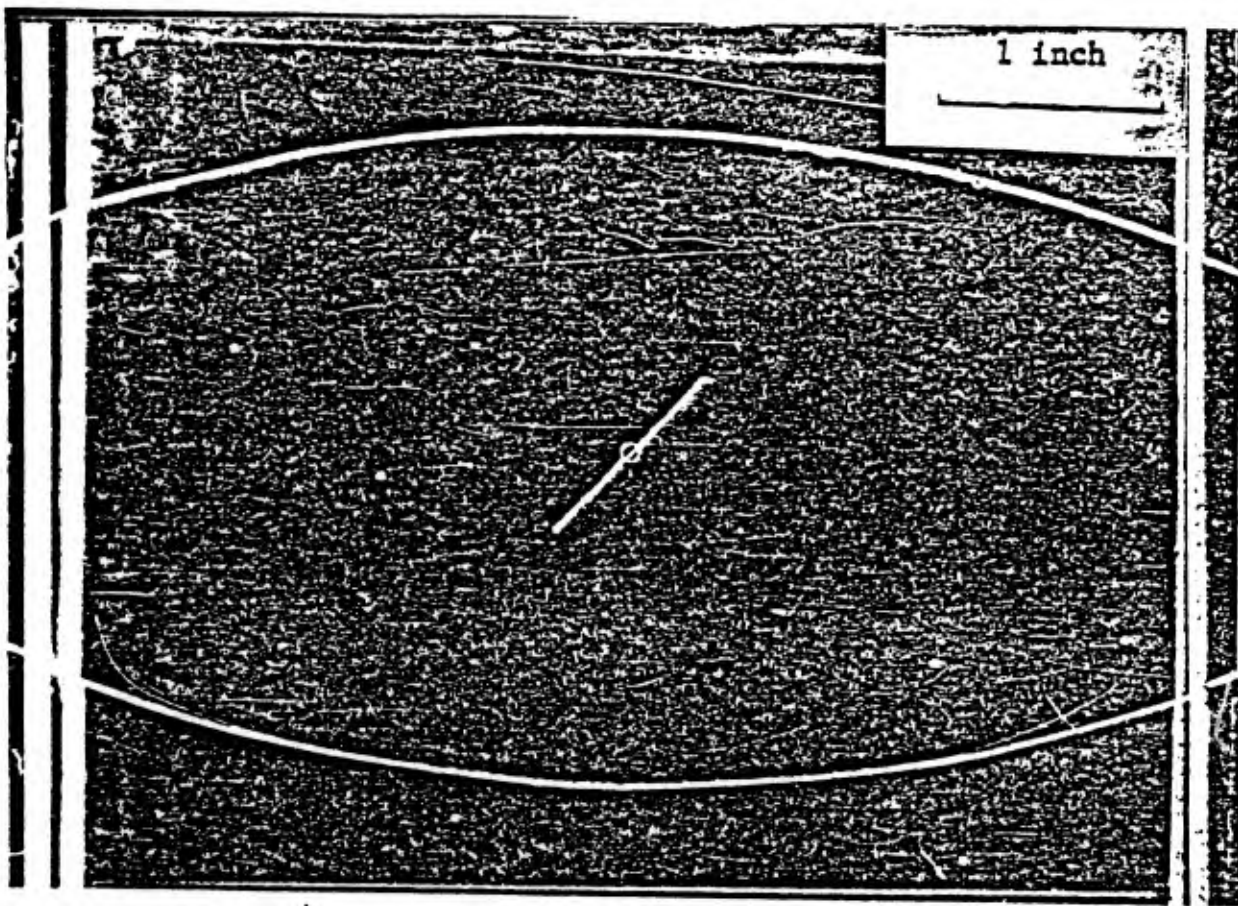


Figure 1a

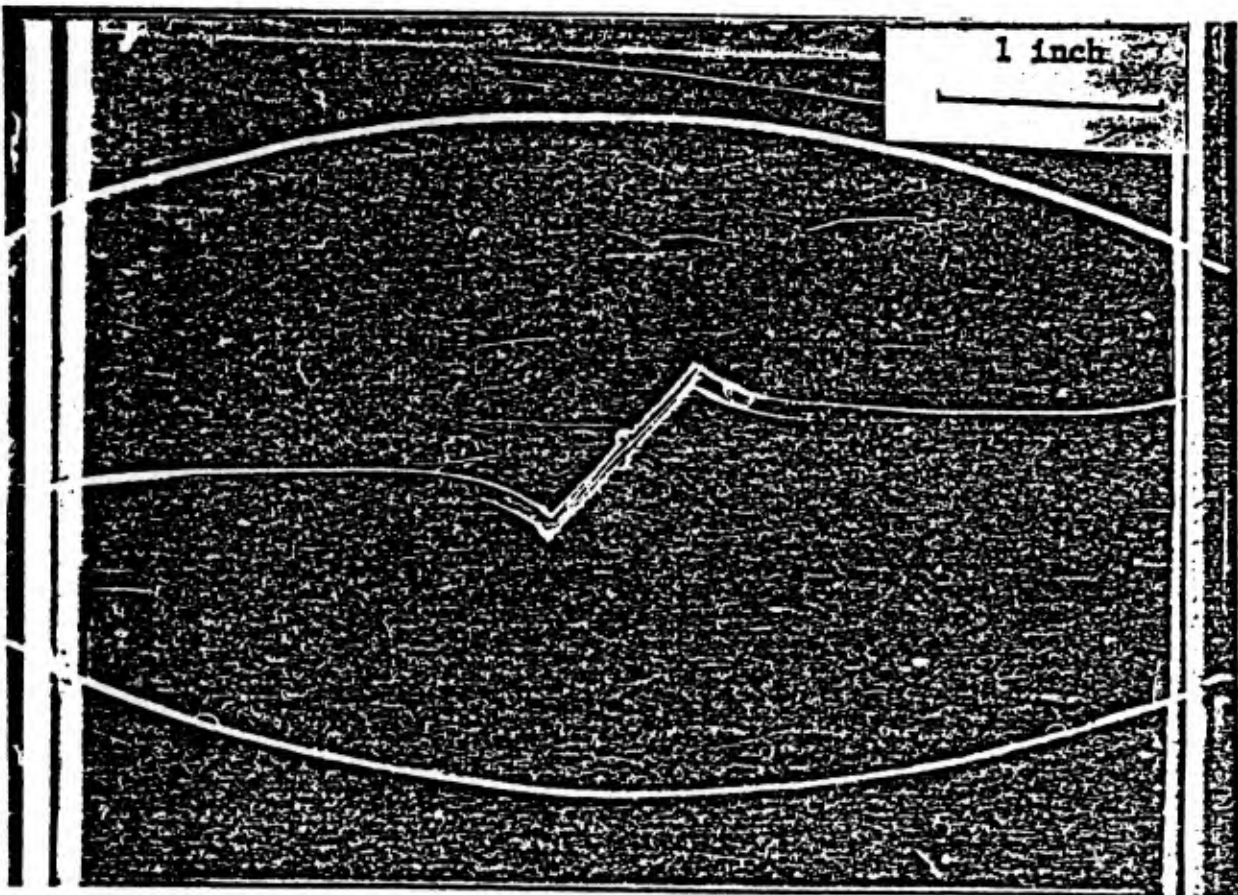


Figure 1b

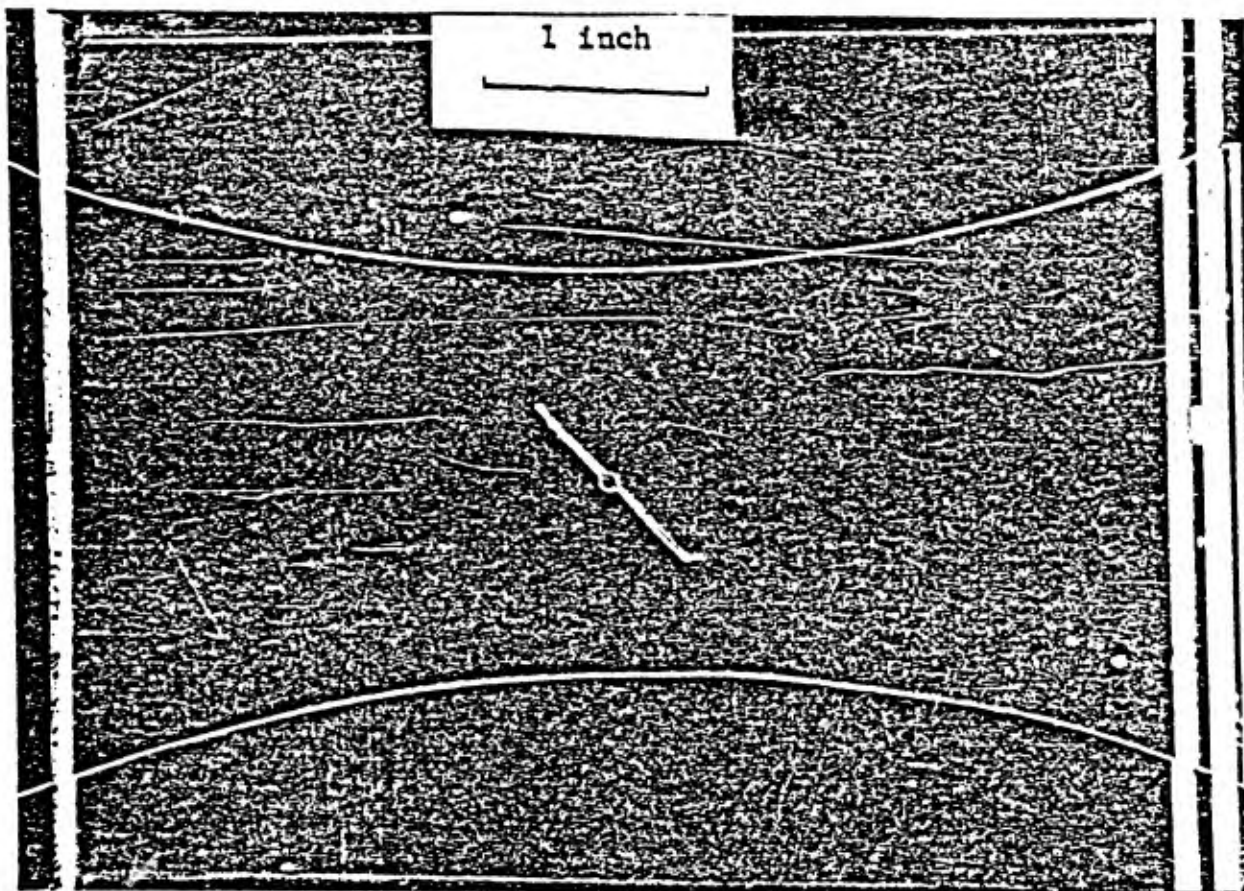


Figure 2a

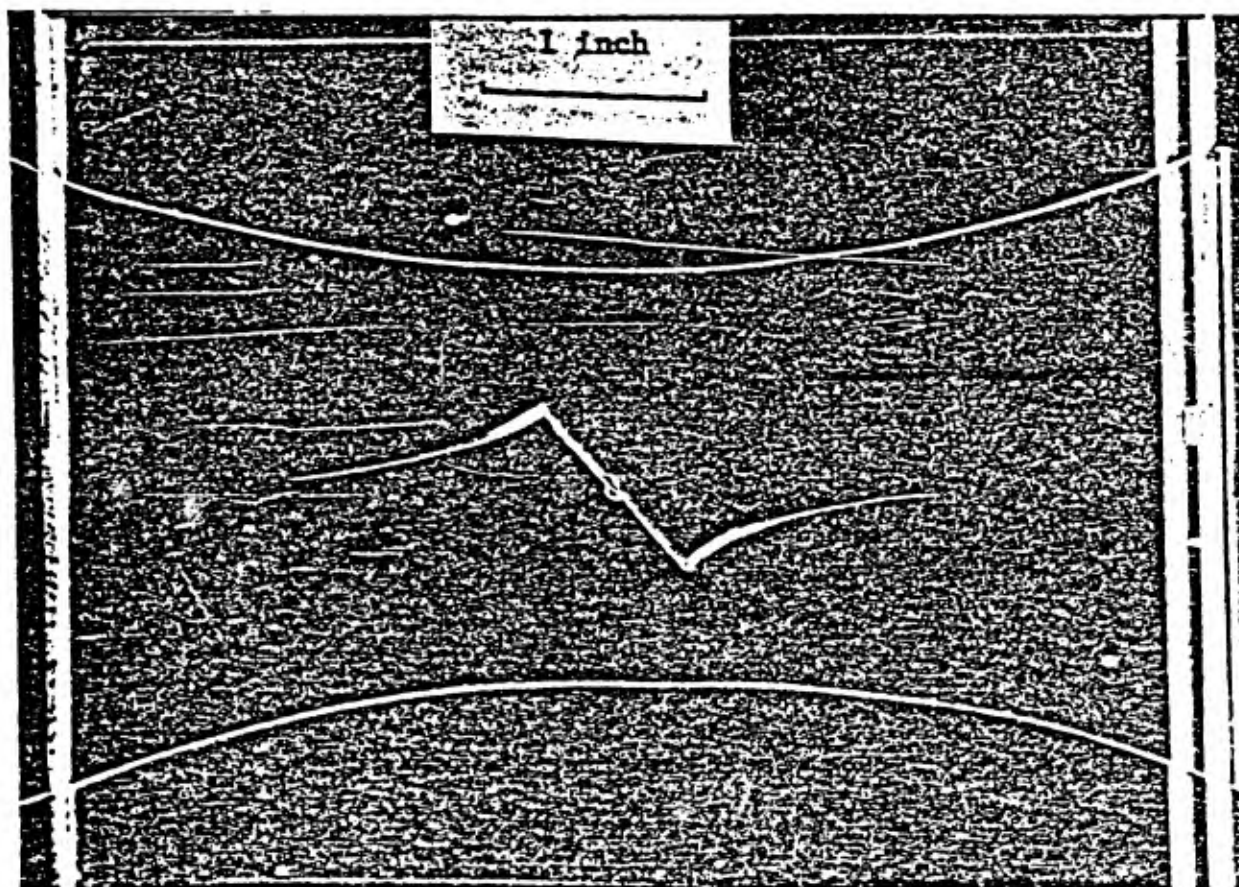


Figure 2b

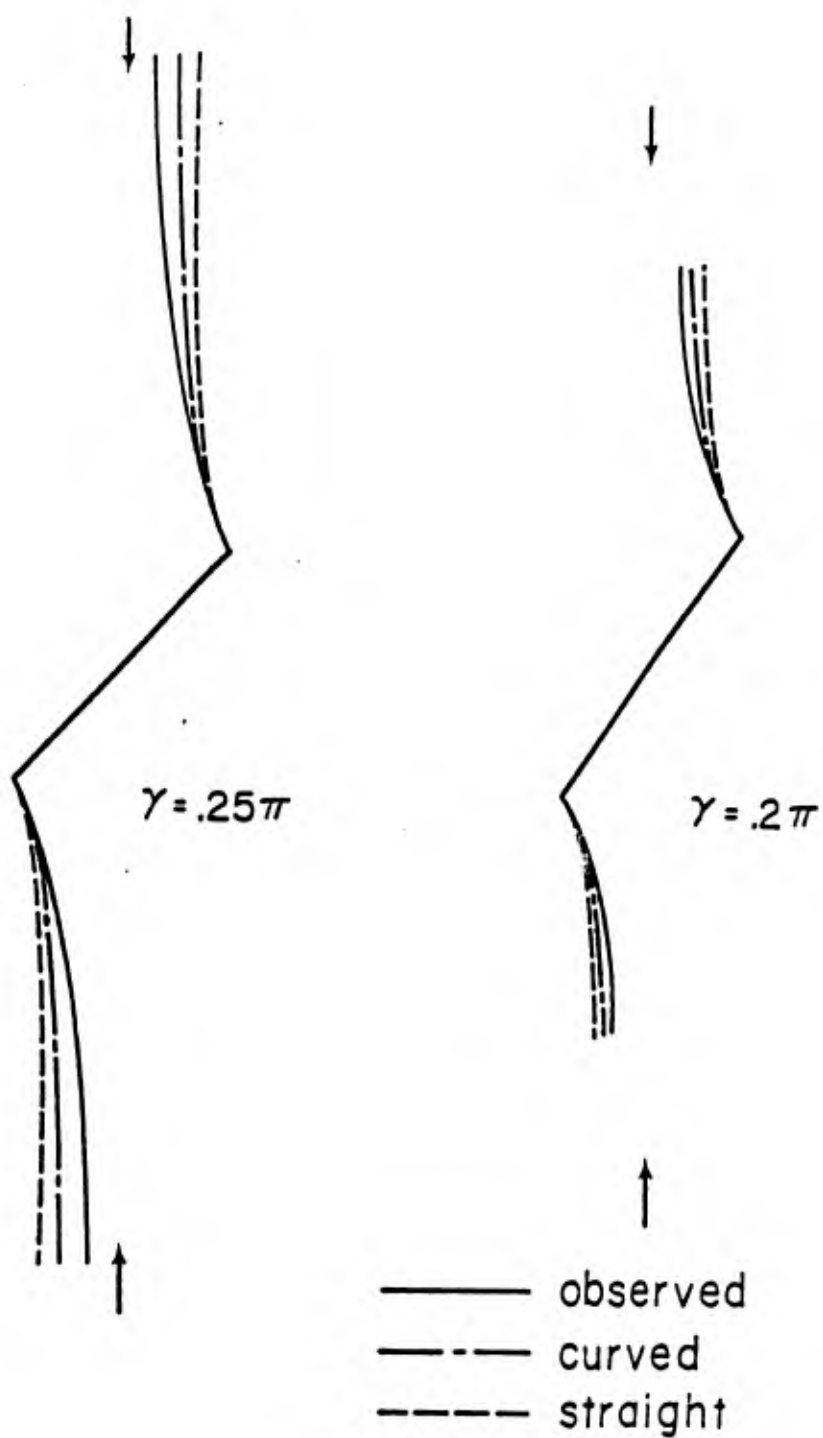


Figure 3

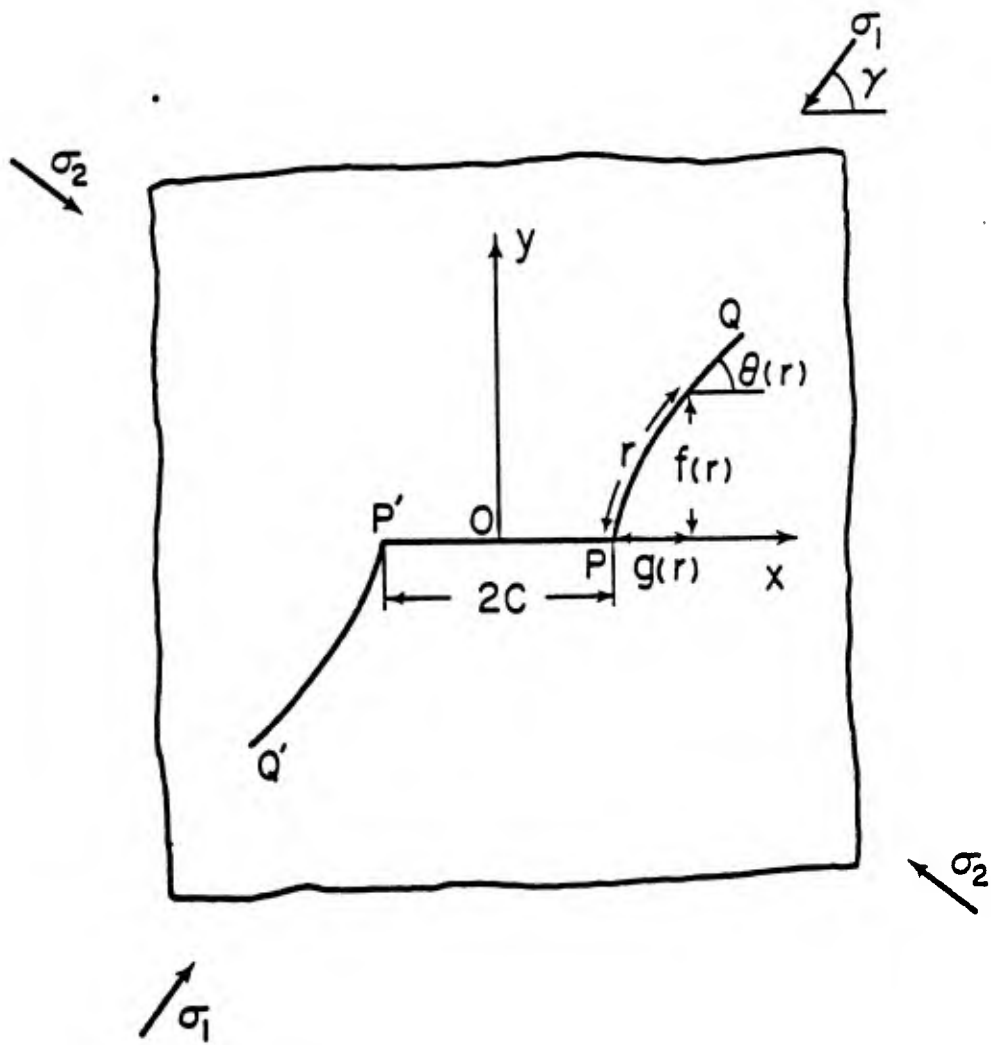


Figure 4

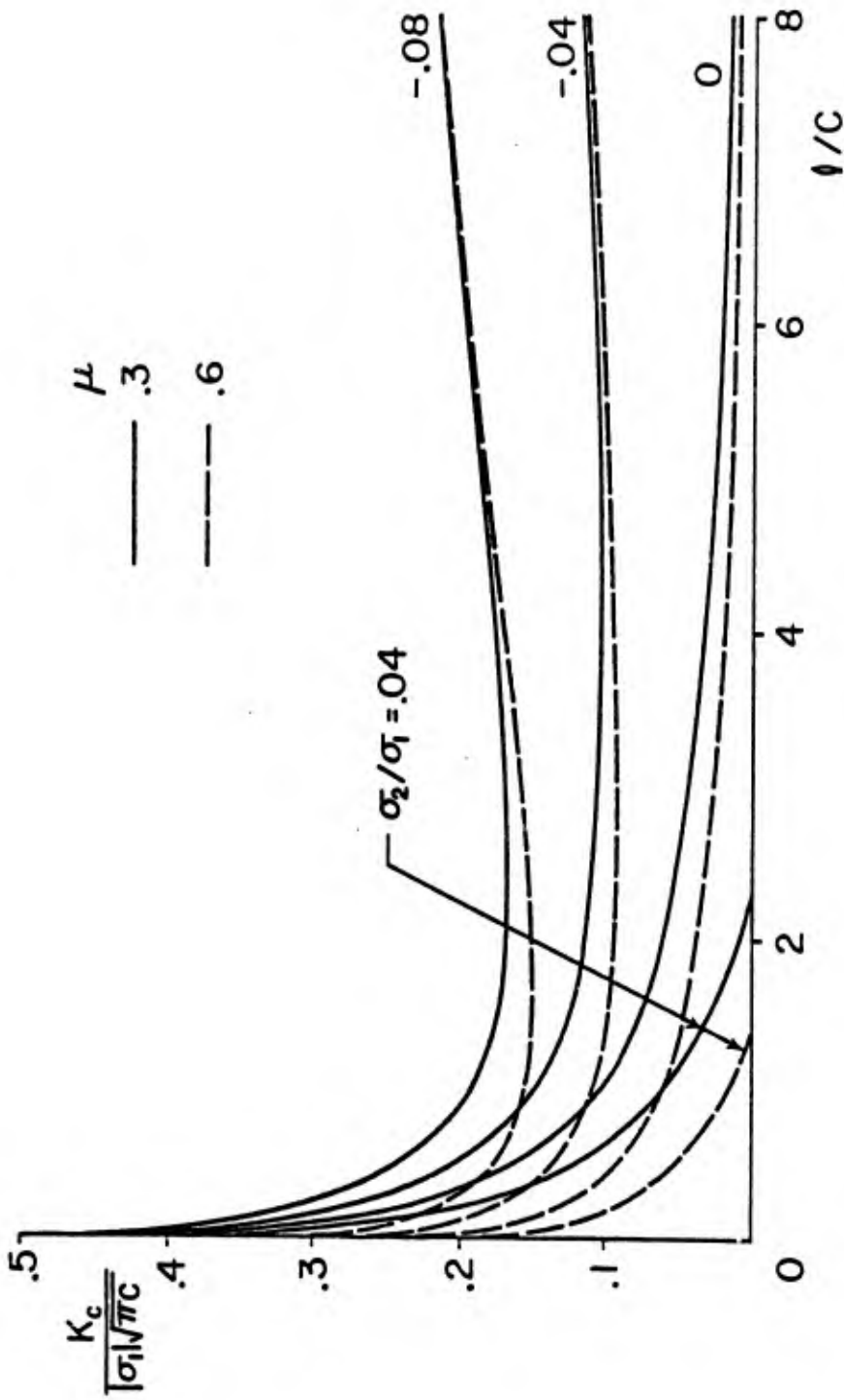


Figure 5a

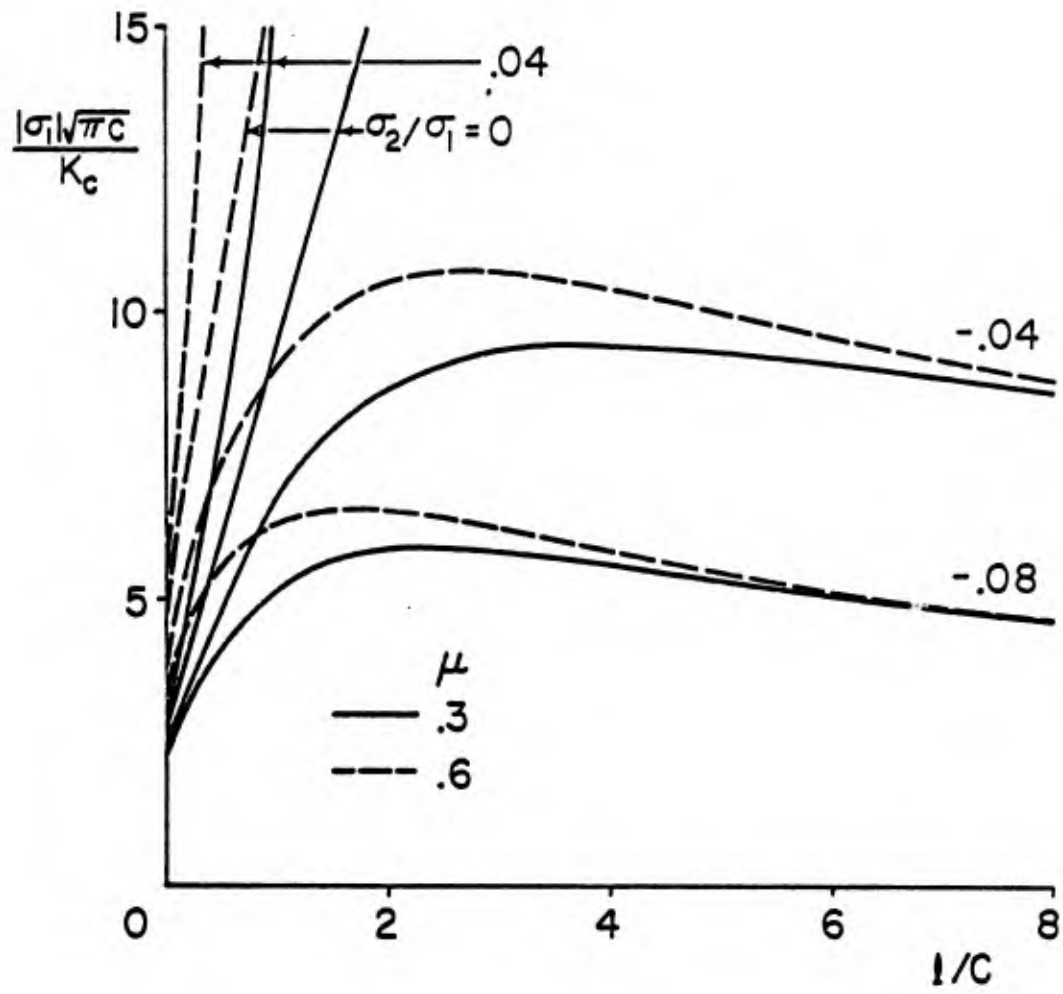


Figure 5b

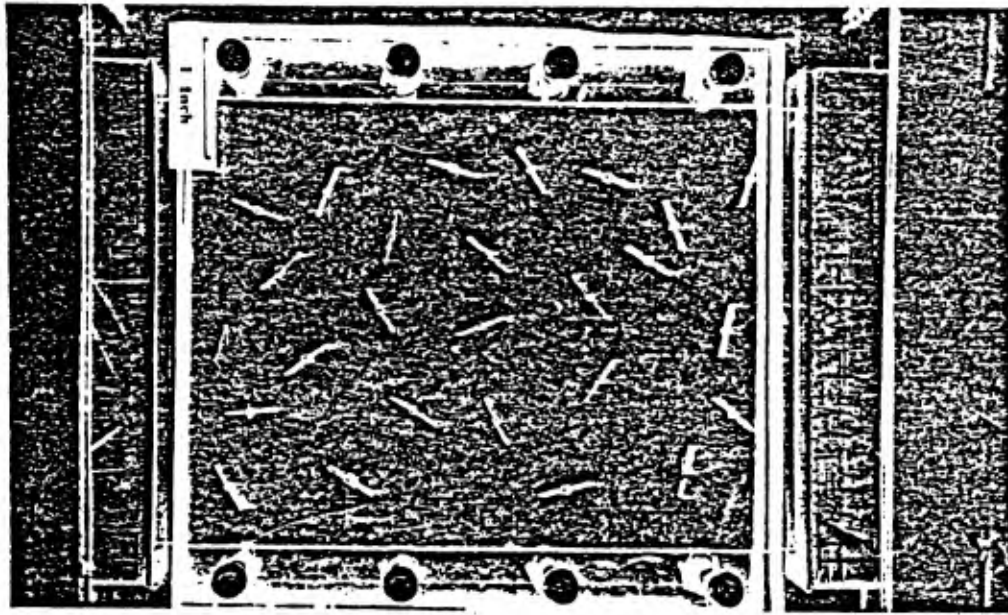


Figure 6a

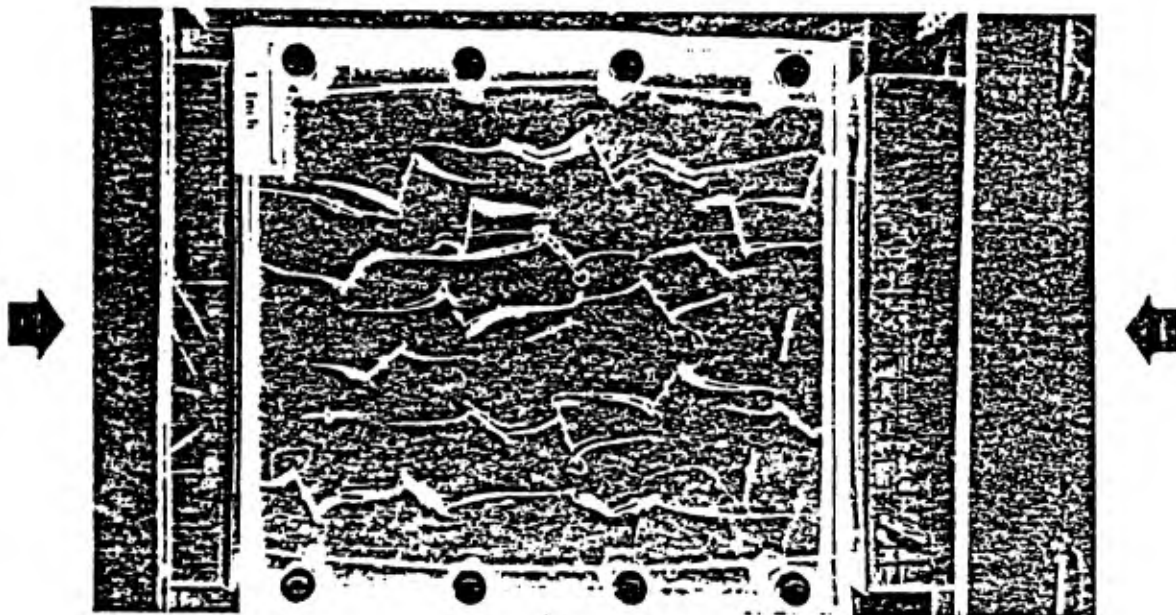


Figure 6b

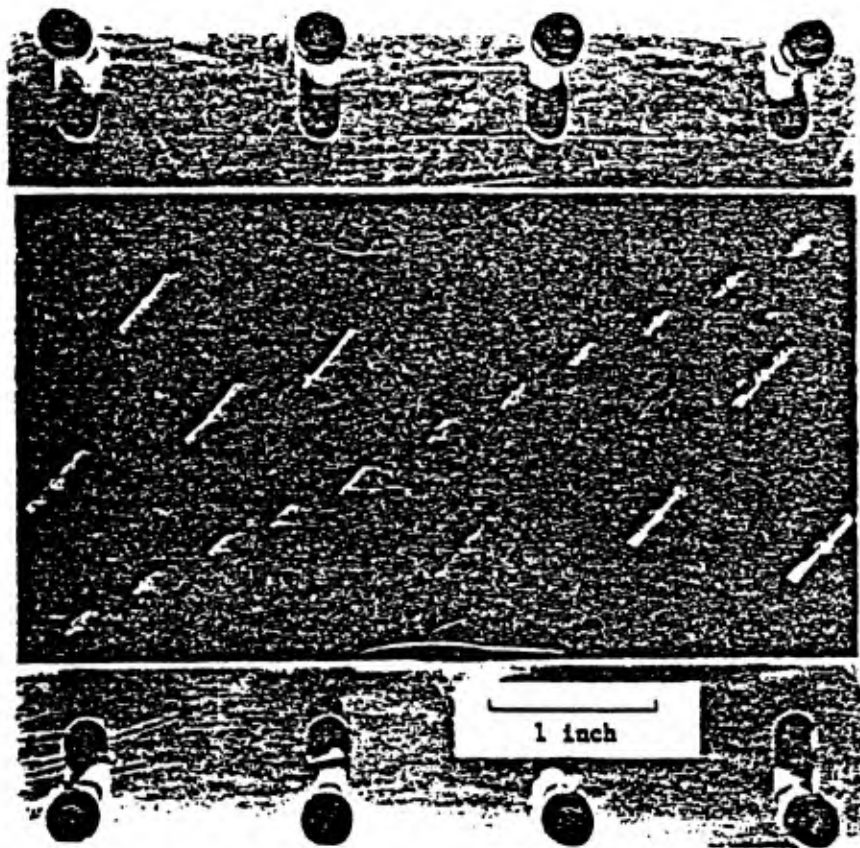


Figure 7a

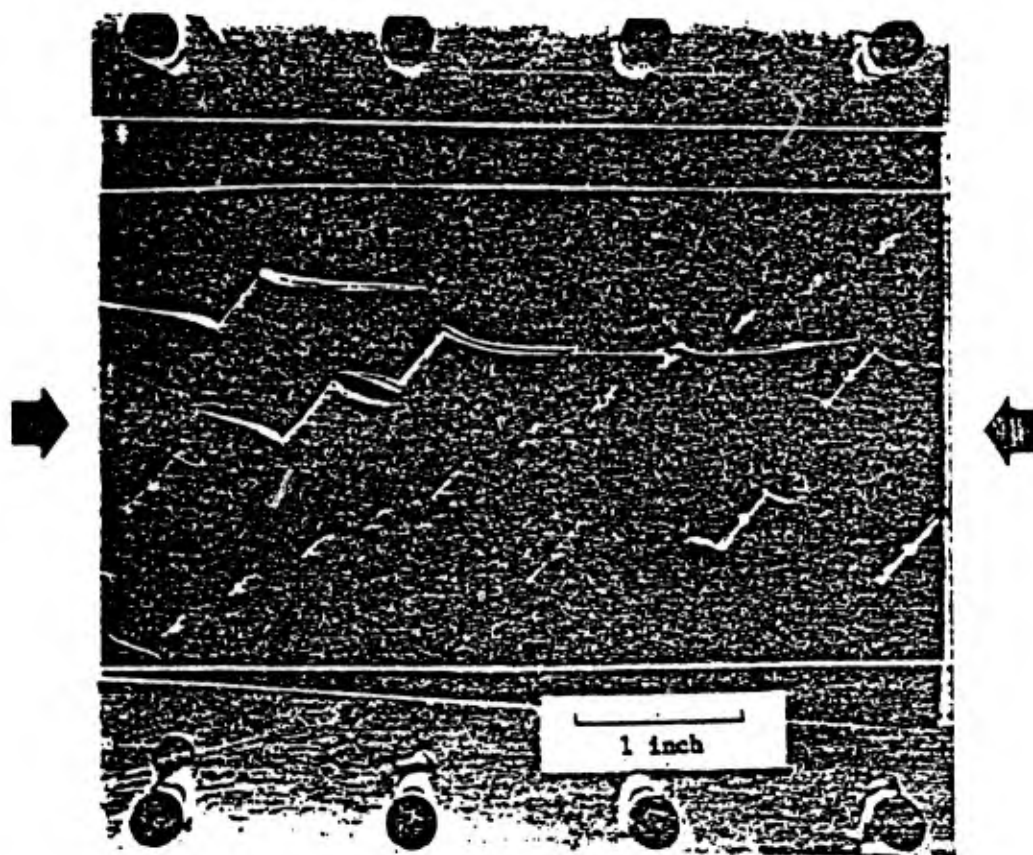


Figure 7b

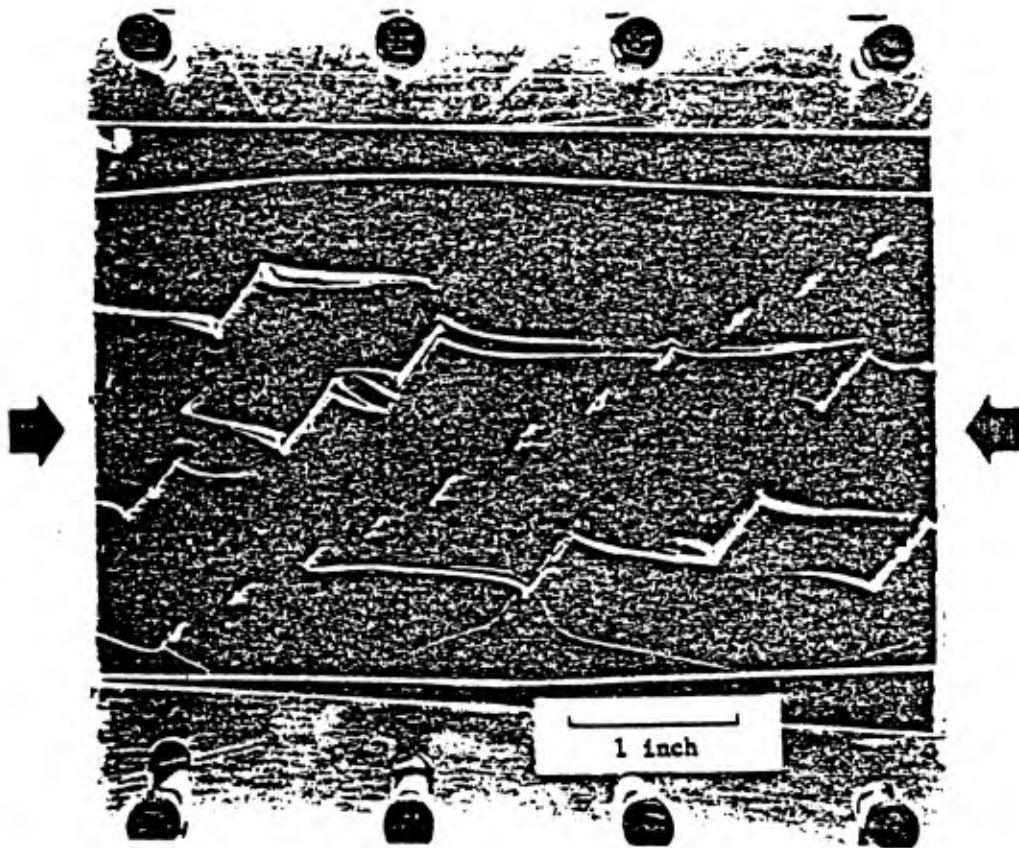


Figure 7c

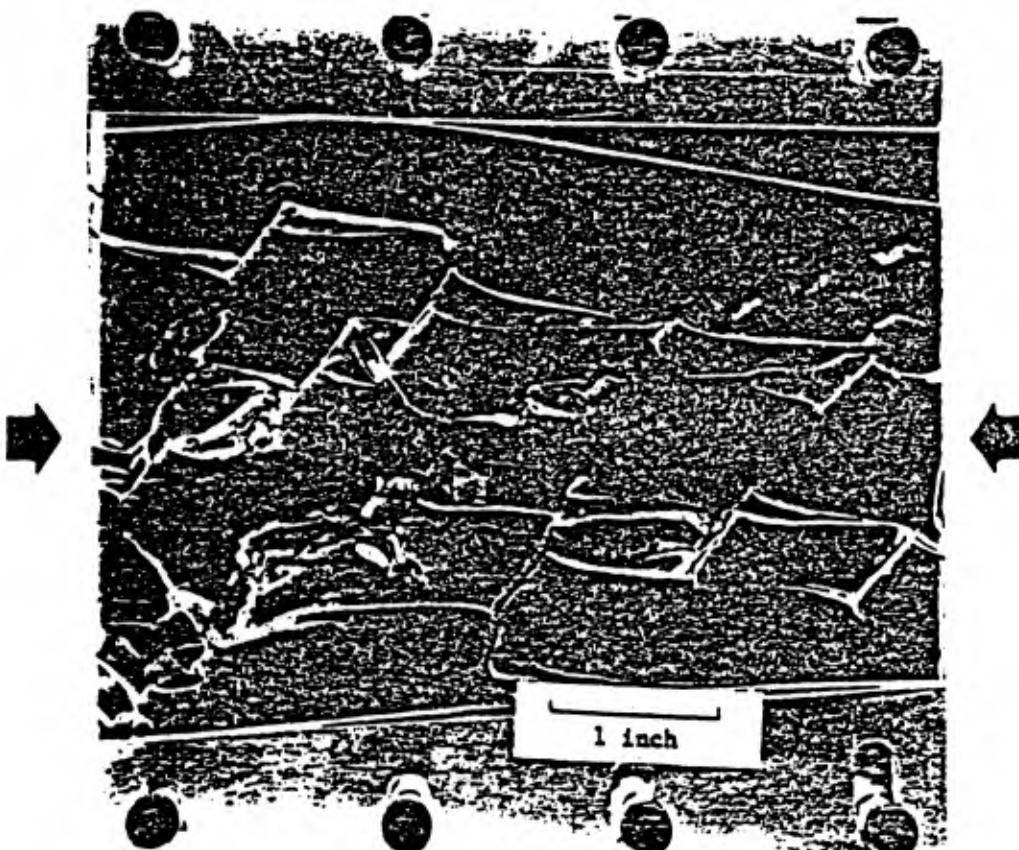


Figure 7d

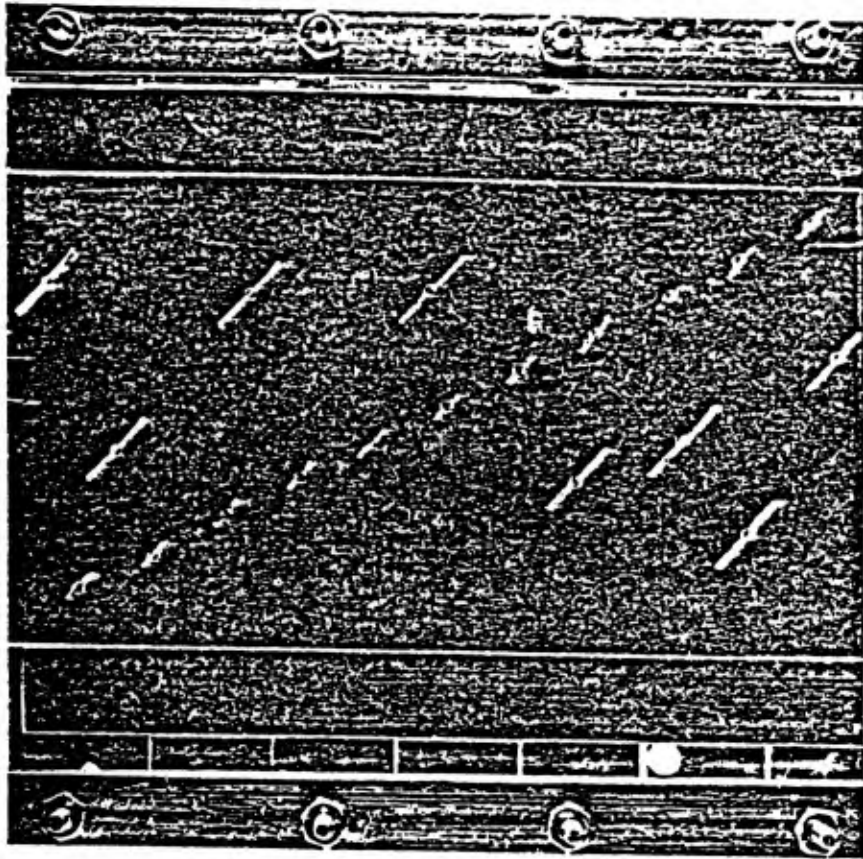


Figure 8a

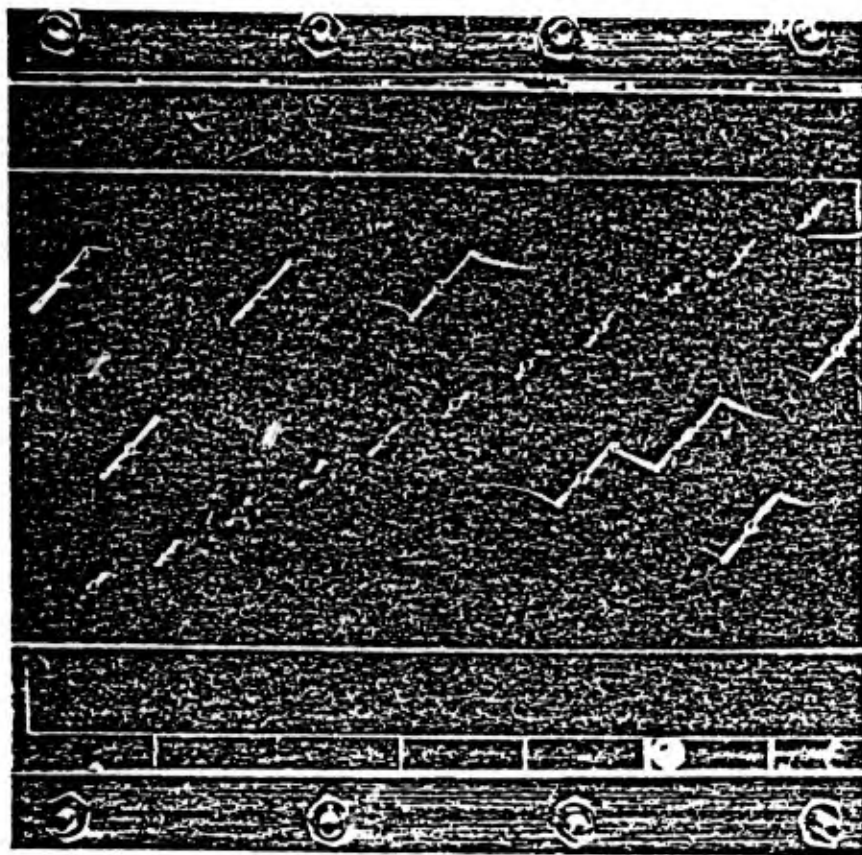


Figure 8b

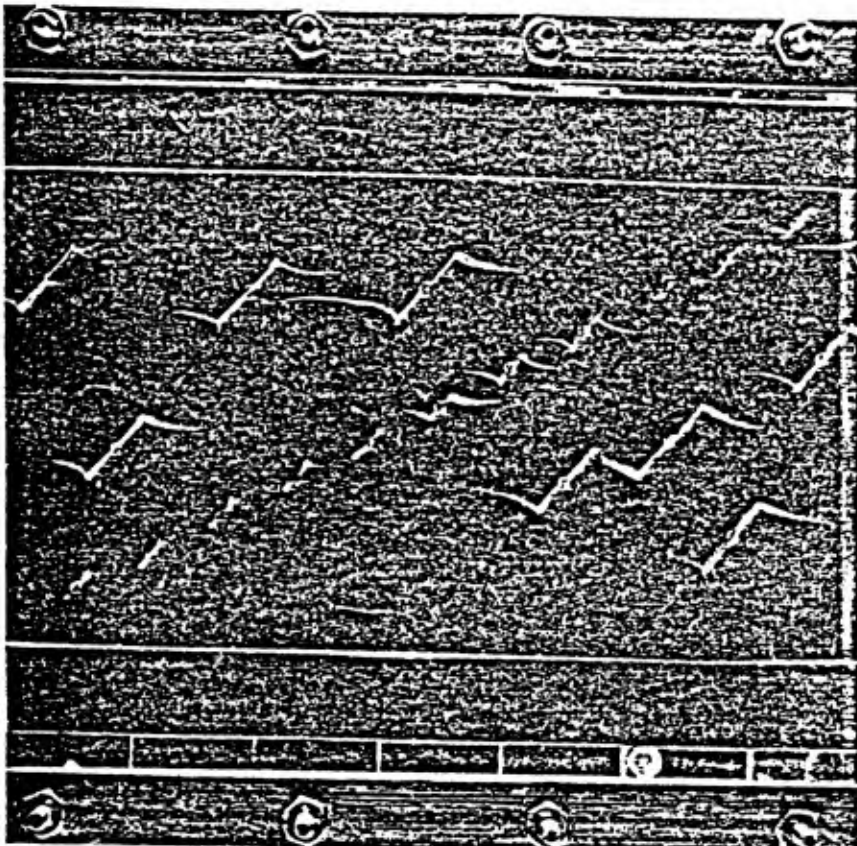


Figure 8c

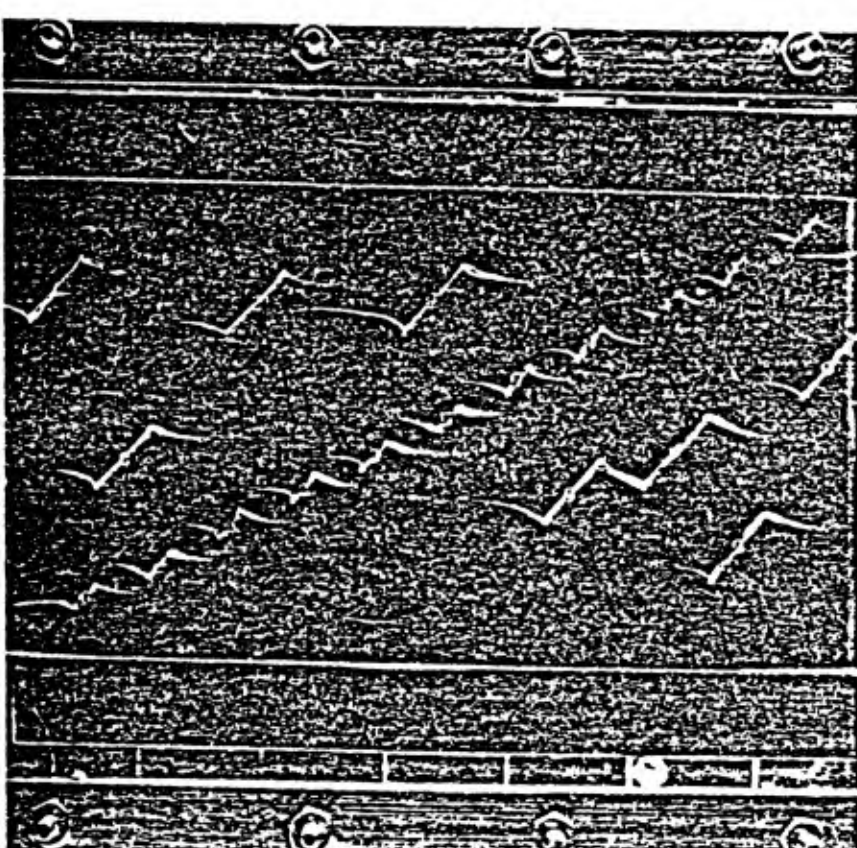


Figure 8d

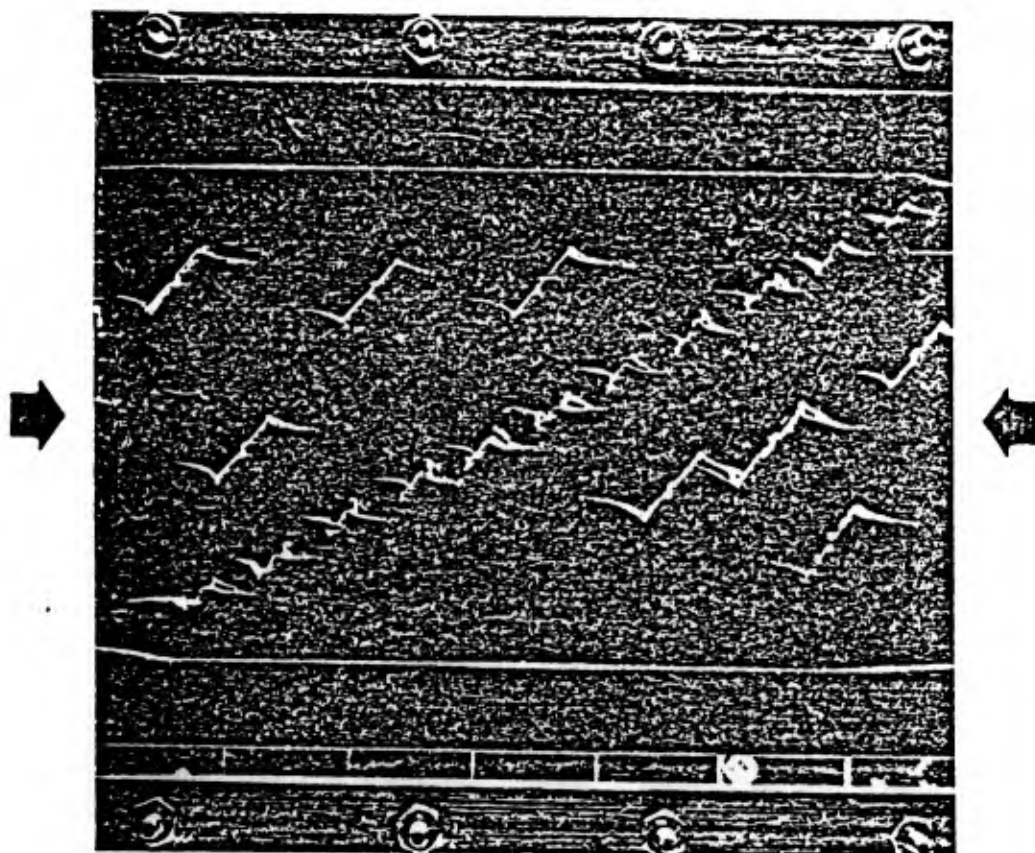


Figure 8e

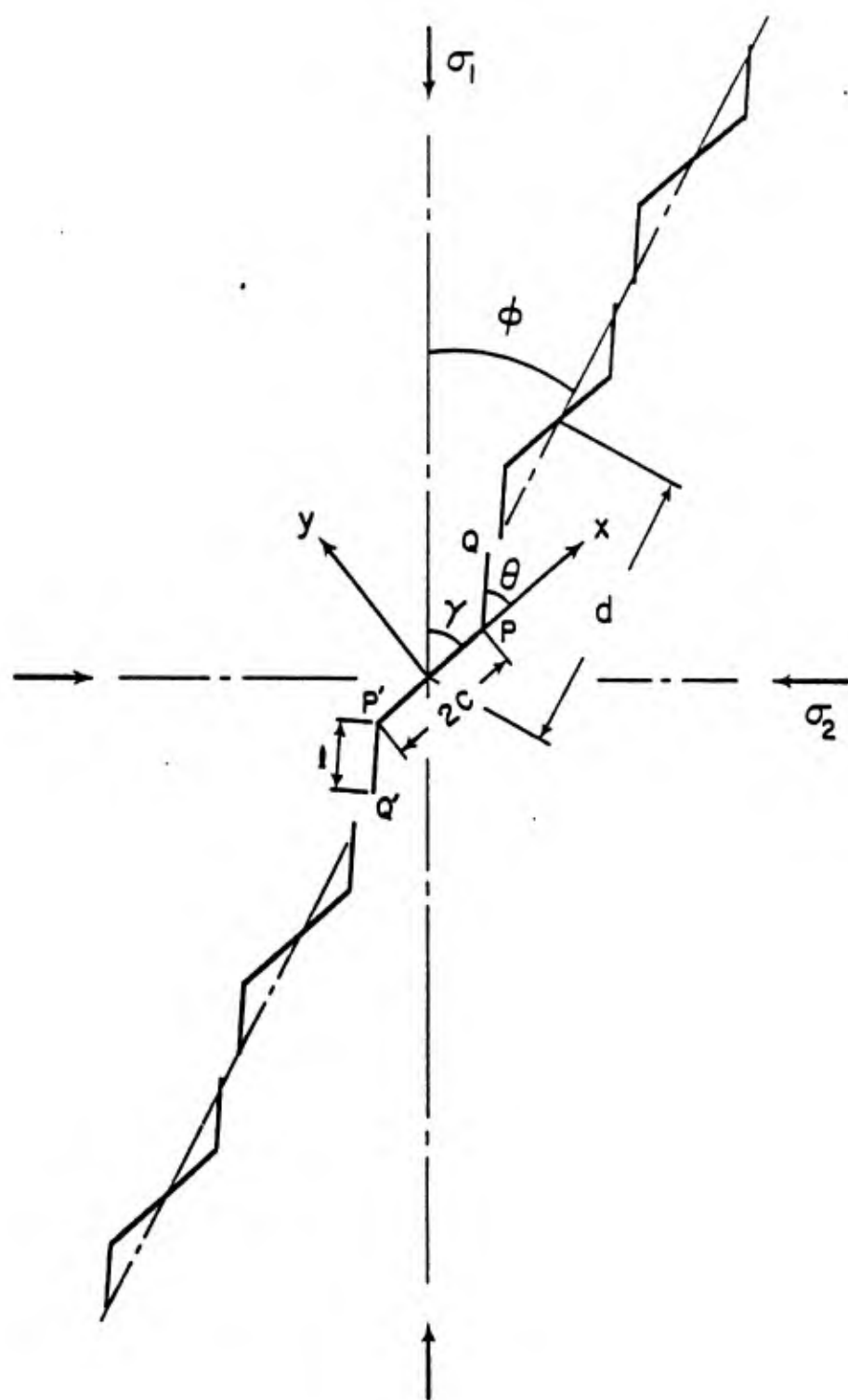


Figure 9

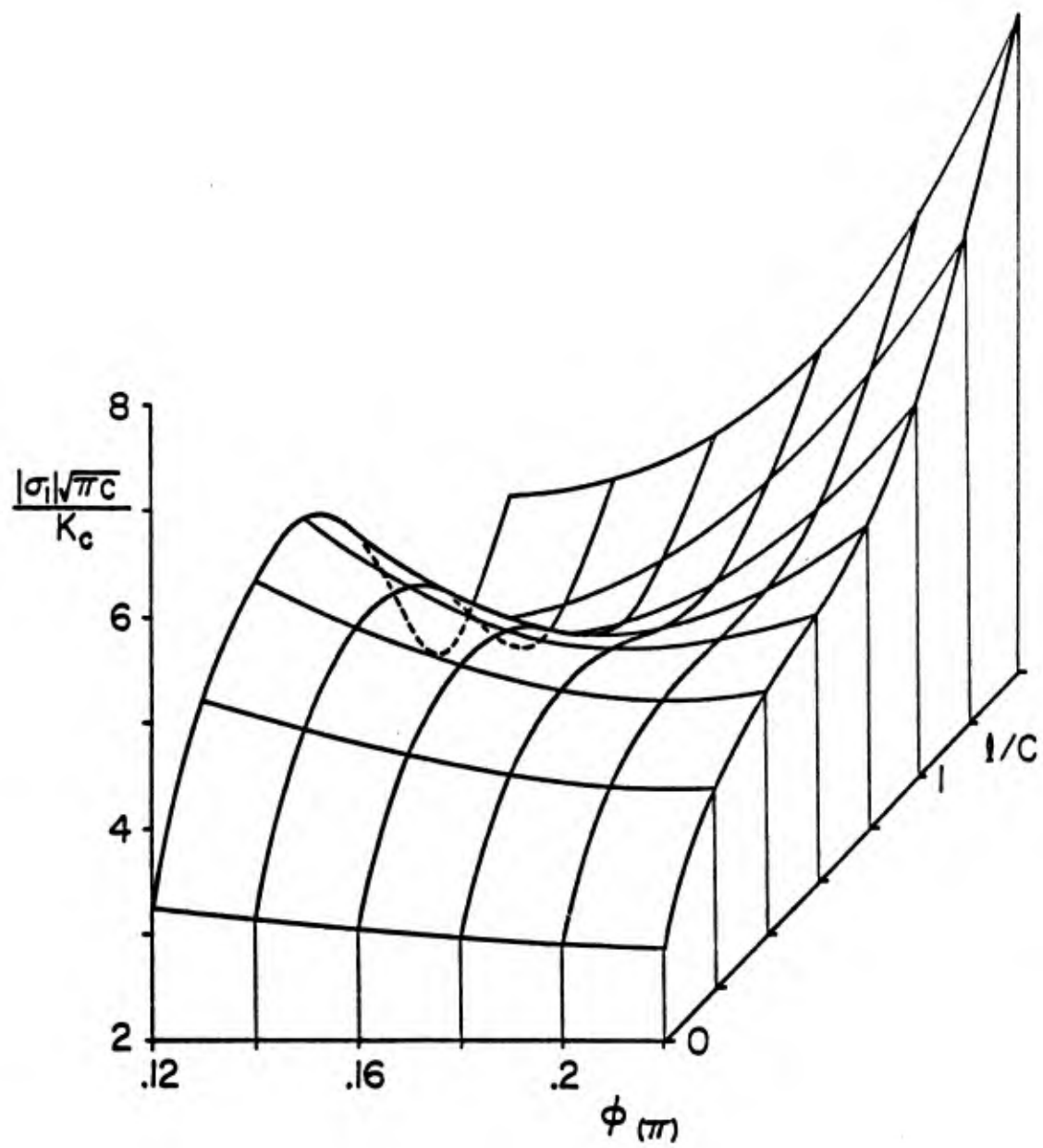


Figure 10

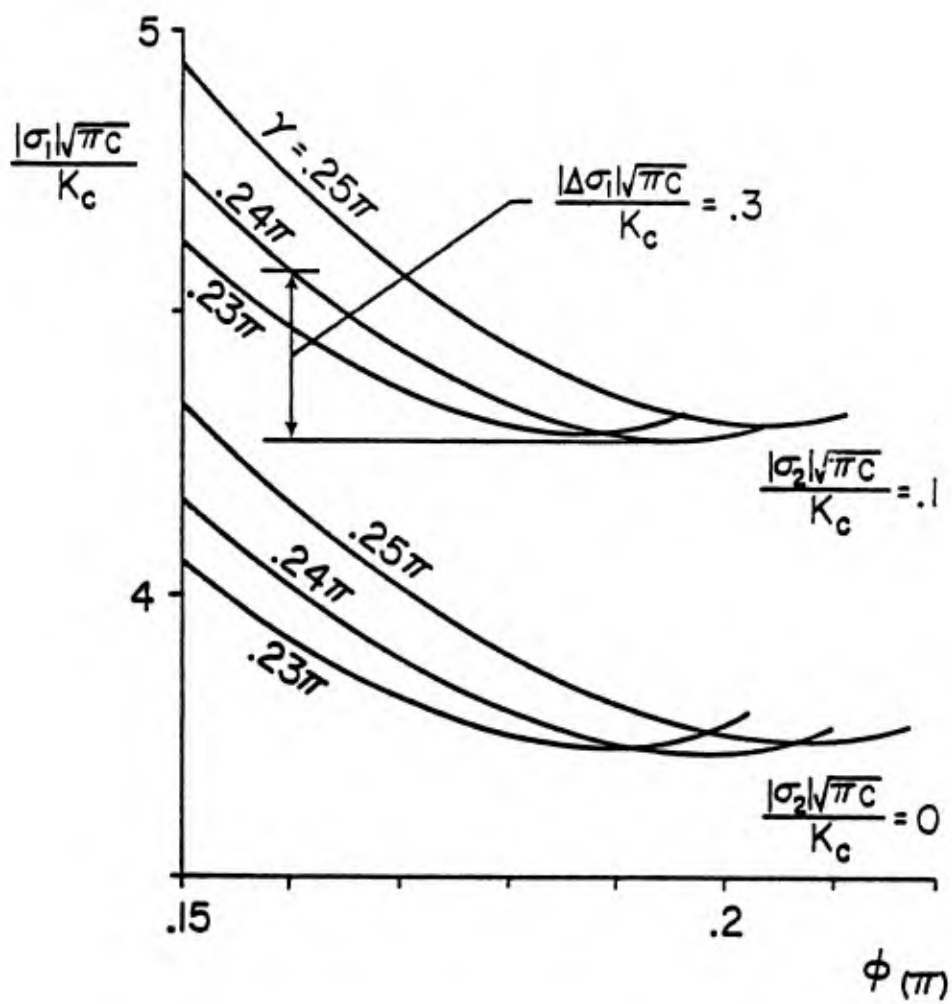


Figure 11

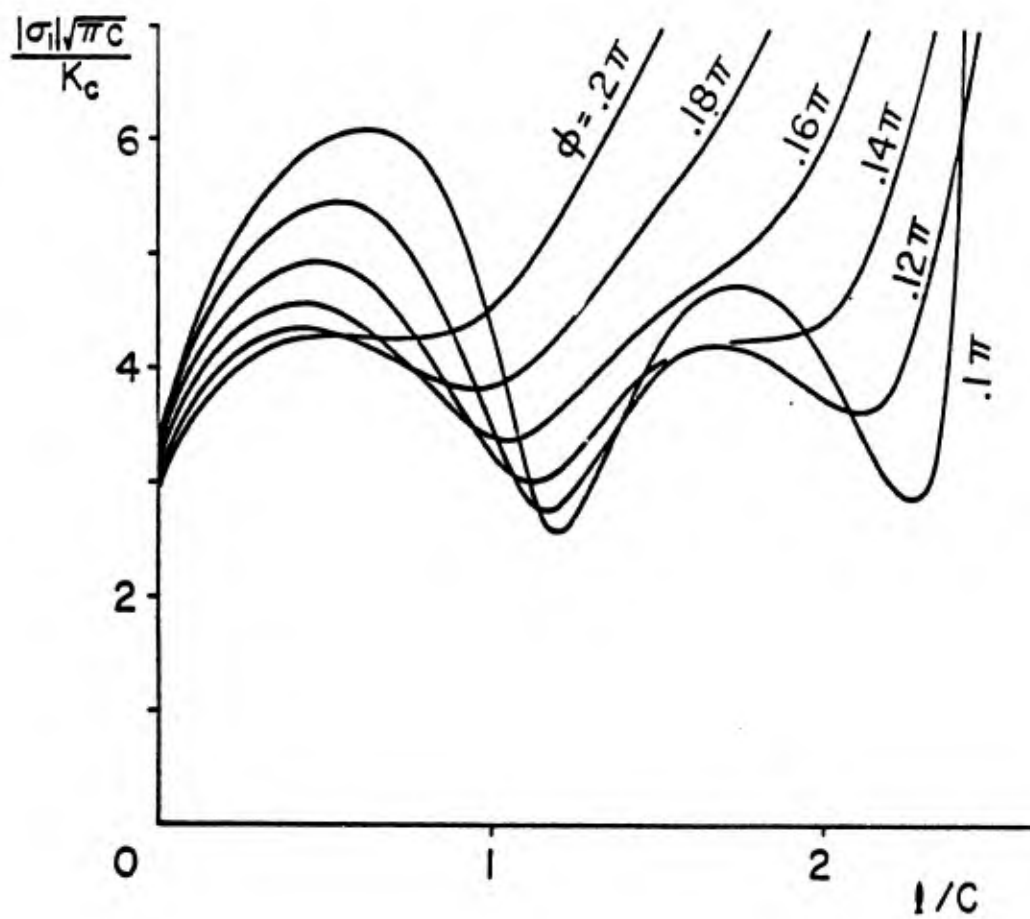


Figure 12

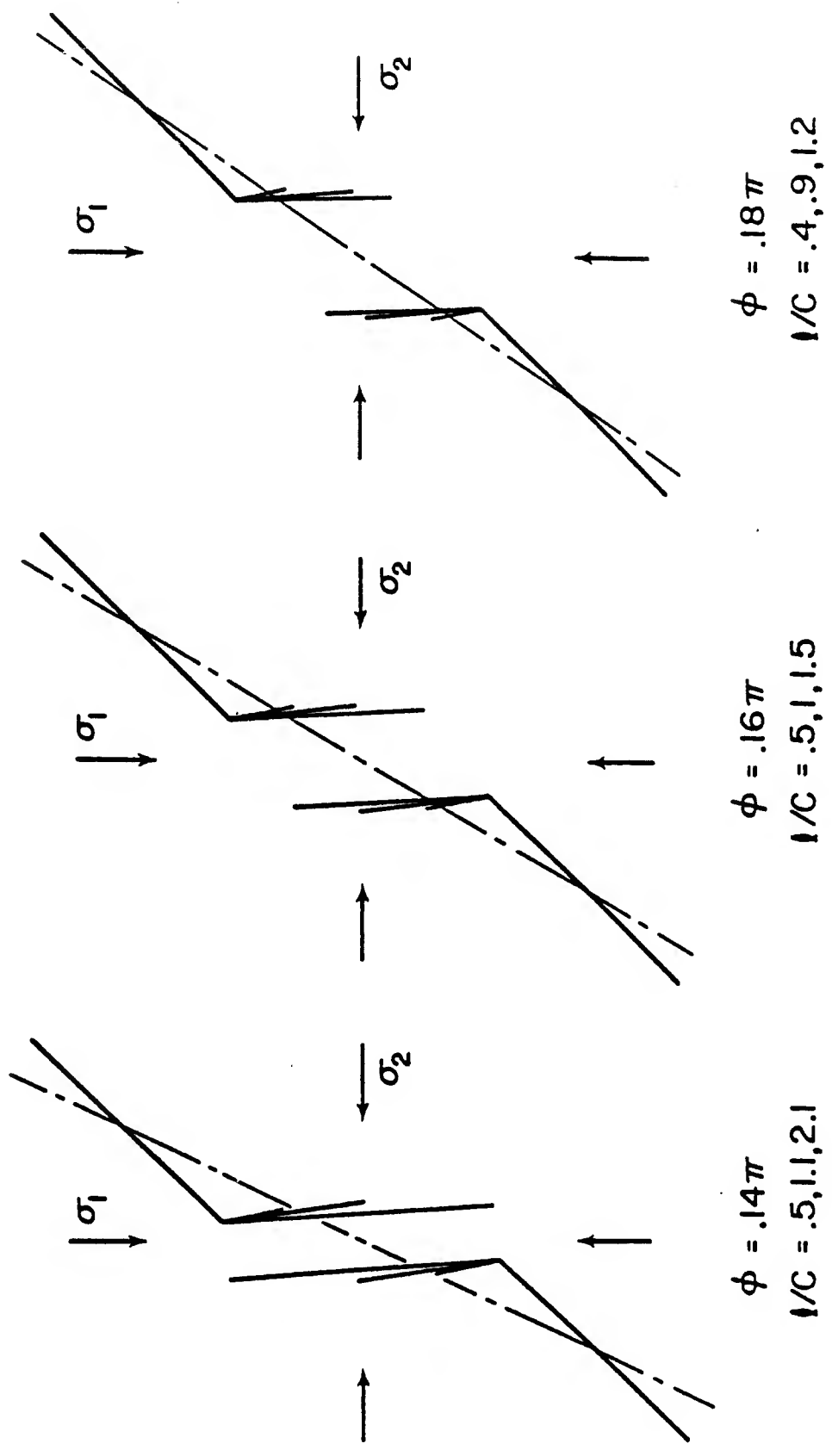


Figure 13

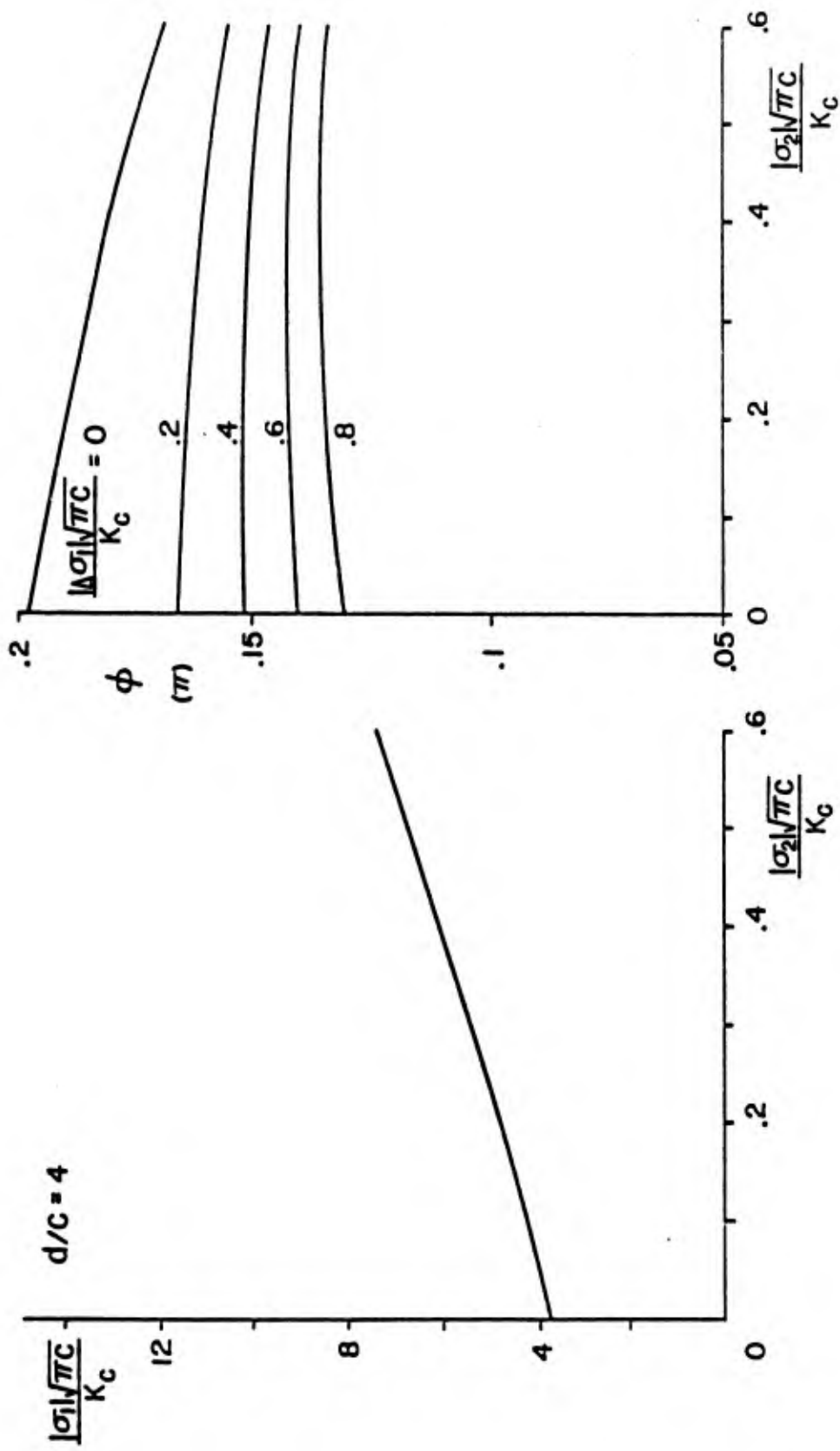


Figure 14

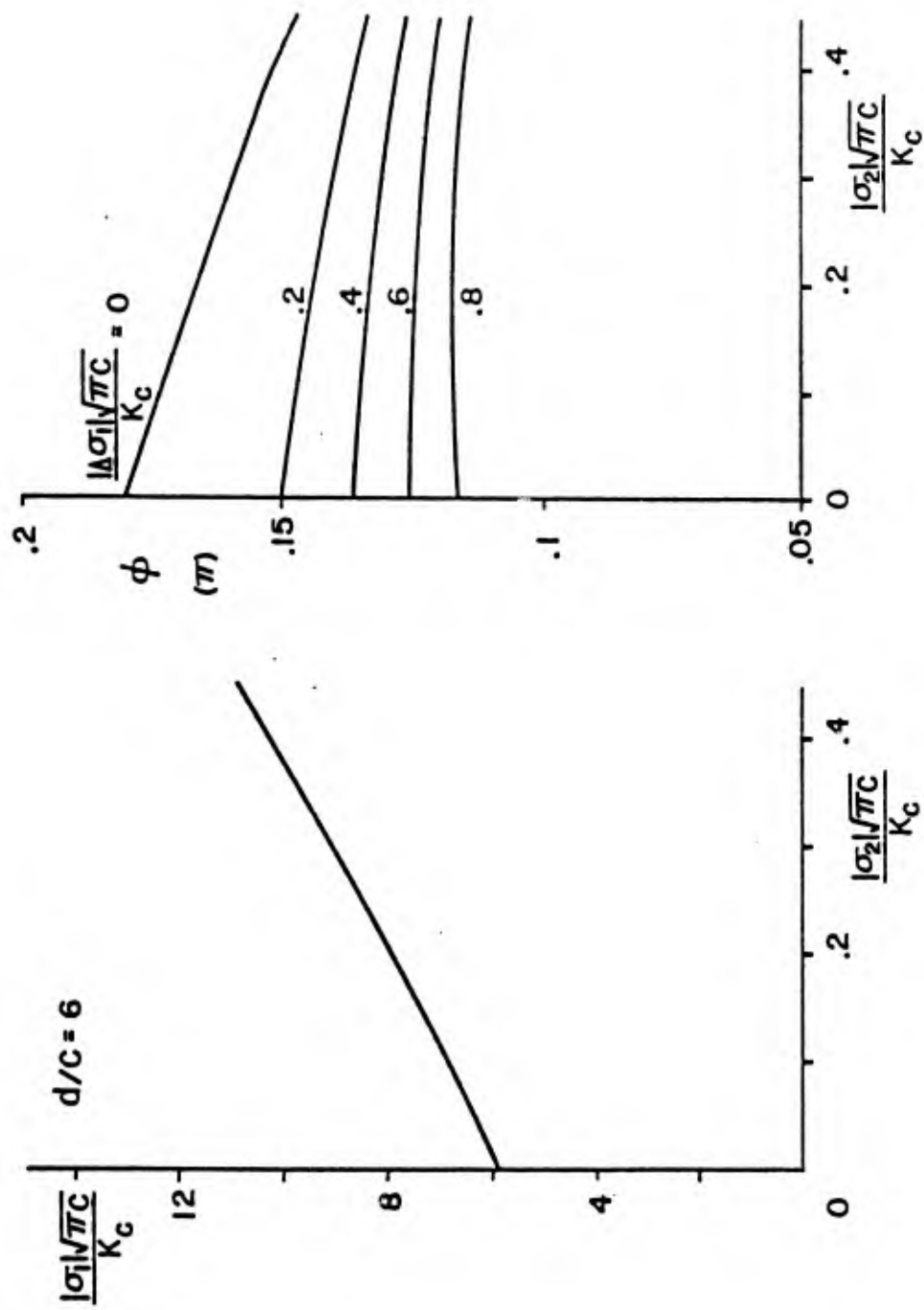


Figure 15

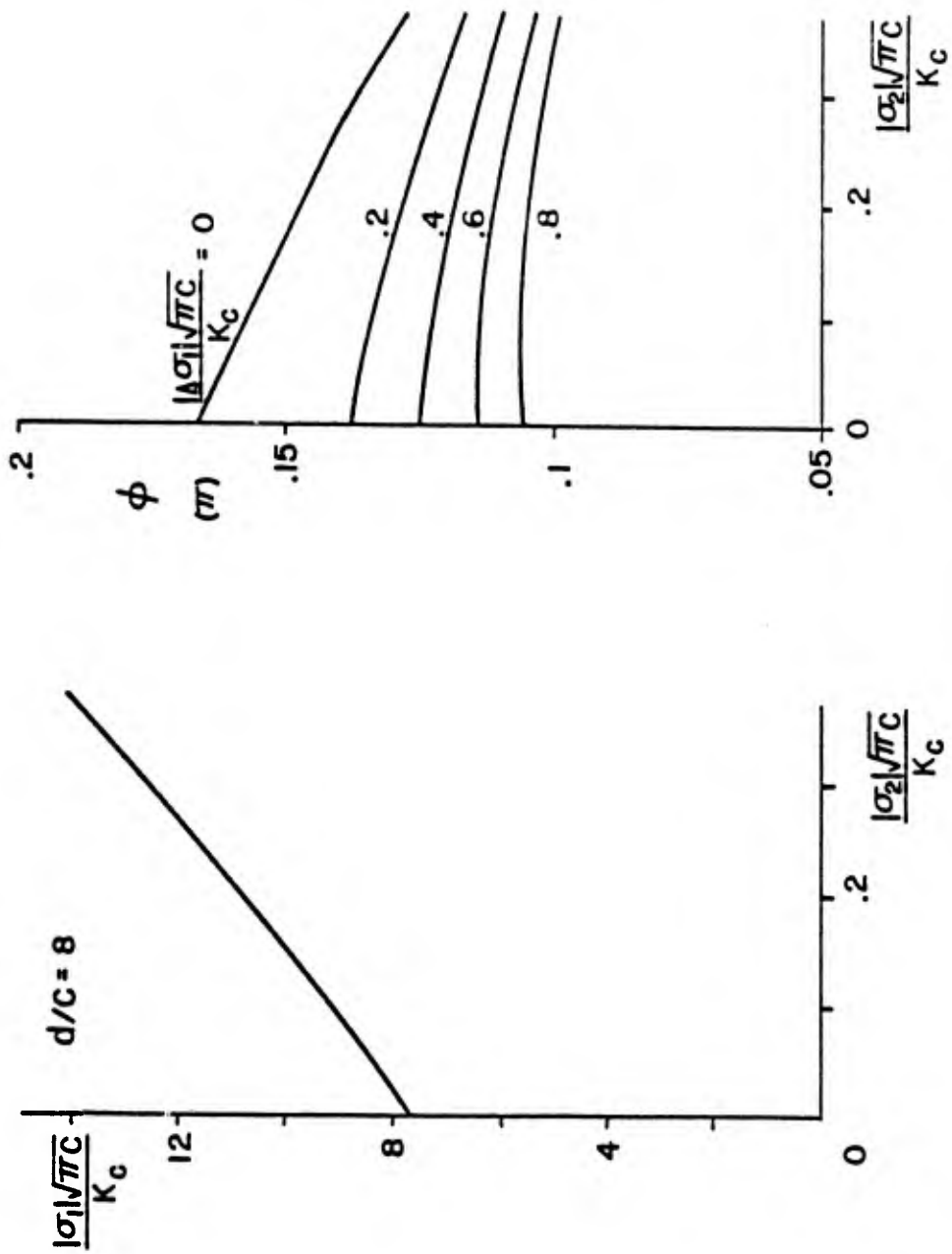


Figure 16

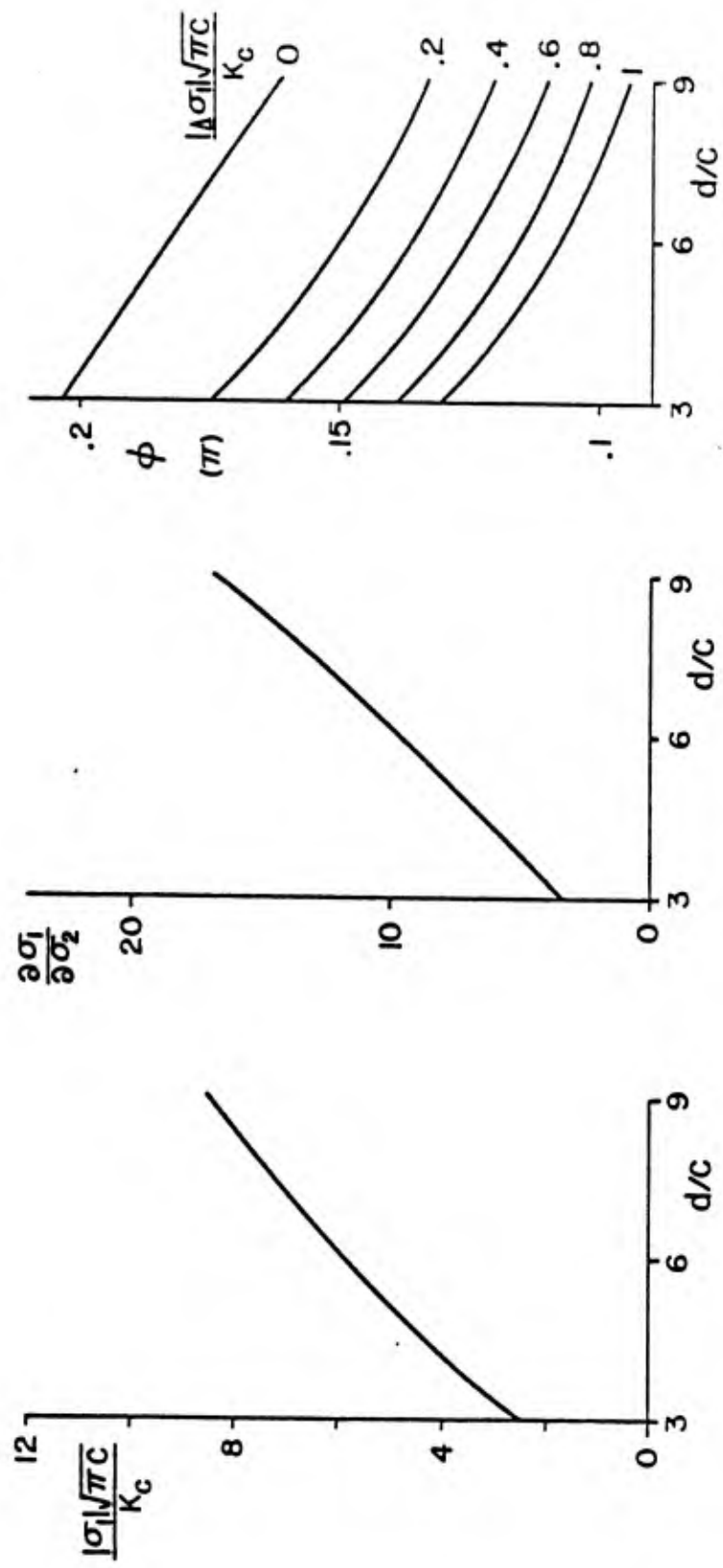


Figure 17

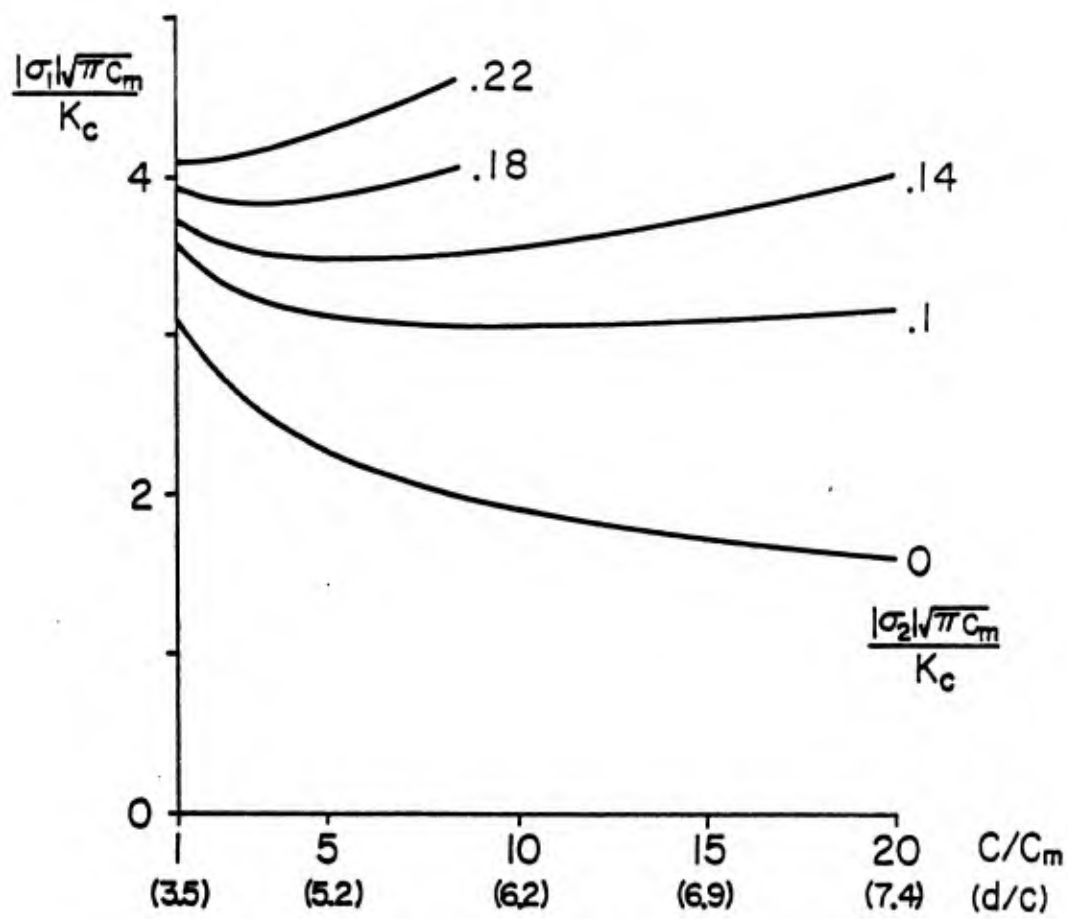


Figure 18

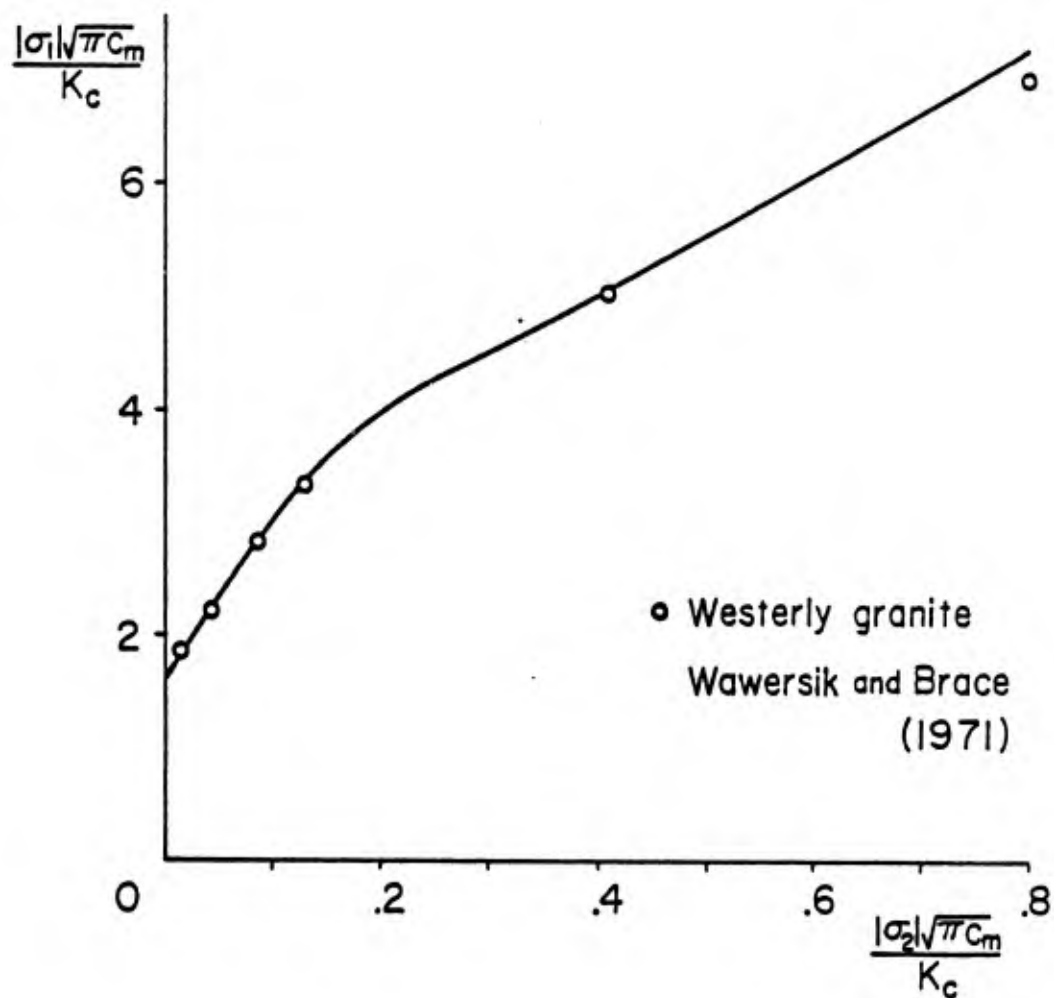


Figure 19a

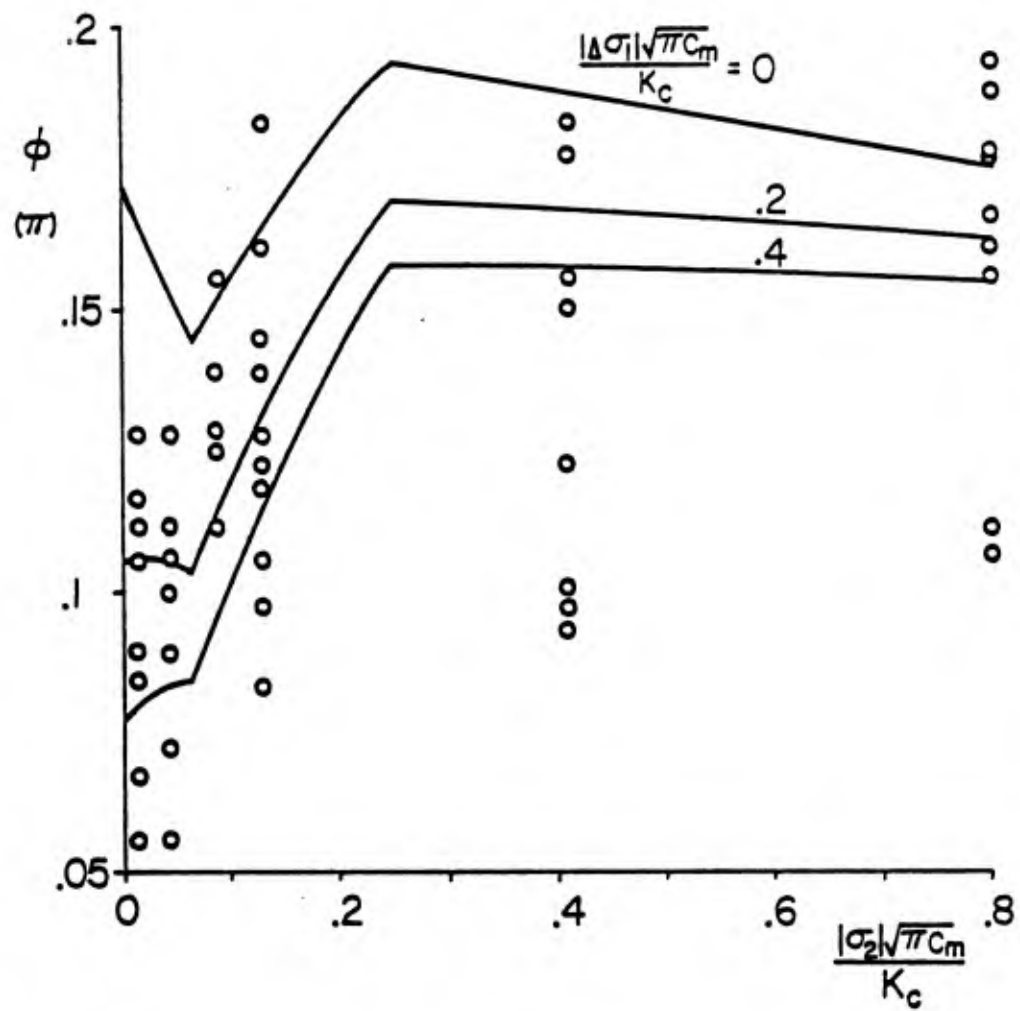


Figure 19b

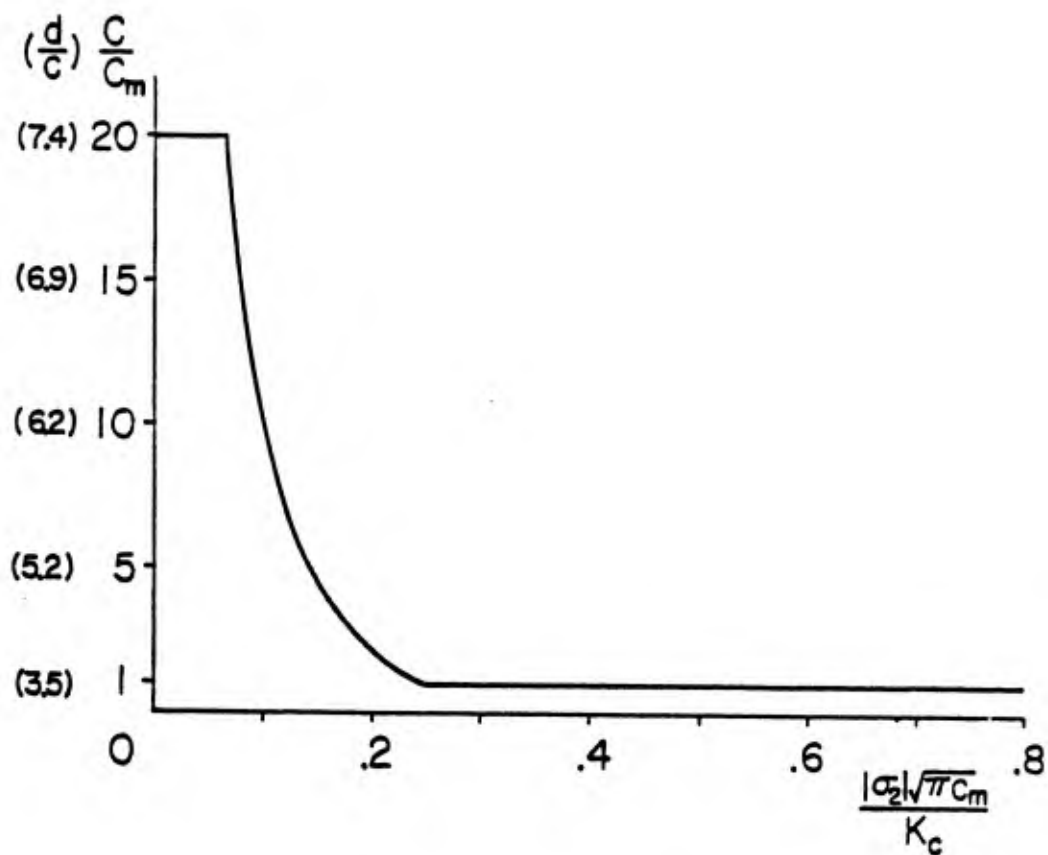


Figure 19c

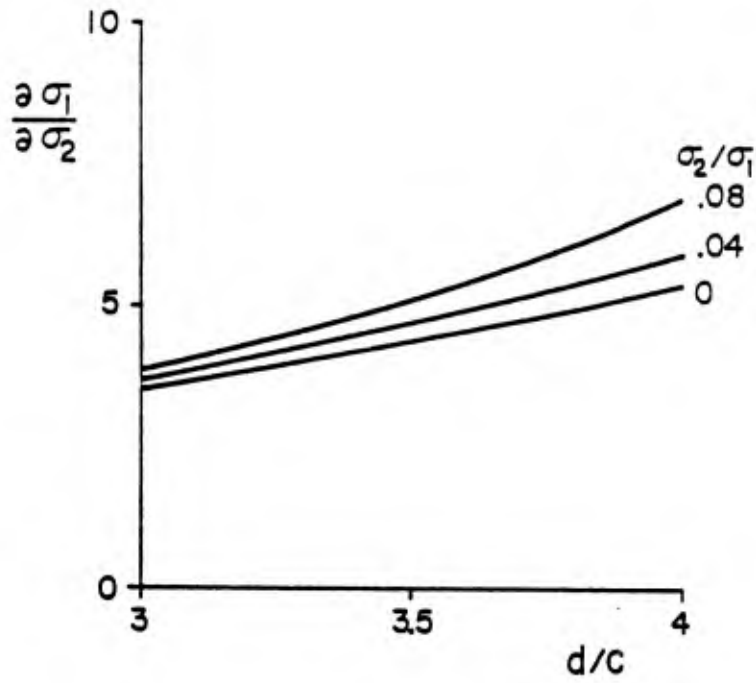


Figure 20a

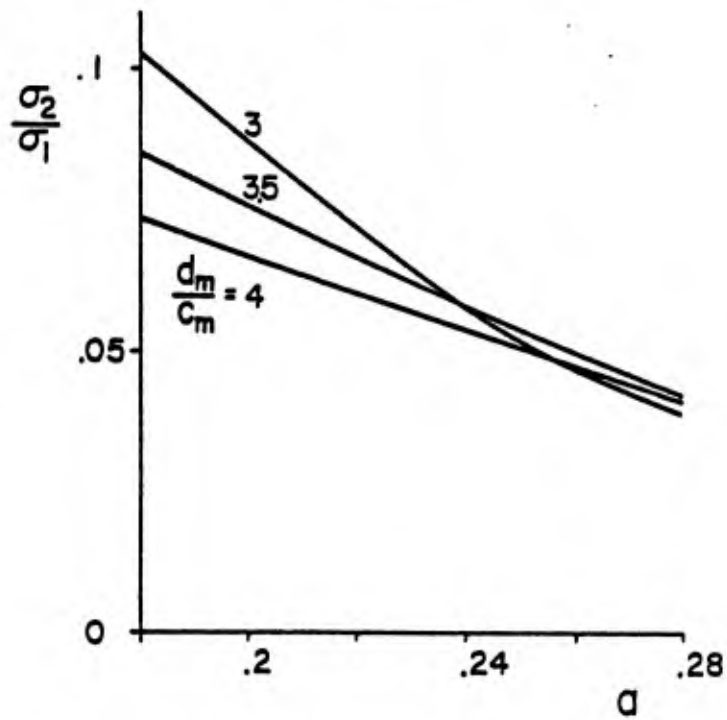


Figure 20b

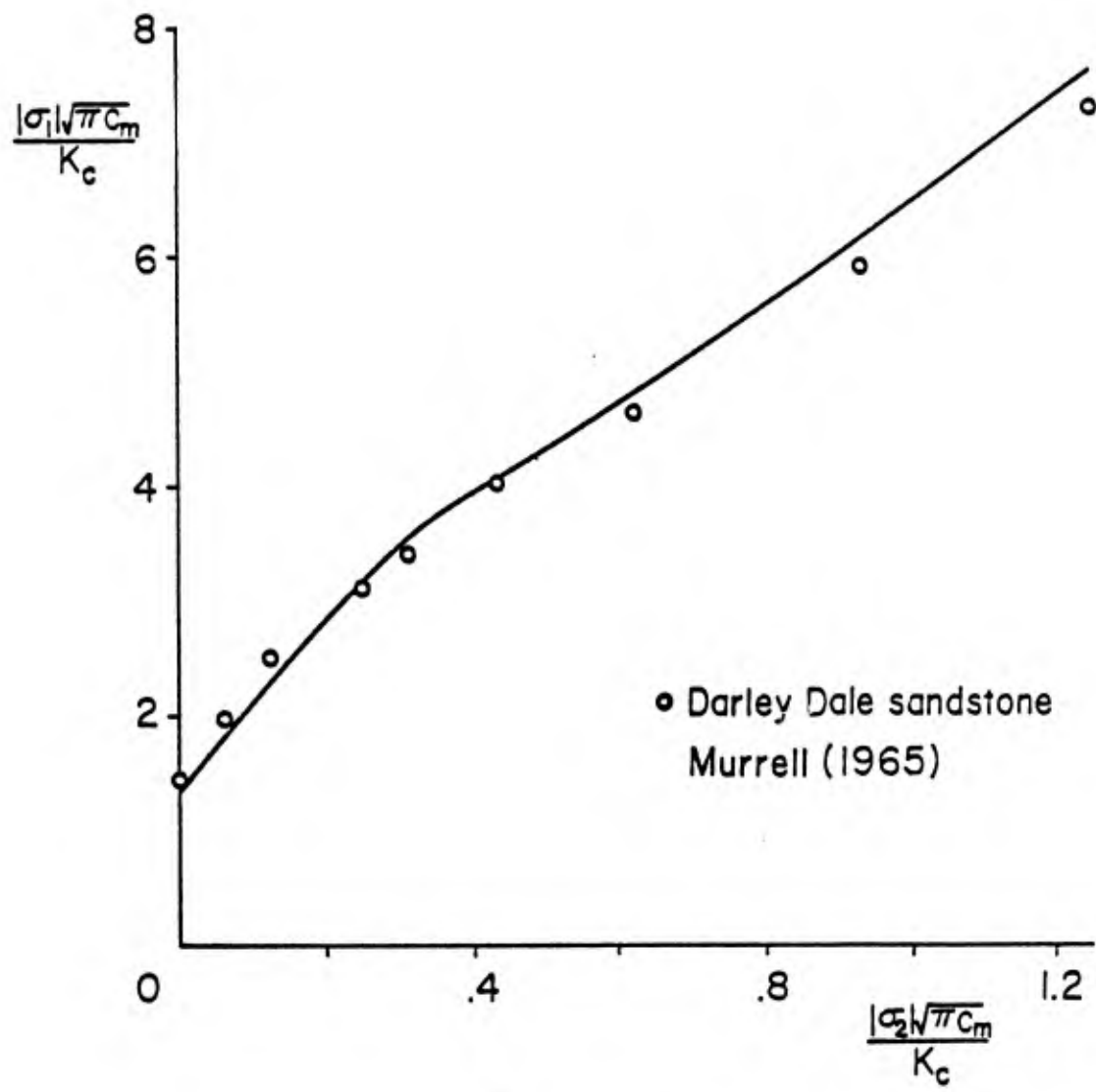


Figure 21a

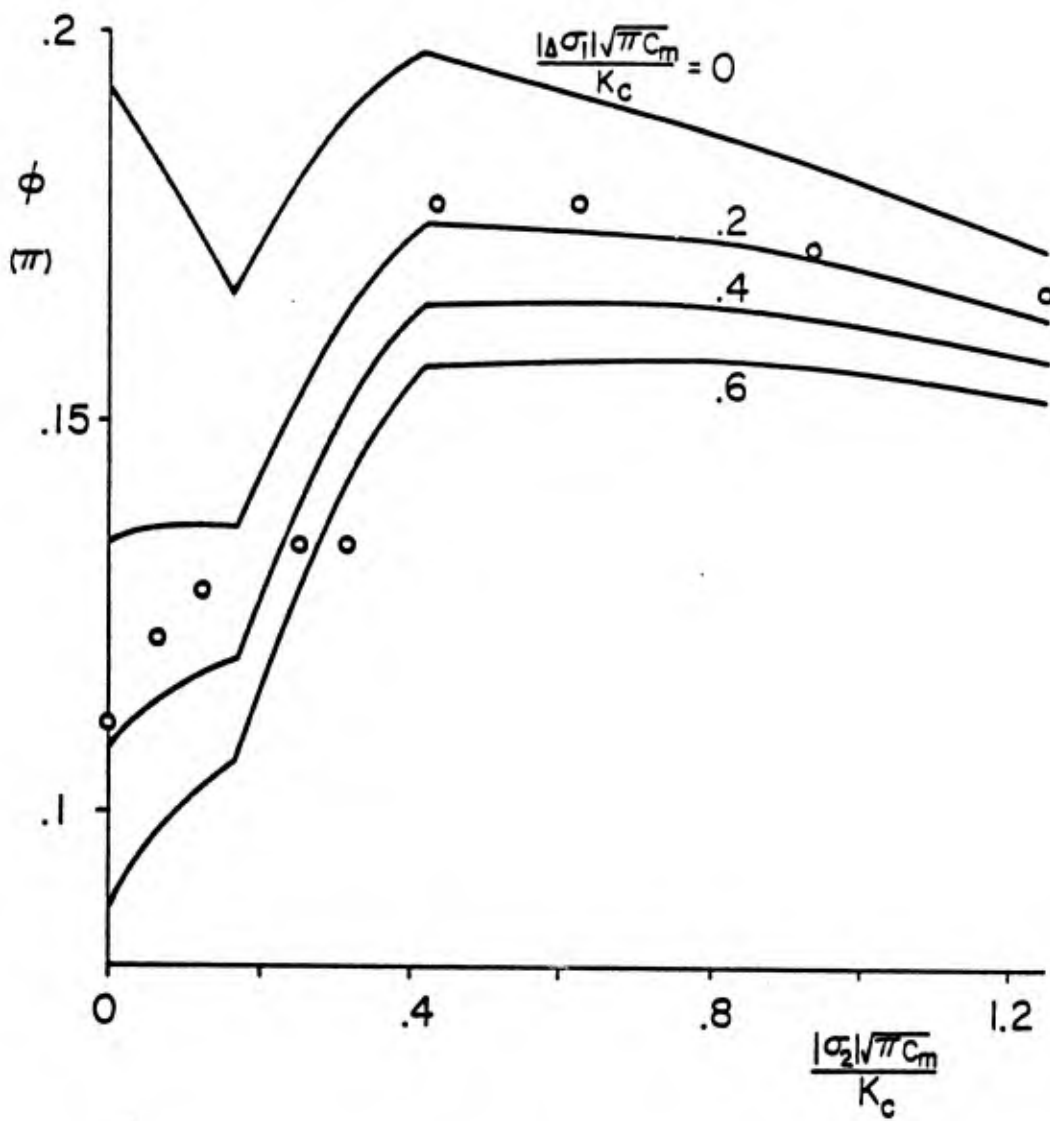


Figure 21b

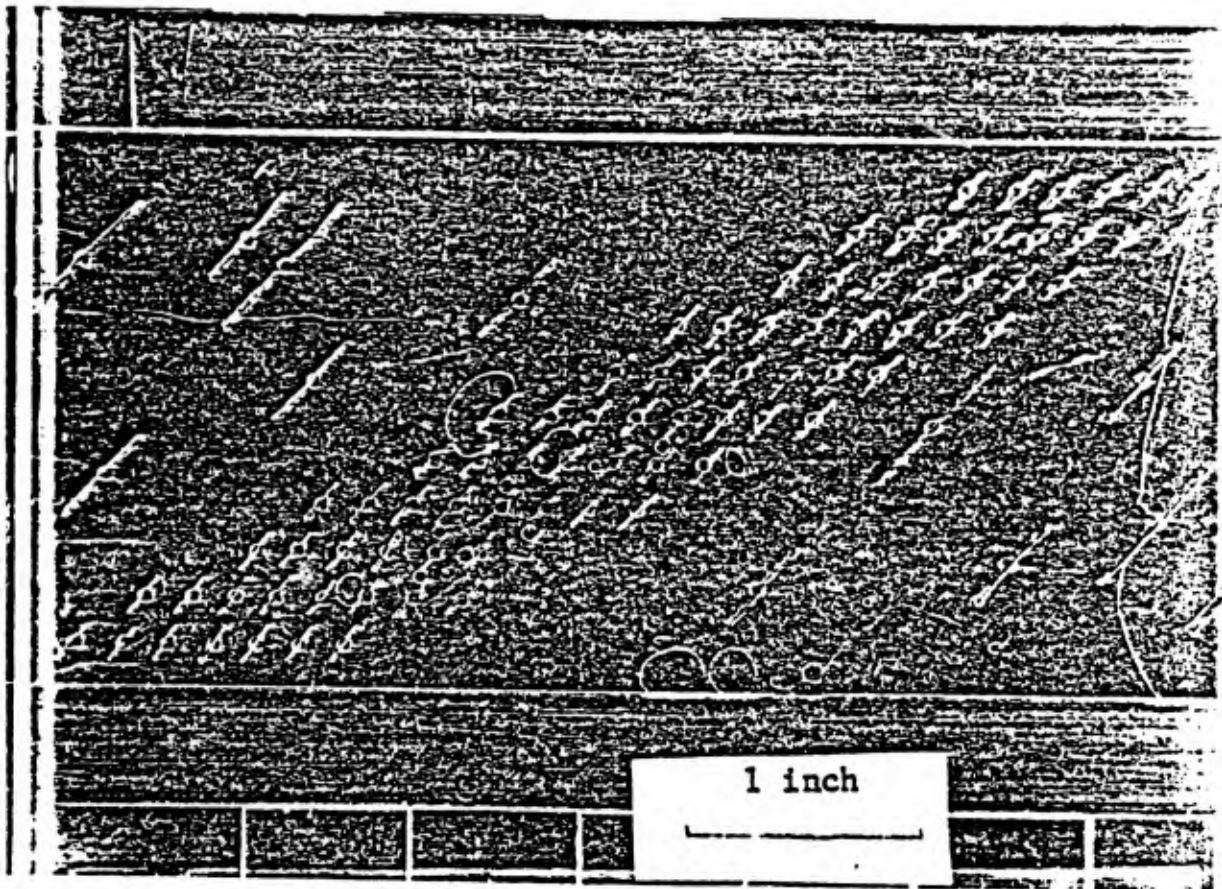


Figure 22a

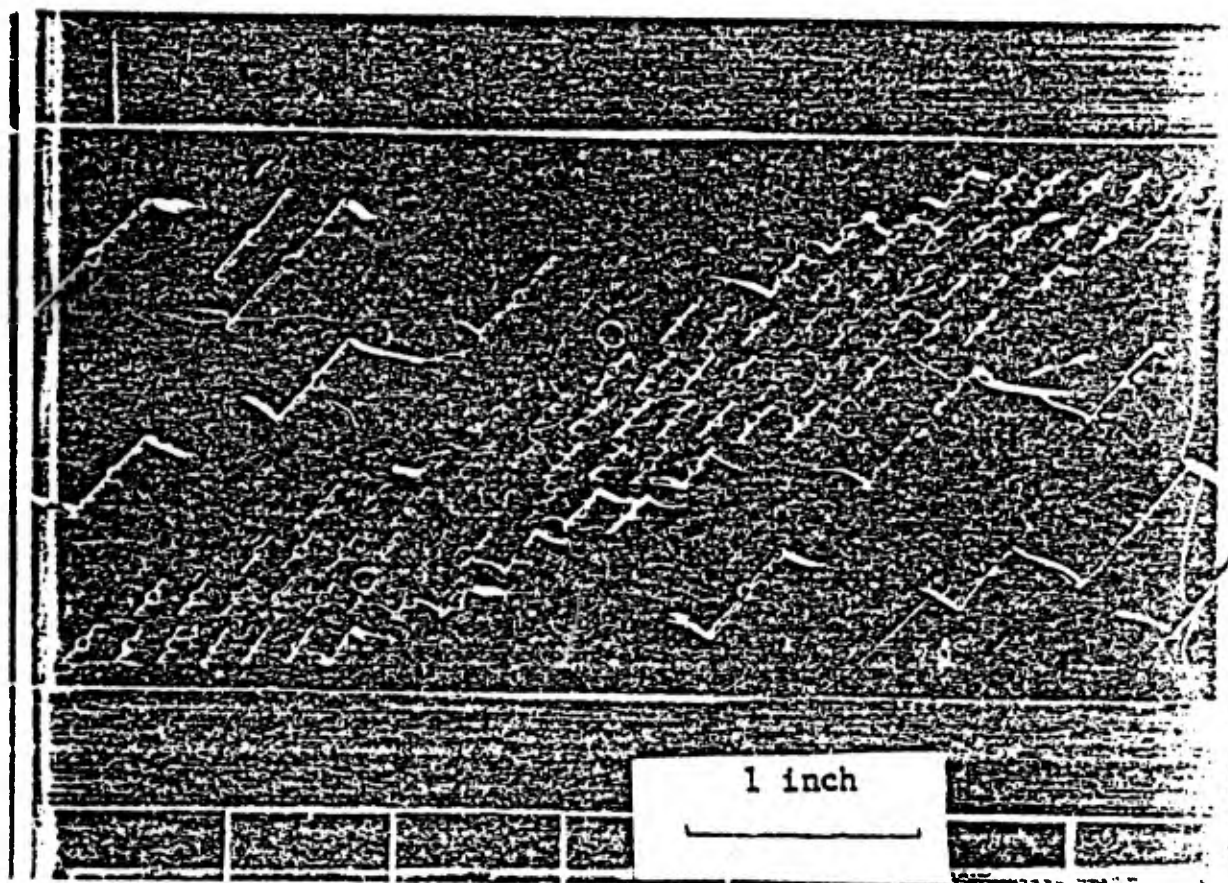


Figure 22b

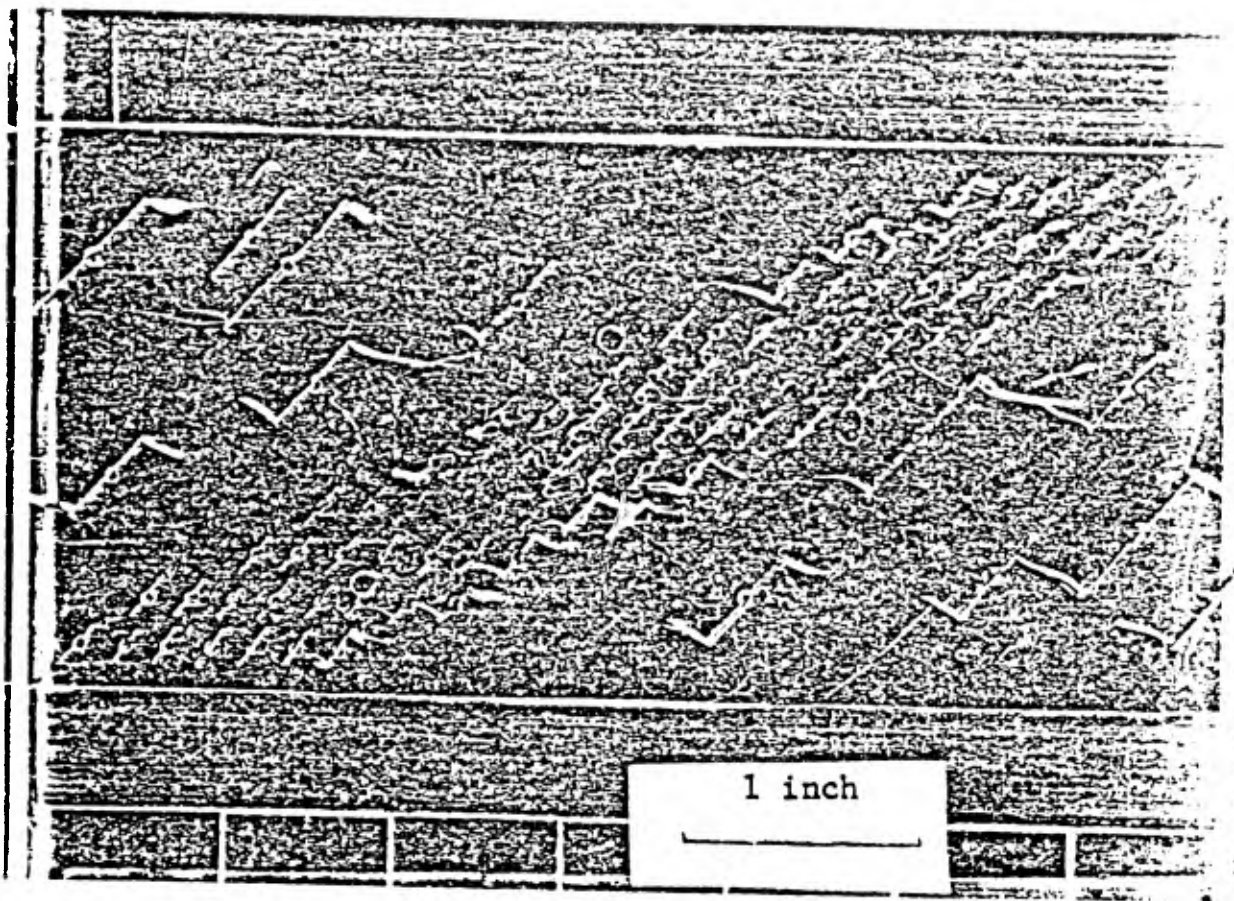


Figure 22c

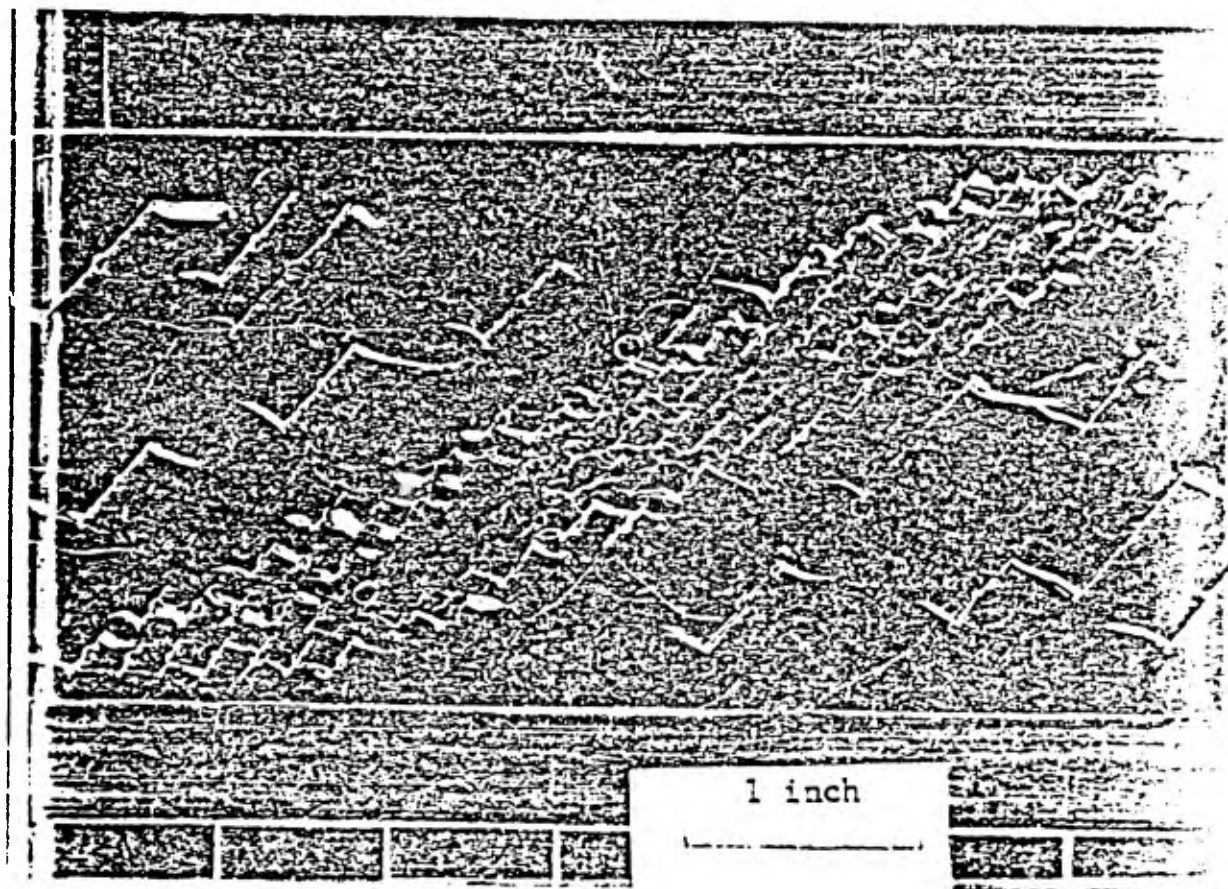


Figure 22d

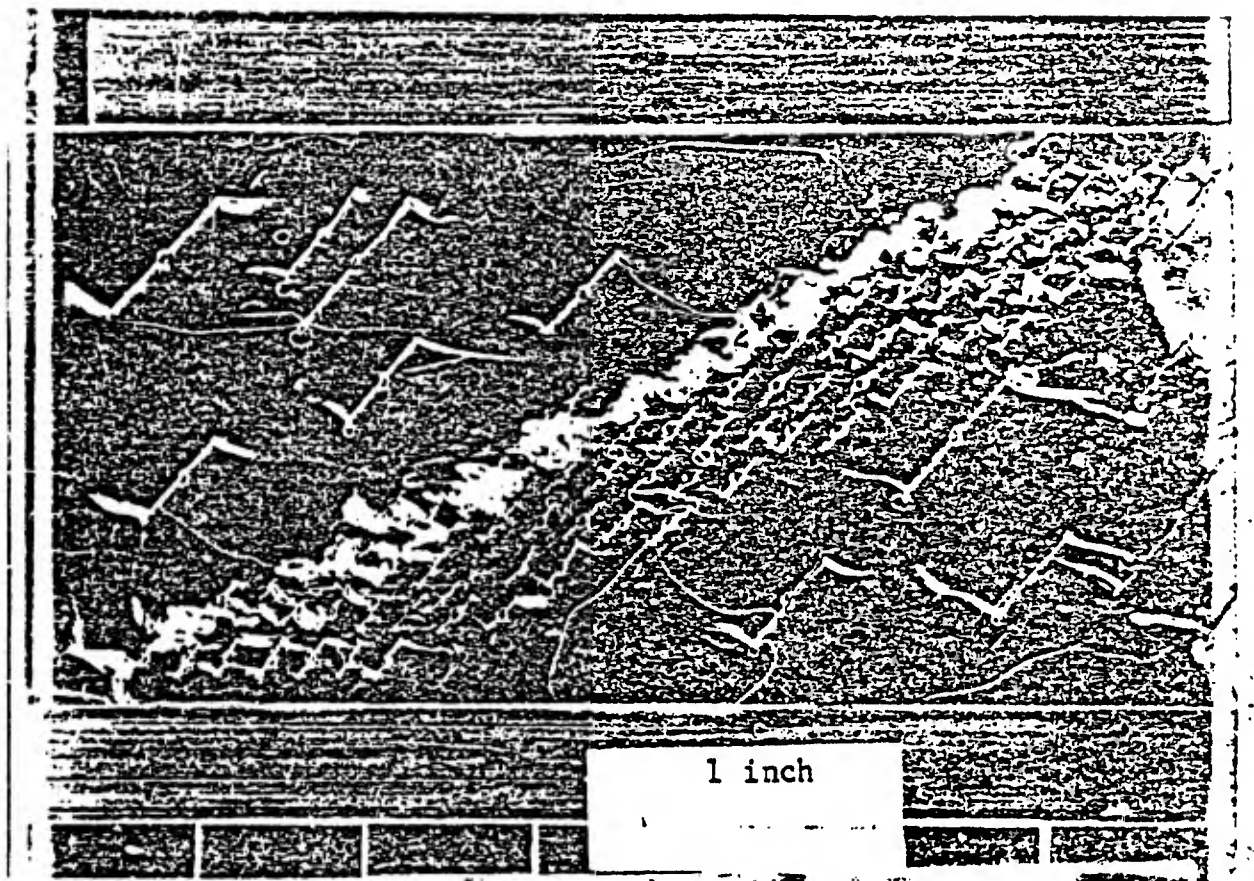


Figure 22e

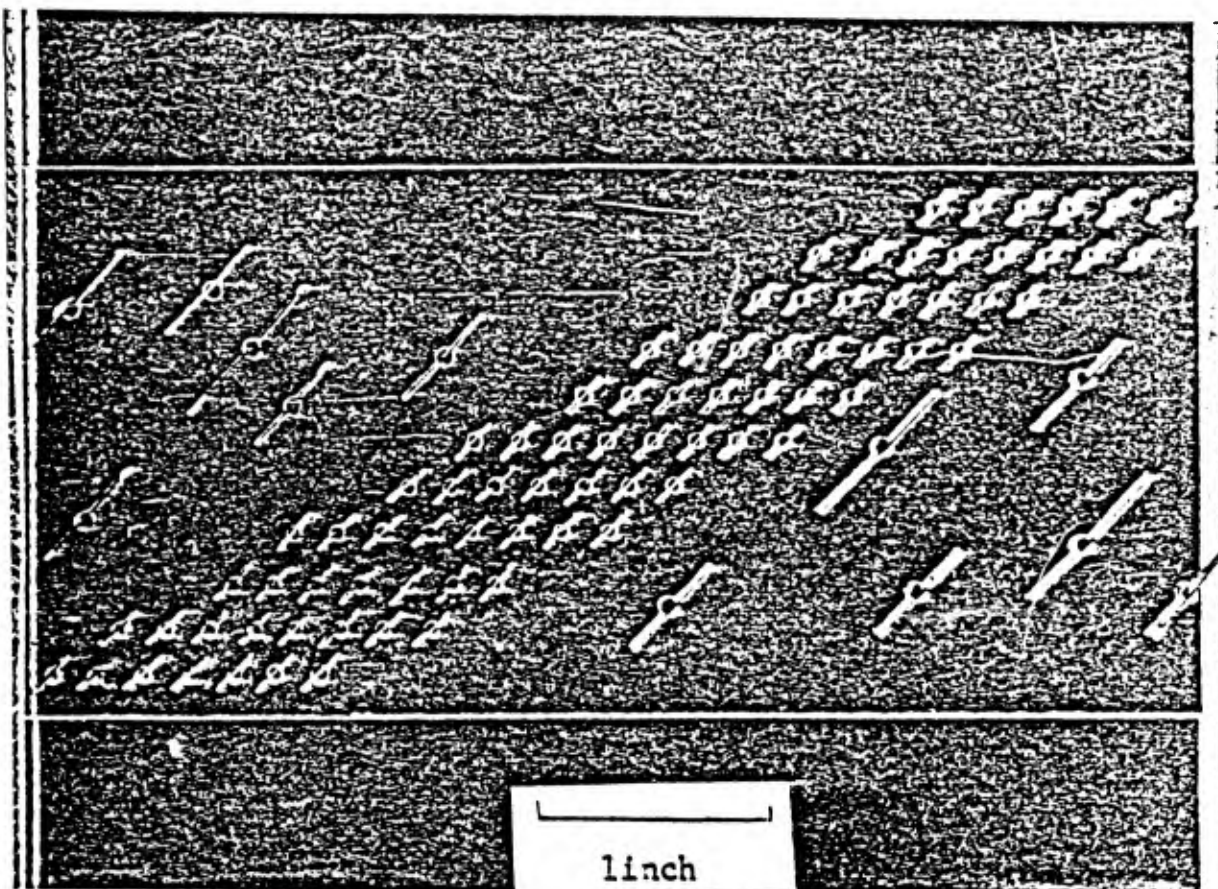


Figure 23a

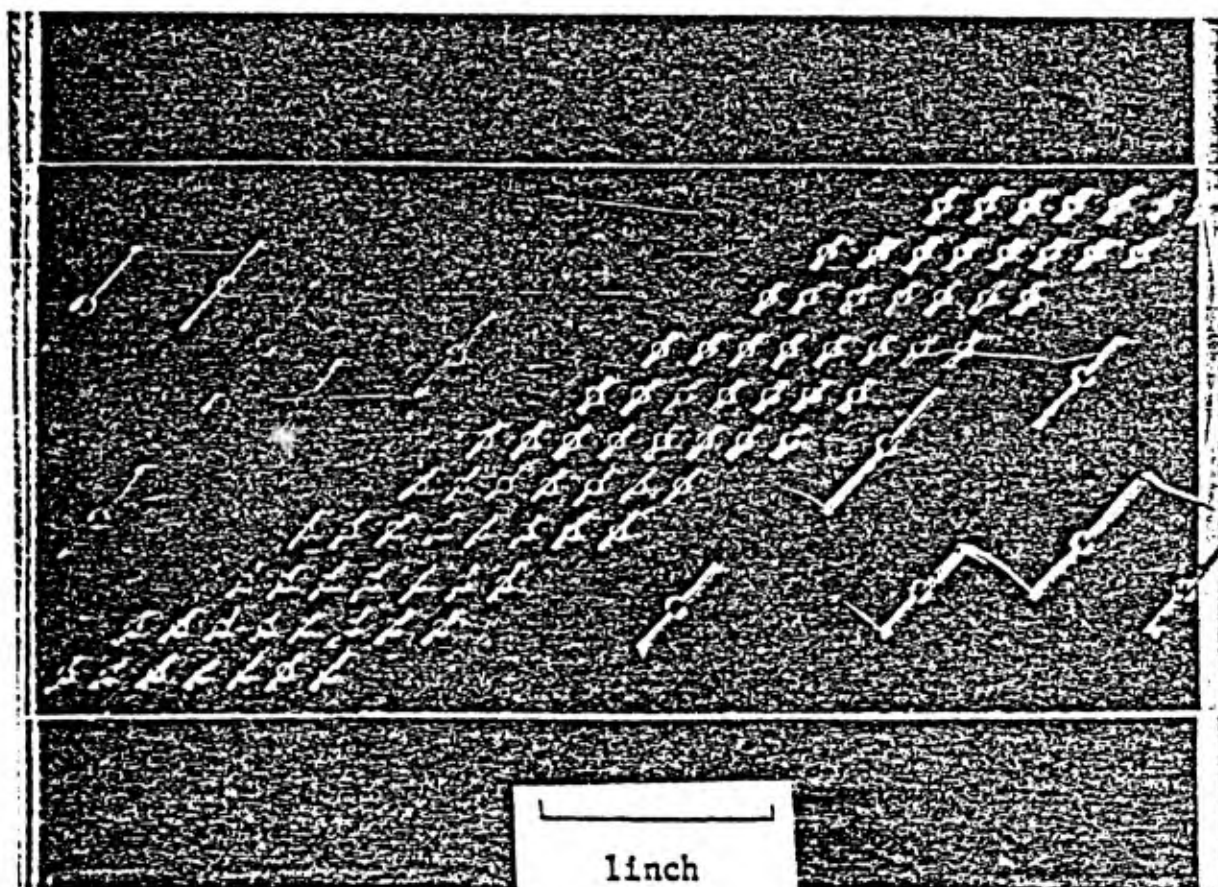


Figure 23b

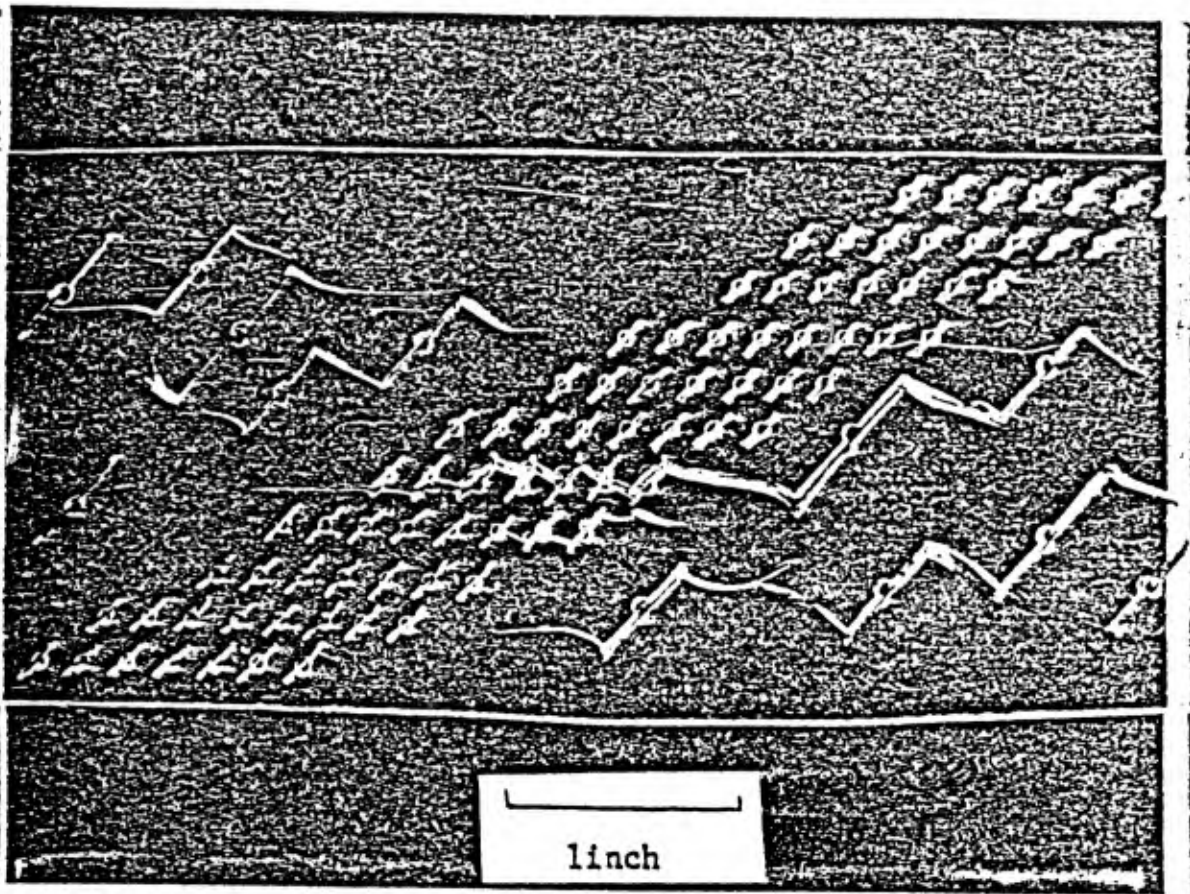


Figure 23c

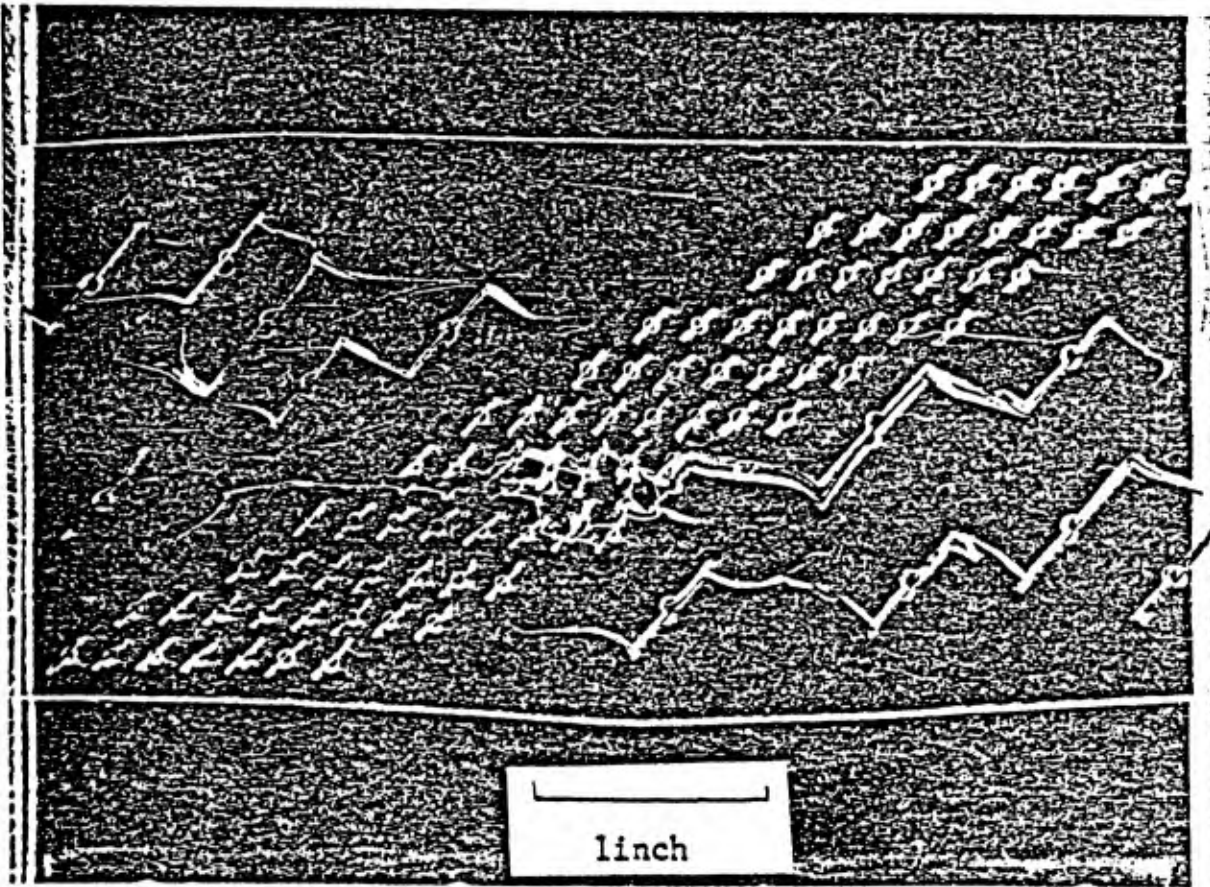


Figure 23d

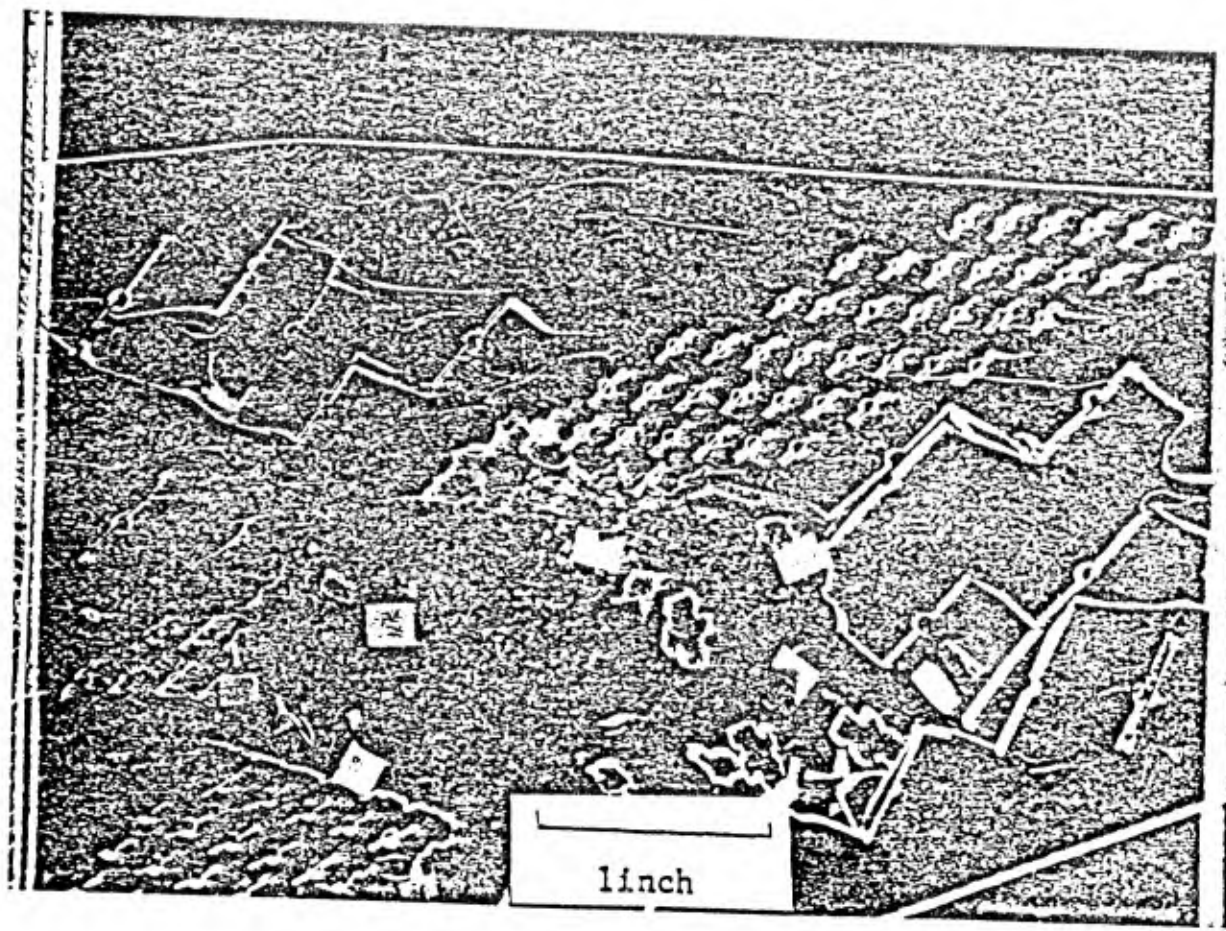


Figure 23e

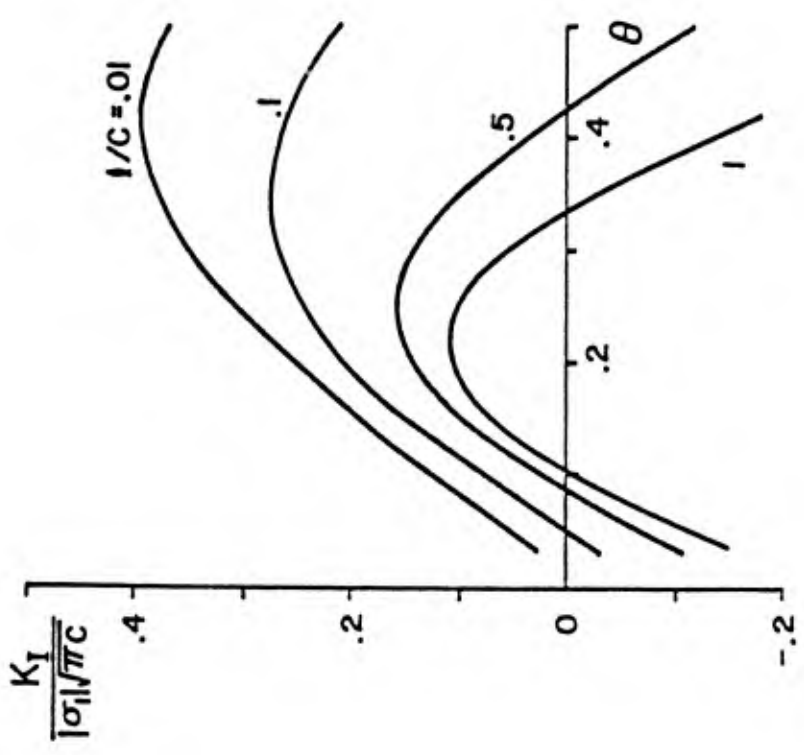
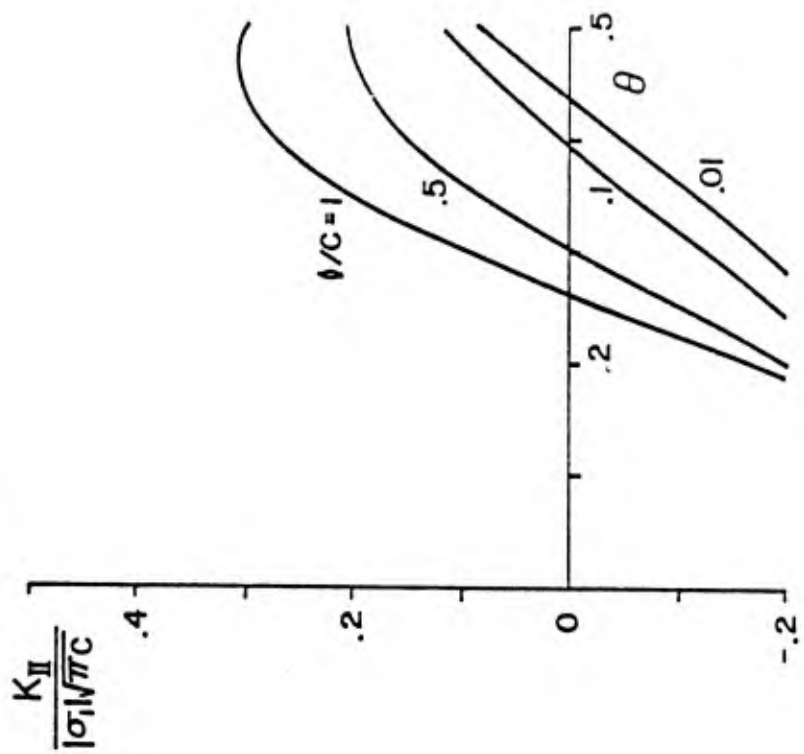


Figure A1

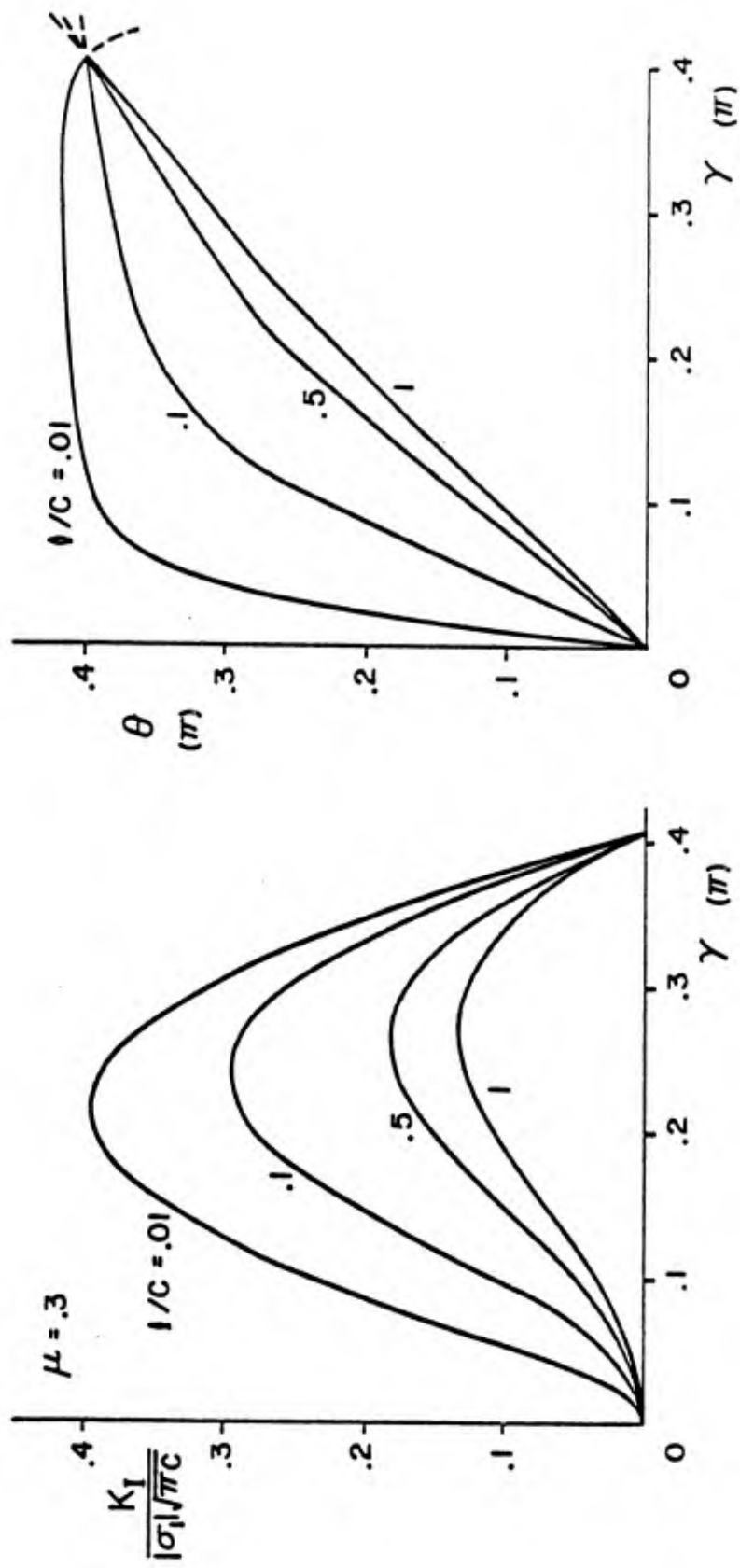


Figure A2

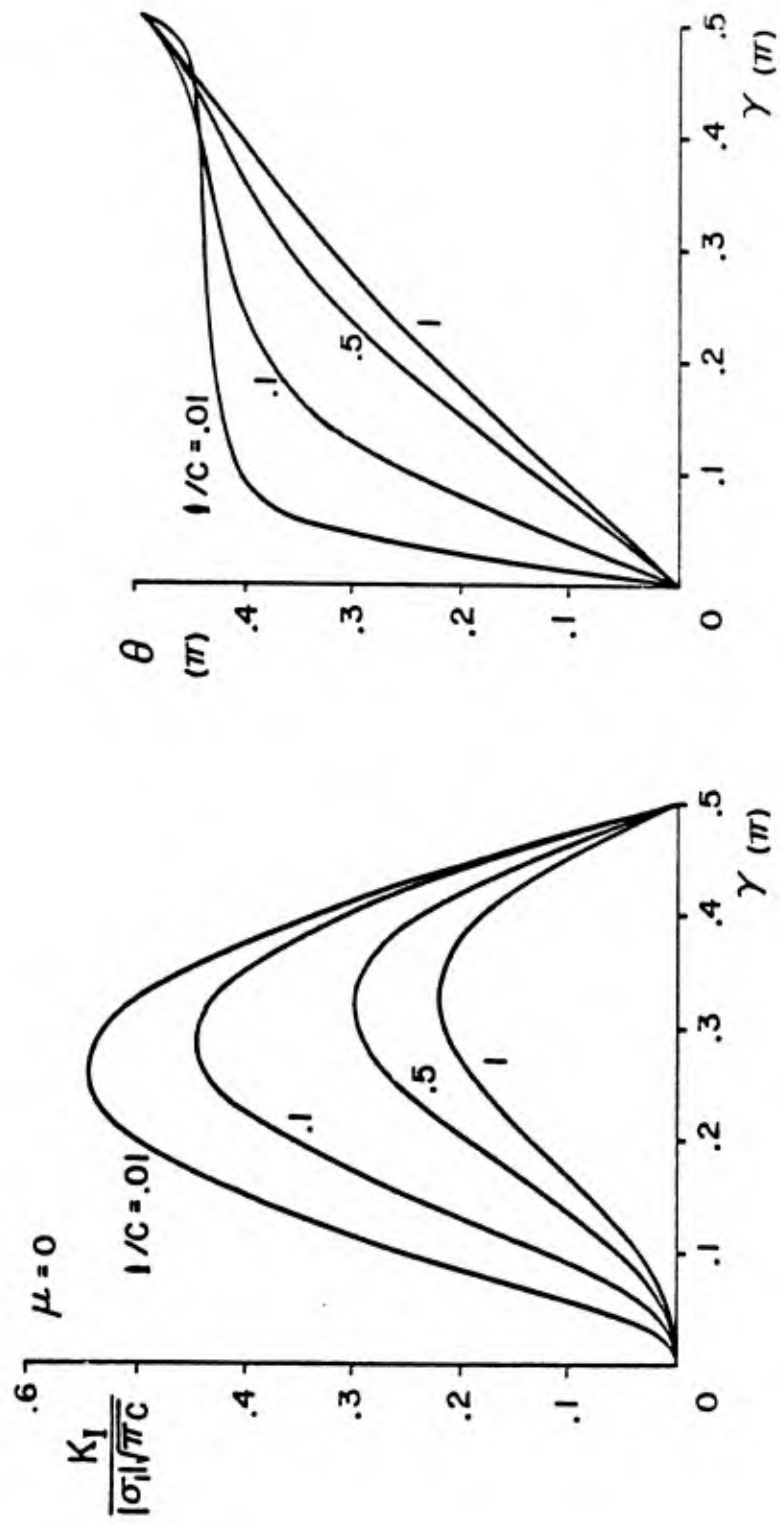


Figure A3

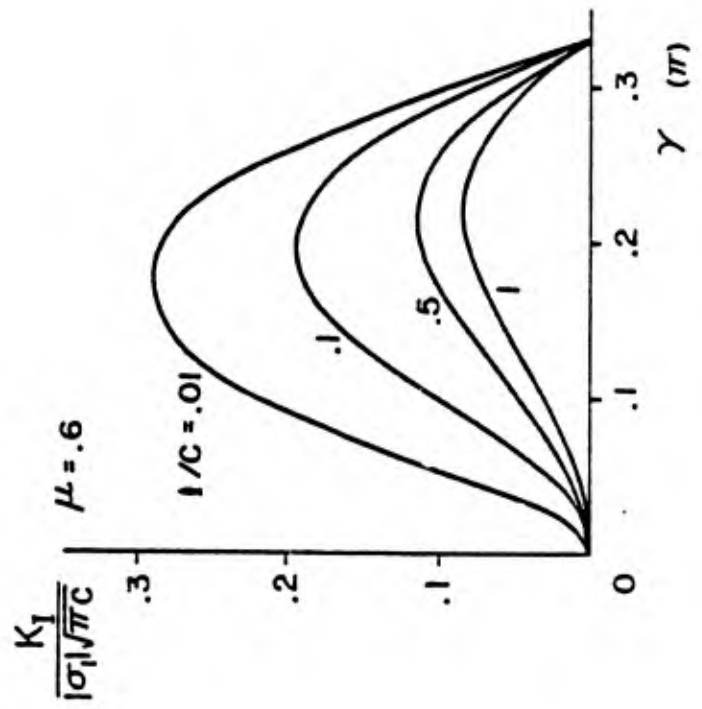
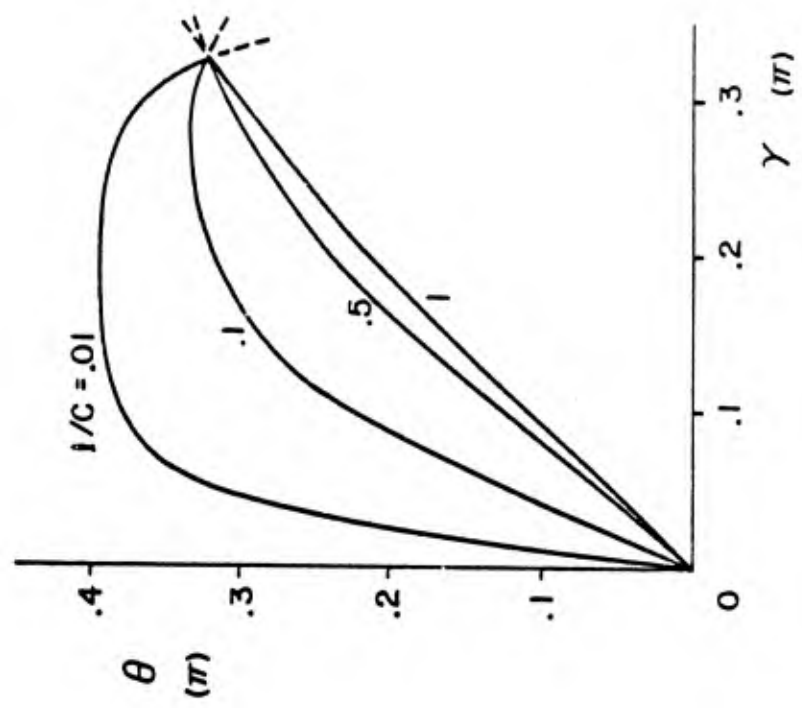


Figure A4

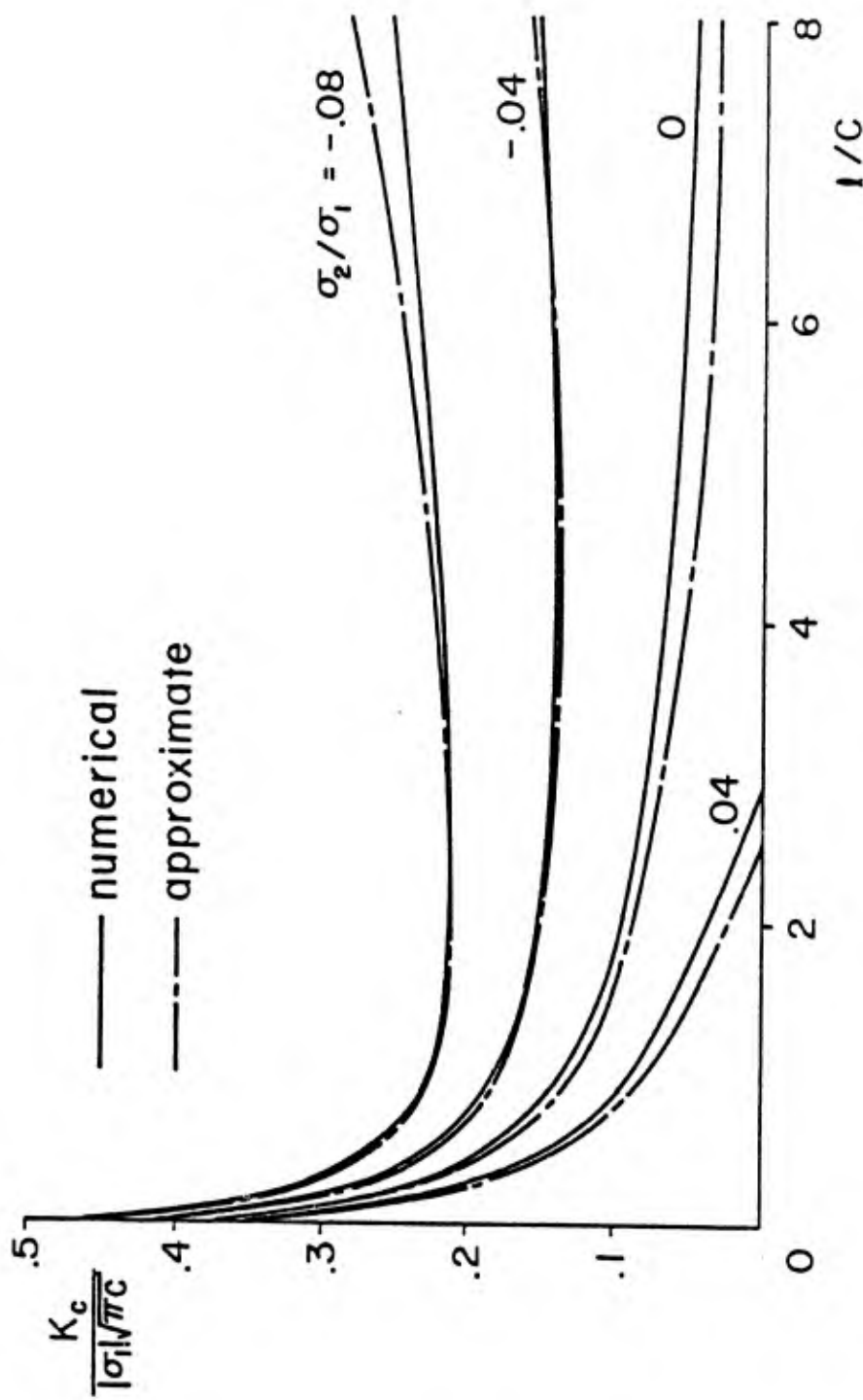


Figure A5

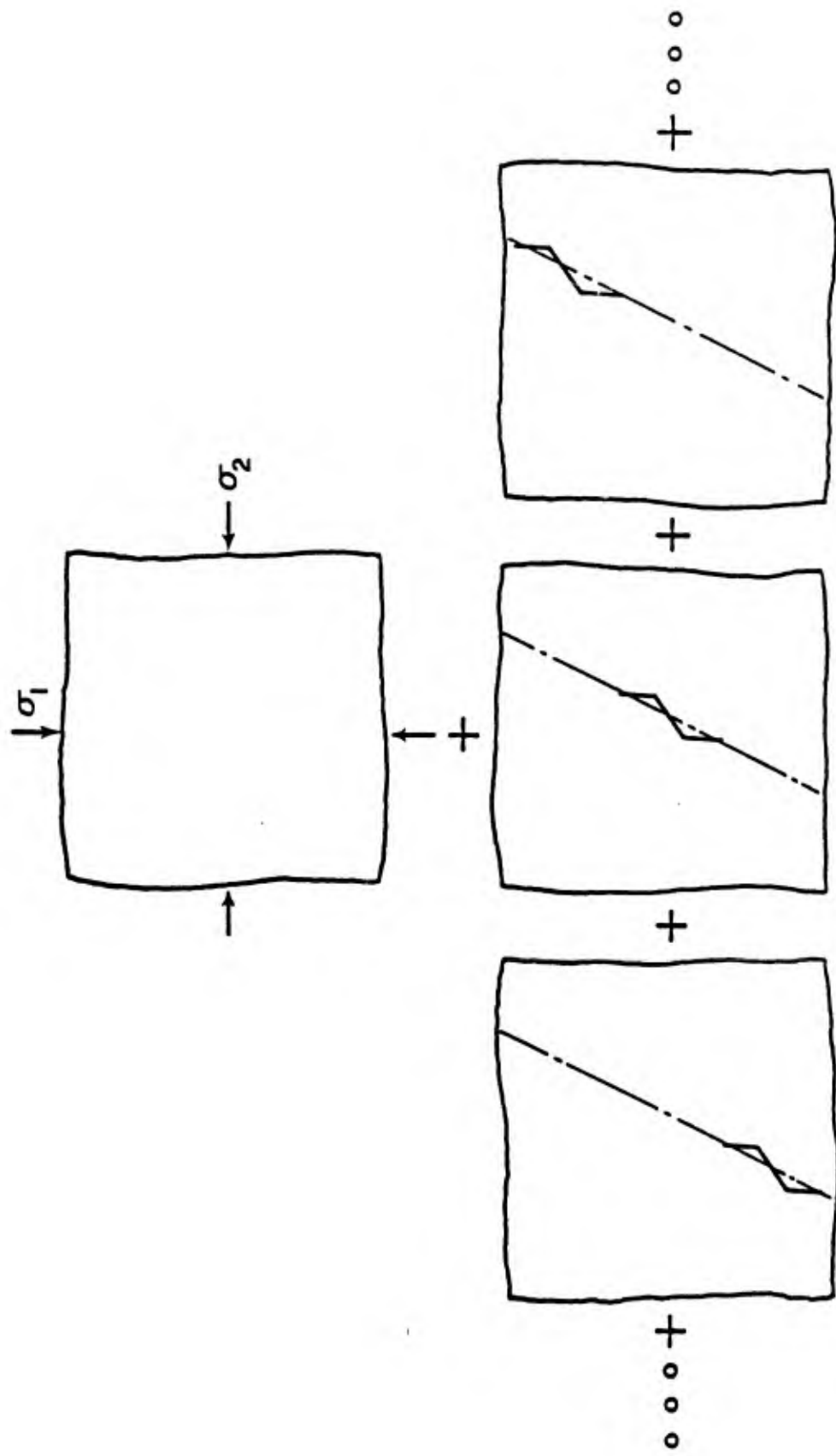


Figure B1

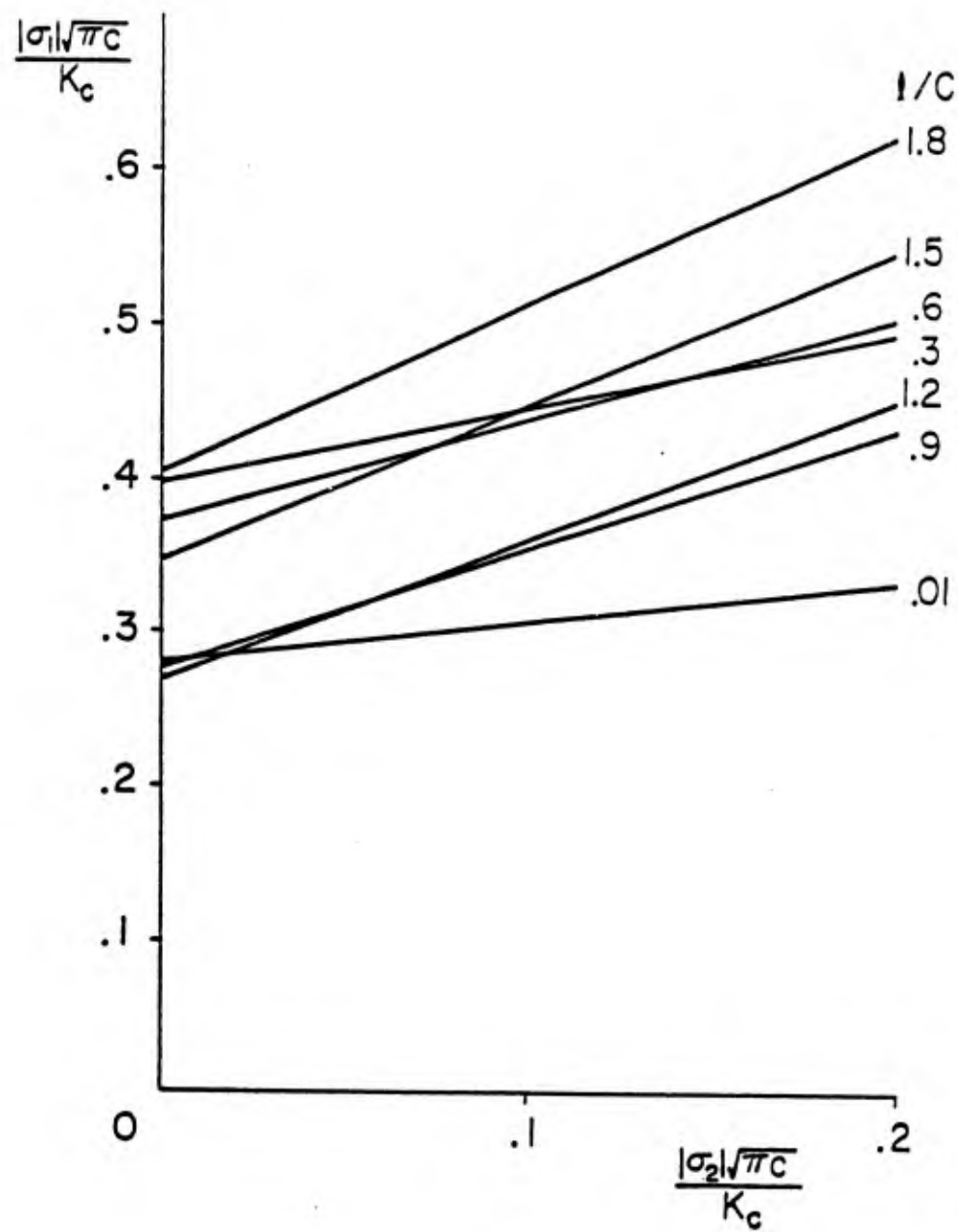


Figure B2

CHAPTER V

FINITE STRAIN ROCK PLASTICITY; STRESS TRIAXIALITY, PRESSURE, AND
TEMPERATURE EFFECTS*

by

B. Rowshandel and S. Nemat-Nasser

TABLE OF CONTENTS

	Page
ABSTRACT	213
1. INTRODUCTION	214
2. FORMULATION	218
3. TRUE TRIAXIAL TEST	226
4. STATE OF STRESS WITHIN EARTHQUAKE FAULTS	231
5. CONVENTIONAL TRIAXIAL TEST	235
6. RESULTS AND DISCUSSION	237
APPENDIX	253
ACKNOWLEDGMENT	256
REFERENCES	257
TABLES 1 - 4	261
LIST OF FIGURES	263
FIGURES 1 - 12 AND A-1	266 - 279

*Submitted to: Journal of Geophysical Research

FINITE STRAIN ROCK PLASTICITY; STRESS TRIAXIALITY, PRESSURE, AND
TEMPERATURE EFFECTS

B. Rowshandel and S. Nemat-Nasser

Department of Civil Engineering
Northwestern University
Evanston, IL 60201

ABSTRACT

A rate-independent elasto-plasticity theory is used to model the deformation of geological materials at shallow crustal depths, where rate effects may be regarded as secondary. The effects of confining pressure, material strain hardening (or softening due to volumetric strains), and temperature are included. The corresponding elasto-plastic rate constitutive relations are developed. To study the effects of pressure and temperature on the constitutive parameters, we use some published data of laboratory experiments on certain rocks. It is shown that the model gives a reasonable (at least qualitatively) description of the behavior of a wide variety of geological materials over a relatively wide range of pressures and moderate temperatures. Based on this theory, dilatancy (inelastic volumetric expansion) of a granite is studied, and it is found that for conventional triaxial stress states, dilatancy sets in once the deviatoric stress reaches the kinetic shear resistance of the rock. As an illustration, stress-strain curves for granite are then predicted at various depths, for possible application to the study of crustal deformation and to the prediction of fault behavior.

1. INTRODUCTION

Over the past two decades there has been growing interest in experimental rock mechanics, aimed at a better understanding of crustal deformation and concomitant earthquake mechanisms. A review of some work on the shear strength of rocks is given by Barton (1976), and recent advances in the rheology of the lithosphere are examined by Kirby (1983).

For earthquake prediction, the description of the thermomechanical properties of fault materials, the process of fault deformation, and the associated fault instability are of major concern. For the actual calculation of fault deformation, many authors have assumed simple behavior for the fault; see, for example, Stuart (1979) and the more recent review on the models of crustal deformation by Rundle (1983). The concept of a diffusionless dilatancy model for earthquake precursors is discussed by Stuart (1974). In this model, the nonlinear weakening of the fault zone (embedded in an elastic continuum) is viewed as the cause of instability. As pointed out by Stuart (1974), in this and related earthquake models, the assessment of instability critically depends on the type of constitutive relations employed for the fault zone, as well as for the intact elastic earth. Therefore, a systematic development of realistic constitutive relations for fault materials, and crustal rocks, is central to any type of quantitative estimate of fault instability.

The process of flow and fracture of crustal rocks, especially at great depths, is very complex due to the simultaneous presence of many factors. Pressure, temperature, and strain rate are the most influential factors.

The development of accurate constitutive equations for the fault zone requires results of laboratory tests on rocks, particularly for the post-failure phase of deformation and under conditions similar to those of the fault itself. However, not enough experimental data exist. Particularly due to the high compliance of conventional testing machines, little is known about the post-peak behavior of rocks under general loading conditions. The results of a few controlled laboratory tests on intact rock samples (e.g., Wawersik and Fairhurst, 1970, Wawersik and Brace, 1971, Rummel, Alheid, and Frohn, 1978, and Wong, 1982) suggest an initial elastic behavior followed by pre-peak dilation which is an indication of microcrack formation, post-peak dilation, and a phase of deformation at nearly constant sliding stress.

The dominant small-scale mechanisms of deformation in rocks in both laboratory and crustal conditions corresponding to shallow earthquakes, appear to be cataclastic microcracking and plastic flow. Cataclastic behavior is due to microcracking and the relative movement of microcrack surfaces. This mechanism of deformation basically involves the nucleation of microcracks and their frictional sliding. Consequently, it is expected to be strongly pressure-dependent. The mechanism of both shearing and dilatant behavior in this phase of

deformation is similar to that which occurs in soils and other granular materials.

Constitutive equations representing the nonlinear behavior of fault materials, must include the effects of the complete state of stress (that is, the confining pressure, differential stress, and stress triaxiality), temperature, dilatancy, pore pressure, strain-rate, and strain hardening. Constitutive equations which include all these factors are not available. Also, it will be quite some time before enough quantitative information on the deformation of rocks and minerals is obtained to develop comprehensive relations.

Common failure criteria such as those of Navier-Coulomb and Mohr, for example, involve only the major and minor principal stresses. The intermediate principal stress, however, has an appreciable effect on both the yield stress and the fracture stress. This has been demonstrated by Mogi (1971,1972) through a series of tests. The state of stress in the fault region is in fact triaxial, and different types of faulting (i.e. strike-slip, thrust, and normal) are associated with different orientations of the three principal stress components within the crust, relative to the ground surface; Price (1966).

Various theories have been developed in order to model the behavior of geomaterials under stress. For example, Rudnicki and Rice (1975), considering pressure and dilatancy, have suggested a 'vertex' theory for the behavior of brittle rocks under compressive

stresses. Nemat-Nasser and Shokooh (1980) established a theory for the flow of compressible materials by modifying the classical J_2 theory of plasticity. Their theory accounts for plastic dilatancy, pressure, and frictional effects. This theory was further generalized by Dorris and Nemat-Nasser (1982) to take into account the effect of the intermediate principal stress. Its practical applicability, especially for sand, has been demonstrated by these authors. There are several other related studies, and the reader is referred to Mroz (1980), Nemat-Nasser and Shokooh (1980), and Dorris and Nemat-Nasser (1982), for discussion and additional references.

Since the behavior of intact rocks after the initiation of microcracking is cataclastic, dilatant, pressure sensitive, and accompanied by finite deformation, a similar theory could describe the deformation of intact rocks after the onset of inelasticity, as well as the behavior of fault materials at shallow depths. A qualitative study has been done by Nemat-Nasser (1980). In the present study, the above theory is used to describe the behavior of intact rocks under laboratory conditions, as well as that of shallow crustal rocks.

2. FORMULATION

The total deformation rate \underline{D} is regarded to consist of two accompanying contributions: an elastic recoverable one, \underline{D}^e , and an inelastic one, \underline{D}^i ,

$$\underline{D} = \underline{D}^e + \underline{D}^i \quad (2.1)$$

For intact rocks, as well as for particulate frictional materials, the elastic deformation is usually very small, and therefore, one may employ Hooke's law to describe this contribution.

The inelastic deformation rate \underline{D}^i , in general, consists of a rate-independent component \underline{D}^p and a rate-dependent part \underline{D}^v ,

$$\underline{D}^i = \underline{D}^p + \underline{D}^v \quad (2.2)$$

where superscript p corresponds to the slip-induced plastic flow common in crystalline solids at moderate temperatures, and superscript v pertains to linear and nonlinear viscous flow or creep prevalent at elevated temperatures. Both mechanisms persist throughout the crustal depth into the lower part of the lithosphere. However, the mechanism of rate-independent, slip-induced inelasticity is expected to be dominant at shallow depths, whereas nonlinear creep characterizes inelasticity at greater depths. Based on dislocation models and on experiments, the thermally activated creep of crystalline materials at elevated temperatures is often described by the following one-dimensional creep law:

$$\dot{\gamma} = A_0 \left(\frac{\tau}{\tau_0} \right)^n e^{-\frac{Q}{RT}} \quad (2.3)a$$

where $\dot{\gamma}$ is the strain-rate, τ is the stress, Q is the activation energy, R is the gas constant, T is the absolute temperature, τ_0 is a reference stress, and the exponent n varies with the material; see, for example, Heard (1963), Carter and Ave'Lallemant (1970), Heard and Raleigh (1972), Carter (1976), Heard (1976), Weertman (1978), Tullis (1979), Kirby (1980), Carter et al. (1981), Caristan (1982), and Kirby (1983). A useful three-dimensional version of this expression would be

$$\underline{D}^V = A_0 \left(\frac{\bar{\tau}}{\tau_0} \right)^{n-1} \underline{\underline{\sigma}} \tau_0 e^{-\frac{Q}{RT}} \quad (2.3)b$$

where $\underline{\underline{\sigma}}$ is the stress tensor and $\bar{\tau}$ is representative of the overall stress; for example, one may choose

$$\bar{\tau} = \sqrt{J_2}, \quad J_2 = \frac{1}{2} \sigma'_{ij} \sigma'_{ij} \quad (2.4)$$

where prime denotes the deviatoric part and repeated indices are summed.

The main objective of the current paper is to develop the constitutive relations associated with the slip-induced, highly pressure-sensitive part of the deformation rate designated above by \underline{D}^P . As mentioned before, \underline{D}^P is expected to be the dominant part of

the inelastic flow at shallow crustal depths. Indeed, for the sake of modeling, it may be reasonable to assume that for typical crustal temperature gradients down to depths of 10-15 km, the deformation rate tensor is given by

$$\underline{D} = \underline{D}^e + \underline{D}^p \quad (2.5)$$

and at greater depths it is given by

$$\underline{D} = \underline{D}^e + \underline{D}^v \quad (2.6)$$

Naturally, this is an arbitrary subdivision, but it is useful for constitutive modeling. Of course, in the actual application, all three components of the deformation rate may be included. In the remaining part of this work, we shall concentrate on developing constitutive relations for the deformation mechanisms associated with (2.5).

It is convenient to consider a fixed rectangular Cartesian coordinate system with coordinate axes x_i , $i = 1, 2, 3$, to denote the velocity field by v_i , and to express the components of the deformation rate tensor by

$$D_{ij} = \frac{1}{2} (v_{i,j} + v_{j,i}) \quad (2.7)$$

where comma followed by an index denotes partial differentiation with respect to the corresponding coordinate. Similarly, the components of the material spin tensor, \underline{W} , are given by

$$W_{ij} = \frac{1}{2} (v_{i,j} - v_{j,i}) \quad (2.8)$$

At finite strains and rotations the material rate of stress is not objective, since it also includes the rate of change of stress observed in the fixed reference coordinates, because of the spin of the material element. A commonly used objective stress rate is

$$\overset{*}{\sigma}_{ij} = \dot{\sigma}_{ij} - W_{ik} \sigma_{kj} - W_{jk} \sigma_{ki} \quad (2.9)$$

This is the stress flux measured in the coordinate system which is currently spinning with the material.

Using an isotropic hypoelastic relation, we write for the elastic part of the deformation rate

$$D_{ij}^{e'} = \frac{\overset{*}{\sigma}_{ij}}{2\mu}, \quad D_{kk}^e = \frac{\overset{*}{\sigma}_{kk}}{3\kappa} \quad (2.10)a,b$$

where μ and κ are the shear modulus and the bulk modulus, respectively.

The part \tilde{D}^P is assumed to be derivable from a plastic potential g ,

$$D_{ij}^P = \lambda \frac{\partial g}{\partial \sigma_{ij}} \quad (2.11)$$

where λ is calculated from the consistency condition $\dot{f} = 0$, which

guarantees that the stress state remains on the yield surface $f=0$ during the plastic flow.

The flow potential g and the yield function f are hyper-surfaces in the six-dimensional stress space. The yield surface marks the boundary of the region in which the material state is elastic and on which it is elasto-plastic. Stress states outside of the yield surface are not admissible. When the flow potential coincides with the yield surface, we have the so-called associative flow rule. This generally applies to pressure-insensitive, plastically incompressible metals. Geomaterials, in general, are highly pressure-sensitive and plastically compressible (dilatant). It has been shown by Nemat-Nasser and Shokooh (1980) that an associative flow rule for materials of this kind leads to contradiction, because it then requires that the overall friction coefficient which is always positive, equals the rate of plastic volumetric strain which may be positive, negative, or zero, depending on the deformation state. In the present work, therefore, we shall use a nonassociative flow rule.

Following Dorris and Nemat-Nasser (1982), we consider the following yield function and flow potential, which include the effects of pressure, intermediate stress, plastic volumetric strain, and plastic distortional strain:

$$f \equiv \bar{\tau} [1 + C(\eta)] - F(p, \Delta, \gamma; T) \quad (2.12)$$

$$g \equiv \bar{\tau} [1 + C(\eta)] + G(p, \Delta, \gamma; T) \quad (2.13)$$

In these equations, T is the temperature as before, $\bar{\tau}$ is defined by equation (2.4), Δ is the total plastic volumetric strain measured from a reference state of mass density ρ_0 , γ is the effective distortional plastic strain, η represents the effect of the third stress invariant, and p is the hydrostatic pressure. These quantities are given by

$$p = \frac{1}{3} \sigma_{kk}, \quad \Delta = \int_0^\theta \frac{\rho_0}{\rho} D_{kk}^p d\theta', \quad \gamma = \int_0^\theta (2D_{ij}^{p'} D_{ij}^{p'})^{1/2} d\theta',$$

$$\eta = \frac{J_3}{\bar{\tau}}, \quad J_3 = \frac{1}{3} \sigma'_{ij} \sigma'_{jk} \sigma'_{ki} \quad (2.14)$$

where ρ is the current mass density, and θ measures time (a monotone load parameter). Note that, when $C = 0$, the influence of Δ and γ is suppressed and $G = -F$ is assumed, then the classical J_2 plasticity theory results; Hill (1950).

It is convenient to represent the function C as

$$C(\eta) = \beta\eta \quad (2.15)$$

where β is a scalar function of the stress state.

The condition $\dot{f} = 0$ is used to obtain the scalar multiplier λ in equation (2.11). Differentiating (2.12) with respect to time parameter θ and using equations (2.11)-(2.15), we have

$$\lambda = \frac{\dot{\bar{\tau}} + \beta \left(\frac{J_3}{\bar{\tau}^2} \right) \cdot - \dot{p} \frac{\partial F}{\partial p}}{\frac{\rho_0}{\rho} \frac{\partial F}{\partial \Delta} \frac{\partial G}{\partial p} + r\sqrt{2} \frac{\partial F}{\partial \gamma}} \quad (2.16)$$

Here r is defined by

$$r = \left(\frac{\partial g}{\partial \sigma'_{ij}} \frac{\partial g}{\partial \sigma'_{ij}} \right)^{1/2} \quad (2.17)$$

and hence

$$\dot{\gamma} = r\sqrt{2} \lambda \quad (2.18)$$

Differentiating equation (2.13) with respect to σ'_{ij} and substituting the result into equation (2.11), we obtain the following expression for the plastic part of the deformation rate:

$$D^p_{ij} = \lambda \left\{ \frac{\sigma'_{ij}}{2\bar{\tau}} + \beta \left(\frac{\sigma'_{ik}\sigma'_{kj}}{\bar{\tau}^2} - \frac{\sigma'_{ij} J_3}{\bar{\tau}^4} \right) - \frac{\delta_{ij}}{3} \left(2\beta - \frac{\partial G}{\partial p} \right) \right\} \quad (2.19)$$

The corresponding spherical and deviatoric parts are

$$D^p_{kk} = \lambda \frac{\partial G}{\partial p} \quad (2.20)$$

$$D^p_{ij} = \lambda \left\{ \sigma'_{ij} \left(\frac{1}{2\bar{\tau}} - \beta \frac{J_3}{\bar{\tau}^4} \right) + \beta \left(\frac{\sigma'_{ik}\sigma'_{kj}}{\bar{\tau}^2} - \frac{2}{3} \delta_{ij} \right) \right\} \quad (2.21)$$

respectively. Equation (2.20), combined with (2.18) and (2.14b), yields

$$\frac{\partial G}{\partial p} = r\sqrt{2} \frac{D_{kk}^p}{\dot{\gamma}} = r\sqrt{2} \frac{\rho}{\rho_0} \frac{\dot{\Delta}}{\dot{\gamma}} \quad (2.22)$$

3. TRUE TRIAXIAL TEST

In this case the three principal stresses, σ_1 , σ_2 , and σ_3 , are distinct. Let $\sigma_1 > \sigma_2 > \sigma_3$. The stress tensor in the principal coordinate system then is

$$\mathbf{g} = \begin{bmatrix} \sigma_1 & 0 & 0 \\ 0 & \sigma_2 & 0 \\ 0 & 0 & \sigma_3 \end{bmatrix} \quad (3.1)$$

We define the triaxiality parameter by

$$b = \frac{\sigma_2 - \sigma_3}{\sigma_1 - \sigma_3} \quad (3.2)$$

Using equation (3.2), the maximum shear stress

$$\tau = \frac{\sigma_1 - \sigma_3}{2} \quad (3.3)$$

and the pressure*

$$p = \frac{\sigma_1 + \sigma_2 + \sigma_3}{3} \quad (3.4)$$

we obtain

*We use the term 'pressure' for the spherical part, p , of the stress tensor, as stated in equation (3.4). For conventional triaxial tests, $\sigma_1 > \sigma_2 = \sigma_3$, the term 'confining pressure' usually refers to the lateral pressure, $\sigma_2 = \sigma_3$. To avoid confusion, we use the term 'lateral pressure' for the case of conventional triaxial tests.

$$\mathbf{g}' = \begin{bmatrix} (2/3)\tau(2 - b) & 0 & 0 \\ 0 & (2/3)\tau(-1 + 2b) & 0 \\ 0 & 0 & -(2/3)\tau(1 + b) \end{bmatrix} \quad (3.5)$$

which is the deviatoric part of the stress. Using (3.5) in equation (2.14), we obtain the following expressions for the deviatoric stress invariants J_2 and J_3 and for η :

$$\bar{\tau}^2 = J_2 = A^2 \tau^2, \quad J_3 = B^3 \tau^3, \quad \eta = \frac{B^3}{A^3} \quad (3.6)$$

where A and B depend on b only,

$$A^2 = \frac{4}{3} (b^2 - b + 1), \quad B^3 = \frac{8}{27} (2b^3 - 3b^2 - 3b + 2)$$

The yield function f and the flow potential g (equations (2.12) and (2.13), respectively) become

$$f = \xi \tau - F(p, \Delta, \gamma; T) \quad (3.7)$$

$$g = \xi \tau + G(p, \Delta, \gamma; T) \quad (3.8)$$

where

$$\xi = A + \beta \frac{B^3}{A^2} \quad (3.9)$$

which depends on b only.

From equations (2.20) and (2.21) it is seen that as far as the plastic potential g is concerned, only $\frac{\partial G}{\partial p}$ appears in the formula-

tion. To obtain an expression relating this parameter to $\frac{\partial F}{\partial p}$ (from equation (2.12)), the rate of plastic work will be computed and compared with an approximate value of the energy dissipation. The rate of plastic work per unit current volume is

$$\dot{W}_p = \sigma_{ij} D_{ij}^p = \sigma'_{ij} D_{ij}^p + p D_{kk}^p \quad (3.10)$$

where the first term on the right-hand side is the rate of distortional plastic work and the second term is the rate of plastic work associated with volumetric strain. The first term, using equations (2.11) and (2.18), becomes

$$\sigma'_{ij} D_{ij}^p = \frac{\dot{\gamma}}{r\sqrt{2}} \xi \tau \quad (3.11a)$$

and the second term, in view of equation (2.20), reduces to

$$p D_{kk}^p = p \frac{\dot{\gamma}}{r\sqrt{2}} \frac{\partial G}{\partial p} \quad (3.11b)$$

Therefore the total rate of plastic work is

$$\dot{W}_p = \frac{\dot{\gamma}}{r\sqrt{2}} \left(p \frac{\partial G}{\partial p} + \xi \tau \right) \quad (3.12)$$

To derive an expression for the rate of energy dissipation, we start with the yield function as expressed in equation (3.7),

$$f = \xi\tau - F$$

from which it follows that

$$\frac{d\tau}{dp} = \frac{1}{\xi} \frac{\partial F}{\partial p} \quad (3.13)$$

which is the change in resistance to flow per unit change in pressure. The parameter $\frac{\partial F}{\partial p}$ is a material property which is related to the coefficient of sliding friction. For constant* $\frac{\partial F}{\partial p}$ we may assume

$$\tau = \frac{1}{\xi} \frac{\partial F}{\partial p} p + \tau_c \quad (3.14)$$

where τ_c is the cohesion and is zero for non-cohesive materials. For intact rocks the initial stage of deformation is governed by Hooke's law and the plastic deformation becomes appreciable after the onset of microcracking; Brace (1976). For the material in a cataclastic regime, one may set $\tau_c = 0$ in equation (3.14).

We then combine (3.14) with the expression given for the effective distortional rate of deformation by equation (2.18) to obtain

$$\dot{W}_f \approx \dot{\tau}\gamma = \left(\frac{1}{\xi} \frac{\partial F}{\partial p} p + \tau_c \right) \dot{\gamma} \quad (3.15)$$

*The change in resistance to flow with pressure, i.e. $\partial F/\partial p$ like the coefficient of internal friction, is a decreasing function of the pressure p , especially for lower pressures. A more realistic form would be (see Figure 5a) $F_0 e^{-ap}$, with F_0 and a as constants depending on the material. However, a constant value for the above parameter is satisfactory if we use its average value in the pressure range $(0, p)$.

Assuming there will be no other source of work or dissipation, we equate (3.12) and (3.15) to obtain

$$\frac{\partial G}{\partial p} = r\sqrt{2} \left(\frac{1}{\xi} \frac{\partial F}{\partial p} + \frac{\tau_c}{p} \right) - \xi \frac{\tau}{p} \quad (3.16)$$

Employing equations (3.6) and (3.16), the expression for the scalar multiplier λ from equation (2.16) can be written in the following form:

$$\lambda = \frac{A\tau(1 + \beta \frac{B^3}{A^3}) - p \frac{\partial F}{\partial p}}{r\sqrt{2} \left[\frac{\partial F}{\partial \gamma} + \frac{\rho_0}{\rho} \frac{\partial F}{\partial \Delta} \left(\frac{1}{\xi} \frac{\partial F}{\partial p} + \frac{\tau_c}{p} - \frac{\xi}{r\sqrt{2}} \frac{\tau}{p} \right) \right]} \quad (3.17)$$

where r is

$$r = \sqrt{1/2 + \beta\eta + \beta^2(2/3 - 4\eta^2)} \quad (3.18)$$

which is obtained using equations (2.17) and (3.8).

4. STATE OF STRESS WITHIN EARTHQUAKE FAULTS

The state of stress within earthquake faults is one of true triaxial compression, as expressed in equation (3.1). The type of faulting (strike-slip, thrust, normal, or any combination of these) depends on the orientation of the principal axes (x_i , $i = 1, 2, 3$) relative to the ground surface. For example, depending on whether σ_1 , σ_2 , or σ_3 is vertical, we have normal, strike-slip, or thrust faulting, respectively. These three cases are illustrated graphically in Figure 1.

In strain-softening earthquake models, instability is usually defined in terms of the relative stiffnesses of the fault zone and the (elastic) surroundings; see, e.g. Rudnicki (1980) and Stuart (1981). Therefore, for the earthquake instability criterion, we assume that it occurs on a plane on which the (magnitude of the) slope of the load-deformation curve in the post-peak region equals the unloading stiffness of the elastic surroundings.

We now introduce a new right-handed coordinate system \bar{X} with \bar{X}_2 normal to the plane of the fault and with \bar{X}_3 along the strike of the fault. Let a be the matrix which transforms X into \bar{X} . Then the state of stress with reference to \bar{X} is

$$\bar{\sigma} = a^T \sigma a \quad (4.1)$$

Similarly the deformation rate tensor becomes

$$\bar{D} = \bar{a}^T D \bar{a} \quad (4.2)$$

The quantities of interest for finding the fault stiffness are the stress rate and the rate of displacement on the fault plane, i.e. $\dot{\bar{\sigma}}_{23}$ and \bar{D}_{23} .

For the case of isotropic, linearly elastic surrounding materials, the plane of shear failure makes an angle of 45° with the maximum and minimum principal stresses. For the purpose of demonstration, we consider a strike-slip fault (Figure 1b). The transformation matrix is (see Figure 2)

$$\bar{a} = \begin{bmatrix} 0 & \sqrt{2}/2 & \sqrt{2}/2 \\ 1 & 0 & 0 \\ 0 & \sqrt{2}/2 & -\sqrt{2}/2 \end{bmatrix} \quad (4.3)$$

The deviatoric stress in the \bar{x} system is

$$\bar{\sigma}' = \begin{bmatrix} -(2/3)\tau(1 - 2b) & 0 & 0 \\ 0 & (1/3)\tau(1 - 2b) & \tau \\ 0 & \tau & (1/3)\tau(1 - 2b) \end{bmatrix} \quad (4.4)$$

Hence from (4.4),

$$\bar{\sigma}'_{23} = \tau$$

which is the maximum shear stress acting on the fault plane; the corresponding elastic and plastic rates of deformation are

$$\bar{D}_{23}^e = \frac{\dot{\tau}}{2\mu} \quad (4.5)$$

$$\bar{D}_{23}^p = \lambda \left\{ \frac{1}{2A} + \beta \left(\frac{2(1-2b)}{3A^2} - \frac{B^3}{A^4} \right) \right\} \quad (4.6)$$

where equations (2.19) and (4.4) are used to obtain (4.6).

We now substitute from (4.5) and (4.6) into (2.5). We also substitute for λ from (3.17). Assuming that the confining pressure does not change appreciably during deformation at a fixed depth, our stress rate-deformation rate equation in the direction of the strike of the fault becomes

$$\bar{D}_{23} = \frac{\dot{\tau}}{2\mu} + \frac{\dot{\tau} \left\{ \left(1 + \beta \frac{B^3}{A^3} \right) \left(\frac{1}{2} + \beta \left[\frac{2(1-2b)}{3A} - \frac{B^3}{A^3} \right] \right) \right\}}{r\sqrt{2} \left\{ \frac{\partial F}{\partial \gamma} + \frac{\rho_0}{\rho} \frac{\partial F}{\partial \Delta} \left(\frac{1}{\xi} \frac{\partial F}{\partial p} + \frac{\tau_c}{p} - \frac{\xi}{r\sqrt{2}} \frac{\tau}{p} \right) \right\}} \quad (4.7)$$

Equation (4.7) provides the information on the stiffness of the fault. The constants β , b , A , B , ξ , and r , as defined in equations (2.15), (3.2), (3.6), (3.9), and (3.18), depend on the rate of stress. However, it is noted that, of these six constants, only the first two (i.e. b and β) are independent. The rest are functions of b , β , or both. On the other hand, μ (the elastic shear modulus of the fault), $\frac{\partial F}{\partial \gamma}$, $\frac{\partial F}{\partial \Delta}$, and $\frac{\partial F}{\partial p}$ are material dependent. As discussed by Dorris and Nemat-Nasser (1982), the parameter, $\frac{\partial F}{\partial \gamma}$, may be taken in the form (see Appendix)

$$\frac{\partial F}{\partial \gamma} = \alpha e^{-\hat{\rho}\gamma} \quad (4.8)$$

where α and $\hat{\rho}$ are material constants.

To choose a set of physically appropriate values for the material constants, we make use of the experimental data in the literature. Most of the laboratory experiments are traditionally performed under uniform lateral confining pressure (conventional triaxial tests, $\sigma_1 > \sigma_2 = \sigma_3$). Accordingly, we write our constitutive equation for this type of loading. This is done in the following section.

5. CONVENTIONAL TRIAXIAL TEST ($\sigma_1 > \sigma_2 = \sigma_3$)

For this type of loading, we have

$$b = 0, \quad \beta = 0 \quad (5.1)a,b$$

Using (5.1)a,b in equations (3.6), (3.9), and (3.18), we obtain

$$J_2 = \frac{\tau^2}{3} = \frac{4}{3} \tau^2, \quad J_3 = \frac{16}{27} \tau^3, \quad A^2 = \frac{4}{3}, \quad B^3 = \frac{16}{27}, \quad (5.1)c-h$$

$$\xi = \frac{2}{\sqrt{3}}, \quad r = \frac{\sqrt{2}}{2}$$

For each test the axial deformation is measured against the differential stress ($\sigma_1 - \sigma_3$), applied at various 'lateral' pressures σ_3 . Therefore, to use the experimental data, we express the differential stress in terms of D_{11} . Using equations (2.19), (3.5), (3.16), and (5.1)c,d, we obtain

$$D_{11}^p = \frac{\sqrt{3}}{3} \lambda \left\{ 1 + \frac{1}{2} \frac{\partial F}{\partial p} - \frac{2}{3} \frac{\tau}{p} + \frac{\sqrt{3}}{3} \frac{\tau_c}{p} \right\} \quad (5.2)$$

For constant lateral pressure σ_3 , using equations (3.3) and (3.4), we have

$$\dot{p} = \frac{2}{3} \dot{\tau} \quad (5.3)$$

Substitution of (5.1) and (5.3) into (3.17) yields

$$\lambda = \frac{\dot{\tau} \left(\frac{2}{\sqrt{3}} - \frac{2\sqrt{3}\partial F}{9\partial p} \right)}{\frac{\partial F}{\partial \gamma} + \frac{p_0}{p} \left(\frac{\sqrt{3}}{2} \frac{\partial F}{\partial p} + \frac{\tau_c}{p} - \frac{2}{\sqrt{3}} \frac{\tau}{p} \right) \frac{\partial F}{\partial \Delta}} \quad (5.4)$$

Therefore equation (5.2) becomes

$$D_{11}^p = \frac{\dot{\tau} \left(\frac{2}{3} - \frac{2\sqrt{3}\partial F}{9\partial p} \right) \left(1 + \frac{1}{2} \frac{\partial F}{\partial p} - \frac{2}{3} \frac{\tau}{p} + \frac{\sqrt{3}}{3} \frac{\tau_c}{p} \right)}{\frac{\partial F}{\partial \gamma} + \frac{\rho_0}{\rho} \left(\frac{\sqrt{3}}{2} \frac{\partial F}{\partial p} + \frac{\tau_c}{p} - \frac{2}{\sqrt{3}} \frac{\tau}{p} \right) \frac{\partial F}{\partial \Delta}} \quad (5.5)$$

Note that in the present case,

$$\dot{\gamma} = \lambda \quad (5.6)$$

From Hooke's law and since σ_3 is kept constant, it follows that

$$D_{11}^e = \frac{\dot{\tau}}{K_e} \quad (5.7)$$

where K_e is the Young modulus of the material. Substituting from (5.5) and (5.7) into (2.5), we get the expression for the total rate of deformation in terms of $\dot{\tau}$ and the material parameters. Using this expression, the slope of the differential stress, axial strain curve is written as

$$K = \frac{(\sigma_1 - \sigma_3) \dot{\tau}}{D_{11}} \quad (5.8)$$

$$= \left\{ \frac{1}{K_e} + \frac{\left(\frac{1}{3} - \frac{\sqrt{3}}{9} \frac{\partial F}{\partial p} \right) \left(1 + \frac{1}{2} \frac{\partial F}{\partial p} - \frac{2}{3} \frac{\tau}{p} + \frac{\sqrt{3}}{3} \frac{\tau_c}{p} \right)}{\frac{\partial F}{\partial \gamma} + \frac{\rho_0}{\rho} \left(\frac{\sqrt{3}}{2} \frac{\partial F}{\partial p} + \frac{\tau_c}{p} - \frac{2}{\sqrt{3}} \frac{\tau}{p} \right) \frac{\partial F}{\partial \Delta}} \right\}^{-1}$$

Figure 3 is a schematic representation of equation (5.8).

6. RESULTS AND DISCUSSION

Experimental data have been used to evaluate the material parameters in the constitutive equation (5.8) for the case of the conventional triaxial state of stress. These parameters include the distortional hardening, $\frac{\partial F}{\partial \gamma}$, the dilatancy hardening, $\frac{\partial F}{\partial \Delta}$, the change in resistance to flow with confining pressure, $\frac{\partial F}{\partial p}$, and the elastic modulus, K_e . All these parameters, in general, depend on many factors, the most important ones being pressure, temperature, and strain-rate.

The effects of pressure and temperature have been studied rather extensively by many investigators; e.g., Griggs, Turner, and Heard (1960), Paterson (1970), Balderman (1974), Stesky et al. (1974), Tullis and Yund (1977), Evans and Goetze (1979), Caristan (1982), and Wong (1982).

The early work of Griggs, Turner, and Heard (1960) is a thorough study of the effect of temperature on the deformation of a wide variety of rocks under high confining pressures. A review of more recent research on high-temperature deformation of rocks and minerals is given by Tullis (1979). Although the degree of sensitivity to temperature is different for different rocks and minerals, the overall influence seems to be the same. Decrease in strength and cataclastic deformation and increase in ductility are observed with a rise in temperature.

Increasing pressure tends to increase strength and ductility; Paterson (1970) and Heard (1976). It promotes ductility by

inhibiting the opening of cracks and the sliding of faults. The effect of pressure on rock-strength (i.e. on peak stress) is more pronounced in the brittle regime. While high-temperature creep of rocks is relatively insensitive to pressure, a negative pressure sensitivity of strength is reported by Caristan (1982) for Maryland diabase in the brittle- ductile transition regime.

Another important factor affecting the deformation process in rocks is pore pressure. This effect is directly related to the dilatancy and therefore should be more pronounced for brittle failure. It usually has an effect opposite to that of the confining pressure, and hence the confining pressure minus the pore pressure is used as the effective pressure; Byerlee and Brace (1972). However, the importance of this depends on the strain-rate as compared with the permeability of the fissured rock, and on whether or not the rock is saturated. For example, a high permeability and a low deformation rate allow the flow of fluid from the surroundings into the fractured rock, and so the concept of effective stress is applicable. On the other hand, if the combined effect of permeability and strain-rate does not lead to 'fast' flow of fluid into the fractured zone, the resistance of the material to deformation is believed to increase, i.e. dilatancy hardening; Rice (1975), Rice and Rudnicki (1979), and Rudnicki (1983). If the fractured zone is already saturated, then small permeability causes weakening if there is densification, and

hardening if there is dilatancy.* Therefore, the coupling of pore fluid diffusion and rock deformation also introduces a time-dependency in the response of the brittle rock during deformation. A review of pore pressure effects in rock deformation is given by Martin (1979).

Strain-rate, roughly speaking, is observed to have an effect opposite to temperature. That is, decreasing the strain-rate causes ductility to increase and strength to decrease; e.g., Heard (1963, 1972), Heard and Raleigh (1972), Rutter (1972), and Balderman (1974). More precisely, the influence of strain-rate depends on the type of deformation mechanism. For example, at low pressures and temperatures, where the mechanism of deformation is cataclastic, rate-dependence is very small, while at higher pressures, and especially at elevated temperatures, this dependence is significant; Heard (1963) and Heard and Raleigh (1972). The strength of Maryland diabase has been observed not to change appreciably with the strain-rate in the brittle regime but to decrease with decreasing strain-rate in the creep and transitional regimes; Caristan (1982). Steady-state flow prevails at high temperatures and low strain-rates; e.g., Heard (1972).

Often, the main purpose of laboratory experiments is to simulate conditions at crustal depths. Due to the relatively fast rate of

*This phenomenon is most vivid in saturated cohesionless sands, where a tendency toward densification may lead to a complete loss of instantaneous strength, i.e. liquefaction; see Nemat-Nasser and Shokooh (1979).

loading in these tests, the measured strength and the pressure and temperature obtained for the brittle-ductile transition are always considerably larger than field evidence seems to suggest; Heard (1960), Paterson (1970), and Rutter (1972).

Shallow earthquakes usually occur at depths of up to 20 km. The confining pressure and temperature at these depths could be as high as 10 kb (for compressive tectonic regions) and $\sim 400-600^{\circ}\text{C}$, depending on the geological structure and the metamorphism of the rock. For example, Heard (1976) reports ranges of $250-400^{\circ}\text{C}$ at 15 km and $450-600^{\circ}\text{C}$ at 30 km in depth for the continental crust, based on the findings of several researchers. Strain-rates across geological faults could vary within a wide range, depending on the tectonic velocity within the region and the geometry of the fault; Sibson (1977). The largest strain-rate believed attainable in nature, accompanying quasi-static crustal deformation, is still orders of magnitude smaller than the laboratory ones. As far as the pore pressure is concerned, considering the probable crushed and porous nature of the material, faults could be a suitable conduit of water, even in dry regions. Accordingly, there is no doubt that a thorough study of the effect of the above factors on the behavior of both intact and crushed rocks is essential for a better understanding of crustal deformation.

Laboratory investigations of pre- and post-failure flow and fracture of rocks have produced large amount of significant data; see e.g., Griggs, Turner, and Heard (1960), Heard (1960, 1963), Paterson

(1970), Heard and Raleigh (1972), Rutter (1972), and Tullis and Yund (1977) for data on the pre-failure regime, and Wawersik and Fairhurst (1970), Wawersik and Brace (1971), and Rummel, Alheid, and Frohn (1978) for data on the post-failure regime. Therefore, satisfactory theories could be developed with these and similar experimental data as guides.

The equations developed in Section 5 are used with some of the experimental results to investigate the effects of pressure and temperature, and the combined effect of both, on the material parameters, $\frac{\partial F}{\partial p}$, $\frac{\partial F}{\partial \Delta}$, $\frac{\partial F}{\partial \gamma}$ (through α and $\hat{\rho}$), and K_e in the constitutive equation (5.8). Stress-strain curves are then developed for certain rocks.

6.1. Pressure Effect

For illustration, we use the experimental stress-strain curves on granite at various pressures obtained by Rummel, Alheid, and Frohn (1978) (see Figure 4a). The numerical values of the corresponding parameters obtained for the theoretical stress-strain curves in Figure 4b are listed in Table 1 and plotted in Figures 5a-d. A quick look at the data points in these figures indicates that the effect of pressure on all the parameters decreases as the pressure increases. Therefore, we use exponential expressions of the following form to represent the effect of pressure on these parameters:

$$C_0 + C_1 e^{-C_2 \sigma_3} \quad (6.1)$$

where C_0 , C_1 , and C_2 are constants. Based on the data in Table 1, we obtain

$$\frac{\partial F}{\partial p}(\sigma_3) = 0.8 + 0.6 e^{-1.8\sigma_3} \quad (6.2)$$

$$\frac{\partial F}{\partial \Delta}(\sigma_3) = 2750 - 2550 e^{-0.95\sigma_3} \quad (6.3)$$

$$\alpha(\sigma_3) = 775 - 500 e^{-3\sigma_3} \quad (6.4)$$

$$\hat{p}(\sigma_3) = 40 + 120 e^{-4\sigma_3} \quad (6.5)$$

Equations (6.2)-(6.5) are shown graphically in Figures 5a-d (solid curves), along with the corresponding data points. The only remaining material parameter in equation (5.8) is K_e , the elastic modulus, or alternatively, the slope of the stress-strain curve at zero strain. According to Figure 4a the initial slope does not change appreciably with pressure. However, a slight increase in the slope with lateral pressure is noticeable. In general, an increase of the elastic modulus with pressure is expected, due to closure of microcracks. The following expression is used to describe this dependency:

$$K_e(\sigma_3) = 280 (1 - 0.1 e^{-0.9\sigma_3}) \quad (6.6)$$

Using equations (6.2)-(6.6) in (5.8), the corresponding theoretical stress-strain curves are obtained and presented in Figure 4b.

Examination of Figures 5a-d reveals the following:

a) The change of flow resistance with pressure, $\frac{\partial F}{\partial p}$ (which is a measure of internal friction), is a decreasing function of pressure (Figure 5a). The Coulomb theory of failure predicts a constant coefficient of friction, and Mohr's theory predicts one which decreases with pressure. These theories, however, are satisfactory for relatively low confining pressures and when the state of stress is not too complex.

b) The variation of parameter $\frac{\partial F}{\partial \Delta}$ is shown in Figure 5b. An almost linear change in this parameter is observed for lower pressures. This dependency seems to be reduced at intermediate pressures and the curve levels off at higher pressures.

c) The distortional hardening parameter, $\frac{\partial F}{\partial \gamma}$, seems to be an increasing function of pressure at low pressures (e.g., $\sigma_3 < 0.5$ kb), and to be pressure-independent at higher pressures. This conclusion is embedded in Figures 5c,d which show the variation of distortional hardening coefficients α and $\hat{\rho}$, respectively. The dependence of α on pressure, as shown in Figure 5c, seems to be significant for lateral pressures greater than ~ 0.5 kb, while for lower pressures, σ_3 is an increasing function of pressure. This is, perhaps, an indication of low pressure-sensitivity in the brittle regime of the deformation process, which was discussed earlier in light of experimental results. The hardening exponent $\hat{\rho}$ is a decreasing function of pressure for lower pressures (0-0.5 kb) and is constant for higher pres-

tures (Figure 5d).

d) The initial slope of the stress-strain curves in Figures 4a,b seems to be a weak function of pressure. This is probably due to the fact that this material has been originally intact and relatively flawless. A pronounced increase in the moduli with pressure is expected for rocks with initial flaws and microcracks.

In Figures 5a-d it is observed that all curves level off beyond a certain lateral pressure σ_3 . This pressure sensitivity of material parameters at low pressures and low sensitivity at higher pressures, is in agreement with experimental results.

Based on the variation of the parameters with pressure, stress-strain curves for other confining pressures can be obtained. This is especially useful in determining the pressure at which the transition from brittle to ductile behavior occurs. As can be seen from Figure 4a, the granite rock tested indicates a brittle behavior for all confining pressures used in the test (up to 3 kb), and the post-peak drop in stress is pronounced even at 3 kb pressure. Dilatancy, however, diminishes with confining pressure. This is observed in experiments on rocks by several researchers; e.g., Brace, Paulding, and Scholz (1966), Scholz (1968), Edmond and Paterson (1972), and Rummel, Alheid, and Frohn (1978).

At the brittle-ductile transition, the drop in stress disappears. Figure 6 shows the theoretical stress-strain curves at various pressures obtained, using the values of the parameters listed in

Table 1. Based on this figure, the behavior of the considered rock (at room temperature and for loading rate corresponding to the experiment) is estimated to be brittle at 20 kb pressure, and to involve a stress-drop on the order of a few kilobars. Therefore, based on the extrapolation made here, the brittle-ductile transition pressure, under the conditions of this experiment (Rummel, Alheid, and Frohn, 1978), is predicted to be somewhat above 20 kb. However large, this value seems to be consistent with experimental results. For example, Byerlee and Brace (1969) report unstable faulting of various rocks at room temperature and 7-10 kb confining pressure. Byerlee (1967), based on extrapolation of frictional and shear strength data, suggests 10 kb as the brittle-ductile transition pressure for Westerly granite. Brittle shear fracture is observed in some materials by Bridgman (1936) at normal stresses as high as 50 kb. Of course, compared with the transition pressure within the crust, a value of 20 kb is too large. However, if we include the effect of high crustal temperatures (of the order of hundreds of degrees C), low geological strain-rates (about 10^{-10} - 10^{-15} /sec versus 10^{-1} - 10^{-6} /sec for most laboratory experiments), and other factors contributing to ductility, the predicted value appears reasonable; Brace and Byerlee (1970).

Figure 7 shows the theoretical volumetric strain curves for granite at various pressures as functions of axial strain. The solid curves correspond to pressures shown in Figures 4a,b and the dotted ones are obtained for higher pressures, based on extrapolation. A slight initial compaction is observed for all pressures. The low

level of compaction must be due to the originally non-porous nature of the rock. Dilatancy, that is, plastic volumetric expansion, on the other hand, reaches an appreciable level. As can be seen from Figure 7, both the magnitude and the rate of dilatancy are larger at lower pressures. This is in agreement with the experimental results discussed earlier. The onset of dilatancy is also pressure-dependent. The ratio of the stress at which dilatancy begins to the peak stress is given in Table 2 for pressures corresponding to Figure 4b. This ratio varies between 0.4-0.7 for the considered experiment. Laboratory experiments on various rocks suggest that dilatancy in rocks begins at stresses of approximately half the peak stress; e.g., Wawersik and Fairhurst (1970), Wawersik and Brace (1971), Brace (1976), and Rummel, Alheid, and Frohn (1978).

6.2. Temperature Effect

To incorporate the effect of temperature, we use the results of experiments on granite and basalt by Griggs, Turner, and Heard (1960), performed at 5 kb pressure and at temperatures ranging from room temperature to 800 °C. The experimental curves are shown in Figures 8a,b for granite and basalt, respectively, and the corresponding numerical values of parameters $\frac{\partial F}{\partial p}$, $\frac{\partial F}{\partial \Lambda}$, α , and $\hat{\rho}$ are listed in Tables 3 and 4. To study the dependence of various parameters on temperature, they are plotted in Figures 9a-d for both rocks. From these figures the following conclusions are obtained:

a) The internal friction parameter, $\frac{\partial F}{\partial p}$, is a decreasing function of temperature. This is probably due to the smoothing effect that temperature has on the sliding surfaces (see Figure 9a). This drop with temperature, however, seems to be faster at higher temperatures. This may be due to a change in the deformation mechanism at elevated temperatures. From Figure 9a, we take 400 °C as the temperature above which this parameter begins to decrease substantially with increasing temperature, for both granite and basalt. Based on this reference temperature, the following relations seem to describe the variation of $\frac{\partial F}{\partial p}$ with temperature for the two rocks:

$$\frac{\partial F}{\partial p} (T) = \begin{cases} 0.9 - 0.13\left(\frac{T}{400}\right)^2, & \text{(granite)} \\ 0.8 - 0.08\left(\frac{T}{400}\right)^2, & \text{(basalt)} \end{cases} \quad (6.7)_{a,b}$$

b) Figure 9b shows that data points do not follow any clear pattern for the variation of $\frac{\partial F}{\partial \Delta}$ with temperature. This may be due to the fact that the complete post-peak behavior of the rock is not known for the set of experimental results used here. Hence, we assume that this parameter is temperature independent and use the following constant values:

$$\frac{\partial F}{\partial \Delta} (T) = \begin{cases} 1050, & \text{(granite)} \\ 550, & \text{(basalt)} \end{cases} \quad (6.8)_{a,b}$$

Dilatancy itself, however, decreases with temperature. This is because of the effect that temperature has on enhancing ductility and preventing microcrack formation.

c) The parameters α and $\hat{\rho}$ in the distortional hardening expression are decreasing functions of temperature for both rocks, as can be seen from the data points in Figures 9c,d. The following relations are chosen to fit the data points:

$$\alpha(T) = \begin{cases} 75 + 170 e^{-0.0043T}, & \text{(granite)} \\ 6 + 37 e^{-0.0055T}, & \text{(basalt)} \end{cases} \quad (6.9)_{a,b}$$

$$\rho(T) = \begin{cases} 5 + 25 e^{-0.004T}, & \text{(granite)} \\ 50 e^{-0.004T}, & \text{(basalt)} \end{cases} \quad (6.10)_{a,b}$$

The appreciable effect that temperature has on reducing both the initial distortional hardening parameter, α , and the rate of hardening, defined by $\hat{\rho}$, should probably be attributed to the lesser entanglement and faster removal of dislocations at higher temperatures.

d) The variation of the initial slope of the stress-strain curves with temperature is represented by the following relations:

$$K_0(T) = \begin{cases} 400 \left(1 - \frac{T}{1200}\right), & \text{(granite)} \\ 700 \left(1 - \frac{T}{1100}\right), & \text{(basalt)} \end{cases} \quad (6.11)_{a,b}$$

Based on equations (6.7)-(6.11), or equivalently, on Figures 9a-d, the corresponding theoretical stress-strain curves are developed for both granite and basalt. These are presented in Figures 10a,b, respectively.

No attempt is made here to discuss the brittle-ductile transition temperature of these two rocks using the results of our theory. In fact, since we have treated the temperature as a parameter, have not explored the possibility of other deformation mechanisms at elevated temperatures, and also have ignored rate effects at large temperatures, we are in no position to draw any conclusions on the value of the transition temperature. This is because the mechanism of deformation at high temperatures changes from basically microcracking and faulting to one of dislocation glide and climb, which is rate-controlled and highly temperature-sensitive; Weertman (1978).

6.3. Depth Effect

Next we consider the combined effect of pressure and temperature. In particular, we are interested in the deformation process at shallow crustal depths. We assume that pressure and temperature affect deformation independently. We also assume constant pressure and temperature gradients within the crust. For example, we use a pressure gradient of 0.25 kb/km, and a temperature gradient of 30 °C/km. The 30 °C/km temperature gradient is large compared to the 10-20 °C/km, usually taken for the continental crust. However, for illustration, the above value is chosen, assuming the temperature distribution to be higher in shear zones and earthquake faults, due to possible heat anomaly there. The pressure σ_3 and the temperature T are, therefore, expressed as

$$\sigma_3(X_1) = 0.25 X_1 \quad (6.12)$$

$$T(X_1) = 30 X_1 \quad (6.13)$$

where, in the above relations, X_1 , σ_3 , and T are in units of km, kb, and °C, respectively. Substituting for σ_3 and T , we obtain the following relations for the material parameters in terms of depth X_1 :

$$\frac{\partial F}{\partial p}(X_1) = (0.8 - 0.6 e^{-0.46X_1})(1 - 8 \times 10^{-4} X_1^2) \quad (6.14)$$

$$\frac{\partial F}{\partial \Delta}(X_1) = 2500 - 2000 e^{-0.23X_1} \quad (6.15)$$

$$\alpha(X_1) = (600 - 400 e^{-0.75X_1})(1 + 5 e^{-0.12X_1}) \quad (6.16)$$

$$\hat{\rho}(X_1) = (8 + 24 e^{-X_1})(1 + 5 e^{-0.12X_1}) \quad (6.17)$$

$$k_0(X_1) = (340 - 40 e^{-0.23X_1})(1 - 0.025X_1) \quad (6.18)$$

Figures 11a-e are graphic representations of these relations.

Note that two different sets of experimental data are used to obtain equations (6.14) to (6.18): one set for the temperature effect (Figure 8a) reported by Griggs, Turner, and Heard (1960); and the other set for the pressure and dilatancy effects (Figure 4a) published by Rummel, Alheid, and Frohn (1978). Even though in both tests granite (Westerly granite in the former and Fichtelgebirge

granite in the latter) is used, the two tests are essentially unrelated. In view of this, the assumption that there is no coupling between pressure and temperature, and the fact that rate effects are not included, the results embodied in equations (6.14) to (6.18) should be regarded as illustrative rather than conclusive.

Figure 12 shows our estimate of the stress-strain curves for granite down to a 30 km depth. This figure reveals the pronounced effect that temperature has on lowering the strength, the brittleness, and the dilatancy of this rock (compare Figures 12 and 6). Based on this figure, the rock has its maximum strength at depths of around 15 km. Near the surface, it is brittle and has a low shear strength. This is due to the low confining pressure at shallow depths. It is also observed from Figure 12 that the post-peak stress-drop is larger at smaller depths. This corresponds to larger dilatancy near the surface due to lower pressure, as discussed earlier. At greater depths, on the other hand, especially due to high temperatures, the ductility is greater, and the material attains its maximum strength at larger strains. Dilatancy decreases with depth and is not noticeable beyond a 15 km depth, according to Figure 12. This figure also suggests a maximum differential stress of about 8 kb at a depth of ~15 km for intact granite. The figure, however, is developed from experiments performed at very high loading rates compared to the tectonic ones. Hence, any conclusion based on this figure is appropriate in the event that the strain-rate does not substantially affect the deformation. This could be the case at rela-

tively low temperatures, i.e. for crustal rocks at shallow depths and where the temperature gradient is small. For Westerly granite, Wong (1982) reports low sensitivity to the strain-rate at temperatures up to 600 °C when the strain-rate is in the range 10^{-5} - 10^{-4} /sec. As mentioned earlier, the effect of the strain-rate is important at elevated temperatures (e.g., 450 C assumed at 15 km depth). Thus, the predicted 8 kb differential stress seems to be too large for intact crustal granitic rocks. For temperatures above 500 °C, the rate and viscosity effects must be explicitly included in the constitutive modeling of this kind of rocks. However, treating the strain-rate as a parameter, as we did temperature, we may quantitatively study the effect of the strain-rate on the constitutive functions, and in this manner estimate stress-strain curves for rocks at various strain-rates.

As a final point, we should like to mention that the objective is to develop a general constitutive equation for crustal rocks, and especially for the material within fault zones. The results may then be used for a detailed study of the mechanics of earthquake faulting. The emphasis in the present study has been to incorporate the factors affecting deformation at shallow depths.

ACKNOWLEDGMENT

This work has been supported by the U.S. Air Force Office of Scientific Research under grant no. AFOSR-80-0017 to Northwestern University.

APPENDIX

Selection of the Constitutive Parameters

From equation (5.8) we have, for the slope of the differential stress-axial strain curve,

$$K = \left\{ \frac{1}{K_e} + \frac{\left(\frac{1}{3} - \frac{\sqrt{3}}{9} \frac{\partial F}{\partial p}\right) \left(1 + \frac{1}{2} \frac{\partial F}{\partial p} - \frac{2}{3} \frac{\tau}{p} + \frac{\sqrt{3}}{3} \frac{\tau_c}{p}\right)}{\frac{\partial F}{\partial \gamma} + \frac{\rho_0}{\rho} \left(\frac{\sqrt{3}}{2} \frac{\partial F}{\partial p} + \frac{\tau_c}{p} - \frac{2}{\sqrt{3}} \frac{\tau}{p}\right) \frac{\partial F}{\partial \Delta}} \right\}^{-1} \quad (A.1)$$

A typical response is sketched in Figure (A-1). To find the appropriate values for the material parameters, K_e , $\frac{\partial F}{\partial p}$, $\frac{\partial F}{\partial \Delta}$, and $\frac{\partial F}{\partial \gamma}$, we first make the following assumptions and observations, using this figure:

1. The deformation for very small strain is essentially elastic, even though plastic deformation begins with the onset of loading. This implies that

$$K_e \approx K_0 \quad (A.2)$$

where K_0 is the initial slope of the curve.

2. The hardening effect disappears at large strains, i.e.

$$\frac{\partial F}{\partial \gamma} \rightarrow 0 \quad \text{as } \gamma \rightarrow \infty \quad (A.3)$$

Accordingly, an exponentially decaying form is assumed for $\frac{\partial F}{\partial \gamma}$ as follows:

$$\frac{\partial F}{\partial \gamma} = \alpha e^{-\hat{\rho}\gamma} \quad (\text{A.4})$$

(for further discussion, see Nemat-Nasser and Shokooh, 1980). α and $\hat{\rho}$ in equation (A.4) are material-dependent parameters.

3. At large strains, sliding occurs on failure planes at a constant differential stress, the kinetic shear resistance τ_k , i.e.

$$\tau(\gamma) \rightarrow \tau_k \text{ as } \gamma \rightarrow \infty \quad (\text{A.5})$$

4. Also at large strains, the stress-strain curve levels off, so the slope becomes zero,

$$K \rightarrow 0 \text{ as } \gamma \rightarrow \infty \quad (\text{A.6})$$

Using equations (A.1), and (A.4)-(A.6) we obtain the following results.

$$\frac{\partial G}{\partial p} \rightarrow 0 \text{ as } \gamma \rightarrow \infty \quad (\text{A.7})$$

$$\frac{\partial F}{\partial p} = \frac{4}{3} \frac{\tau_k}{p} - \frac{2}{\sqrt{3}} \frac{\tau_c}{p} \quad (\text{A.8})$$

Substituting (A.8) into (3.16) and using (5.1), we get

$$\frac{\partial G}{\partial p} = \frac{2}{\sqrt{3}} \frac{\tau_k - \tau}{p} \quad (\text{A.9})$$

This equation suggests that the material dilates when the shear stress exceeds the frictional sliding strength, τ_k , and that the

onset of pre-peak dilatancy is marked by $\tau = \tau_k$.

5. At the peak of the stress-strain curve,

$$\gamma = \gamma_m, \quad \tau = \tau_m, \quad K = 0 \quad (\text{A.10})$$

and using (A.1) and (A.9), we get the following expression for α in terms of $\hat{\rho}$ and $\frac{\partial F}{\partial \Delta}$:

$$\alpha = \frac{2}{\sqrt{3}} \frac{\rho_0}{\rho} e^{\hat{\rho} \gamma_m} \frac{\partial F}{\partial \Delta} \frac{\tau_m - \tau_k}{p} \quad (\text{A.11})$$

6. After the onset of microfracturing and in the cataclastic regime, the internal cohesion may be neglected. Therefore, equation (A.8) reduces to

$$\frac{\partial F}{\partial p} \approx \frac{4}{3} \frac{\tau_k}{p} \quad (\text{A.12})$$

Equations (A.2), (A.8), (A.9), (A.11), and (A.12) can be used to obtain numerical values for the parameters. Then, since these parameters do not depend on the state of stress, they can be used in the constitutive equation for the fault material (equation (4.7)) to investigate stable deformation and earthquake instability within the fault.

ACKNOWLEDGMENT

This work has been supported by the U.S. Air Force Office of Scientific Research under grant no. AFOSR-80-0017 to Northwestern University.

REFERENCES

- Balderman, M. A., The effect of strain rate and temperature on the yield point of hydrolytically weakened synthetic quartz, J. Geophys. Res., 79, 1647-1652, 1974.
- Barton, N., Rock mechanics review, the shear strength of rock and rock joints, Int. J. Rock Mech. Min. Sci. & Geom. Abstr., 13, 255-279, 1976.
- Brace, W. F., Direct observation of dilatant voids in rock, in The Effects of Voids on Material Deformation, edited by S. C. Cowin and M. M. Carroll, 1-12, ASME, 1976.
- Brace, W. F., and J. D. Byerlee, California earthquakes: Why only shallow focus? Science, 168, 1573-1575, 1970.
- Brace, W. F., B. W. Paulding, and C. Scholz, Dilatancy in the fracture of crystalline rocks, J. Geophys. Res., 71, 3939-3953, 1966.
- Bridgman, P. W., Shearing phenomena at high pressure of possible importance for geology, J. Geol., 44, 653-669, 1936.
- Byerlee, J. D., Frictional characteristics of granite under high confining pressure, J. Geophys. Res., 72, 3639-3648, 1967.
- Byerlee, J. D., and W. F. Brace, High-pressure mechanical instability in rocks, Science, 164, 713-715, 1969.
- Byerlee, J. D., and W. F. Brace, Fault stability and pore pressure, Bull. Seis. Soc. Amer., 62, 657-660, 1972.
- Caristan, Y., The transition from high temperature creep to fracture in Maryland diabase, J. Geophys. Res., 87, 6781-6790, 1982.
- Carter, N. L., Steady state flow of rocks, Rev. Geophys. Space Phys., 14, 301-360, 1976.
- Carter, N. L., D. A. Anderson, F. D. Hansen, and R. L. Kranz, Creep and creep rupture of granitic rocks, in Mechanical Behavior of Crustal Rocks, Geophys. Mono. Ser. 24, edited by N. L. Carter, M. Friedman, J. M. Logan, and D. W. Stearns, 61-82, AGU, 1981.
- Carter, N. L., and H. G. Ave'Lallemant, High temperature flow of dunite and peridotite, Geol. Soc. Amer. Bull., 81, 2181-2202, 1970.

- Dorris, J. F., and S. Nemat-Nasser, A plasticity model for flow of granular materials under triaxial stress states, Int. J. Solids Struct., 18, 497-531, 1982.
- Edmond, J. M., and M. S. Paterson, Volume changes during the deformation of rocks at high pressures, Int. J. Rock Mech. Min. Sci., 9, 161-182, 1972.
- Evans, B., and C. Goetze, The temperature variation of hardness of olivine and its implication for polycrystalline yield stress, J. Geophys. Res., 84, 5505-5524, 1979.
- Griggs, D. T., F. J. Turner, and H. C. Heard, Deformation of rocks at 500 to 800°C, in Rock Deformation, Mem. 79, edited by D. T. Griggs and J. W. Handin, 39-104, Geol. Soc. Amer., 1960.
- Heard, H. C., Transition from brittle fracture to ductile flow in Solenhofen limestone as a function of temperature, confining pressure, and interstitial fluid pressure, in Rock Deformation, Mem. 79, edited by D. T. Griggs and J. W. Handin, 193-226, Geol. Soc. Amer., 1960.
- Heard, H. C., Effect of large changes in strain rate in the experimental deformation of Yule marble, J. Geol., 71, 162-195, 1963.
- Heard, H. C., Steady-state flow in polycrystalline halite at pressure of 2 kilobars, in Flow and Fracture of Rocks, Geophys. Mono. Ser. 16, edited by H. C. Heard, I. Y. Borg, N. L. Carter, and C. B. Raleigh, 191-209, AGU, 1972.
- Heard, H. C., Comparison of the flow properties of rocks at crustal conditions, Phil. Trans. R. Soc. Lond., A, 283, 173-186, 1976.
- Heard, H. C., and C. B. Raleigh, Steady-state flow in marble at 500 to 800°C, Geol. Soc. Amer. Bull., 83, 935-956, 1972.
- Hill, R., The Mathematical Theory of Plasticity, Oxford University Press, 1950.
- Kirby, S. H., Tectonic stresses in the lithosphere: Constraints provided by the experimental deformation of rocks, J. Geophys. Res., 85, 6353-6363, 1980.
- Kirby, S. H., Rheology of the lithosphere, Rev. Geophys. Space Phys., 21, 1458-1487, 1983.
- Martin, R. J., Pore pressure effects in crustal processes, Rev. Geophys. Space Phys., 17, 1132-1137, 1979.

- Mogi, K., Fracture and flow of rocks under high triaxial compression, J. Geophys. Res., 76, 1255-1269, 1971.
- Mogi, K., Fracture and flow of rocks, Tectonophysics, 13, 541-568, 1972.
- Mróz, Z., Deformation and flow of granular materials, in Theoretical and Applied Mechanics, edited by F. P. J. Rimrott and B. Tabbarok, 119-132, North Holland, Amsterdam, 1980.
- Nemat-Nasser, S., On constitutive behavior of fault materials, in Solid Earth Geophysics and Geotechnology, Proc. ASME Symp., AMD-Vol. 42, edited by S. Nemat-Nasser, 31-37, ASME, 1980.
- Nemat-Nasser, S., and A. Shokooh, A unified approach to densification and liquefaction of cohesionless sand in cyclic shearing, Canadian Geotechnical J., 16, 659-678, 1979.
- Nemat-Nasser, S., and A. Shokooh, On finite plastic flows of compressible materials with internal friction, Int. J. Solids Struct., 16, 495-514, 1980.
- Paterson, M. S., Experimental deformation of minerals and rocks under pressure, in Mechanical Behavior of Materials Under Pressure, edited by H. U. D. Pugh, Chap. 5, Elsevier Publishing Company, Amsterdam, 1970.
- Price, N. J., Fault and Joint Development in Brittle and Semi-Brittle Rock, Pergamon Press, London, 1966.
- Rice, J. R., On the stability of dilatant hardening for saturated rock masses, J. Geophys. Res., 80, 1531-1536, 1975.
- Rice, J. R., and J. W. Rudnicki, Earthquake precursory effects due to pore fluid stabilization of a weakening fault zone, J. Geophys. Res., 84, 2177-2193, 1979.
- Rudnicki, J. W., An inclusion model for processes preparatory to earthquake faulting in Solid Earth Geophysics and Geotechnology, Proc. ASME Symp., AMD-Vol. 42, edited by S. Nemat-Nasser, 38-52, ASME, 1980.
- Rudnicki, J. W., Effect of pore fluid diffusion on deformation and failure of rock, in William Prager Symposium on Mechanics of Geomaterials: Rocks, Concretes, Soils, edited by Z. P. Bazant, John Wiley and Sons, London, 1983, in press.
- Rudnicki, J. W., and J. R. Rice, Conditions for the localization of deformation in pressure-sensitive dilatant materials, J. Mech. Phys. Solids, 23, 371-394, 1975.

- Rummel, F., H. J. Alheid, and C. Frohn, Dilatancy and fracture induced velocity changes in rock and their relation to frictional sliding, Pure Appl. Geophys., 116, 743-764, 1978.
- Rundle, J. B., Models of crustal deformation, Rev. Geophys. Space Phys., 21, 1454-1458, 1983.
- Rutter, E. H., The effects of strain-rate changes on the strength and ductility of Solenhofen limestone at low temperatures and confining pressures, Int. J. Rock Mech. Min. Sci., 9, 183-189, 1972.
- Scholz, C. H., Microfracturing and the inelastic deformation of rock in compression, J. Geophys. Res., 73, 1417-1432, 1968.
- Sibson, R. H., Fault rocks and fault mechanisms, J. Geol. Soc. London, 133, 191-213, 1977.
- Stesky, R. M., W. F. Brace, D. K. Riley, and P.-Y. F. Robin, Friction in faulted rock at high temperature and pressure, Tectonophysics, 23, 177-203, 1974.
- Stuart, W. D., Diffusionless dilatancy model for earthquake precursors, Geophys. Res. Lett., 1, 261-264, 1974.
- Stuart, W. D., Strain softening prior to two-dimensional strike-slip earthquakes, J. Geophys. Res., 84, 1063-1070, 1979.
- Stuart, W. D., Stiffness method for anticipating earthquakes, Bull. Seis. Soc. Amer., 71, 363-370, 1981.
- Tullis, J., High temperature deformation of rocks and minerals, Rev. Geophys. Space Phys., 17, 1137-1154, 1979.
- Tullis, J., and R. A. Yund, Experimental deformation of dry Westerly granite, J. Geophys. Res., 82, 5705-5718, 1977.
- Wawersik, W. R., and W. F. Brace, Post-failure behavior of a granite and diabase, Rock Mech., 3, 61-85, 1971.
- Wawersik, W. R., and C. Fairhurst, A study of brittle rock fracture in laboratory compression experiments, Int. J. Rock Mech. Min. Sci., 7, 561-575, 1970.
- Weertman, J., Creep laws for the mantle of the earth, Phil. Trans. R. Soc. Lond., A. 288, 9-26, 1978.
- Wong, T.-F., Effects of temperature and pressure on failure and post-failure behavior of Westerly granite, Mechanics of Materials, 1, 3-17, 1982.

Table 1: Material parameters in the constitutive equation for granite at various pressures.

σ_3 (kb)	0	0.075	0.17	0.33	0.55
$\partial F/\partial p$	1.60	1.32	1.19	1.07	1.02
$\partial F/\partial \Delta$	820	1270	1460	1650	1860
α	260	365	510	650	620
\hat{p}	1000	130	100	62	49
σ_3 (kb)	0.78	1.08	1.57	2.46	3.00
$\partial F/\partial p$	0.95	0.89	0.85	0.81	0.80
$\partial F/\partial \Delta$	2000	2170	2480	2660	2650
α	720	775	690	714	775
\hat{p}	45	49	40	50	42

Table 2: Ratios of the stress at which dilatancy starts to the peak stress for granite at various pressures.

σ_3 (kb)	0	0.075	0.17	0.33	0.55
τ/τ_{\max}	0.32	0.38	0.42	0.43	0.49
σ_3 (kb)	0.78	1.08	1.57	2.46	3.00
τ/τ_{\max}	0.50	0.52	0.59	0.60	0.62

Table 3: Material parameters in the constitutive equation for granite at various temperatures.

$T(^{\circ}\text{C})$	25	300	500	800
$\partial F/\partial p$	0.90	0.84	0.63	0.41
$\partial F/\partial \Delta$	1060	1090	1280	930
α	230	115	145	95
\hat{p}	27	13	4.0	5.0

Table 4: Material parameters in the constitutive equation for basalt at various temperatures.

$T(^{\circ}\text{C})$	25	300	500	700	800
$\partial F/\partial p$	0.82	0.79	0.66	0.43	0.25
$\partial F/\partial \Delta$	430	730	490	450	670
α	330	75	41	13	10
\hat{p}	45	20	7.0	2.3	2.0

LIST OF FIGURES

- Figure 1: State of stress for different types of faulting ($\sigma_1 > \sigma_2 > \sigma_3$ are the principal stresses):
- Normal faulting,
 - Strike-slip faulting,
 - Thrust faulting.
- Figure 2: The principal \bar{X} - and the \bar{X} - coordinate systems; fault plane is the \bar{X}_2, \bar{X}_3 - plane.
- Figure 3: Graphs of equations (2.4) and (5.8).
- Figure 4a: Experimental stress-strain curves for intact granite at various pressures σ_3 (from Rummel, Alheid, and Frohn, 1978).
- Figure 4b: Theoretical stress-strain curves for intact granite at various pressures σ_3 .
- Figure 5a: Variation of $\frac{\partial F}{\partial p}$ with pressure σ_3 for granite.
- Figure 5b: Variation of $\frac{\partial F}{\partial \Delta}$ with pressure σ_3 for granite.
- Figure 5c: Variation of α with pressure σ_3 for granite.
- Figure 5d: Variation of \hat{p} with pressure σ_3 for granite.
- Figure 6: Theoretical stress-strain curves for intact granite at various pressures σ_3 .
- Figure 7: (Plastic) volumetric strain-axial strain curves for

intact granite at various pressures σ_3 .

Figure 8a: Experimental stress-strain curves for granite at 5 kb pressure σ_3 and various temperatures. (from Griggs, Turner, and Heard, 1960).

Figure 8b: Experimental stress-strain curves for basalt at 5 kb pressure σ_3 and various temperatures. (from Griggs, Turner, and Heard, 1960).

Figure 9a: Variation of $\frac{\partial F}{\partial p}$ with temperature for granite and basalt at 5 kb pressure.

Figure 9b: Variation of $\frac{\partial F}{\partial \Delta}$ with temperature for granite and basalt at 5 kb pressure.

Figure 9c: Variation of α with temperature for granite and basalt at 5 kb pressure.

Figure 9d: Variation of \hat{p} with temperature for granite and basalt at 5 kb pressure.

Figure 10a: Theoretical stress-strain curves for granite at 5 kb pressure and various temperatures.

Figure 10b: Theoretical stress-strain curves for basalt at 5 kb pressure and various temperatures.

Figure 11a: Variation of $\frac{\partial F}{\partial p}$ with depth for granite.

Figure 11b: Variation of $\frac{\partial F}{\partial \Delta}$ with depth for granite.

Figure 11c: Variation of α with depth for granite.

Figure 11d: Variation of $\hat{\rho}$ with depth for granite.

Figure 11e: Variation of K_0 with depth for granite.

Figure 12: Stress-strain curves for granite at various depths.

Figure A-1: Schematic diagram showing a typical stress-strain curve for rocks in conventional triaxial loading.

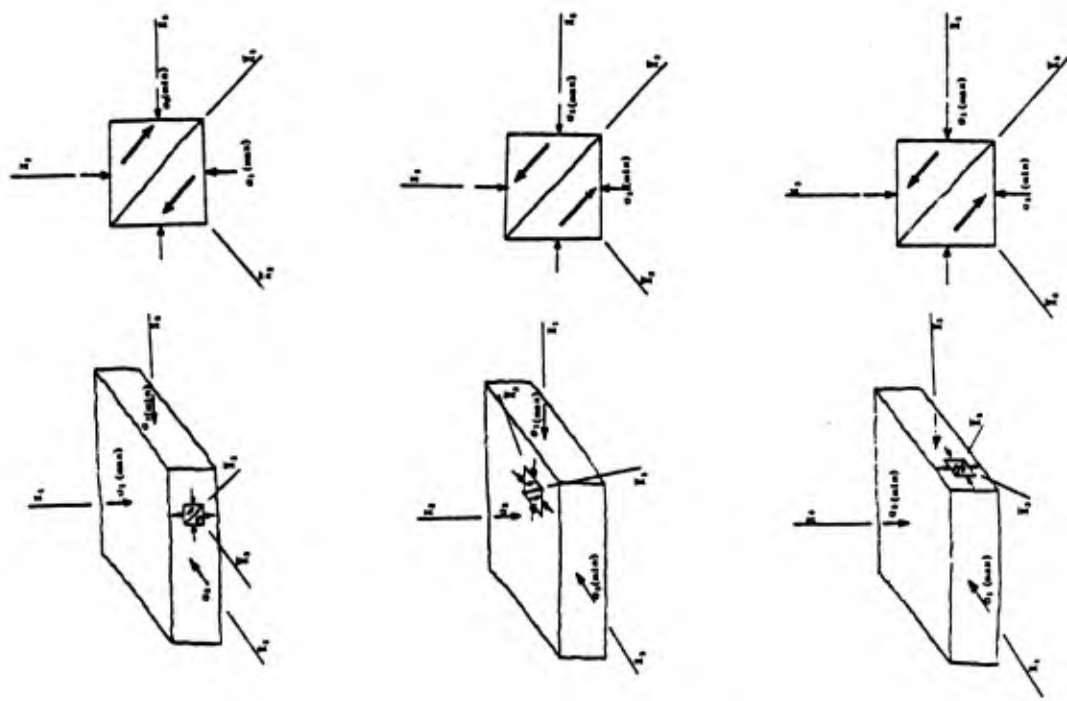


Figure 1

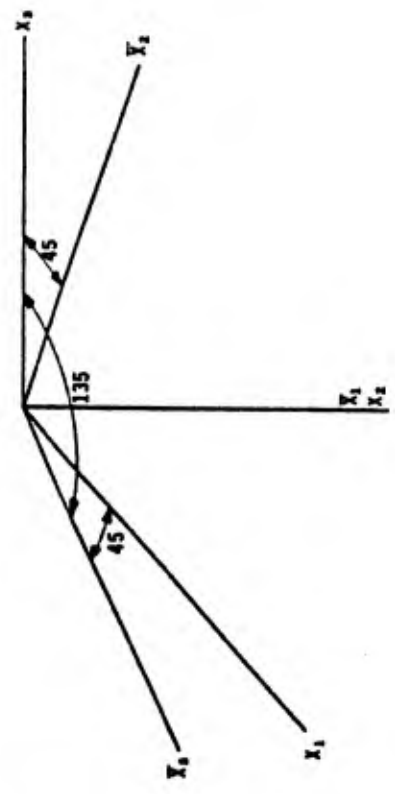


Figure 2

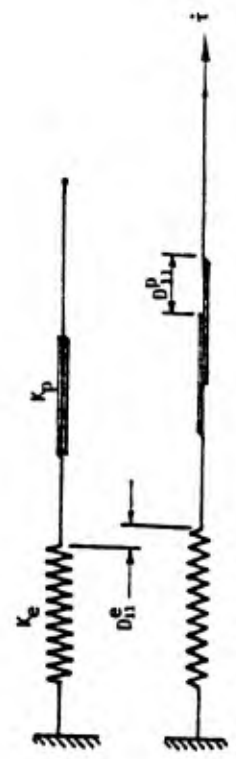


Figure 3

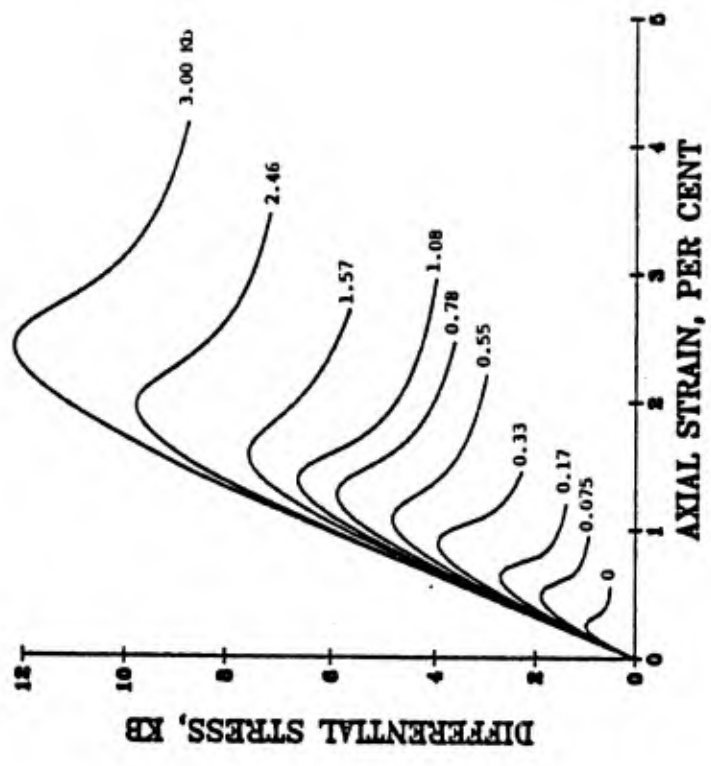


Figure 4b

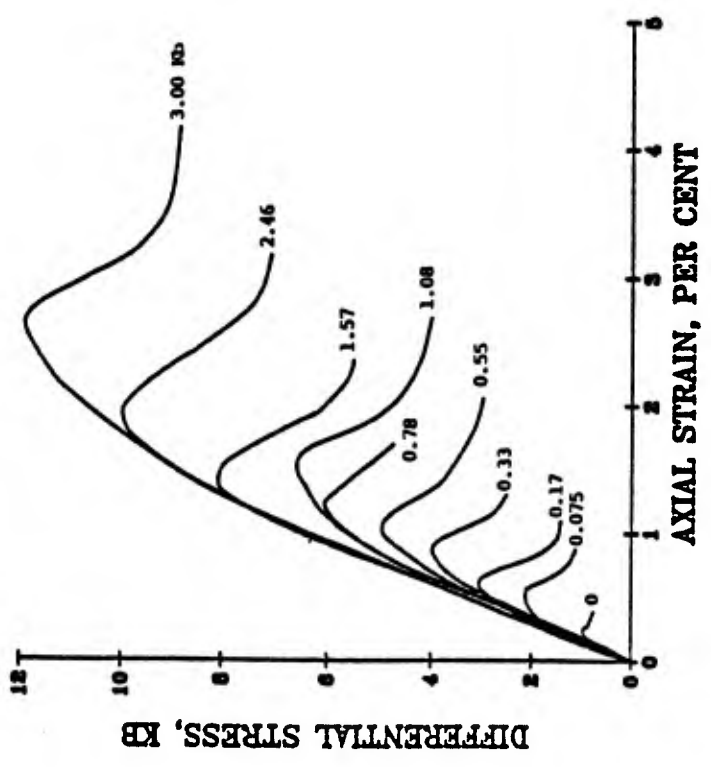


Figure 4a

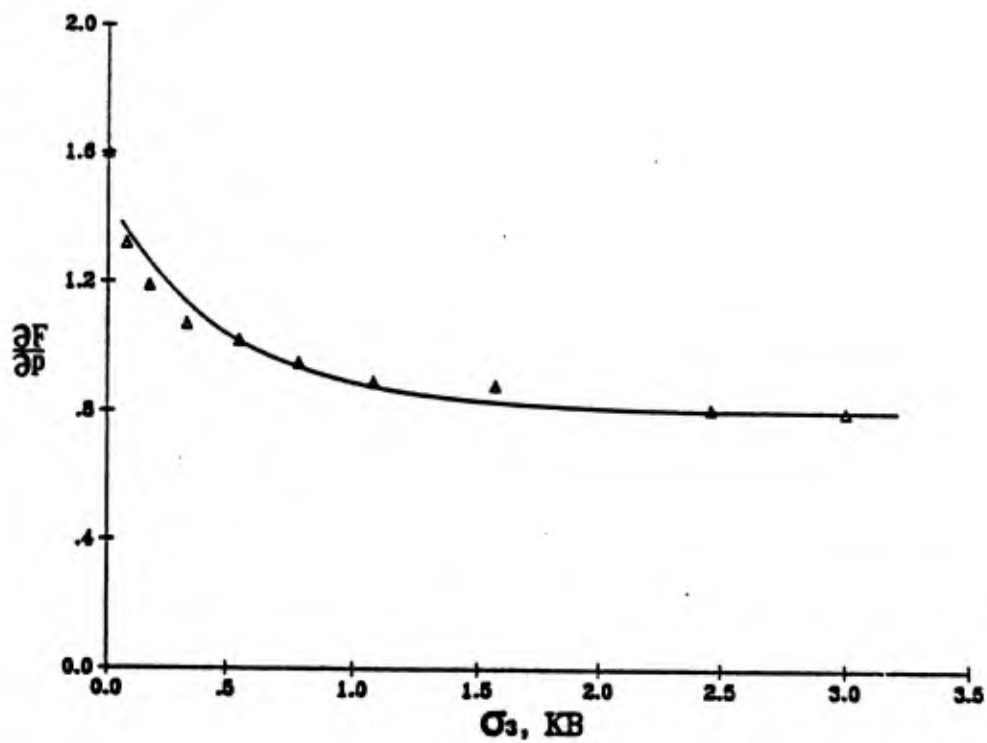


Figure 5a

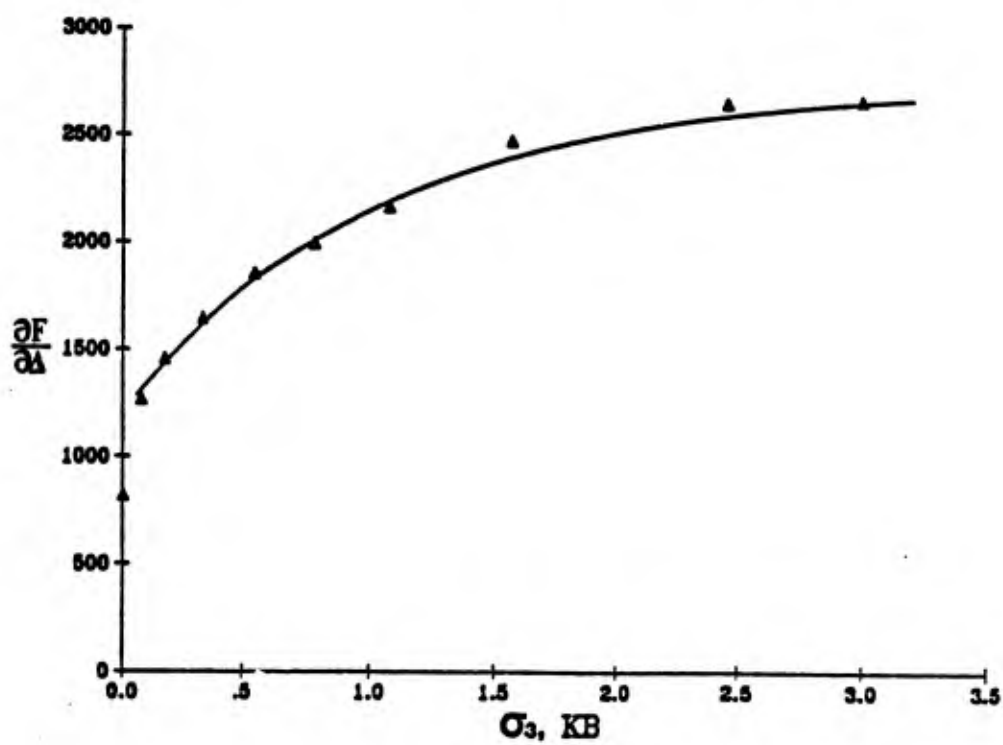


Figure 5b

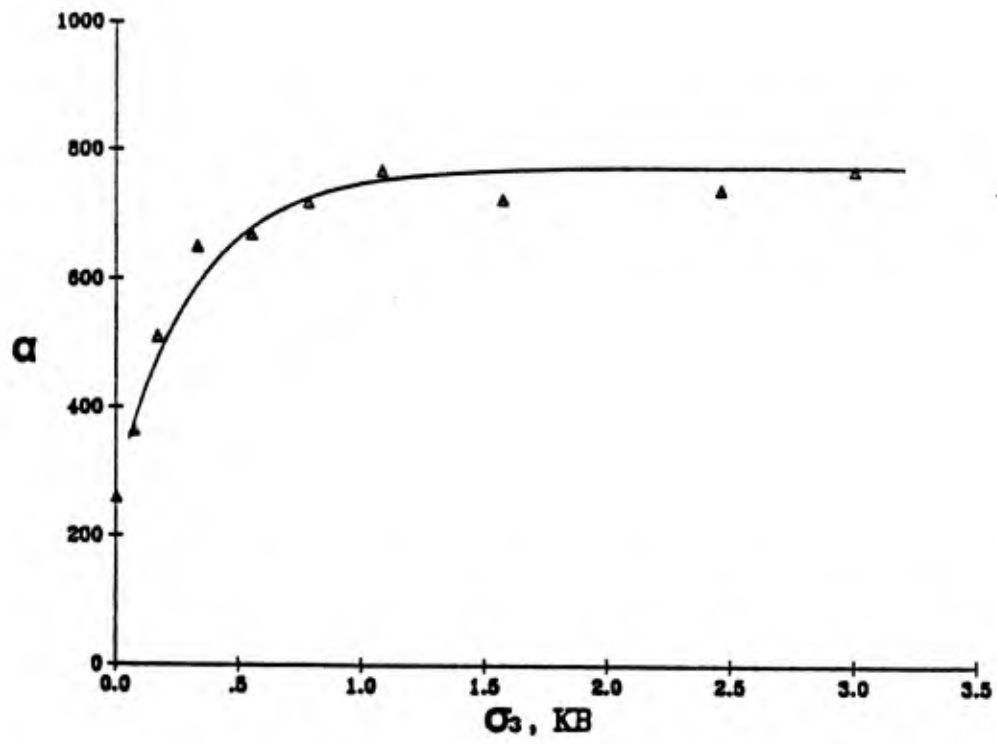


Figure 5c

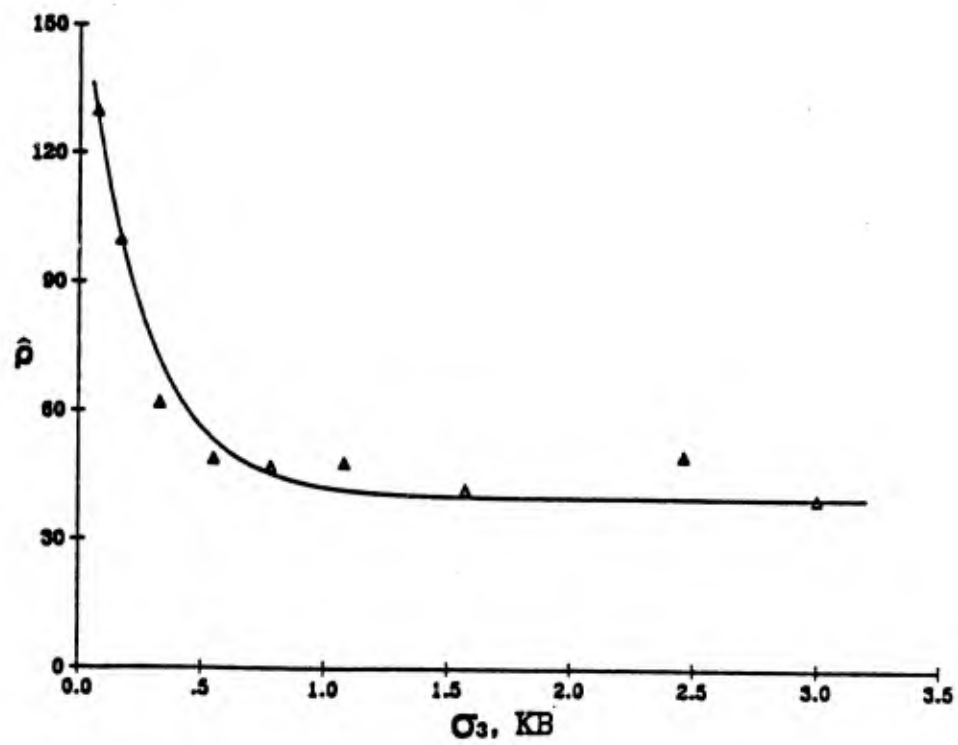


Figure 5d

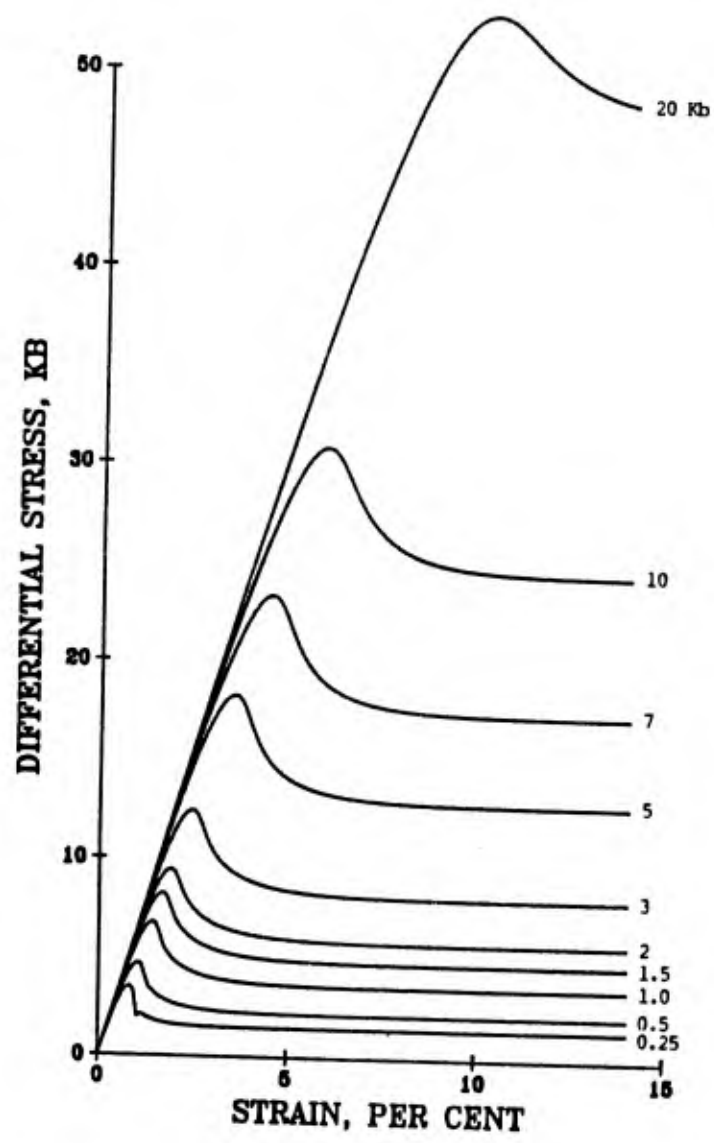


Figure 6

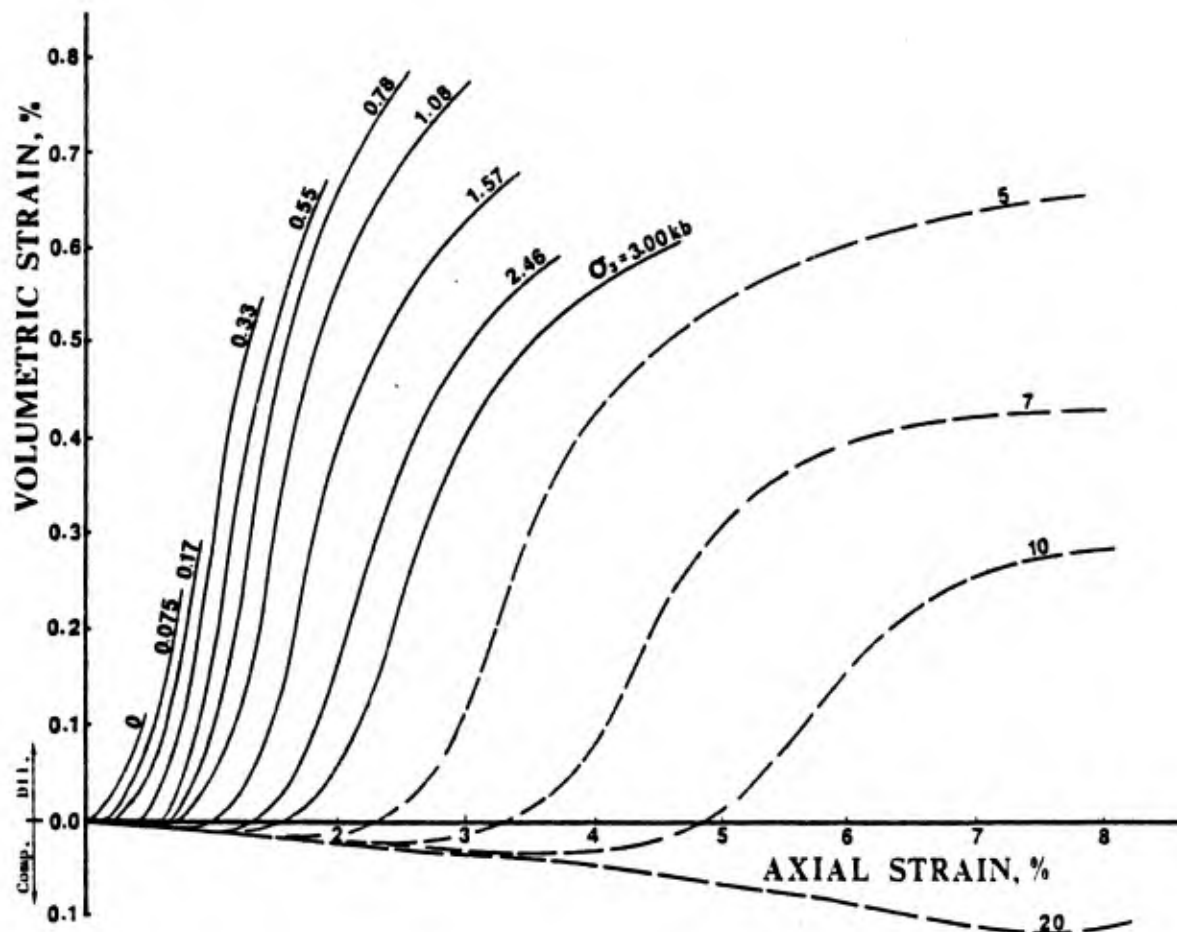


Figure 7

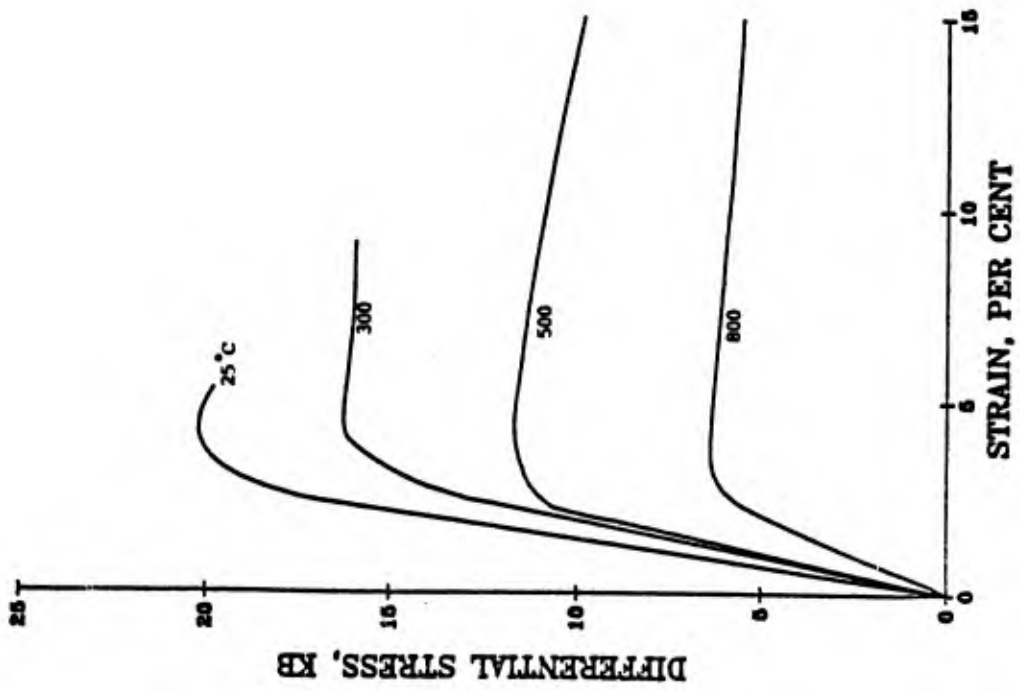


Figure 8a

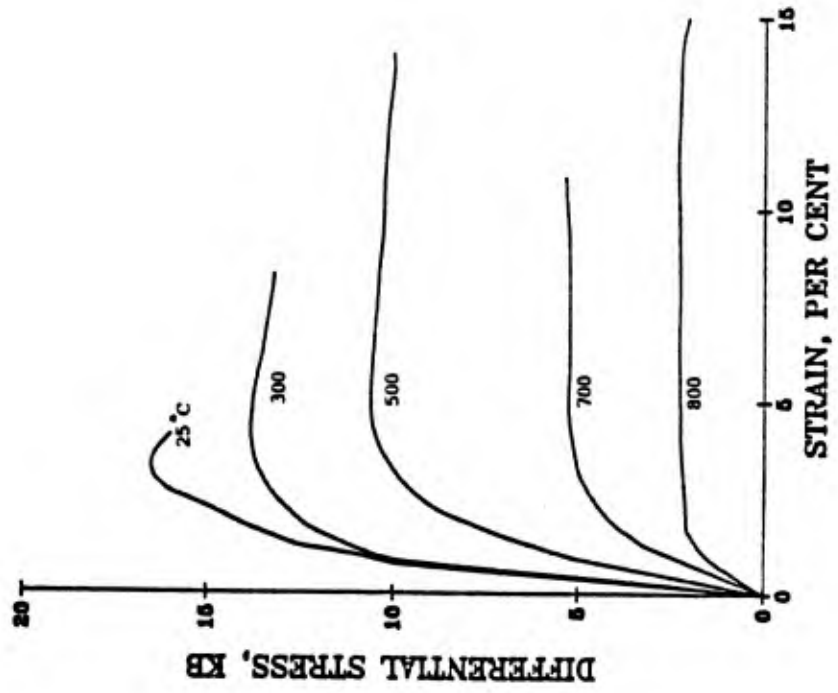


Figure 8b

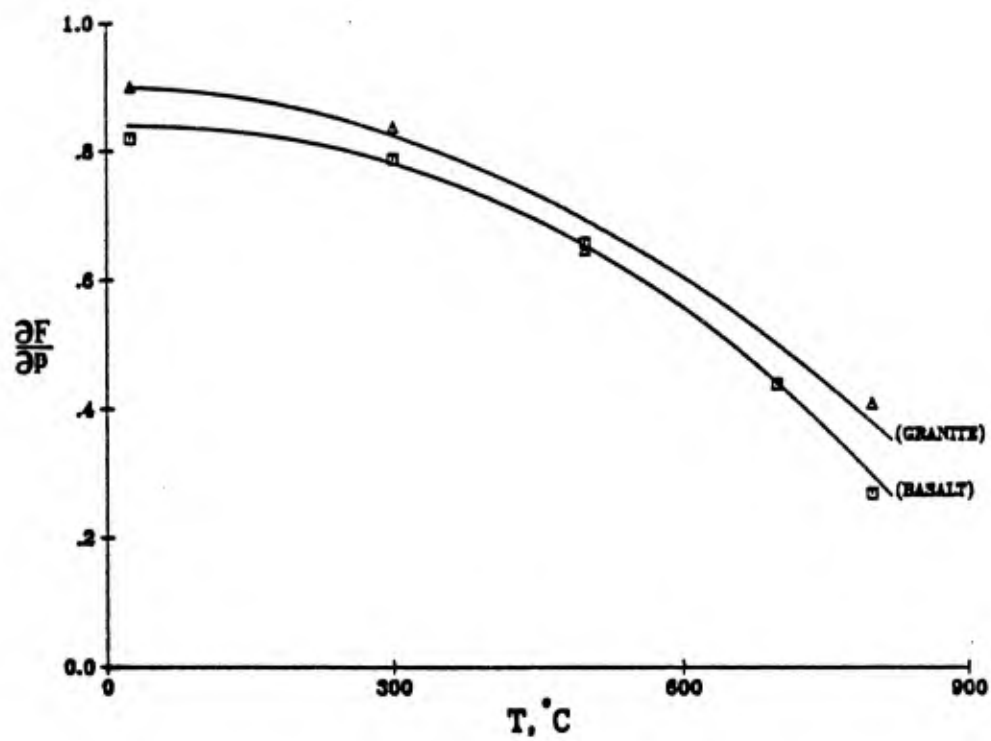


Figure 9a

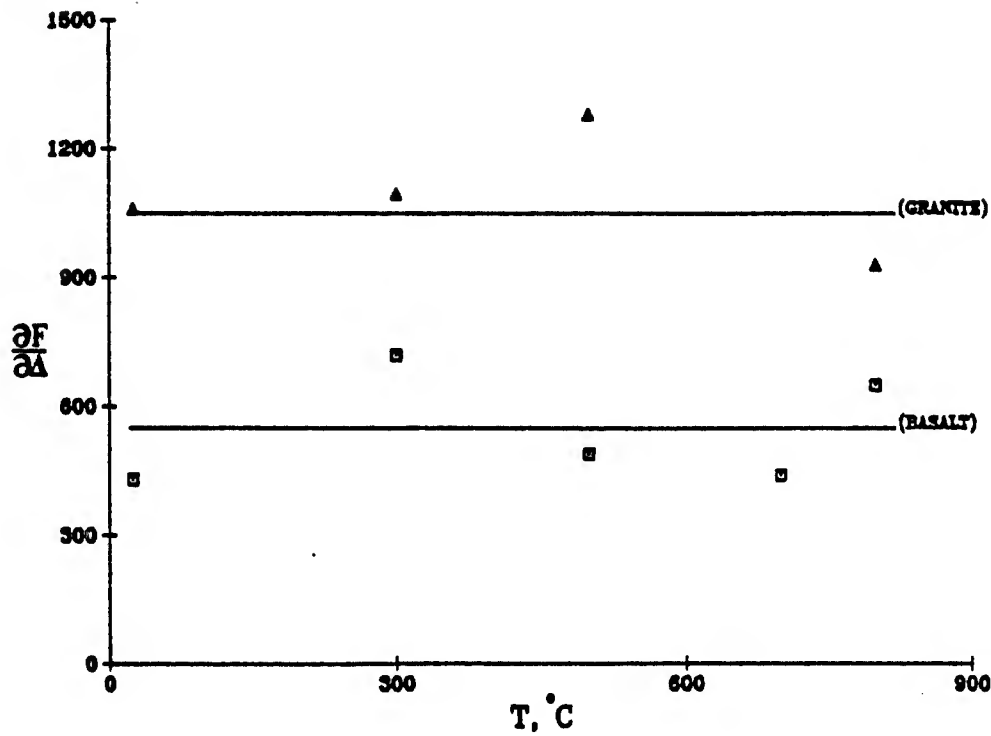


Figure 9b

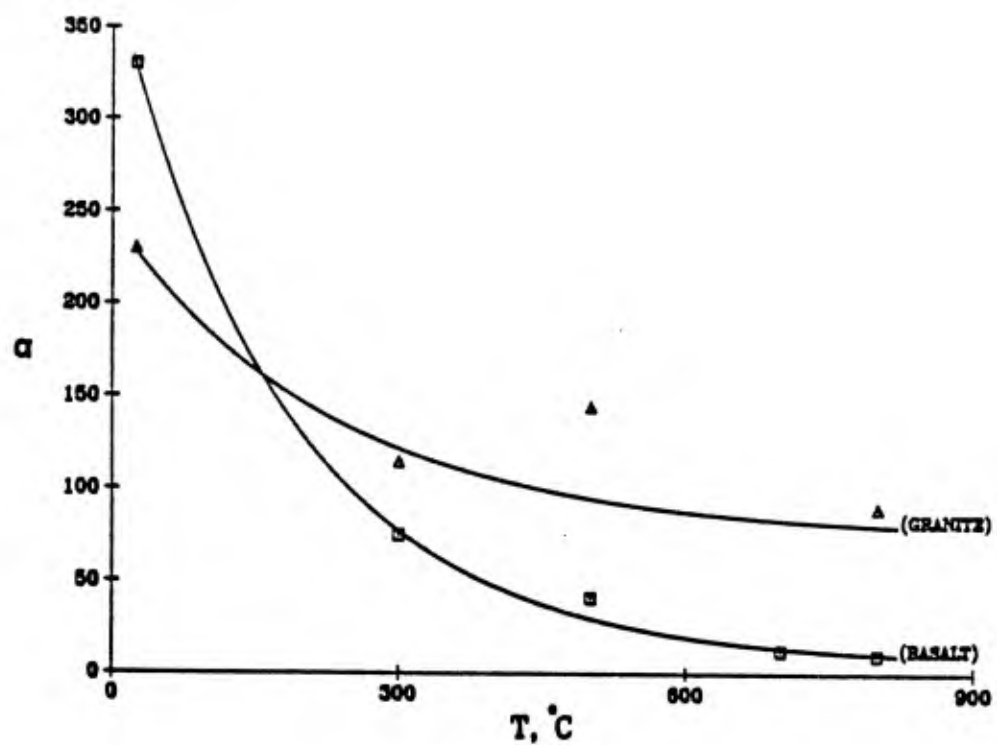


Figure 9c

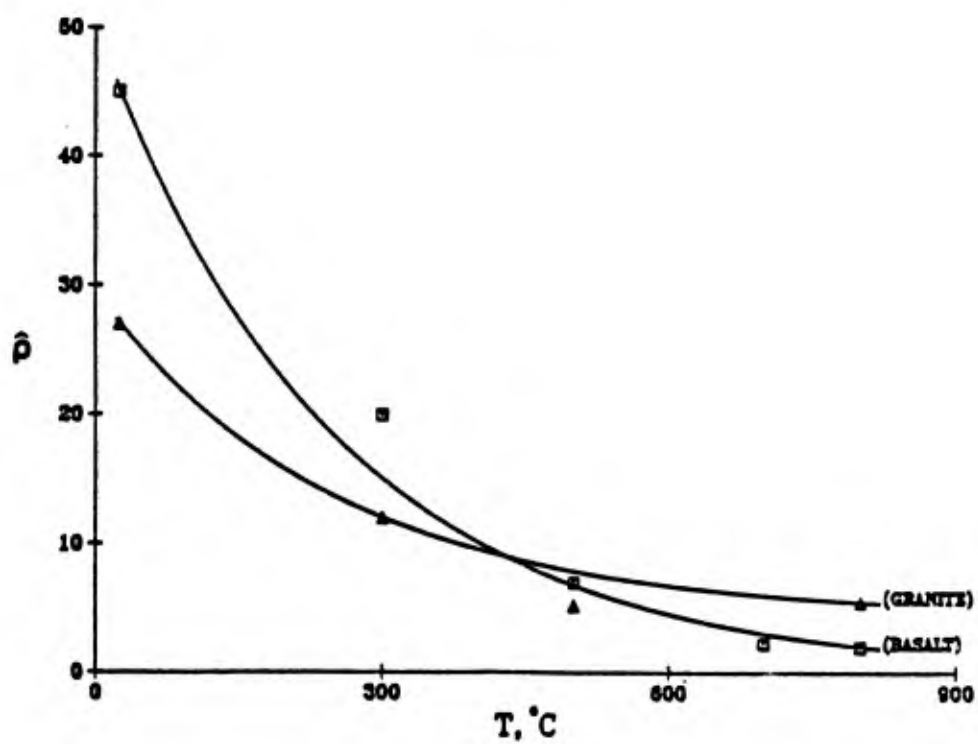


Figure 9d

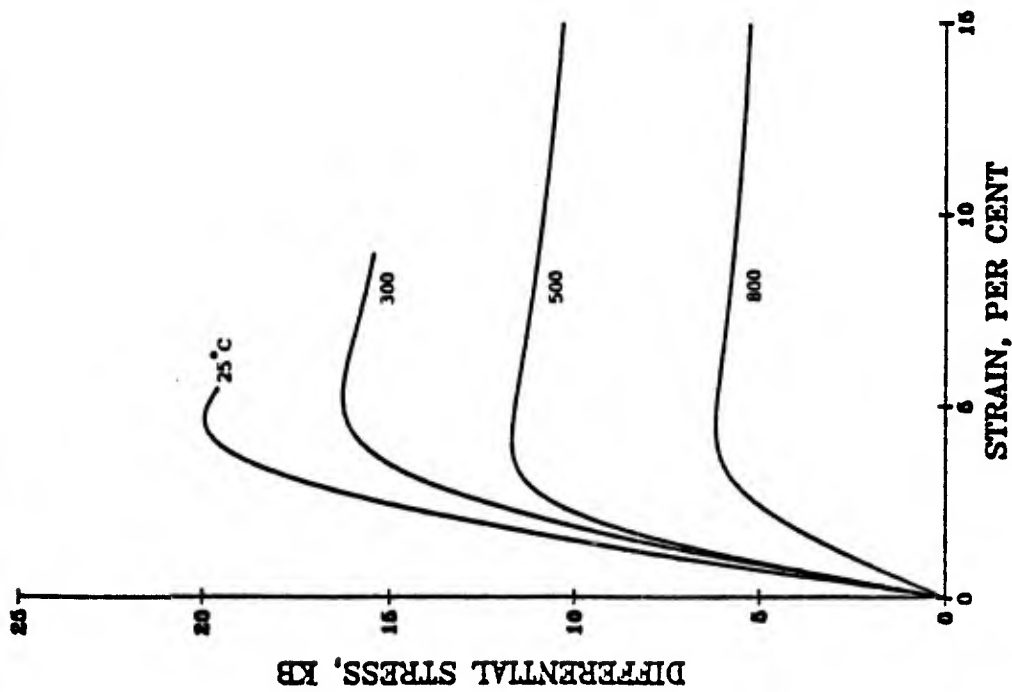


Figure 10a

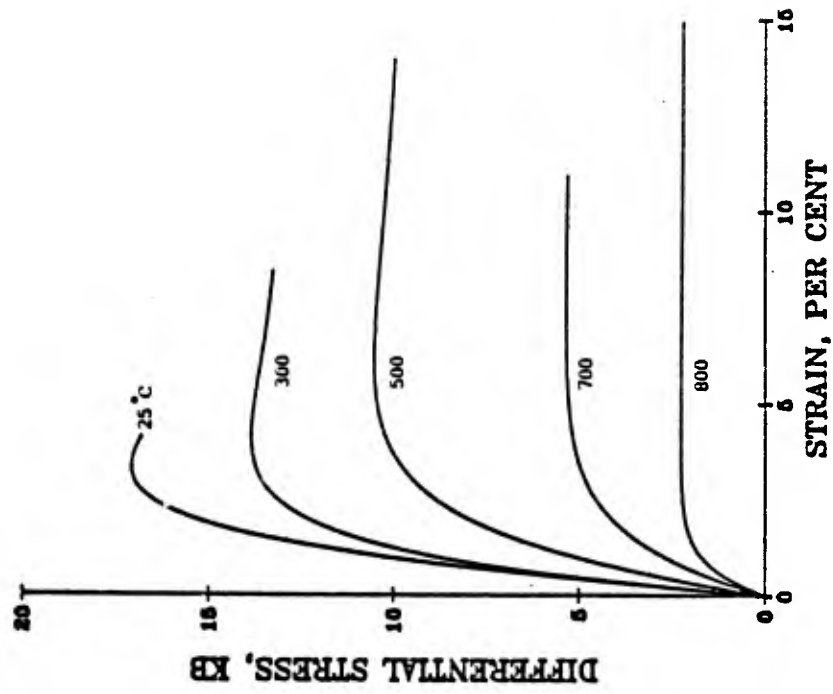


Figure 10b

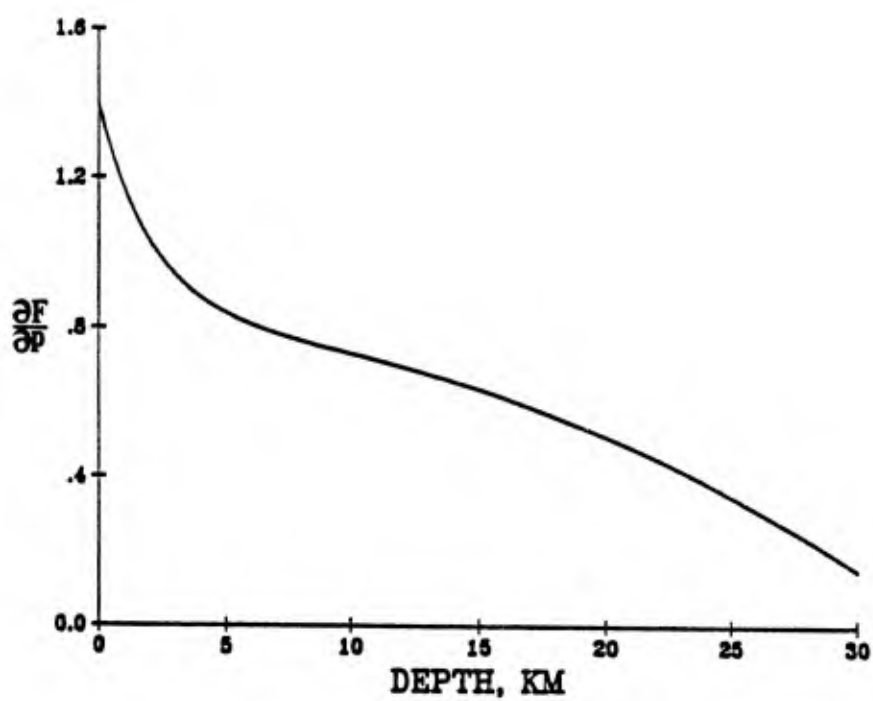


Figure 11a

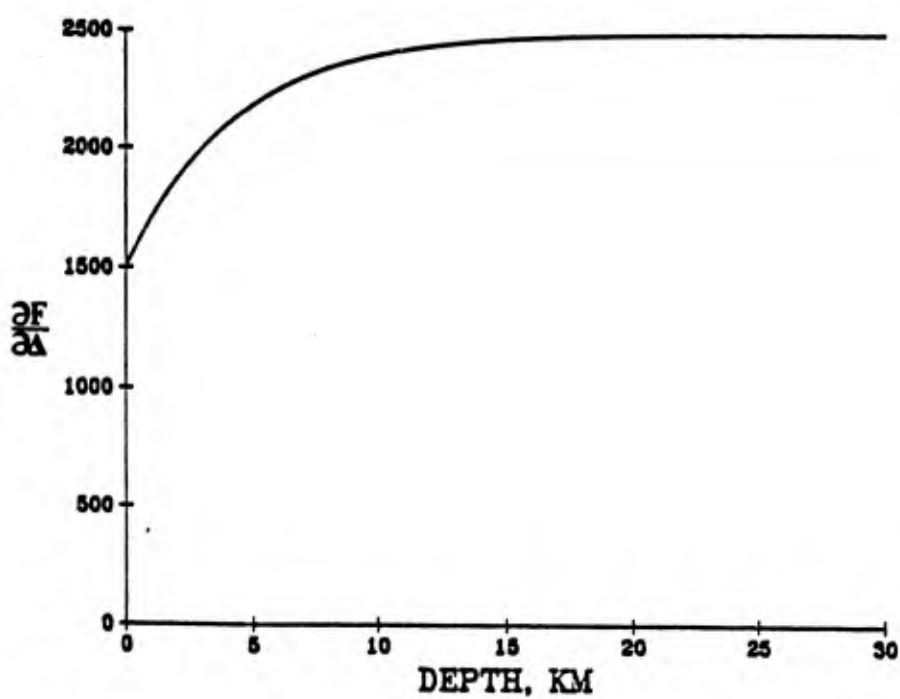


Figure 11b

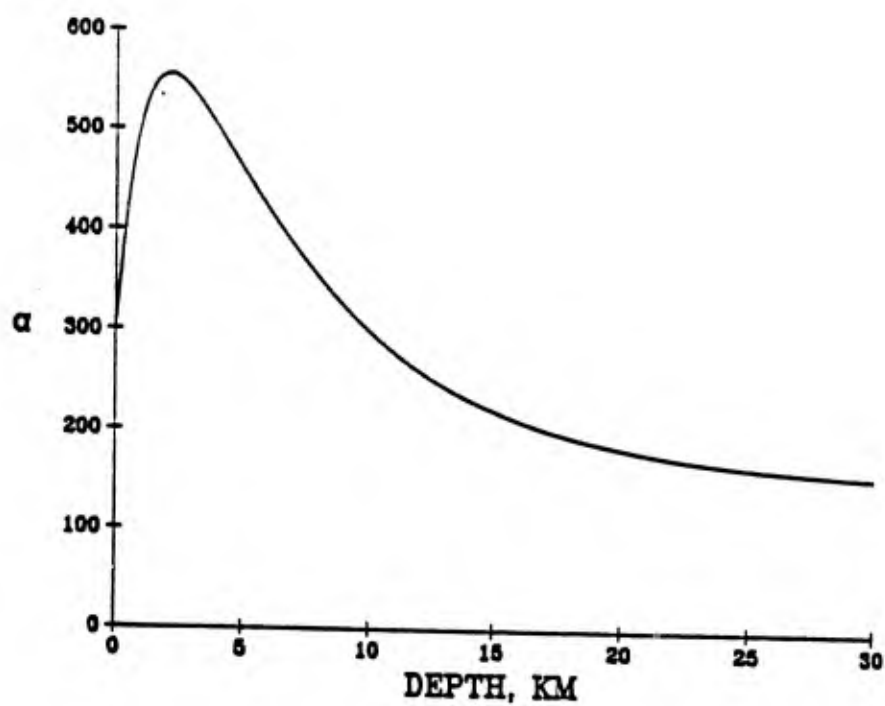


Figure 11c

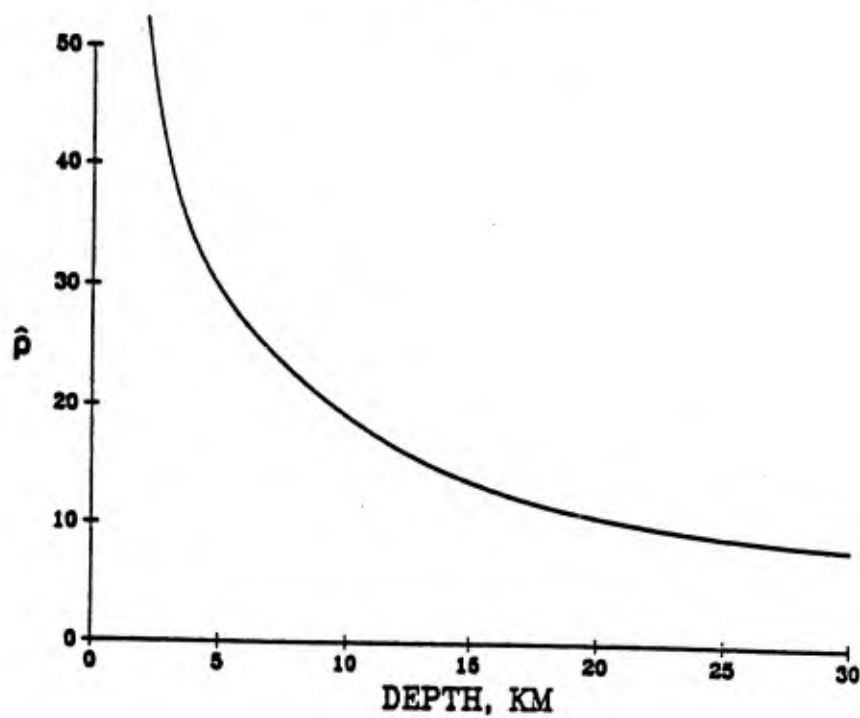


Figure 11d

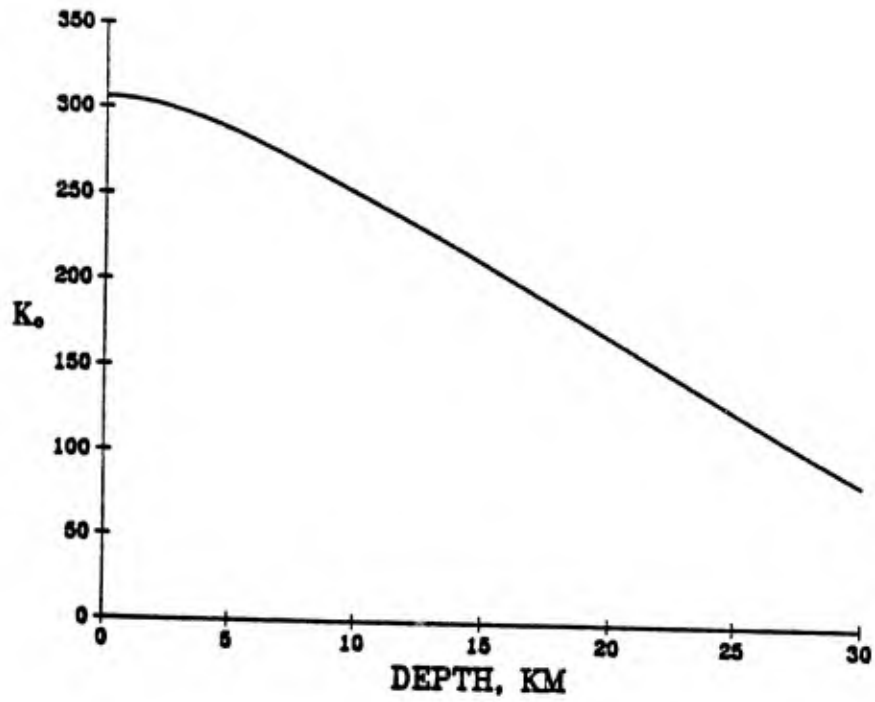


Figure 11e

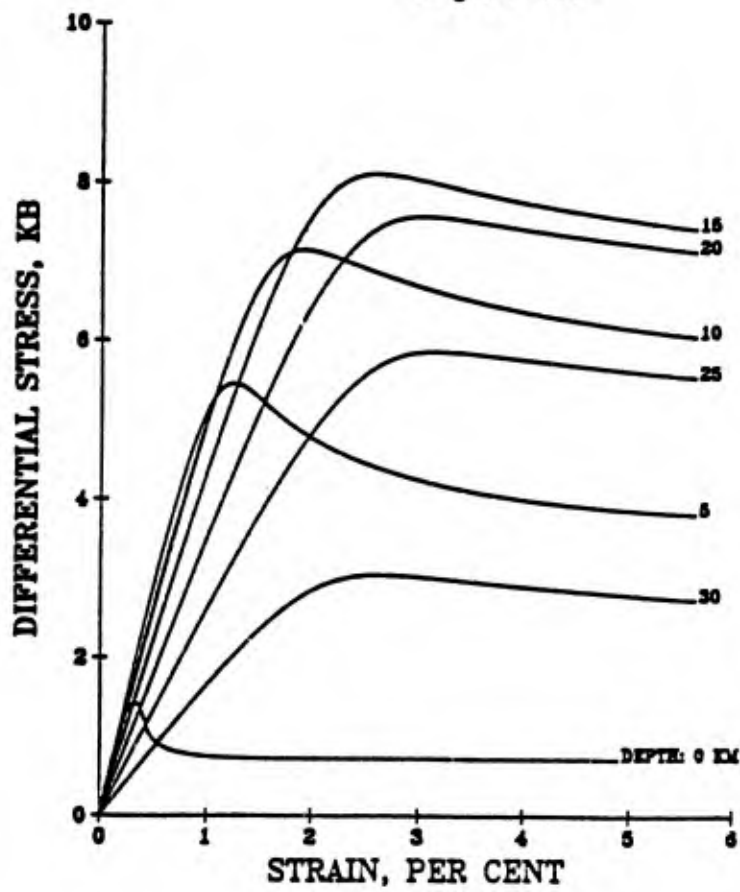


Figure 12

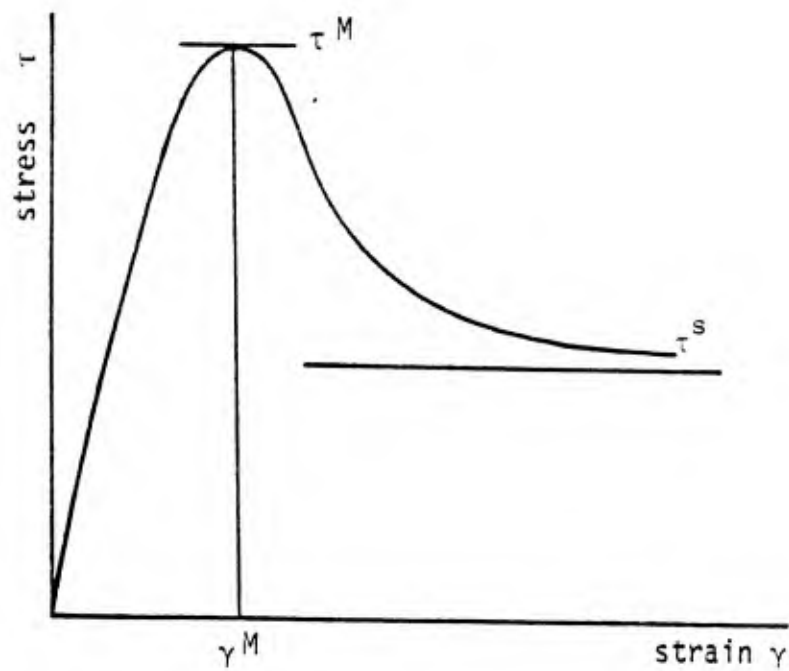


Figure A-1